Vortex-Induced Waves and the Mechanism of Drop Entrainment in Transition from Stratified to Dispersed Oil-Water Pipe Flows

by

Mohd Izzudin Izzat Bin Zainal Abidin

Submitted to the Department of Chemical Engineering in partial fulfilment of the requirements for the degree of

Doctor of Philosophy (Ph.D.) in Chemical Engineering

at University College London

March, 2019

Declaration

I, Mohd Izzudin Izzat Bin Zainal Abidin declares that this thesis has been composed solely by myself and that it has not been submitted, in whole or in part, in any previous application for a degree. Except where states otherwise by reference or acknowledgment, the work presented is entirely my own.

Mohd Izzudin Izzat Bin Zainal Abidin
March 2019

Acknowledgements

My pursuit of Ph.D. feels like travelling on a journey. Just like a long drive towards a vague destination, the biggest challenge is to take the right turns. Therefore, I would like to express my sincere gratitude to my supervisor, Prof. Panagiota Angeli for her continuous guidance and support to ensure that I am always heading towards the correct direction and providing me with a very strong foundation in this field of studies. Without exception, most parts of the journey are rough and bumpy. However, I was lucky to be surrounded by many great minds such as Dr. Park Kyeong Hyeon, Dr. Viktor Voulgaroupoulos and Teng Dong, just to name a few. I appreciate the motivations, encouragements and inspirations. Without them my journey would not be the same and as meaningful. There were times when I felt that I am struggling through many difficult moments. However, I was never alone and prayers from my parents and siblings have always be on my side. They are my strength that drives me towards my goal. I dedicate this thesis to my parents, Zainal Abidin and Rosidah Mamat.

Abstract

This dissertation presents new insights on flow pattern transition from stratified to non-stratified of two-phase oil and water flows in horizontal pipes. A novel approach is implemented to facilitate investigation of drop entrainment which identifies onset of the particular transition, where a cylindrical bluff body is located transverse to flow direction to induce instabilities in the form of vortex-induced interfacial waves in stratified flows. Numerical investigations of two-dimensional single-phase flows performed with CFD code FLUENT shows that vortex shedding frequency increases with decrease in the cylinder diameter while the size of vorticity region expands with increase in cylinder diameter. From the findings, two cylinder diameters, 2 mm and 8 mm are selected for experimental investigation in two-phase flows to generate vortex shedding frequency in the range of 1 to 100 Hz. Findings of high-speed visualization on the flow patterns and interfacial wave characteristics showed that higher instabilities were achieved with increasing cylinder diameter where the transition boundaries were shifted towards lower mixture velocities and waves with higher amplitude were produced. This is attributed to the size of vorticity regions, which are attached to the interface to actuate the vortex-induced waves as demonstrated by the particle image velocimetry (PIV) results. Variations of the vortex shedding behavior achieved by various cylinder diameters were found to be reflected on the resulting vortex-induced waves. The cylindrical bluff body approach is further implemented for the investigations of drop entrainment using a cylinder diameter that corresponds to gap ratio of 0.656 as it provides high instabilities at minimum wall effects. The use of simultaneous PLIF and PIV was introduced to visualize the wave's evolution with high spatial and temporal resolution while obtaining the velocity field around the waves at the same time. Drop entrainment was identified to occur through detachment of drop from interfacial waves and is formulated into a phenomenological model developed based on force balance. Further analysis of the deformed wave dynamics during drop detachment shows relation to the input flowrate ratio, *r*.

Impact statement

This work exhibits not only the new observation and understanding of the flow pattern transition from stratified to dispersed liquid-liquid flows but also our unique approach and methods on achieving the goal. The work is constructed from various elements which include the use of novel approach to facilitate difficult experiments, utilization of numerical analysis in the design phase prior to experimental investigation and the implementation of recent and advance technique for the purpose of improvements over the use of conventional techniques. For academia, the work provides new ideas and visions to plan and structure new research works. The bluff body approach and findings from this work could inspires various novel applications, i.e. to enhance mixing and mass transfer between two fluids and pioneers numerous studies by manipulating its shape. In addition, the recent measurement techniques used in this work could motivates its applications in different studies. The findings of the work particularly on the further understandings of the fundamentals of drop entrainment possess impact and contribution to the industries with flow patterns and phase distribution are of particular interest. With the new findings, modelling of the drop entrainment can be further improved and accuracy of the equipment and process design could be increased.

List of Figures

List of Tables

List of Symbols

A_{eff}	Effective area to calculate drag force
A	Cross sectional area of a pipe
C_D	Drag coefficient
C_L	Lift coefficient
D	Cylinder diameter
D_{eff}	Effective diameter to calculate drag force
D_h	Hydraulic diameter
D_p	Pipe diameter
D_{neck}	Neck diameter
D_{swell}	Swell diameter
f	frequency
f_v	Frequency of vortex shedding
Fr	Froude number
F_D	Drag force
F_σ	Interfacial tension force
h	Distance from bottom cylinder to adjacent wall
h_{swell}	Swell height
h_{top}	Height of swell top
h_{bottom}	Height of swell bottom
Q_o	Flowrate of oil
Q_w	Flowrate of water
$Q_{w/g}$	Flowrate of water/glycerol
r	Flowrate ratio
u	Velocity
u_i	Three components of the velocity vector
u_{mix}	Mixture velocity
u_{so}	Superficial velocity of oil phase
u_{surr}	Velocity of surrounding phase
u_{sw}	Superficial velocity of water phase
$u_{sw/g}$	Superficial velocity of water/glycerol phase
u_{swell}	Swell velocity
u_{max}	Maximum velocity
t	Time
Re_{pipe}	Pipe diameter based Reynolds number
Re_D	Cylinder diameter based Reynolds number
Re_i	Phase Reynolds number: '*i*' denotes the phase
k	Kinetic energy

St	Strouhal number
x, y, z	Three components of the spatial coordinate (streamwise, lateral and spanwise)

Greek letters

ε	Dissipation rate
ρ	Density
ρ_{oil}	Density of oil phase
$\rho_{w/g}$	Density of water/glycerol phase
μ	Viscosity
μ_{oil}	Viscosity of oil phase
$\mu_{w/g}$	Viscosity of water/glycerol phase
γ	Gap ratio
γ_s	Surface gap ratio
ω_i	Three components of the vorticity vector
σ	Interfacial tension

List of Abbreviations

CFD	Computational fluid dynamics
DC (O/W)	Dual continuous flow with oil drops
DC (O/W and W/O)	Dual continuous flow with oil and water drops
FFT	Fast Fourier transform
I.D.	Internal diameter
O	Oil
W	Water
W/G	Mixture of water and glycerol
PIV	Particle image velocimetry
PLIF	Planar laser induced fluorescent
ST	Stratified flow

List of Contents

Chapter 1

Introduction

1.1 Motivations

Two-phase gas-liquid and liquid-liquid flows in pipes are encountered in various industrial operations, for instance, in the energy, oil and process industries. Due to their wide range of applications, extensive studies on two-phase flows have been conducted, both experimental and theoretical. Although both fluid pairs are of great importance, existing literature covers mainly gas-liquid systems with relatively less studies available for liquid-liquid systems. Gas-liquid mixtures have large density and viscosity ratios which allow certain simplifications to be made that enable the development of models associated to their hydrodynamic behaviour. Liquid-liquid in contrast, have smaller viscosity and density ratio which result to small buoyancy effects (Taiter and Dukler, 1976). Therefore, due to the different flow behavior, hydrodynamic models developed for gas-liquid systems may not always be applicable to liquid-liquid ones.

The flow of two immiscible liquids is commonly found in petroleum industry where oil and water are often transported together for long distances. During their flows, the phases can be geometrically distributed in various ways resulting to diverse flow patterns or regimes. The flow pattern is one of the important features of two-phase flows, while each pattern has their own unique hydrodynamic characteristics. As a result, it significantly influences various flow properties and thus affecting the accuracy of operation design as well as flow measurements. Baker (1954) initially reported experimental observations of distinct changes in the pressure drop of oil-water horizontal flows related to changes in the flow patterns. In addition, the interfacial area per unit volume which is dependent on flow patterns significantly influences the rate of heat, momentum and mass transfer (Rouhani and Sohal, 1982). In a recent example, Zhai et al. (2015) highlights that knowing the flow pattern behaviour is essential to develop accurate well production logging instruments. The efforts on the study of the flow patterns have mainly focused on the identification of the patterns that

form at various flow conditions (i.e. liquid properties, flow properties and pipe inclinations).

Although the classifications of flow patterns for liquid-liquid systems have been consistent and well accepted in the literature, the dynamics of their transitions which involve drop entrainment, are yet to be fully understood. Studies on drop entrainment in two-phase flows have mostly been conducted in gas-liquid systems where it was found that drops are entrained through four different mechanisms namely, roll wave, wave undercut, bubble burst and liquid impingement (Berna et al., 2014). In liquid-liquid systems, only the first two types are expected to occur due to the relatively small viscosity difference between the two phases. However, due to the complexity of the experimental investigations as both phases may travel at high velocity, limited studies are available.

Studies of the occurrence of transition from stratified to non-stratified flows have been carried out mainly with high-speed imaging techniques (Trallero, 1997; Al-Wahaibi et al., 2007; Al-Wahaibi and Angeli, 2011; Barral and Angeli, 2013). It was found that the transition is associated with the increase in flow velocities and the appearance of interfacial waves. However, due to limited experimental observations available in the literature, the actual physical mechanism of drop entrainment from breaking interfacial waves is still not clear. Theoretical approaches based on the Kelvin-Helmholtz (KH) stability analysis have also been used to predict the boundaries between stratified and non-stratified flows (Al-Wahaibi and Angeli, 2007; and Carlos Torres, 2016).

1.2 Previous Works

Previously a novel approach was introduced in the work of Park et al. (2016) and Chinaud et al. (2017) by locating a cylindrical bluff body transverse to flow direction in the water phase of stratified oil-water flows to spatially localize the formation and breaking of interfacial waves in the wake of the cylinder. It was found that the approach results to passive actuation of flow pattern transition from stratified to non-stratified. The studies were conducted in a 37 mm I.D. acrylic pipe section using a single cylinder diameter of 5 mm.

Park et al (2016) found that presence of the cylinder shifted the boundary of transition from stratified (ST) to dual continuous flow (DC) towards lower mixture velocities as presented in a flow pattern map in Figure 1.1 while the change in flow pattern sustained at 7 m downstream the cylinder. The findings suggest that the presence of cylinder actuates instability in the two-phase flows that promotes the transition to occur. From the analysis by particle image velocimetry (PIV) technique, Chinaud et al. (2017) had reported that the flow fields in the wake of the cylinder for single phase flows were comparable with those obtained in a rectangular channel under two-dimensional (2D) flow conditions as presented in Figure 1.2. The results suggest that in the middle of the pipe (at which the flow field was obtained), the flow can be considered as two-dimensional with no effects of pipe curvature for the conditions investigated. The studies also revealed that the vortices shed behind the cylinder actuated interfacial waves that had the same frequency as the vortices.

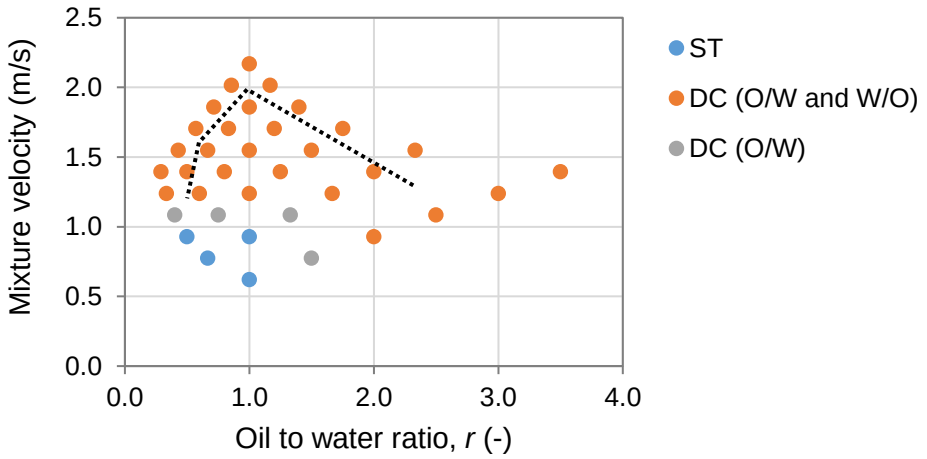

Figure 1.1: Flow pattern map at 7m downstream for a system with 5 mm diameter bluff body. *Dotted line presents the transition boundary for system without a cylinder. **Park et al. (2016)

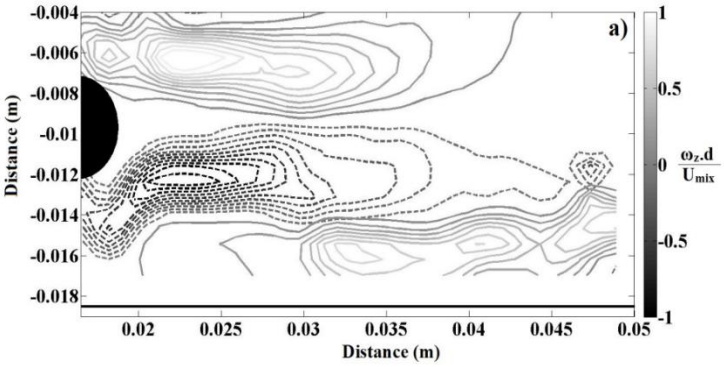

Figure 1.2: Time averaged span wise vorticity over distance from cylinder. *The solid lines correspond to positive regions while dashed lines correspond to negative regions. **Chinaud et al. (2017)

From findings of the previous works, it can be concluded that the bluff body approach promotes instability in two-phase liquid-liquid flows, which results to actuation of flow pattern transition at lower mixture velocities. This suggests that the approach can be further used to facilitate investigations of drop entrainment in stratified flows. Although it was revealed that the interfacial waves were generated at the frequency of vortex shedding which implies possibility to control the wave properties through the bluff body design, the studies are limited to a single cylinder diameter of 5 mm where the frequency range was limited between 8 to 32 Hz for the flow conditions investigated. Therefore, the influence of vortex shedding behaviour in two-phase stratified flows has not been fully understood. In this work, the cylinder diameters were varied to modify the vortex shedding behaviour and its effects on the stratified flow instability were investigated.

The similarity between the flow fields in the wake of cylinder on a two-dimensional plane at the middle of the pipe to unbounded flow suggests that it can be represented with a two-dimensional flow simulation. From this finding, the use of two-dimensional simulations to reproduce and investigate the wake can be implemented to reduce numerical simulation costs compared to three-dimensional simulations.

1.3 Objectives and Approaches

The main objectives of this work are to initiate the transition from stratified to dispersed flows in a controlled manner and to use this to study the mechanism of drop entrainment. The work includes the investigation of the dynamics of oil-water flows in the wake of cylinder of various diameters and visualization of drop entrainment mechanism in stratified flows. To achieve these objectives the following approaches were taken

- To select the cylinder diameters that can deliver a range of frequencies for the experimental investigations, numerical computational fluid dynamics (CFD) simulations were conducted. Two-dimensional simulations of single-phase (water) are performed as previous findings showed that this approach could represent the flow field in the middle plane of the pipe. The results of the simulations are analyzed to select the cylinder sizes based on the frequency of vortex shedding and the size of the vorticity region in the wake of cylinder.

- Experimental analysis was performed using the selected cylinder diameters from the numerical investigations. In order to understand the effects of cylinder size on the instabilities of two-phase stratified flows, two separate investigations were conducted in the wake of cylinders with different diameters, namely the properties of vortex shedding and the characteristics of interfacial waves. The vortex shedding behaviour were investigated by employing the particle image velocimetry (PIV) technique. Their effects on the flow instability are observed based on the flow pattern transition boundaries and the amplitude of interfacial waves measured with high-speed visualization.

- A novel approach was used to investigate the drop entrainment mechanism where an investigation region was created by a cylindrical bluff body which actuate and localize the drop entrainment immediately behind the cylinder. To achieve this, from the findings of the first objective, a pipe section was designed with a cylinder diameter that would give the maximum instability while minimizing the wall effects. Recently introduced advanced laser based technique was implemented to visualize the

entrainment mechanism and to obtain details of the flow in the pipe section.

1.4 Thesis Outline

This dissertation is structured into eight chapters. In this first chapter, a brief introduction of the topic was presented, while the aim and objectives of this work are given and the approaches are discussed.

In chapter 2, a literature review on flow pattern transitions in two-phase liquid-liquid flows is presented together with a review of flows across cylindrical bluff body. The review mainly focuses on the transition from stratified to non-stratified flows which involves the drop entrainment process. The aim of this review is to gather the information from existing works in the literature and to indicate the current state of research progress in this topic as well as the challenges. This information will help to formulate the objectives of this work.

The study is initiated with numerical analysis that is performed to investigate the properties of vortex shedding from cylinders of various diameters, presented in chapter 3. The objective of this investigation is to select suitable cylinder diameters for the experimental work. Details of the simulation setup are given and compared with experimental data by Chinaud et al. (2017). The vortex shedding properties generated by cylinders of various sizes are analyzed and discussed. Based on the frequency and the size of the vorticity region produced in the cylinder wake, two cylinder diameters are chosen that produce a wide range of vortex shedding frequencies and magnitudes.

With the cylinder diameters selected in chapter 3, inlet test sections are designed with the cylinder located transverse to flow direction in the water phase. Details of the inlet are presented in chapter 4 together with a description of the oil-water flow facilities used. Chapter 4 also presents various techniques implemented to acquire the velocity components, capture the waves generated in the wake of cylinder and visualize the drop entrainment events.

The results of the experimental investigations on the effect of cylinder diameter on flow pattern transitions in stratified oil-water flows are presented and discussed in chapter 5. The vortex shedding properties in the wake of cylinder are obtained from the analysis of the PIV measurements, both in single and two-phase flows. The findings of single-phase flows are also compared with the numerical analysis conducted in chapter 3. The instability of the two-phase flows

is characterized by the amplitude of interfacial waves generated in the wake of the cylinder. Investigation of the wave amplitude was performed from the high-speed visualization results. The connection between the vortex shedding properties and the interfacial wave characteristics is discussed in this chapter.

From the findings of chapter 5, the cylinder diameter that results to high instability in the stratified oil-water flows is identified. A geometrically similar but smaller in size inlet is designed for the second flow facility that has a smaller test section. In this flow facility, the refractive index of the aqueous and the organic phase is matched to enable PLIF and PIV measurements. With the combined techniques the deformation of interfacial waves in the wake of cylinder and the drop entrainment events can be visualized while the velocity of the aqueous phase around the deformed waves can also be measured. The results are presented in chapter 6. From the analysis of the captured wave deformation and drop entrainment events, a criterion for drop entrainment is proposed, based on a force balance analysis. The proposed criterion was validated by using the detailed experimental data on wave deformation and velocity fields measured in the aqueous phase.

The studies on the drop entrainment are further extended to investigate the dynamics of the deformed waves that lead to drop entrainment, presented in chapter 7. For this purpose, the deformed wave dynamics are characterized from the captured PLIF images. The results are analyzed in relation to the input parameters.

In chapter 8, the main findings from all chapters are summarized and final remarks are given. Conclusions from this study are drawn and recommendations for future work are proposed.

1.5 Conferences and Publications

Throughout the studies, progress and findings of this work have been presented in various local and international conferences. The results and findings were also reported in research journals, which were submitted for publications. The lists of conferences where the work in the thesis has been presented are as follows;

Research Journals

- European Journal of Mechanics - B/Fluids

  Title: *Vortex-Induced Waves in Two-Phase Liquid-Liquid Flows across Bluff Body of Various Sizes*

  Status: Revised manuscript has been submitted on Feb 2019.

  This research paper reports the findings of Chapter 3: Numerical Investigation of Single Phase Flows Past Cylinder of Various Sizes and Chapter 5: Flow Dynamics in The wake of Cylinder of Various Diameters.

- Chemical Engineering Science

  Title: *Mechanism of Drop Entrainment in Stratified Liquid-Liquid Flows in Horizontal Pipes: Drop Detachment from Interfacial Waves*

  Status: Under review

  This research paper reports the findings of Chapter 6: Drop Entrainment from Interfacial Waves in Stratified Flows.

Oral Presentations

- UK Fluid Conference 2016, Imperial College London, UK (Sept 2016)
- APS Division of Fluid Dynamics 2016, Portland, Oregon, US (Nov 2016)
- APS Division of Fluid Dynamics 2017, Denver, Colorado, US (Nov 2017)
- TMF Consortium, Imperial College London, UK (Sept 2018)

Poster presentations

- UCL Industrial Advisory Board Meeting, London, UK (Feb 2016)
- UK ChemEngDay 2016, Bath, UK (March 2016)
- UK ChemEngDay 2017, Birmingham, UK (March 2017)
- UK ChemEngDay 2018, Leeds, UK (March 2018)

Chapter 2

Literature Review

2.1 Two-Phase Liquid-Liquid Flows

In this section, the flow patterns of two-phase and particularly oil-water flows in pipes are reviewed from relevant works available in the literature. Distinct features of each flow regime are discussed with the aim of gaining better understanding of the classification and the transition boundaries between the flow regimes.

2.1.1 Types of flow patterns

The flow configuration or flow pattern established during the two-phase flows remains as one of the most important features of the flow due to its significant influences on the resulting flow properties such as the transfer rate, pressure drop and hold up which are essential design parameters.

In liquid-liquid system, formation of the flow structure is mainly caused by the large momentum transfer capacity and small buoyancy effects due to the small density difference between the phases. Therefore, the mechanism of phase distribution differs from the gas-liquid systems, which have large density differences and buoyancy effects. The type of flow pattern established during the two-phase flow determines important parameters which include pressure drop, heat and mass transfer coefficients. As a result, each flow pattern can have different properties which may be desirable or detrimental depending on the process. Therefore, one of the motivations for the study of flow patterns comes from the potential to choose or control the flow pattern that forms in a process to provide optimum results.

The types of flow patterns established are influenced by various factors. These include the fluid properties (density and viscosity), flow properties (velocity and volume fraction) and the geometry of the flow system (inlet conditions, pipe size, material and inclination). Many studies, particularly for the oil-water flows have been reported in the literature which have mostly concentrated on the identification and classification of the flow patterns. A summary of the works is

presented in Table 2.1. Initially, direct visual observation techniques were the most common approaches for identification of the flow patterns. For this purpose, experiments were conducted in transparent pipes and images were captured or recorded externally with a high-speed camera. In some cases, however, there are difficulties to accurately distinguish between the two phases. This may occurs due to poor visibility especially at high flow velocities, very disturbed interfaces and in the presence of dispersions. Therefore, with the advancement of instrumentation for in-situ measurements in the flow, visual observation techniques can be complemented by instruments such as conductivity probes for the flow pattern identification (Angeli & Hewitt, 2000; Brauner, 2002).

The various types of flow patterns that have been observed in oil-water flows can be observed in Table 2.1. As can be seen, the pipe size and the oil viscosity affect the patterns significantly. The annular, slug and plug flow patterns are only observed for flow in pipes with small diameter and for very high oil viscosities (Beretta et al., 1997; Shi and Yeung, 2017). The other major types of flow pattern are observed in almost of the studies. Although the authors had used different nomenclatures, the classifications of flow patterns in low-viscosity oil-water flows have been consistent. Trallero et al. (1997) had proposed a widely accepted classification of flow for low-viscosity oil-water flows in horizontal pipes which are categorized into two main categories: separated and dispersed flow regime.

The separated flow regime is associated with the existence of two-continuous layers with an interface that could be either smooth or wavy. The flow patterns included in this category are stratified flow (ST) and stratified with mixing at the interface (ST and MI) with the presence of drops which is also introduced as dual continuous flow (DC). Stratified flow with smooth interface is commonly observed at very low flow velocities and as the velocity is increased, the interface becomes disrupted and interfacial waves are formed. As an intermediate flow pattern between stratified and dispersed flow regime, dual continuous flow pattern appears in a wide range of mixture velocities and input oil volume fractions especially for the case of low viscosity oil making this flow regime to be one the important regime to be studied (Lovick and Angeli, 2004).

Table 2.1: Experimental studies of oil-water flow patterns in a pipe.

Authors	Pipe ID (mm)	Pipe material	Oil Properties			Flow Patterns	Identification Methods
			μ (mPa s)	ρ (kg/m^3)	σ (mN/m)		
Guzhov et al. (1973)	39.4	Steel	21.8	896	44.8	ST, o/w emulsion and w/o emulsion	Visualization
Trallero et al. (1997)	50	Acrylic	28.8	884	36	ST, ST & MI, Do/w & w, o/w, Dw/o & Do/w, w/o.	Visualization
Beretta et al. (1997)	3	Glass	(i) 6.17 (ii) 4.55 (iii) 0.85	(i) 866.48 (ii) 886.25 (iii) 865.50	(i) 31.5 (ii) 36.0 (iii) 37.4	Dispersed, plug, annular, slug and bubbly.	Visualization
Nadler and Mewes (1997)	59	Perspex	22-35	841	-	ST, ST & MI, w/o and o/w	Conductivity probe
Angeli and Hewitt (2000)	24	Steel Acrylic	1.6	801	17	ST, ST with drops, three layers, St with water layer, mixed.	Visualization and impedance probe
Shi et al. (2001)	100	Plexiglass	3	820	33.4	ST and mixed dispersion.	Visualization
Lovick and Angeli (2004)	38	Steel	6	828	39.6	ST, Dw/o, Do/w, DC	Visualization, conductivity and impedance probe.

Table 2.1 (cont.): Experimental studies of two-phase oil-water flow patterns in a pipe.

Authors	Pipe ID (mm)	Pipe material	Oil Properties			Flow Patterns	Identification Method
			μ (mPa s)	ρ (kg/m^3)	σ (mN/m)		
Edomwonyi-Out & Angeli (2015)	14	Acrylic	5.5	828	39.6	ST, ST & MI (DC), Do/w, Dw/o, rivulet.	Visualization
Hanafizadeh et al. (2015)	20 (Horizontal and inclined)	Acrylic	1	840	-	ST, bubbly, slug, churn, annular, DC.	Visualization
Zhai et al. (2015)	20	Acrylic	11.984	845	35	ST, ST & MI (DC), Dw/o & Do/w, Do/w & w, Do/w, Dw/o.	Conductance probe
Shi and Yeung (2017)	26	Perspex	(i) 3300 (ii) 16000	-	-	Annular, oil plug in water, dispersed oil lumps in water.	Visualization

In the dispersed flow regime, one of the phases has lost its continuity and is distributed in the form of drops in the other phase, resulting in either dispersion of oil in water or dispersion of water in oil. Dispersed flow patterns can be dispersion of oil in water and water (Do/w & w), dispersion of water in oil (Dw/o) and dispersion of oil in water (Do/w). Schematics of the major flow regimes reported in the literature for low-viscosity oil-water flows in horizontal pipes are presented in Figure 2.1. In this work, the interest is on the low-viscosity oil-water flows in a considerably large pipe.

2.1.2 Flow pattern map

For a quantitative description of the conditions which lead to the transition of flow patterns from one to another, two of the main flow parameters may be used to define a coordinate system where the boundaries between various flow patterns can be shown. The resulting graph is called the flow pattern map and the boundaries between the flow patterns can be identified as transition lines (Rouhani & Sohal, 1983). An example of a flow pattern map for an oil-water system is shown in Figure 2.2 with the lines representing the transition boundaries. There are many coordinate systems for flow pattern maps proposed by different investigators. For oil-water flows, the superficially velocities of the phases are commonly used as coordinates system such as in the work of Beretta et al. (1997), Trallero et al. (1997) and Shi and Yeung (2017). Trallero et al. (1997) and Angeli & Hewitt, (2000) also used the water cut and the mixture velocity as coordinates of the map.

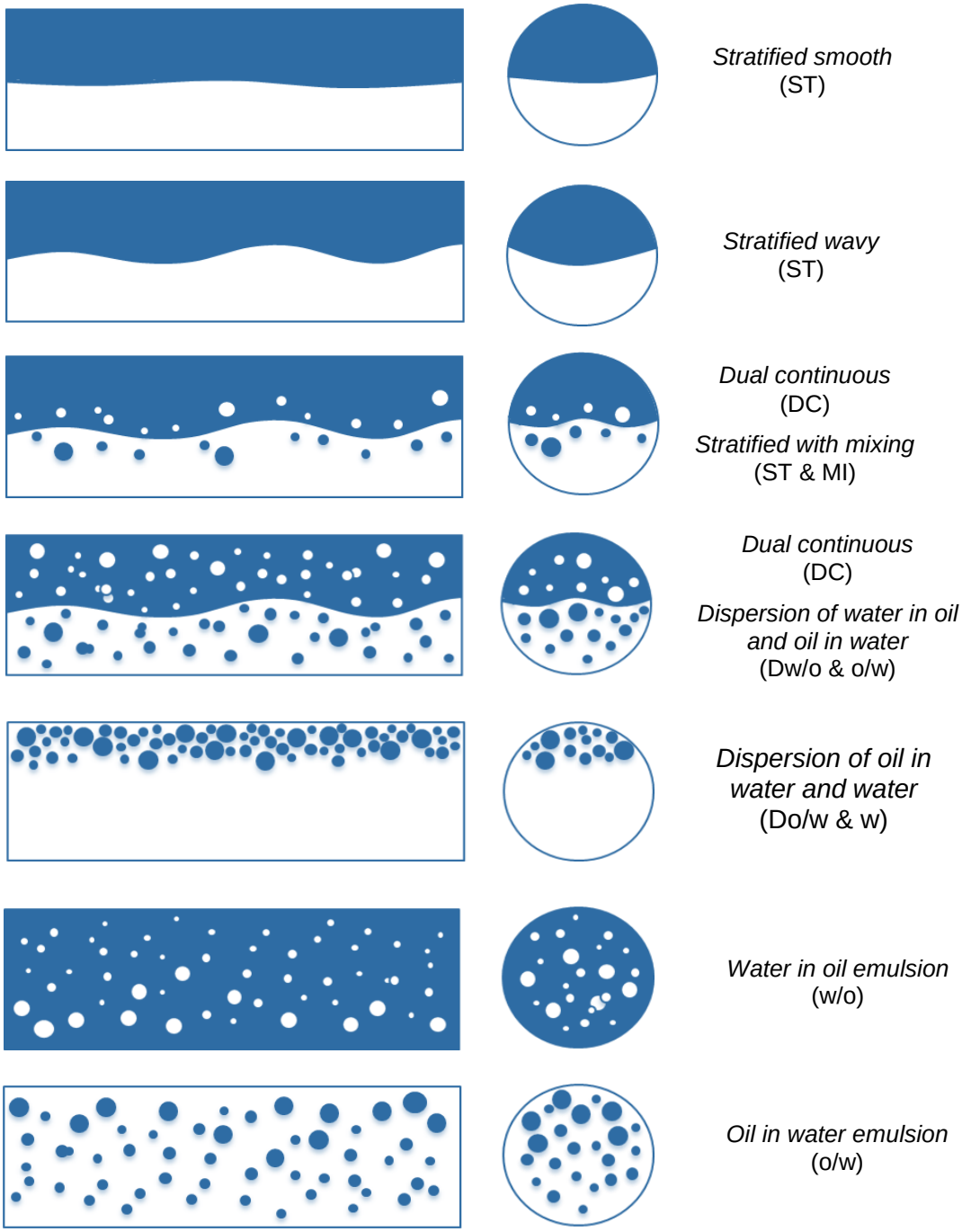

Figure 2.1: Illustration of common types of flow patterns observed in oil-water flows in a pipe.

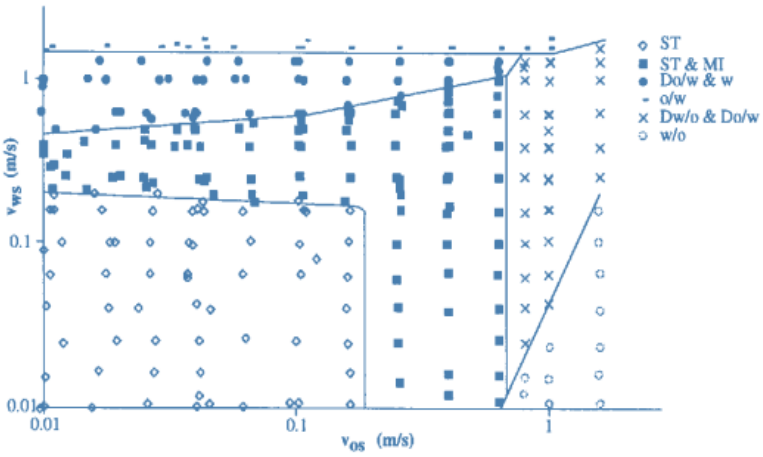

Figure 2.2: Flow pattern map for oil-water system.*Trallero et al. (1997)

The maps, however, are limited to the investigated fluids in a fixed geometry and often it is difficult to compare results from different investigators. In addition, the flow pattern transitions are complex and may depend on various factors other than the two variables used as coordinates system in the flow pattern map (e.g. inlet conditions, pipe wettability). Therefore, the flow pattern maps cannot be generalized for different fluids and systems and to be used for the prediction of flow pattern transitions. At the moment there is no universal flow pattern map to identify the transition boundaries for different systems. This highlights the importance of further studies on the mechanisms underpinning flow pattern transitions.

2.2 Flow Pattern Transition

This section reviews the flow pattern transition with focus on the transition from stratified to dual continuous and dispersed flows. The phenomena observed in oil-water stratified flows that lead to flow pattern instability are discussed.

2.2.1 Transition from stratified to dispersed flow

Generally, the transition from stratified to dispersed flows happens through entrainment of drops and dispersion process while transition from dispersed to stratified flow occurs as a result of coalescence. Studies on entrainment and

coalescence are often conducted separately. The transition from stratified to dual continuous and dispersed flows happens when drops of one phase entrain into the other from the breakage of its continuous layer. Therefore, the transition from stratified to non-stratified flow is identified with the formation of interfacial waves, their breakage and the onset of drop entrainment. Experimental investigations of the transition are conducted near the flow pattern boundaries where the drop entrainment occurs. In the following section, literature review on this particular type of transition is presented.

2.2.2 Interfacial waves in stratified flows

The relation between formation of unstable interfacial waves and drop entrainment had led to investigations of the interface characteristics during transition from stratified to non-stratified flows. This transition is mainly caused by the increase in the flow velocities. Guzhov et al. (1973) explained that at high velocities, the action of turbulent vortex motion near the interface causes the interface to roll and deform. Theoretically, the interfacial wave formation has been linked to the Kelvin Helmholtz (KH) instability occurring when there is velocity difference between the two fluids. The shear created at the interface induces formation of vorticity and causes the interface to roll, forming waves. Therefore, in liquid-liquid flow, interfacial waves are formed when the phases are moving at different velocity which can be characterized by the oil to water flowrate ratio, r, defined as the ratio of oil flowrate to water flowrate. Barral & Angeli (2015) reported that interfacial waves are not observed when the two phases are moving at the same velocity.

2.2.3 Interface characteristics and instability in stratified flows

Studies of interfacial waves in two-phase liquid-liquid flows are of great importance as key parameters such as pressure drop and hold up are influenced by the wave characteristics as demonstrated by Rodriguez and Baldani (2012). In the work of Edomwonyi-Otu and Angeli (2015), a two-fluid model modified to include the interface waviness was able to improve predictions of pressure drop compared to a model that considered a flat interface.

The significance of interfacial waves on the transition from stratified flows had been reported in previous studies such as in the review of Rouhani and Sohal (1983) and Trallero et al. (1997). However, experimental data on the wave

instability and flow pattern transitions particularly in liquid-liquid flows are still limited and the mechanism of drop entrainment is not clear. An attempt to investigate the interfacial wave instabilities was made by Al-Wahaibi and Angeli (2007) who investigated experimentally oil-water flow in horizontal pipe using high-speed video imaging. They found that waves with short wavelength and small amplitude will normally decay downstream the test section while waves with long wavelengths are unstable and will grow in amplitude as they propagate along the pipe. It was also reported that unstable interfacial waves have to reach a certain critical amplitude value before entrainment can occur. This was validated in subsequent work (Al-Wahaibi and Angeli, 2011) in which wave characteristics were studied with high speed imaging and a parallel wires conductivity. It was concluded that in stratified flow, waves must become unstable for drop entrainment to occur.

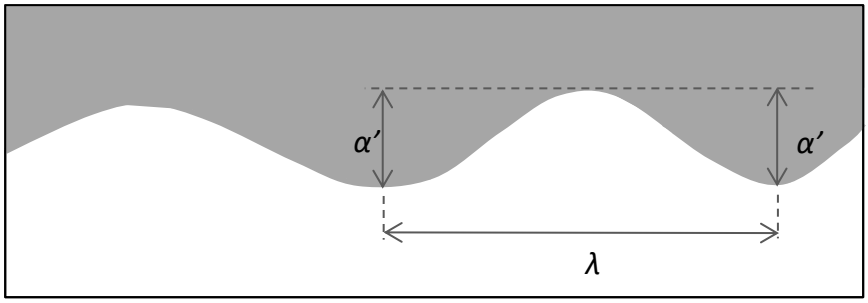

Figure 2.3: Measurement of wavelength and amplitude of interfacial wave.

Castro et al. (2012) investigated the geometrical and kinematic properties of oil-water interfacial waves and obtained the wavelength, λ and amplitude, α as illustrated in Figure 2.3. It was reported that the wave wavelength and amplitude are influenced by the hold up, inclination and relative velocity of the phases which was characterized by the Froude number, *Fr* which was defined as the inertia through the relative velocity between phases, to the gravitational forces. Unstable waves with large amplitude and long wavelengths were observed at low *Fr* (large velocity difference between the two phases) while the waves were also steeper (high amplitude and short wavelength).

Barral and Angeli (2013) investigated the oil-water flow interface characteristics using a double wire conductance probe and reported that large waves are only observed near to inlet where the two phases join for flow ratio, *r* different than one, which however disappeared soon after. The transition to dual

continuous flow is delayed to high mixture velocities for flow conditions which corresponds to r = 1. The delayed transition seems to be cause by the absence of interfacial waves when r = 1 which was further confirmed by Barral et al., (2015). Increasing the mixture velocities at constant flowrate ratio only lead to waves with rougher interface, but not the average interface height.

2.3 Drop Entrainment

The drop entrainment process is discussed in this section based on literature in both gas-liquid and liquid-liquid systems. Current approaches on modelling the drop entrainment are also reviewed.

2.3.1 Mechanism of drop entrainment

In two-phase flows, drop entrainment was reported to occur through the breakage of interfacial waves forming as a result of the Kelvin-Helmholtz (KH) instability (Trallero, 1997). The entrainment process, however, is still not clear with very limited experimental observations reported in the literature. Studies on drop entrainment in two-phase flows have been mostly conducted in gas-liquid systems. Berna et al. (2014) summarizes that for concurrent flows, drops can be entrained into the other phase through four types of entrainment mechanisms, namely roll waves, wave undercut, bubble burst and liquid impingement. However, in liquid-liquid systems, only the first two types are expected to occur (refer Figure 2.4) due to the relatively small density and viscosity difference between the phases. In liquid-liquid systems, entrainment of either phase or both phases could occur depending on the physical properties of the fluids and the flow conditions.

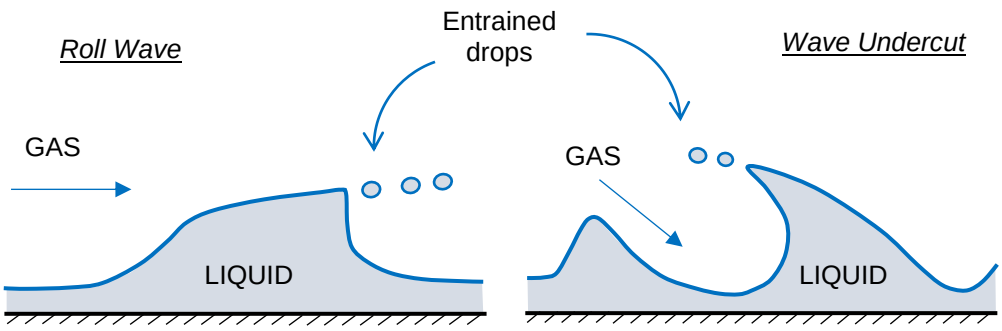

Figure 2.4: Drop entrainment through rolled wave and wave undercut.

2.3.2 Visualization of drop entrainment events

While many works have reported that the drop entrainment is initiated by formation of unstable interfacial waves, experimental observation on the mechanism of drop entrainment particularly in liquid-liquid flows are limited with most studies were conducted for gas-liquid system. Examples of work in gas-liquid annular flows include the visualization of drop entrainment events by Lecoeur et al. (2010) which employed axial-view high-speed imaging technique while in recent work of Alekseenko et al. (2014), laser induced fluorescent (LIF) technique was employed. The technique allows one to perform field measurements of the local film thickness with high spatial and temporal resolution. This gives the possibility to investigate spatial and temporal evolution of the drops simultaneously with evolution of the waves.

In liquid-liquid flows Al-Wahaibi and Angeli (2007) and Al-Wahaibi et al., (2007) visualized the drop entrainment using high-speed imaging. The authors reported that an interfacial wave deforms before its crests elongates and forms a ligament from which a drop detaches. An example of the entrainment event is presented in Figure 2.5. This mechanism of drop formation is similar to the breakdown of disturbance waves by undercutting as described by Hewitt and Hall-Taylor (1970) and Ishii and Grolmes (1975) for gas-liquid flows.

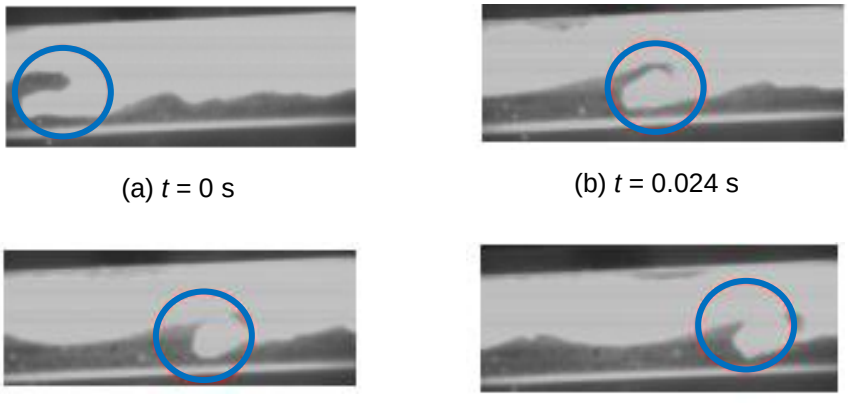

(a) t = 0 s (b) t = 0.024 s

(c) t = 0.032 s (d) t = 0.040 s

Figure 2.5: Events of drop entrainment for oil-water flows. *u_{so} = 0.44 m/s and u_{sw} = 0.50 m/s

Experimentally, it is challenging to acquire and visualize the drop entrainment process during pipe flow. This is due to the difficulties in conducting

visualization at the boundaries between stratified and dispersed flow as it usually occurs at high flowrates, where the interface is very disturbed. In addition, the drop entrainment process is transient in nature with uncertainty on where it will occur. Thus, the probability of capturing the event is low.

More examples on visualization of drop formation are available for flows in micro channels (e.g. Anna et al. (2003); Garstecki et al. (2006); Husny and Cooper-White (2006); Glawdel et al. (2012); Loizou et al. (2018)). Visualization of drop formation in the small channels is experimentally less complicated and the drop formation can be localized through the geometrical design of the system (T-junction or channel).

2.3.3 Current approach in drop entrainment modeling

In many modeling efforts reported in the literature, a force balance on the wave crest is considered to determine the conditions for drop entrainment. For example, Ishii and Grolmes (1975) and Kataoka et al. (1983) applied it for drop entrainment from waves in gas-liquid annular flow. Two types of forces were considered which are deforming and resisting force where drop is entrained when the deforming force overcomes the resisting force. In two-phase flows, the deforming force is identified as drag force F_D while the resisting forces are the surface tension, F_σ and the gravitational force, F_g;

$$F_D > F_\sigma + Fg \tag{2.1}$$

The drag force, F_D, is caused by the velocity difference between the wave crest and the surrounding fluid and can be estimated as (Al-Wahaibi et al., 2007);

$$F_{\mathrm{D}} = C_{\mathrm{D}} A_{oil\ wave} \rho_{\mathrm{w/g}} \frac{(u_{\mathrm{w}} - u_{\mathrm{oil}})^2}{2} \tag{2.2}$$

In Eq. 2.2, C_D is the drag coefficient, $A_{oil\ wave}$ is the area of oil wave crest, ρ_w is density of the water phase, u_{sw} is the superficial velocity of the water phase and u_{so} is the superficial velocity of the oil phase.

For drops, unlike solid particles, the drag coefficient depends on the internal circulation as a result of interfacial friction. Buzzard and Nedderman (1967) found significant dependence of C_D from the drop viscosity. The effect of

internal circulation can be characterized by the viscosity ratio between the liquid in the wave and the surrounding fluid which has to be considered in the estimation of C_D (Kelbaliyev, 2011). Kataoka et al. (1983) proposed a correlation for C_D, for waves in gas-liquid annular flow:

$$C_D = 286 Re_{Lf}^{1/6} Re_g^{-2/3} \left(\frac{\rho_g}{\rho_{Lf}}\right)^{1/3} \left(\frac{\mu_g}{\mu_{Lf}}\right)^{-2/3} \quad (2.3)$$

In Eq. 2.3, *Re* is the Reynolds number, ρ is the density and μ is the phase viscosity. The *Lf* represents the annular liquid film while *g* is the gas phase. Al-Wahaibi et al. (2007) modified the correlation to be used for liquid-liquid system as follows:

$$C_D = 286 Re_{slower\ phase}^{1/6} Re_{faster\ phase}^{-2/3} \left(\frac{\rho_{oil}}{\rho_{w/g}}\right)^{1/3} \left(\frac{\mu_{oil}}{\mu_{w/g}}\right)^{-2/3} \quad (2.4)$$

In Eq. 2.4, the phase Reynolds number is defined as $Re_i = u_i Dw_i \rho_i / \mu_i$ where u_i is phase in situ velocity and D_i is the hydraulic diameter.

The interfacial tension that tends to resists the deformation is modelled based on the interface shape at the onset of entrainment. For interfacial waves, as discussed by Holowach et al. (2002) and Al-Wahaibi et al. (2007), the resisting force is taken as the interfacial tension force acting on the wave crest in the direction that tends to restore the wave to its original shape (see Figure 2.6).

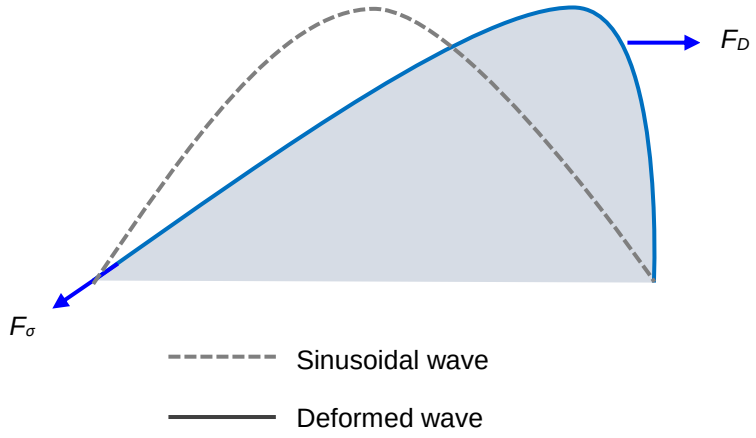

Figure 2.6: Force balance on a deformed interfacial wave prior to entrainment. *Re-illustrated from Al-Wahaibi et al. (2007)

In the case of drop formation from a nozzle (e.g. Scheele and Meister, 1968) or from T-shaped microchannel (Glawdel et al. 2012), the interface can take the shapes as shown Figure 2.7. The following equation can be to estimate the interfacial tension force, F_σ on the neck (Husny and Cooper-White, 2006);

$$F_\sigma = \pi\sigma D_{neck} \tag{2.5}$$

In Eq. 2.5, where σ is the interfacial tension and D_{neck} is the diameter of the neck. In these cases the width of the channel or opening of the orifice/nozzle is used, as the neck is bounded by its width.

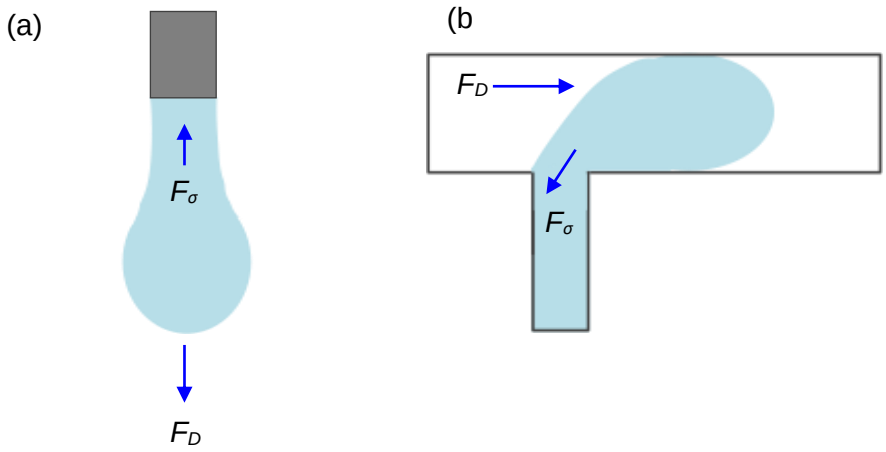

Figure 2.7: Force balance on drop formation. (a) from nozzle (b) at T-junction

Holowach et al. (2002) extended the force balance approach and calculated the maximum volume of liquid that can be entrained from a wave in a gas-fluid system. The force balance approach was also applied to develop an entrainment criterion in stratified liquid-liquid pipe flows by Al-Wahaibi et al. (2007).

To validate proposed models on drop entrainment, information on wave characteristics and phase velocities is required. Most experimental investigations have employed photographic technique to study the drop entrainment process. These are however limited to cases where the interfaces are not very disturbed. Velocity fields can be obtained with particle image velocimetry techniques (PIV). For example, Timgren et al. (2008) applied PIV to study velocity fields in both phases during drop formation at a junction.

2.4 Flows Across a Bluff Body

In this section, experimental and numerical studies on flows across a bluff body and the vortex dynamics in its wake are reviewed. Incompressible flow past a bluff body is encountered in various processes such as heat exchangers and off-shore structures. The problem usually involves incoming flows across a no-slip body as illustrated in Figure 2.8. Studies on flows across various bluff body shapes have been conducted such as rectangular (e.g. Chen et al. 2015; Bruno et al. 2010) or ellipsoidal (Kumagai et al. 2011) and for different configurations i.e. tandem (Ong et al. 2017). However, most of the studies in the literature have focused on flow past a stationary smooth cylindrical bluff which is relevant in many of engineering applications. Therefore, the review will focus on the works conducted on flows across a cylinder.

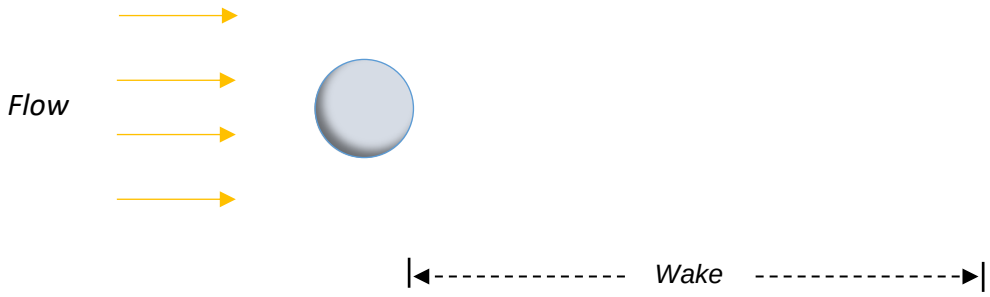

Figure 2.8: Flow across a solid object.

Several phenomena can appear at the wake of the cylinder, which is the region downstream of the cylinder (Figure 2.8). These include flow separation, vortex shedding and turbulence at relatively low flow velocities. Both the laminar and turbulent unsteady flows in the wake of the cylinder have been studied.

2.4.1 Characteristics and properties of flow across a cylinder

2.4.1.1 Flow separation

Most of the dimensionless quantities describing the flow around a smooth cylinder depend on the cylinder Reynolds number, Re_D which is defined in Eq. 2.6, where D is the cylinder diameter, and u is the incoming velocity.

$$Re_D = \rho u D / \mu \tag{2.6}$$

The variation of flow features in the wake of the cylinder is mainly due to the flow separation on the no-slip surface which appears at Re_D = 5 (Williamson, 1996). The phenomenon is associated with the pressure gradient established on the cylinder surface that causes acceleration and deceleration of flow around the surface. The different pressure regions around the cylinder is illustrated in Figure 2.9. The location of the separation points influences the size of the wake region which varies for laminar and turbulent flows. In laminar flow, separation occurs as a result of energy loss due to viscous effects as the boundary layer is unable to adjust with the increasing pressure. For turbulent flow, the separation points are delayed further behind the cylinder due to the higher kinetic energy and result to reduced size of wake as shown in Figure 2.9. The separation point can also vary for different bluff body shapes (Shao and Zhang, 2006).

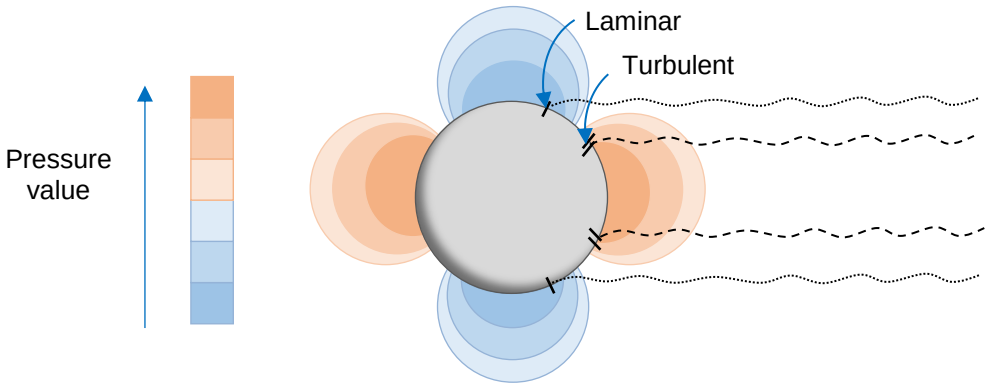

Figure 2.9: Schematic of pressure distribution during flow past a cylinder. *Separation points for laminar and turbulent flow are shown.

2.4.1.2 Cylinder wake regime

The characterization of the flow regime in a bluff body wake has mainly been conducted for smooth cylinders. Depending on the cylinder Reynolds number the wake can be divided into laminar regime for $Re_D < 200$ and turbulent regime for $Re_D > 200$.

In the laminar regime, no separation of flow (creeping flow) is observed at very small $Re_D < 5$. Above this Reynolds number, flow separation begins to occur resulting to a fixed pair of symmetric up to $Re_D = 40$. Up to this Reynolds number, the wake is steady. Unsteady wakes are established with the onset of alternate vortex shedding at $Re_D > 40$ (Williamson, 1996) where a laminar vortex street is formed for of $40 < Re_D > 200$. Transition to turbulent wake happens at $200 < Re_D > 300$ and the wake becomes completely turbulent at $300 < Re_D > 3 \times 10^5$. The latter regime is also called as the subcritical regime. Almost all of the studies reported in the literature have been conducted for cylinder Reynolds numbers up to the subcritical regime. In the following section, the main feature of the flow across cylinder which is the vortex shedding phenomenon that occurs at very wide range of cylinder Reynolds number ($Re_D > 40$) will be discussed.

Vortex shedding occurs as results of flow separation from the top and bottom surface of the cylinder. The separated boundary layers contain significant amount of vorticity and will roll to form vortices in the rear of the cylinder with the sign of vortices identical to the sign of incoming vorticity. Due to instability, one vortex will grow larger than the other. The interaction between the two opposite sign of vortices will lead to shedding of vortices from the top and bottom separated boundary layers (see Figure 2.10). The top boundary layer flows into vortex A with vorticity in clockwise direction while the bottom boundary layer flows into vortex B (anticlockwise). The larger vortex A is presumably strong enough to draw the opposing vortex across. This results to an interaction between the vortices of opposite sign; vortex B will cut the supply of vorticity to A. At some point, vortex A is shed and a new vortex C is created. The detached vortex A will propagate along the flow direction while vortex B will grow in size, repeating the role of vortex A to attract vortex C and finally detaching.

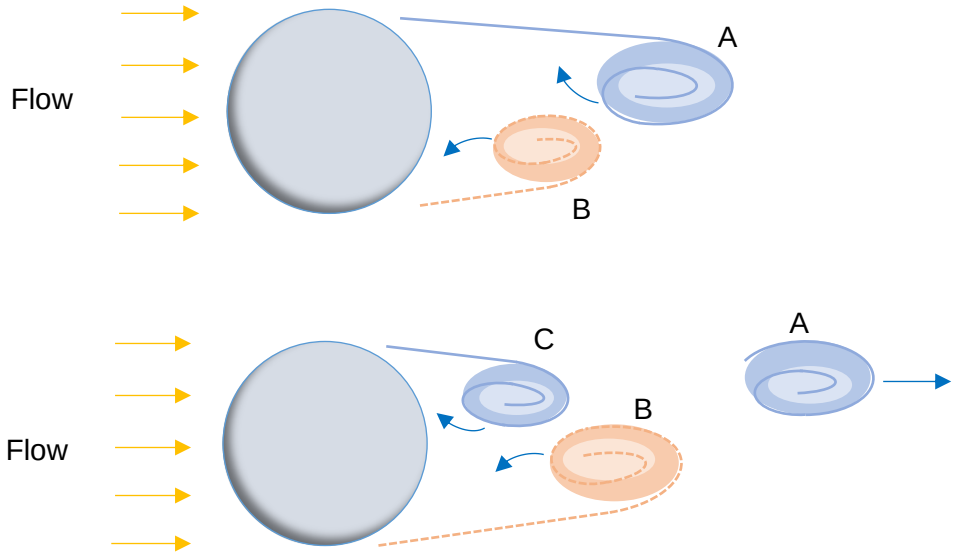

Figure 2.10: Illustrations of the alternate vortex-shedding process.

The alternate vortex shedding results to a pattern similar to the von Karman vortex street in the wake of the cylinder. The vorticity in the wake of cylinder that occurs as the result of vortex shedding is one of the most common parameters to visualize the vortical structures generated behind the cylinder. In the work of Chinaud et al. (2017), the spanwise vorticity, ω_z on a two dimensional plane in cylinder wake are computed from Eq. 2.7, with *u* and *v* are the horizontal and vertical velocity components.

$$\omega_z = \frac{\partial v}{\partial x} - \frac{\partial u}{\partial y} \tag{2.7}$$

The phenomenon also leads to significant variations of flow properties such as the drag and lift forces on the cylinder and the fluctuations of velocity in its wake.

2.4.1.3 Frequency of vortex shedding

The frequency of vortex shedding, f_v can be characterized by the dimensionless Strouhal number, *St*, defined as Eq. 2.8.

$$St = f_v D/u \tag{2.8}$$

For flow past an unbounded smooth cylinder, the resulting Strouhal number was observed to depend on the cylinder based Reynolds number, Re_D. Figure 2.11 shows the values of Strouhal number, *St* at different flow regimes. As can be seen, *St* rises gradually from 0.12 to 0.20 in the laminar wake regime ($40 < Re_D > 200$) where the onset of vortex shedding occurs. In the subcritical regime ($200 < Re_D > 3 \times 10^5$), the turbulent wake is established and the Strouhal number remains almost constant at 0.20 and independent of Re_D. In this regime, the frequency of vortex shedding is proportional to the incoming velocity. With a further increase of the Reynolds number the Strouhal number increases suddenly in the supercritical regime to St = 0.45 and later reduces again to *St* = 0.1 in the upper transition regime. Scattered *St* values were observed during the transcritical regime.

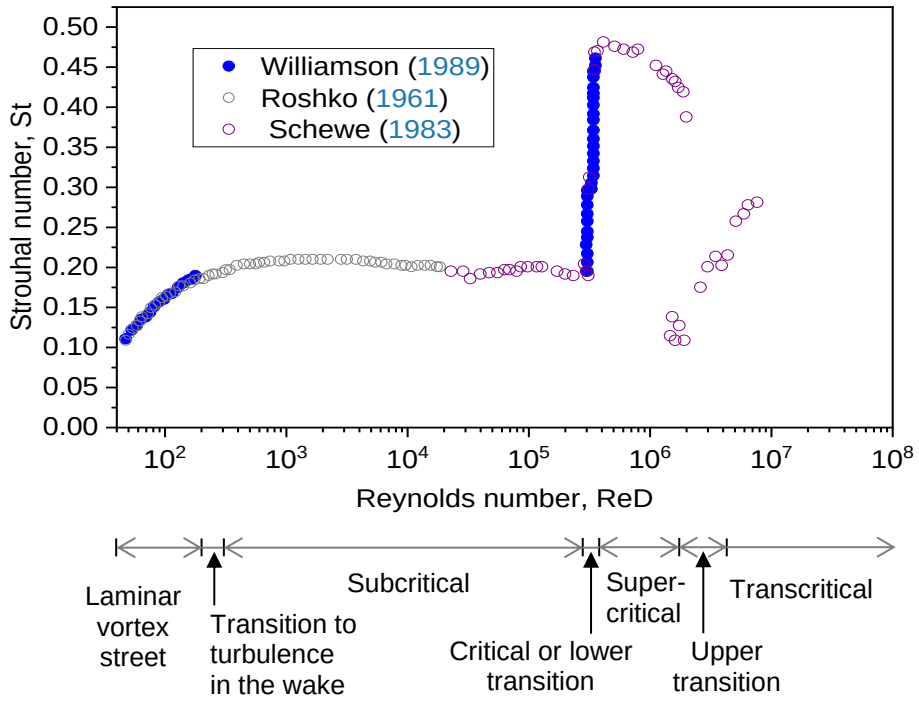

Figure 2.11: Strouhal number for a smooth circular cylinder.

2.4.2 Flow across a cylinder in the presence of boundaries

In the previous section, the flow across a cylinder was discussed for an unbounded or infinite medium. However, in many engineering applications, the flow across a cylinder involves the presence of boundaries which can take the form of solid walls or free surface. The introduction of boundaries limits the flow to the gap between the cylinder and the boundaries and introduces new

parameters. This causes the flow across a cylinder and the wake characteristics in the proximity of boundaries to differ from the case of infinite medium. As a result, more complex wake structures are produced which are reviewed in the following sections.

2.4.2.1 Solid wall proximity

The presence of a wall near the cylinder leads to a blockage of the flow passage Figure 2.12. The solid boundaries may also influence the velocity profile of the incoming flows which may be important in some applications. The influence of the solid wall proximity can be characterized by a dimensionless parameter called gap ratio, γ which is defined as the ratio of distance from the bluff body to the wall boundary, *h* and the diameter of the bluff body, *D*;

$$\gamma = h/D \tag{2.9}$$

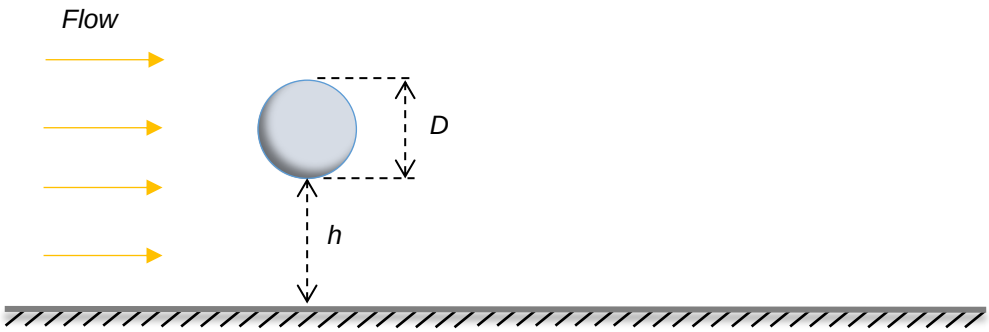

Figure 2.12: Flow across a cylinder in the presence of solid wall.

Zovatto and Pedrizzetti (2001) proposed that the following three factor affects the wake structure in the presence of a solid wall:

1. The wall impermeability results to an irrotational constraint to the cylinder wake which is unable to spread without limit.
2. The presence of rigid walls produces a flow of non-uniform velocity profile approaching the cylinder. Thus, the resulting shear has a non-symmetric influence on the bluff body and the incoming vorticity profile combines with the vorticity separated from the cylinder.
3. Due to the presence of the no-slip wall, the resulting wake could induce the rise of vorticity on the wall boundary layer. As a result, more complex

wake structures may form due to the interactions between the vorticity shed by the cylinder and from the wall.

Experimental investigations

Most of the early works on the effects of solid walls were experimental. The studies were performed in the sub-critical regime at which the vortex shedding is insensitive to the Reynolds number. Experimental works carried by Bearman and Zdravkovich (1978), Zdravkovich (1985) and Lei et al. (1999) have found that the presence of a no-slip wall influences the forces acting on the cylinder and the resulting Strouhal number. Bearman and Zdravkovich (1978) reported that the Strouhal number remains constant for gap ratios γ > 0.30 in the Reynolds number range investigated. Angrili et al. (1982) observed the influence of the wall on the frequency of vortex shedding, which increases as the gap ratio is reduced. As a result, increase in Strouhal number was observed as the cylinder moves closer to the wall. A maximum increase of 10% of the Strouhal number was reported at gap ratio of 0.5.

Zdravkovich (1985) examined the effects of wall proximity on forces acting on the cylinder based on the variation of drag coefficient, C_D and lift coefficient, C_L. The drag coefficient was reported to decrease with the ratio of gap to boundary layer thickness as the cylinder moves closer to the wall boundary layer. The lift coefficient, on the other hand, depends strongly on the gap ratio, and a complex variation of the C_L was observed at different gap ratios. Further experimental work by Lei et al. (1999) shows agreements with the early works where it was concluded that both the drag and lift coefficients are dominated by the gap ratio. Increase in Strouhal number was observed when the gap ratio was reduced from 0.80. It was also found that the vortex shedding becomes weaker as the gap ratio is reduced, which was measured based on the lift coefficient spectrum analysis. At gap ratio of 0.2 -0.3, it was reported that vortex shedding is completely suppressed. From the work, it was also reported that the effects of plane on the force and vortex shedding behavior is negligible at gap ratio higher than 2.0.

To visualize the von Karman vortex street, the velocity field can be determined by particle image velocimetry (PIV) measurements (Price et al., 2002; Rehimi et al., 2008; Wang and Tan, 2008). Price et al. (2002) studied the flow in

the vicinity of the cylinder at various gap ratios and suggested four distinct regions. At very small gaps ($\gamma \leq 0.125$) vortex shedding is completely suppressed or extremely weak. For small gaps ($0.125 < \gamma < 0.25$), similar flow with the previous region was observed but with more pronounced pairing between the inner shear layer from the cylinder and the wall boundary layer. In intermediate gap ratios ($0.5 < \gamma < 0.75$), the onset of alternate vortex shedding was observed with Strouhal number higher than for an isolated cylinder. Separation from the wall was also seen at a periodic manner with vortex shedding from the cylinder. For the large gap ratios investigated ($\gamma > 1.0$), no separation of the wall boundary layer occurs. The flow resembles an isolated flow but with larger *St* values.

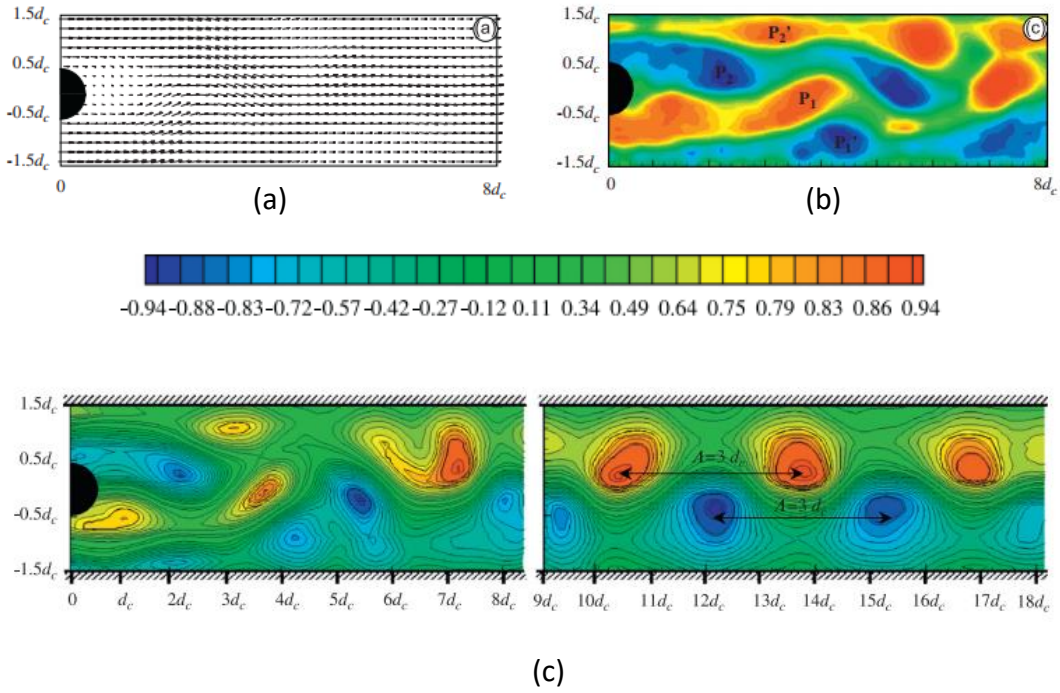

Figure 2.13: Flow visualization in the wake of a cylinder. (a) Velocity components for Re = 129, (b) Iso - Γ_2 criterion for Re =129 and (c) Γ_2 criterion for Re = 159. *Rehimi et al. (2008)

Rehimi et al. (2008) conducted experimental investigations on flow past cylinders placed between two parallel walls by implementing PIV technique. In their work, proper orthogonal decomposition (POD) was used for the detection of coherent structures (based on the energy contribution of the various processes occurring in the wake) and a kinematic criterion, Γ_2 which was proposed by Graftieaux et al. (2001) for the identification of the vortex cores. Examples of the

instantaneous PIV results and the corresponding Γ_2 are presented in Figure 2.13. The Γ_2 criterion allows the visualization of a family of vortices shed by the cylinder denoted by P_1 and P_2 as shown in Figure 2.13(b). Interactions with the adjacent wall at the top and bottom side of the cylinder are seen to generate a second family of vortices near the walls denoted by P_1' and P_2'.

Numerical investigations

The advancement of numerical methods with lower computational cost have led to many numerical studies especially for systems complex geometry. In complex systems, difficulties may arise in getting good quality of experimental data for example at very small gap ratios. Therefore, numerical approaches are not uncommon for the studies of flow past cylinder which may also be used to support experimental investigations. It is important however, to properly validate the numerical simulations. Kang (2006) and Patil and Tiwari (2008) validated their numerical results by comparing the Strouhal number with the experimental values reported in the literature.

Lei et al. (2000) investigated numerically the vortex shedding phenomenon at various gap ratios. The authors analyzed the vortex shedding behavior based on the change of amplitude and the regularity of the fluctuating lift force acting on the cylinder. At large gap ratios (γ > 1.0), the lift coefficient oscillates regularly with large amplitude that proves the occurrence of periodic vortex shedding from the cylinder. As the gap ratio is reduced to γ = 0.4 – 0.5, the amplitude of fluctuating lift coefficient decreases as a result of reduced strength of vortex shedding. Irregularities started at γ = 0.3 while at γ = 0.1, no regular oscillation of the lift coefficient is observed due to complete suppression of vortex shedding.

Numerical analysis by Zovatto and Pedrizzetti (2001) and Patil and Tiwari (2008) showed that the onset of periodic vortex shedding is delayed towards larger Reynolds numbers as the gap ratio is decreased. Zovatto and Pedrizzetti (2001) explained that the variation observed due to the effects of the wall is caused by the interactions between the wake and the wall boundary layers. The interactions are visualized in Figure 2.14 where the time-averaged vorticity contours for various gap ratios of 1.75, 1.25 and 0.75 are presented. For the first two gap ratios, the averaged vorticity structure appears to be symmetric at the

top and bottom of the cylinder. At the lowest gap ratio, asymmetric vorticity structures were observed where the bottom side appears to be shorter than the upper side. A rise of the wall boundary layer can also be seen. At this condition, it was reported that no vortices are shed from the bottom side of the cylinder and the final wake composed of a single row of same-signed vortices.

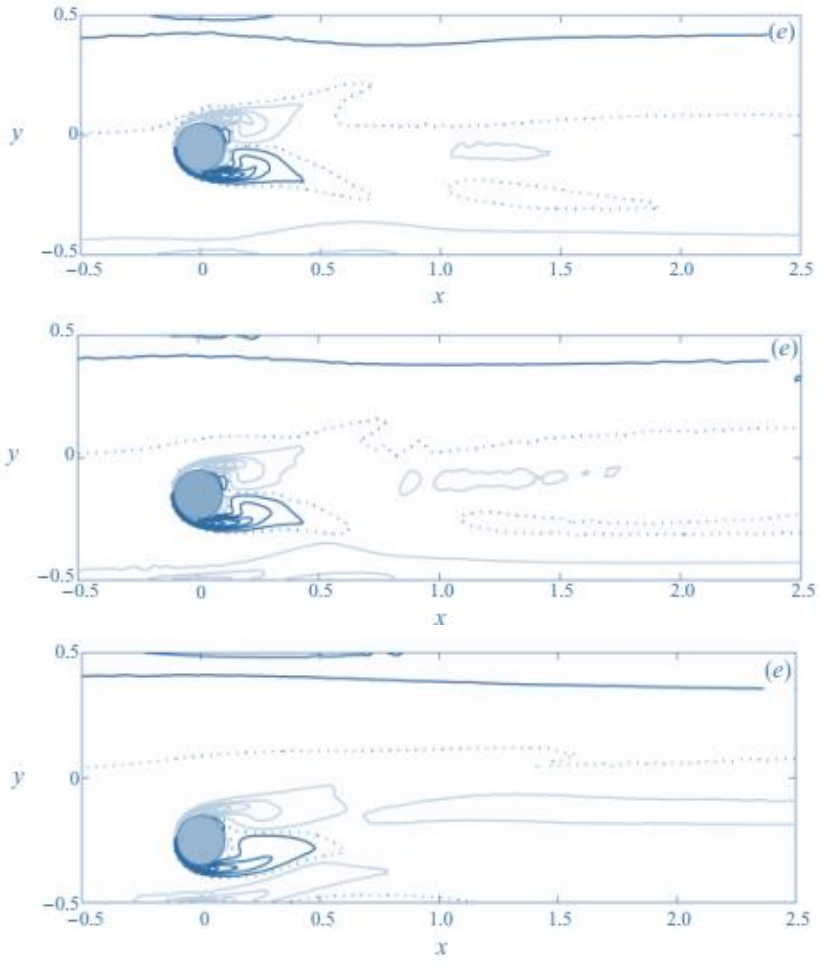

Figure 2.14: Time-averaged vorticity at various gap ratio. (a) γ = 1.75, (b) γ = 1.25 and (c) γ = 0.75 *Zovatto and Pedrizzetti (2001)

In terms of the resulting forces, numerical analysis conducted by Chakraborty et al. (2004), Kang (2006) and Singha and Sinhamahapatra (2010) observed that reducing the gap ratio led to increased drag coefficient at constant Reynolds number as the result blockage effect exerted by the wall.

Remarks on the effects of wall proximity

The works on the flow across a cylinder in solid wall proximity that were discussed in previous section are summarized in Table 2.2. Price et al. (2002) summarized the Strouhal number data at various gap ratio values for several works in the literature and is presented in Figure 2.15.

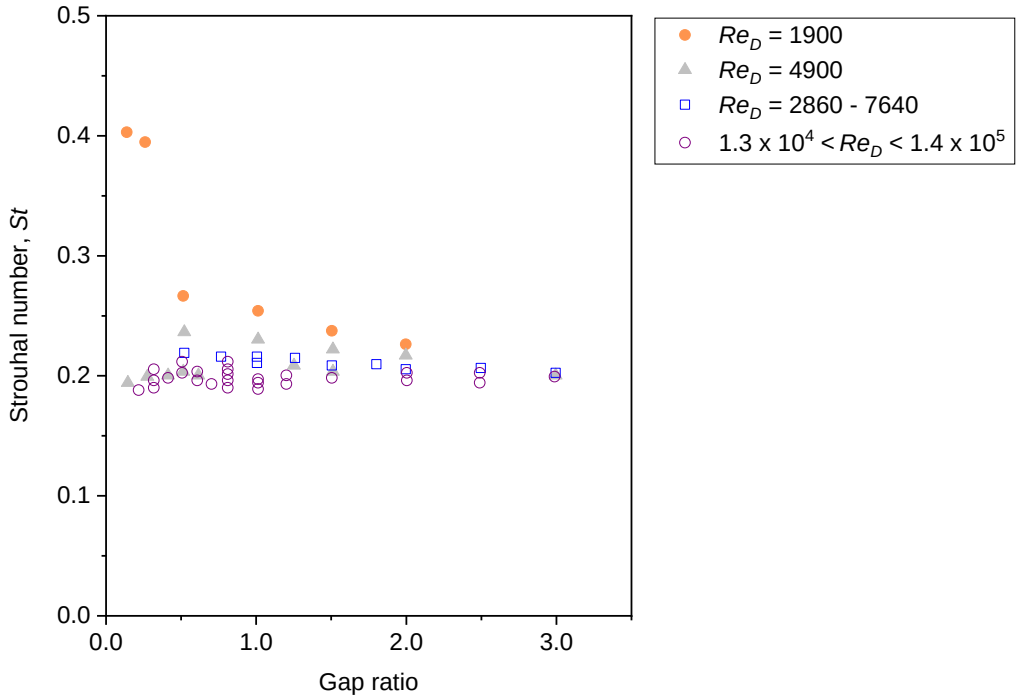

Figure 2.15: Summary of Strouhal number data at various gap ratio.
*Data shown are from various works gathered in Price et al. (2002), Angrili et al. (1982), Bearman and Zdravkovich (1978), Buresti and Lanciotti (1979), Taniguchi and Miyakoshi (1990) and Lei et al. (1999).

A significant finding, as can be seen from Figure 2.15, is that the variation of Strouhal number with gap ratio is very dependent on the Reynolds number. For low Reynolds numbers (Re < 4900), increase in *St* was observed as the gap ratio was reduced from γ < 2.0 where the Strouhal number is greater than the case of unbounded flow (*St* =0.20). However, the *St* becomes insensitive to the gap ratio at high Reynolds numbers (Re_D > 10000).

Table 2.2: Summaries of various studies on flow past a cylinder near a wall.

Authors	Method	Re_D	Gap ratio, γ	Critical gap ratio, γ_c	Effects of gap ratio
Bearman and Zdravkovich (1978)	Experimental	2.5×10^4 and 4.5×10^4	0.0 – 3.5	0.30	ST constant for $\gamma > 0.3$.
Angrili (1982)	Experimental	2860, 3820 and 7640	0.5 – 6.0	-	ST increases with reduction of γ.
Zdravkovich (1985)	Experimental	4.8×10^4 and 3.0×10^5	0.0 – 2.0	-	C_D almost independent to γ while C_L is very dependent.
Lei et al. (1999)	Experimental	1.3×10^4	0.0 – 3.0	0.20 – 0.30	C_D affected by γ. ST increased with decreasing γ.
Lei et al. (2000)	CFD	$80 – 10^3$	0.1 – 3.0	0.20	Decreased strength of vortex shedding at $\gamma < 0.5$.
Zovatto and Pedrizzetti (2001)	CFD	100 - 2000	0.25 – 2.0	0.25	Asymmetric wake structure at $\gamma < 1.75$.
Price et al. (2002)	Experimental	1380 - 4960	0.0 – 2.0	0.125	ST increased for $\gamma < 0.75$.

Table 2.2 (cont.): Summaries of various studies on flow past a cylinder near a wall

Authors	Method	Re_D	Gap ratio, γ	Critical gap ratio, γ_c	Effects of gap ratio
Chakraborty et al. (2004)	CFD	0.1 - 200	1.54 - 20	-	C_D decreased with reduction of γ.
Dipankar and Sengupta (2005)	CFD	1200	0.5 and 1.5	-	Adverse pressure gradient in front of cylinder weakens with increasing γ.
Kang (2006)	CFD	50 - 160	0.05 and 0.1	-	Increased in vortex shedding frequency with increasing γ.
Rehimi et al. (2008)	Experimental	75 - 277	1 and 6.5	-	Dependent of recirculation region on γ.
Patil and Tiwari (2008)	CFD	30 - 300	0.125 – 0.7	-	Dependent of critical Reynolds number for vortex shedding to occurs with γ.
Wang and Tan (2008)	Experimental	2.5×10^4	0.1 – 1.0	0.20	Distinct asymmetric wake structure at $\gamma < 0.6$.
Singha and Sinhamahapatra (2010)	2D - CFD	45 - 250	2.0 – 8.0	0.50	Mean drag coefficient and ST increase with decreasing γ. Delayed of transition from steady to unsteady wake.
Liang et al. (2014)	2D - CFD	2×10^5 and 4×10^5	0.25 – 5.0	-	Diffusion of vorticity which are shifted downstream at low γ.

2.4.2.2 Free surface proximity

The vortices generated behind a cylinder are also affected by the presence of a free surface. The flow problem usually involves incoming flow across a cylinder in the proximity of a surface which commonly is stationary air. The schematic of this flow problem is presented in Figure 2.16. In addition to the cylinder Reynolds number, Re_D and wall gap ratio, γ the presence of the surface boundary introduces two new parameters, the Froude number, *Fr* and the surface gap ratio, γ_s. The Froude number is defined as the ratio of inertial to gravitational forces as follows:

$$Fr = u/\sqrt{gD} \tag{2.10}$$

In Eq. 2.10, where *g* is the gravitational acceleration, *u* is the incoming velocity and *D* is the cylinder diameter. The γ_s is defined as the ratio of submergence depth, h_s to the cylinder diameter;

$$\gamma_s = h_s/D \tag{2.11}$$

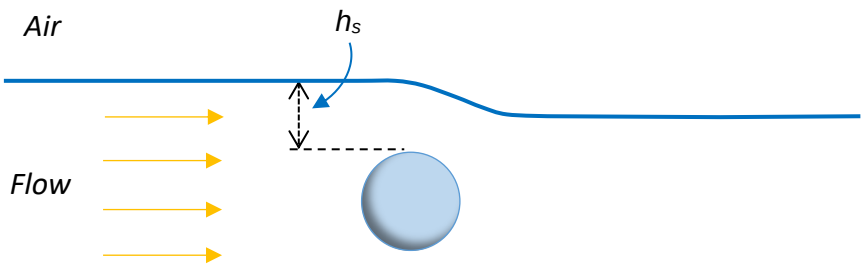

Figure 2.16: Schematic of flow across a cylinder near a free surface.

Effects of free surface proximity

Many works have been conducted to gain fundamental understanding of the flow across a cylinder in the proximity of a free surface that include both experimental and numerical studies. Miyata et al. (1990) conducted experimental and numerical studies of the forces on the cylinder beneath a free surface. An abrupt

decrease of the drag coefficient and a sharp increase of the Strouhal number were found when the depth of submergence was gradually reduced. Asymmetric vortex generation was also observed at low submergence depths due to difference of the flow in the vicinities of the top and bottom of the cylinder.

The experimental investigations on the flow past a cylinder beneath a free surface which was pioneered by Sheridan et al. (1997) provided new insights. The flow components that passed through the cylinder were determined by PIV measurements. It was observed that the near-wake structure exhibits a variety of behaviors as the surface gap ratios, γ_s were varied. The jet of fluid passing over the top of the cylinder (between the cylinder and the free surface) displayed different states depending on the submergence depth. The instantaneous distributions of velocity and vorticity of intermediate to large h_s (0.31, 0.43 and 0.75) are presented in Figure 2.17.

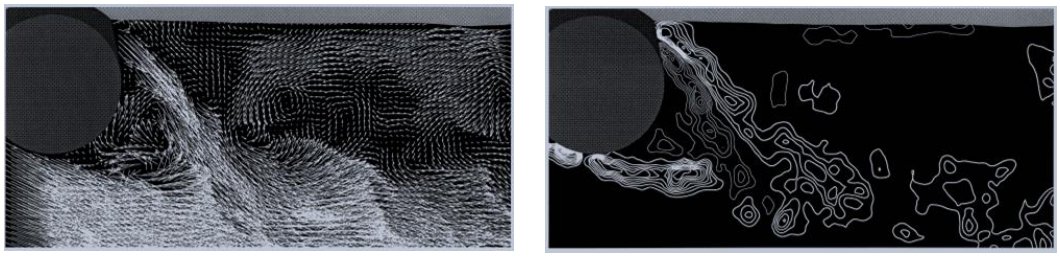

(a) h_s = 0.31

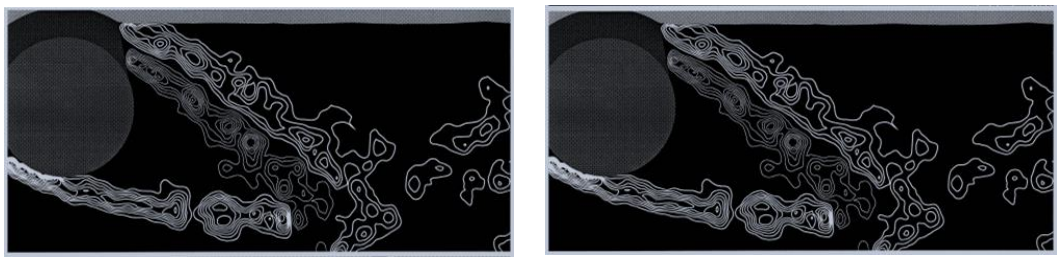

(b) h_s = 0.43

(c) h_s = 0.75

Figure 2.17: Velocity and vorticity in the wake at various submergence depth. Left: Instantaneous velocity fields. Right: Instantaneous vorticity fields. * Sheridan et al. (1997):

For intermediate submergence depths (h_s = 0.31 and h_s = 0.43) detachment of the jet from the surface side of the cylinder was observed with two-regions of large-scale swirl; a clockwise one bounded by the jet and the mixing layer from the cylinder bottom side and a counterclockwise on the opposite side of the jet (top side of the cylinder). At h_s = 0.31, the near wake contains relatively low levels of vorticity and only positive vorticity is evident further downstream the flow. Similar wake structure can be seen at h_s = 0.43 with the location of the jet merging with the mixing layer displaced further downstream. The observation agrees with the vorticity patterns obtained by Bozkaya and Kocabiyik (2014) from numerical simulations who then suggested that there is close relationship between the vorticity layers at the top side of cylinder and the vorticity layer from the surface at low submergence depth.

An interesting effect of the surface proximity was observed at a large submergence depth, h_s = 0.75 where there is significant volume of flow between the surface and the cylinder. In this case, the jet was observed to attach on the free surface resulting to a long interfacial wave. No positive vorticity on the top side of the cylinder formed for this case, as there is no separation from the free surface. The occurrence of surface deformation was also observed in the experimental work of Kumagai et al. (2011) downstream of a cylinder near a free surface. The deformation becomes significant as the cylinder Reynolds number, Re_D and the Froude number, Fr are increased.

The problem was also studied numerically by Reich et al. (2005) and Lin and Huang (2010). More complex cases of surface proximity were investigated by Bozkaya and Kocabiyik (2014) for oscillating cylinders, Chen et al. (2015) for partially submerged cylinders and Ong et al. (2017) for cylinders in tandem. The results of Reich et al. (2005) showed that changes in the vorticity field and free-surface behavior occur as the Froude number is increased at constant surface gap ratio. This is achieved by varying the flow velocities a constant surface height. Significant surface deformation was observed at Fr > 0.3 with the onset of asymmetric vorticity structure in the wake of the cylinder. The surface deformation becomes larger as the Froude number is further increased as shown in Figure 2.18. Increase in surface deformation was also observed when the surface gap ratio is reduced at constant Froude number. According to Reich et al. (2005) the proximity of the surface causes the vorticity from the top size of the

cylinder to diffuse into the surface, leading to rapid reduction of vorticity to form vortices from the top half of the wake.

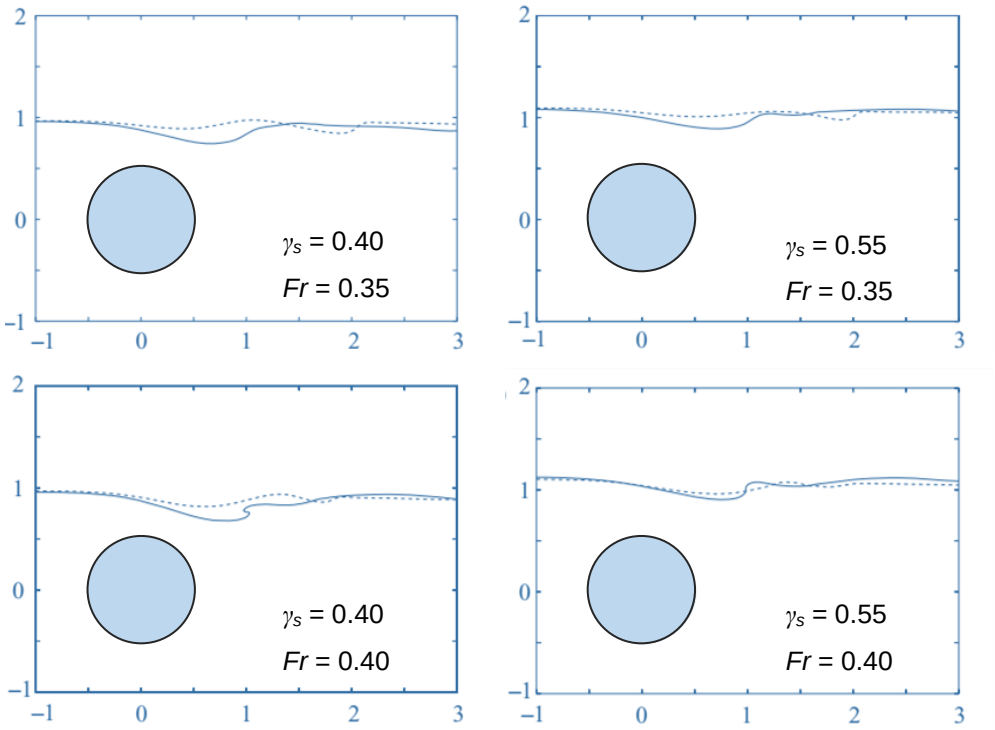

Figure 2.18: Surface position at various submergence depth, γ_s and Froude number, *Fr*. *Reich et al. (2005)

Numerical analysis through vortex and boundary methods was performed by Lin and Huang (2010), which was capable of capturing the complex motion of the free surface and the vortices. The work investigated the effects of Froude number and submergence depth on the surface deformation. The results showed that both parameters influence the degree of surface deformation. The free surface profiles at various Froude number and submergence depth with the resulting vorticity structure are presented in Figure 2.19.

For small Froude number where *Fr* = 0.3 (Figure 2.19(a)), the flow resembles the case of unbounded flow with insignificant surface deformation. The surface deformation becomes substantial as the Froude number is increased further to 0.5 and 0.7 (Figure 2.19(b) and (c)). The larger deformation results to more asymmetric wake downstream of the cylinder which leads to variations in the lift coefficient. Similar trends on the surface deformation were observed when the submergence depths were decreased at constant Froude number (Figure

2.19(d) and (e)). The authors reported that at large submergence depth, the wake is almost similar to the case of infinite medium with almost no effects observed on the structure of the surface. As the submergence depth is reduced, stronger waves are formed at the interface.

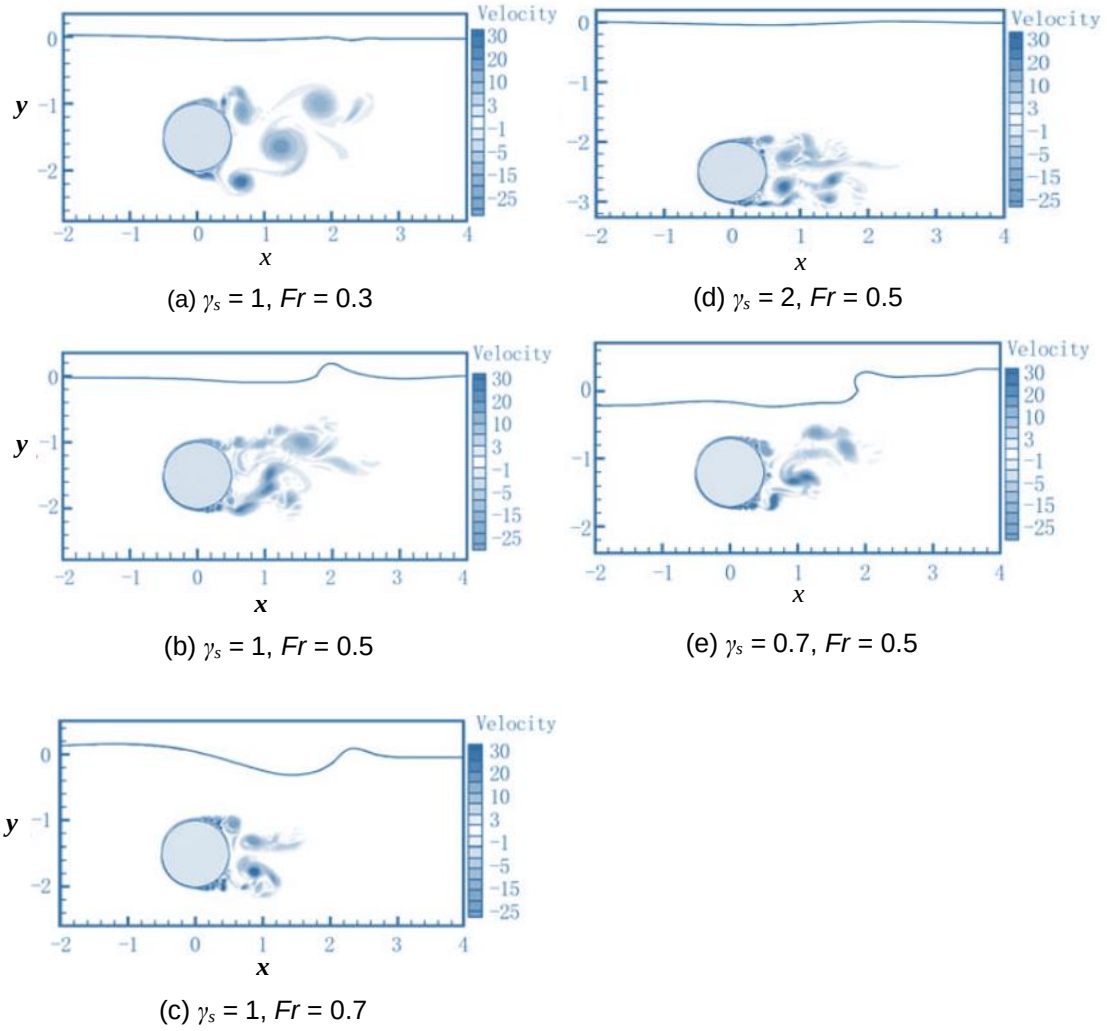

(a) γ_s = 1, *Fr* = 0.3

(d) γ_s = 2, *Fr* = 0.5

(b) γ_s = 1, *Fr* = 0.5

(e) γ_s = 0.7, *Fr* = 0.5

(c) γ_s = 1, *Fr* = 0.7

Figure 2.19: Free surface position and vortex pattern at various surface gap ratio, γ_s and Froude number, *Fr*. *Lin and Huang (2010)

2.5 Concluding Remarks

From the literature review conducted in this chapter, several concluding remarks can be drawn as follows;

- Two phase flow pattern transition boundaries vary depending on the flow and fluids properties. Currently, experimental investigations are still a

more reliable method to identify transition boundaries for a specific system compared to mechanistic models.

- Flow pattern transition from stratified to non-stratified flow has been strongly associated with the formation of interfacial waves as the first criterion for the transition to occur. This implies that studies of the flow pattern transitions can be facilitated by actuating the generation of interfacial waves.

- The dynamics of the transition from separated to dispersed flows and specifically the drop entrainment are not fully understood due to very limited experimental data available in the literature. The physical mechanism of drop entrainment is essential for better understanding the transition process and for developing a drop entrainment model.

- Advanced imaging techniques are required beyond the conventional photography/high speed imaging to study the evolution of interface deformation. Methods such as PIV can provide additional detailed velocity profile data to validate phenomenological models.

- When flows across a cylinder approach a free surface, depending on the submergence depth and Froude number, surface distortion can occur in the form of interfacial waves. In our previous work (Kyeong et al., 2016; Chinaud et al. 2017), the cylinder was used in two-phase liquid-liquid flows for the first time as a novel approach to generate interfacial waves in stratified flows. Although it was shown that the approach successfully generated instabilities that lead to flow pattern transitions, more studies are required to expand the use of cylinders to actuate the flow pattern transitions in a controlled way.

Chapter 3

Numerical Analysis: Investigations of flows past cylinder of various diameters

In many engineering fields involving flows of liquids and gases, the use of computational fluid dynamics (CFD) has grown tremendously and has even become a standard tool (i.e. the work of Huang et al. (2006) and Bai and Li (2011)). In liquid flows, CFD can estimate the resulting fluid dynamics. The application of CFD to conduct virtual experiments has been widely utilized in the design phase to select between different configurations and in the production phase to analyze performance and to carry out parametric studies. With CFD analysis, the need for experiments can be reduced resulting in significant cost and time savings. In addition, CFD can also be used to support and complement experimental investigations especially in a complex system.

With the advancement of numerical methods, various commercial CFD packages have been developed for fluid flows, i.e. CFX and Fluent. Most of the commercial packages are integrated systems which consist of a pre-processor, solver and post-processor that includes visualization tools for the analysis of the results (Iaccarino, 2001). Generally, the numerical techniques adopted in these commercially available CFD codes are well-accepted algorithms that have been published in the literature.

In this chapter, numerical analysis was used as design tools where numerical investigations of single phase flows past a cylinder of various diameters which were performed using a commercial CFD code, FLUENT. The aim of this investigations is to have an overview on the effects of cylinder diameter on the resulting vortex shedding behavior. From the findings, suitable cylinder diameters are chosen for experimental investigations.

3.1 Numerical Methods

The flow of an incompressible fluid can be described by the following equations:

$$\nabla \cdot \boldsymbol{u} = 0 \tag{3.1}$$

$$\frac{\partial \boldsymbol{u}}{\partial t} + (\boldsymbol{u} \cdot \nabla)\boldsymbol{u} = \nu \nabla^2 \boldsymbol{u} \tag{3.2}$$

Eq. 3.1 is the continuity equation derived from conservation of mass and Eq. 3.2 is the momentum or Navier-Stokes equations where *v* is the kinematic viscosity. The momentum equation has the rate of change term and convective term on the left hand side and the diffusion term on the right hand side. The key step of the finite volume method is the integration of Eq. 3.2 over an infinitesimal control volume. In turbulent flow, rapid fluctuations of the velocity field occur in space and time with frequencies that differ several orders of magnitude. Solving the Navier-Stokes equations through direct numerical simulations in such turbulent scales requires very high computational costs. To reduce the computational cost, turbulence models can be used where the Navier-Stokes equations are either averaged (RANS) or filtered (LES).

3.1.1 Reynolds Averaged Navier-Stokes (RANS)

In the RANS approach, the Navier –Stokes equations are time averaged to remove the rapidly fluctuating components (Shao and Zhang, 2006). This results to significant reduction of the computational cost making this approach to be widely used in practical engineering calculations. By averaging, new terms are introduced as Reynolds stress, $\tau_{ij} = -\rho\overline{u_i u_j}$. To close the RANS equations, expressions of the Reynolds stress are required. Many turbulence models have adopted the Boussinesq hypothesis to derive models that represents the Reynolds stresses such as the two-equation model, *k-ε* (standard, RNG and realizable) and *k-ω* (Catalano et al., 2003; Mahbudar et al., 2007).

The *k-ε* model was introduced by Launder and Spalding (1972) and is one of the most common turbulence models in which the Reynolds stresses and the turbulent eddy viscosity, μ_t, are expressed as functions of the turbulent kinetic

energy, *k,* and its dissipation rate, ε. For a standard *k-ε* model, the expressions of τ_{ij} and μ_t are givens as:

$$\tau_{ij} = 2\mu_t S_{ij} - \frac{2}{3}k\delta_{ij} \tag{3.3}$$

$$\mu_t = C_\mu \frac{k^2}{\varepsilon} \tag{3.4}$$

In Eq. 3.3 and Eq. 3.4, S_{ij} is the mean strain-rate tensor and C_μ is a constant. The standard *k-ε* model is relatively simple to implement and valid only for fully turbulent flows as it is derived assuming that the flow is turbulent with negligible effects of molecular viscosity (Mahbudar et. al., 2007). It is widely used for industrial applications due to its robustness and reasonable accuracy with low computational costs compared to other turbulence models. Improved versions of the standard *k-ε* model are the Renormalization Group Method (RNG) and the Realizable *k-ε*. In the RNG *k-ε* model, an additional term in the dissipation rate equation is included for interaction between turbulence dissipation and mean shear. In the Realizable *k-ε* model, the model satisfies certain mathematical constraints on the Reynolds stresses and C_μ is a variable instead of a constant as follows;

$$C_\mu = \frac{1}{A_o + A_s \frac{U^* k}{\varepsilon}} \tag{3.5}$$

$$\overline{u_i^2} \geq 0 \tag{3.6}$$

$$\left(\overline{u_i u_j}\right)^2 \leq \overline{u_i^2 u_j^2} \tag{3.7}$$

In Eq. 3.5, the A_o, A_s and U^* are functions of velocity gradients, Eq. 3.6 ensures positivity of normal stresses and Eq. 3.7 ensures Schwarz's inequality. In general, the *k-ε* models neglect the terms containing kinematic viscosity. As a result, they are not applicable in the proximity of solid walls where viscous effects are important.

In the *k-ω* model, a modified version of the *k* equation in the *k-ε* model and a transport equation for *ω* are solved. The *ω* is an inverse time scale which is associated with the turbulence. The turbulent viscosity is then calculated as;

$$\mu_t = \rho \frac{k}{\omega} \tag{3.8}$$

The advantages and disadvantages of the various RANS turbulence models are presented in Table 3.1. From the table, it can be seen that the standard *k-ε* model is reasonably accurate at low computational cost for simple flow problems that do not involves large pressure gradients, separation and circulation. For moderate to complex flows, improvements of the standard *k-ε* model can be used which are the RNG *k-ε* and Realizable *k-ε* model at increased computational cost. It has to be noted that the *k-ε* model contains a term which cannot be calculated near the wall. Therefore, for flow problems with solid wall boundaries, a wall function should be used. The *k-ω* model is an improvement and can be integrated near the wall without using wall functions and also showed better performance for complex flow with pressure gradient but requires higher computational cost.

Table 3.1: Comparisons of RANS turbulence models.

Model	Advantages	Disadvantages
Standard *k-ε* (SKE)	• Robust and reasonably accurate. • Economical.	Poor performance for very complex flow with large pressure gradients.
RNG *k-ε*	• Better performance than SKE for moderate complex flow (jet impingement, swirling flows etc.)	Does not predict spreading of round jets correctly.
Realizable *k-ε*	• Better accuracy on the spreading rate of planar and round jets. • Better performance for complex flows involving rotation, large pressure gradients, separation and recirculation).	Subject to limitations due to assumption of isotropic eddy viscosity.
k-ω	• Better performance over the *k-ε* models. • Can be integrated to the wall.	Subject to limitations due to assumption of isotropic eddy viscosity.

3.1.2 Large Eddy Simulations (LES)

In the large eddy simulation (LES) approaches the time-dependent Navier-Stokes equations are filtered in either Fourier (wave number) space or configuration (physical) space. In this approach, the large scale turbulence that depends strongly on the special flow configuration and its boundary conditions are solved directly while the small scales are modeled by sub grid scale (SGS) models. The SGS models include the Smagorinsky-Lily model, the Wall Adapting Local Viscosity Model (WALE) and the Dynamic Smagorinsky Model (DSM). The computational cost of LES is much higher than RANS. On the other hand, LES is capable of solving three-dimensional (3D) and transient turbulent flow problems (Breuer, 1998; Shao & Zhang, 2006).

3.1.3 Comparison of RANS and LES approach

Catalano et al. (2003) carried out simulations of flow around a circular cylinder at high Reynolds numbers with steady (RANS), unsteady (URANS) and LES. In general, they reported that the LES solutions are considerably more accurate than RANS and are able to predict correctly the delayed boundary layer separation and reduced drag coefficients. However, the URANS technique was able to predict better vortex shedding patterns in the wake of the cylinder compared to LES, as shown in Figure 3.1. URANS also predicted very consistent lift coefficients, C_L for every cycles compared to LES. Meanwhile, the predictions of the steady RANS were poor and not suitable for the case of flows past a bluff body.

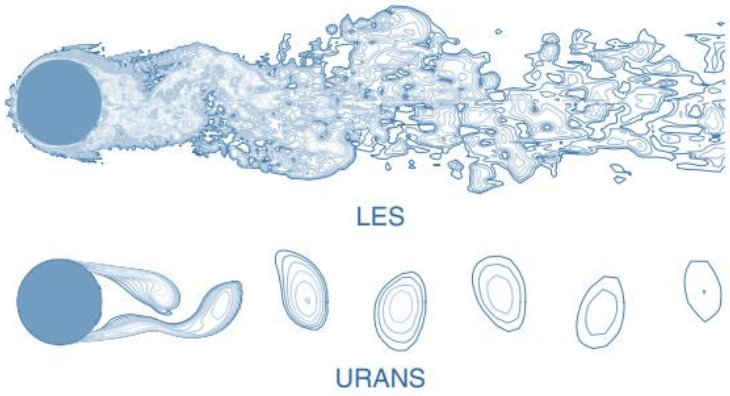

Figure 3.1: Vorticity contour at $Re_D = 1 \times 10^6$ from LES and URANS.*Catalano et al. (2003)

The numerical analysis of Shao and Zhang (2006) also shows that steady RANS was not suitable for simulation of flows past a bluff body. It was found that the two-dimensional (2D) LES could not reproduce the wake after the bluff body. The authors suggested that three-dimensional (3D) LES is necessary to simulate such complex flows. Table 3.2 shows the available works reported in the literature on comparisons of simulation techniques and turbulence models for various flow systems while Figure 3.2 presents their order based on computational cost. Based on the reported studies, it can be concluded that;

- RANS and Unstable RANS (URANS)
  Unsteady RANS (URANS) should be used for cases involving unsteady flow such as flow past a bluff body as it solves for transient solutions.

- Turbulence model
  The standard k-ε model shows good performance for flow past a bluff body and is able to reproduce the wake behind it. For complex flow cases with high flow separation and circulation, the improved two-equation turbulence models (Realizable k-ε, RNG k-ε and k-ω) are more suitable.

- Large Eddy Simulation (LES)
  The LES technique is more suitable for three-dimensional simulations. Strong impact of three-dimensionality on LES was presented by Breuer (1998).

- URANS and LES
  For a simple flow case such as flow past a bluff body, the results from 2D URANS on the wake properties i.e. lift and drag coefficient are comparable to those from LES.

Table 3.2: Comparisons of various numerical techniques and turbulence models for flow simulations.

Reference	Investigated system	Technique	Turbulence model	Remarks
Murakami and Mochida (1995)	Flow past a square cylinder.	2D LES and 3D LES	-	3D LES shows good agreement with experimental results while 2D LES shows poor performance.
Kalro and Tezduyar (1997)	Flow around circular cylinder.	2D LES and 3D LES	-	3D LES were in excellent agreement with experimental results.
Breuer (1998)	Flow past a circular cylinder	2D LES and 3D LES	-	Strong impact of three-dimensionality on LES calculations is presented.
Iaccarino (2001)	Turbulent separated flows in 2D diffuser.	2D RANS by FLUENT	Standard k-ε v^2-f	Poor agreement of standard k-ε model calculation with experimental data.
Catalano et al. (2003)	Flow around a circular cylinder at high Re.	2D RANS and 2D URANS LES by FLUENT	Standard k-ε	Good performance observed for URANS with Standard k-ε model although LES provides higher accuracy.
Iaccarino et al. (2003)	Flow around a square cylinder.	2D URANS by FLUENT	v^2-f	Good match with experimental data

Table 3.2 (cont.): Comparisons of various numerical techniques and turbulence models for flow simulations

Reference	Investigated system	Technique	Turbulence model	Remarks
Shao and Zhang (2006)	Flow around a circular cylinder.	2D RANS, 2D LES and 3D LES by FLUENT	RNG *k-ε*	2D RANS and 2D LES not able to reproduce cylinder wake.
Mahbudar et al. (2007)	Flow past a circular cylinder	2D URANS	Standard *k-ε* Realizable *k-ε* SST *k-ω*	Good performance of Standard *k-ε* and Realizable *k-ε* were observed. The *k-ω* model is preferred at high *Re*.
Drumm et al. (2011)	Flow in rotating disc contactor	2D RANS by FLUENT	Standard *k-ε* RNG *k-ε*	Good performance of standard *k-ε* only at low rpm.
Salim et al. (2011)	Airflow and pollutant dispersion.	3D RANS, URANS and LES by FLUENT	Standard *k-ε*	LES shows better accuracy compared to RANS and URANS

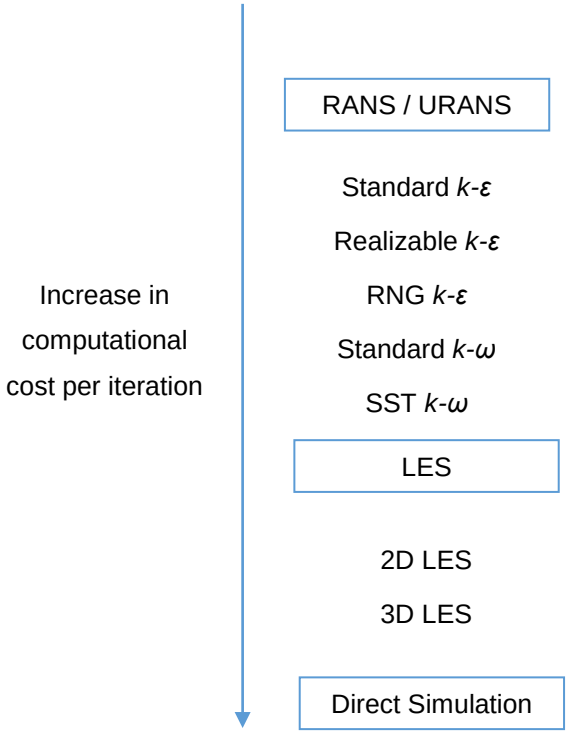

Figure 3.2: The order of simulation techniques and turbulence models based on computational cost per iteration.

From the literature review, it can be concluded that 2D URANS simulation with standard *k-ε* turbulence model is capable of providing satisfactory results for flow past bluff body with well agreement to the experimental data but at a fraction of the computational cost of LES. The wake of the bluff body where the periodic shedding of vortices occurs can be visualized accurately with precise estimation of wake properties such as the velocity field, drag and lift coefficient.

3.2 Computational Fluid Dynamics (CFD)

In this work, CFD is utilized in the design phase prior to experimental investigations to select the size of cylindrical bluff body. The investigations of flow past bluff body of various sizes are conducted through numerical method in which the governing equations are solved in a commercial code, Fluent (ANSYS). Fluent employs the finite volume method (FVM) technique and is one of the most commonly used CFD packages which has been successfully applied for both two-dimensional and three dimensional flow across bluff body by various researchers (Rocchi and Zasso, 2002; Catalano et al., 2003; Shao and Zhang, 2006; Huang et al., 2006; Wang and Tan, 2008; Bai and Li, 2011; Mazumder, 2012).

3.2.1 Problem considerations

The work of Chinaud et al. (2017) showed that experimentally, a 5 mm cylindrical bluff body in 37 mm pipe with gap ratio of γ = 1.35 generates vortices with frequencies ranging from 10 to 40 Hz for fluid velocities in the range of 0.3 to 1 m/s. Based on PIV techniques applied on a thin plane at the center of the pipe, the work reported that the flow field observed at the investigated locations resembles the flow field of two-dimensional flow. The Strouhal number, *St*, was found to agree with the theoretical value for unbounded flow (*St* = 0.2), which signifies that the system configuration was not affected by the presence of the walls. In this work, we aim to investigate the effects of cylindrical bluff body size on the resulting vortex-induced interfacial wave properties in two-phase flows. For this purpose, numerical analysis is conducted for flow past cylindrical bluff body of various sizes and the properties of resulting vortex shedding in the wake of the bluff body are studied. Our interest is to identify the sizes that would deliver vortex-shedding frequencies spanning two orders of magnitude, between 1 and 100 Hz to be used in experimental investigations.

Based on the findings of Chinaud et al. (2017), the flow fields measured with PIV on the two-dimensional plane at the centre of the pipe are comparable to those obtained in rectangular channels. This implies that at least at the centre of the pipe, the flow is not affected by the thee-dimensional pipe curvature. Therefore, in this work, two-dimensional simulations of single-phase flow are considered to reduce the computational cost. Further validation will be conducted by comparing the Strouhal number, *St*, obtained through the two-dimensional simulation in this chapter with the one measured experimentally in a pipe in Chapter 5. In the simulation works, two-dimensional URANS numerical simulation of single-phase flow past a bluff body that is capable of reproducing the experimental data of Chinaud et al. (2017) is first established. The validated numerical setup is then used for parametric studies in which simulations of single-phase flow past bluff body of various sizes were conducted.

3.2.2 Computation domain

In order to be able to validate the results of the numerical method with available experimental data, the computational domain is selected based on the plane of measurement in the experimental work by Chinaud et al. (2017). In the experiments, PIV was applied to a two-dimensional plane at the centre of a pipe.

The distance from the bottom of the cylinder to the wall, *h,* is 0.00675 m, while the centre of the cylinder is located at a distance of 0.25D_P from the inlet. The illustration of the pipe section used in the experimental work is presented in Figure 3.3.

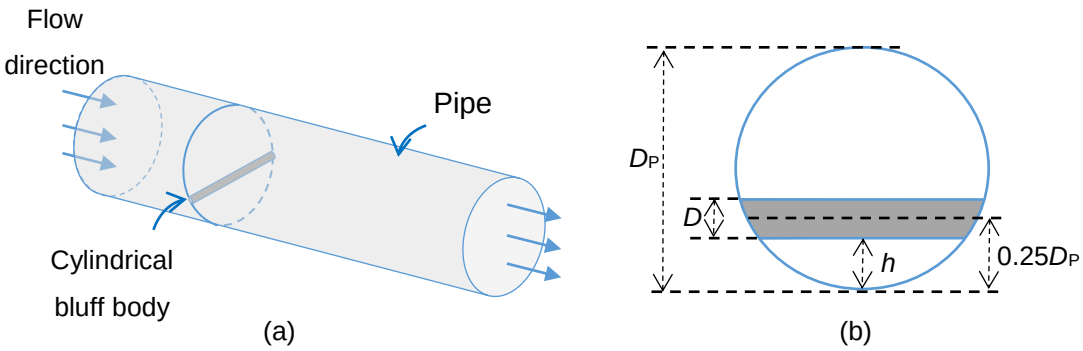

Figure 3.3: Illustrations of bluff body design. (a) Pipe section containing cylindrical bluff body (b) Cross section view

Based on the pipe geometry in Figure 3.3, the computational domain is designed as a two-dimensional plane located at the center of the pipe as presented in Figure 3.4. The computational domain represents the PIV measurement plane in the experimental analysis of Chinaud et al. (2017). The length of the computational domain is 0.6 m (120D) with the cylinder placed at 20*D* from the inlet and 100*D* from the outlet respectively. The cylinder is designed as a hollow circle with a diameter of 5 mm and is located based on the configuration in Figure 3.3(b) with the height of the fluid domain equal to the diameter of the pipe. The dimensions of the computational domain are presented in Figure 3.5.

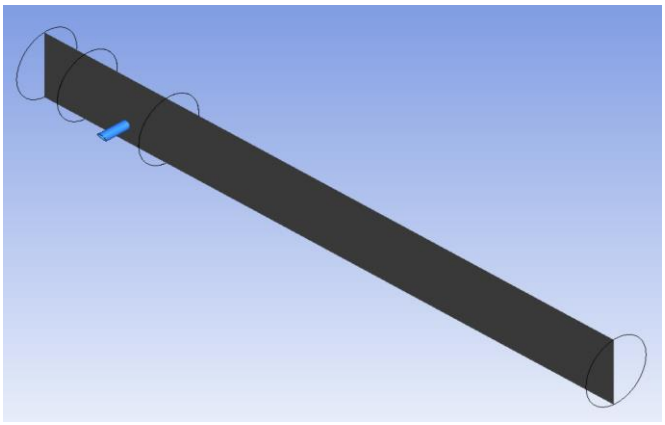

Figure 3.4: Computational domain for two-dimensional simulation.

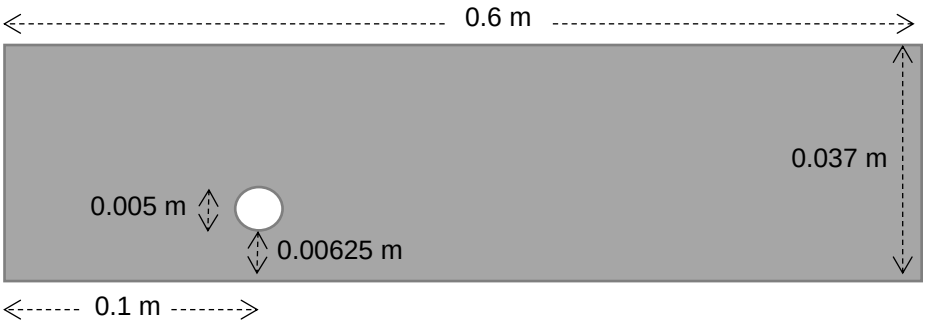

Figure 3.5: Dimensions of computational domain.

3.2.3 Grid/Mesh

The CFD code works by dividing the fluid domain into a number of control volumes. The solution of the flow parameters, such as velocity, is defined at the nodes inside each cell. The number of grid or mesh points has a significant impact on the solution accuracy and CPU time to solve the system. In general, a larger number of cells contributes to higher solution accuracy. However, an increase in number of cells also leads to increased calculation time. Therefore, effective meshing is important for reasonable calculation accuracy with practical computational cost.

The fluid domain in this work is considered as a simple geometry and therefore, the meshes are constructed using quadrilateral elements. For the first step, the fluid domain is meshed using an automatic method which results in a coarse meshing as presented in Figure 3.6 with a magnified image showing the meshing near the cylinder which shows non-uniform elements around the cylinder. For this meshing, the fluid domain contains 380 cells.

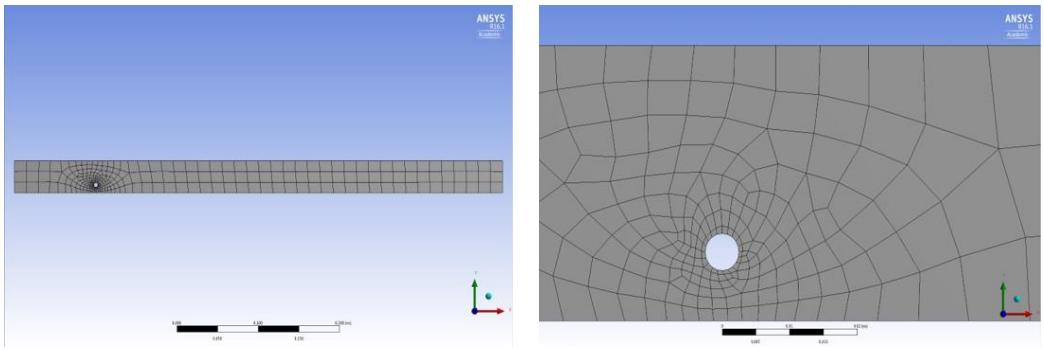

Figure 3.6: Automatic meshing of the computation domain.*The scale on the image is 0.005 m per unit

Generating a uniform and fine meshing over the entire fluid domain will increase the computational cost. Hence, in most cases, optimal meshes are non-uniform and finer meshes are built in areas with large variations of the flow and coarser meshes are used in regions with relatively little changes of flow properties. The meshing thus depends strongly on the investigated system and on the desired accuracy of simulations. In this work, the interest is on the wake that forms behind a cylinder. In the turbulent regime, flow separation occurs in the vicinity of the cylinder which results in alternating vortex shedding after the cylinder. Therefore, finer meshes are required in the region near the cylinder and in the wake of the cylinder. For k-ε model, as the flow involves the presence of pipe walls with no slip conditions, finer meshes are needed in the area near the wall where the velocity gradients are large.

For the purpose of mesh refinement, the fluid domain is divided into several sections as shown in Figure 3.7. Two sections are created around the cylinder and in the wake of the cylinder respectively. The size of the section around the cylinder is 16 mm × 16 mm while the section in the wake of the cylinder is larger with size 22 mm × 200 mm to track the vortices shed by the cylinder.

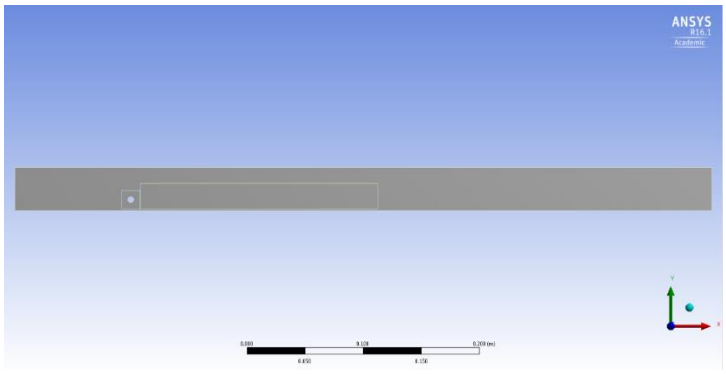

Figure 3.7: Sections created for mesh refinement. *The scale shown in the image represents 0.05 m per unit

Mesh refinement of the region around cylinder (16 mm × 16 mm)

The mapped face meshing function is applied in the 16 mm × 16 mm section created around the cylinder (refer Figure 3.7) to construct a high quality uniform mesh. To produce a very fine mesh, the fluid domain around the cylinder is split further into areas of 100 × 100; each cell has size of 0.16 mm × 0.16 mm as presented in Figure 3.8(a). A further mesh refinement is applied on the wall of the cylinder as shown in Figure 3.8(b). Figure 3.9(c) shows the enlarged image near the cylinder wall. Layers of uniform smaller cells are constructed next to the cylinder wall.

The mesh in the 22 mm × 200 mm section (refer Figure 3.7) created in the wake of the cylinder is split into divisions of cells with the size of 150 × 500 divisions or number of cells. The resulting mesh structure is shown in Figure 3.9. A fine mesh in this region is important to visualize the vortex shedding. The resulting mesh with refinements of the two sections (16 mm × 16 mm and 22 mm × 200 mm) is presented in Figure 3.10. The next step is to refine the coarse meshes in the fluid domain (the region outside of the two sections created in Figure 3.7) as shown in Figure 3.10(a). The fluid domain outside of the two regions does not involve flows with abrupt change in velocity. Therefore, very fine mesh as constructed inside the two regions is not required. The maximum face size of the mesh in the outer fluid domain is set to be 0.0005 m^2 and the resulting mesh structure is presented in Figure 3.10(b). From the figure, better mesh structure with more uniform cells can be observed after the refinement. For the final step, the mesh close to the top and the bottom wall are further refined. The final mesh structure is presented in Figure 3.11. The final mesh of the entire fluid domain consists of 240k cells with non-uniform sizes.

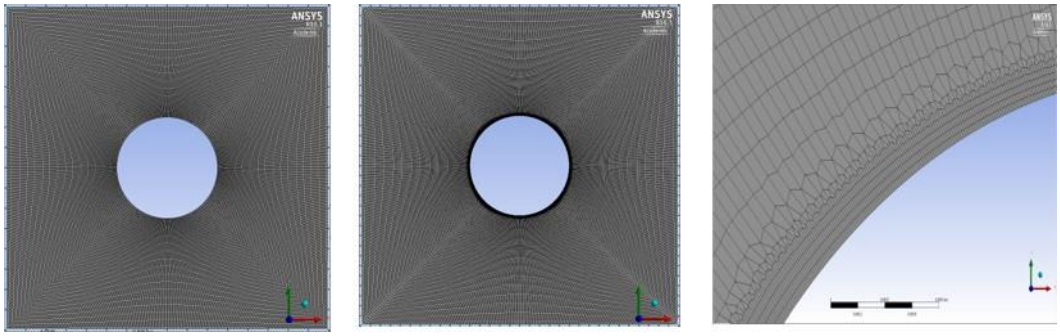

(a) (b) (c)

Figure 3.8: Mesh structure and refinement in region near cylinder. *The scale shown in the image represent 0.00013 m per unit

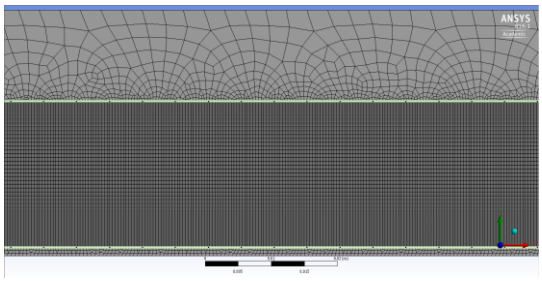

Figure 3.9: Mesh structure in the 22 mm × 200 mm section created in the wake of cylinder. *The scale shown is 0.005 m per unit

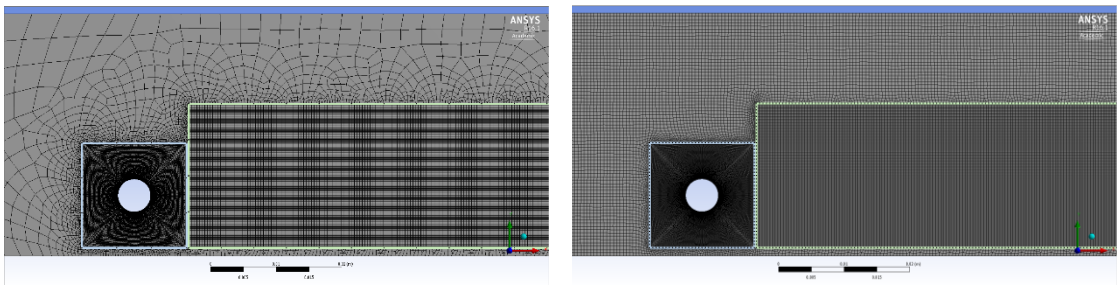

Figure 3.10: Mesh structure in the fluid domain. (a) Before refinement (b) After refinement. *Scale shown in 0.005 m per unit

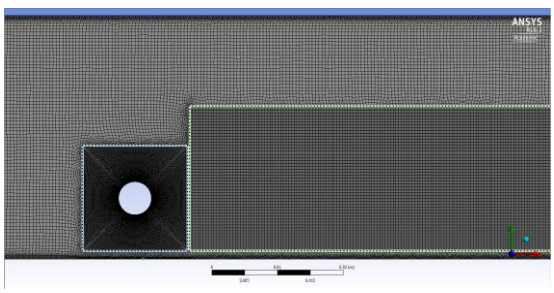

Figure 3.11: Mesh refinement at the pipe walls. *Scale shown in 0.005 m per unit

3.2.4 CFD Setup

The problem set up is specified into the FLUENT solver and includes the type of fluid, the turbulence model and the boundary conditions of the fluid domain. Next, the settings of the solver are specified such as the convergence criteria, step size and number of steps.

3.2.4.1 Boundary conditions

For the problem investigated the pipe walls and the cylinder are set as no-slip boundary conditions, while the front and the end of the fluid domain are set as inlet and outlet conditions respectively. At the inlet, the incoming velocity of the flow is specified. The operating velocities in the work of Chinaud et al. (2017) are chosen for the simulation in order to validate the simulation results against experimental data. Two cylinder based Reynolds numbers, Re_D = 1192 (u = 0.24 m/s) and Re_D = 3250 (u = 0.65 m/s) that correspond to turbulent regime are considered in the simulation. The boundary conditions input into FLUENT solver are presented in Figure 3.12 and in Table 3.3.

Figure 3.12: Boundary of fluid domain.

Table 3.3 Boundary conditions for numerical analysis.

Name	Boundary Conditions
Material	Water (Properties based on FLUENT database)
Inlet	u = 0.24 m/s (Re_D = 1192)
	u = 0.65 m/s (Re_D = 3250)
Outlet	Pressure-outlet
Wall	No-slip wall
Cylinder	No-slip wall

3.2.4.2 Solver setup

The standard *k-ε* is selected as turbulence model, which has been successfully applied by various investigators to simulate two-dimensional flows past bluff bodies as discussed in Section 3.2. An enhanced wall function is applied with the turbulence model for calculations near the wall region. The SIMPLE algorithm and the second order upwind scheme are used for the pressure-velocity coupling and the spatial discretization respectively. To choose the time step, the vortex shedding frequency is considered, which depends on the input inlet velocity. The frequency of the vortex shedding is initially estimated by specifying the Strouhal number, *St* to be 0.20 which is the theoretical value for unbounded flow that has also been confirmed experimentally previously. With *St* = 0.20, the frequency of vortex shedding can be calculated from Eq. 3.9.

$$St = f_v D/\mu \tag{3.9}$$

With bluff body diameter, *D* = 0.005m and for the maximum incoming velocity, *u* = 0.65 m/s, the vortex shedding frequency is calculated to be f_v = 26 Hz. This implies that vortices are shed at every 0.038 s from the top and bottom of the cylinder. Therefore, step size of 0.001s is selected and the cycle of vortex shedding can be captured in 38 time steps. The details of the solver setup are presented in Table 3.4.

Table 3.4: Details of solver setup.

Solver Setup	**Type/Value**
Turbulent model	*k-ε* with enhanced wall treatment
Pressure-velocity coupling	SIMPLE algorithm
Spatial discretization	Second Order Upwind
Step size	0.001s
Number of time steps	2500

The simulation is set for calculating 2500 time steps, which correspond to simulation time of 2.5 s based on a step size of 0.001 s. The length of the

simulation time is considered to be adequate for investigating the resulting wake, as the vortex shedding is a repeated phenomenon over time.

3.2.4.3 Grid sensitivity analysis

Grid sensitivity analysis was conducted to determine the optimum number of cells for the simulation. For the analysis, the number of cell is varied and the resulting Strouhal numbers are compared. Simulations are performed with three grid sizes, namely 150k, 250k and 350k cells. Using a similar simulation setup in Table 3.4, simulations of flow past the 5 mm cylinder are conducted for u = 0.65 m/s and the resulting St and computation time are presented in Table 3.5. The computation time is based on flow time of 2.5 s with time steps of 0.001s.

Table 3.5: Strouhal number and computation time for different grid size.

Cell Count	Strouhal number, *St*	Computation time (Flow time: 2.5 s)
150k	0.21	48 hours
250k	0.202	60 hours
350k	0.202	72 hours

*Processor: Intel (R) Xeon (R) CPU E5-1650 v3 @ 3.50GHz. RAM: 16GB

From Table 3.5, reasonable values of St are obtained for all three cases. In addition, the results agree with the theoretical value of St = 0.20 for unbounded flows. The variations in the value of St are less than 3% while the calculation time differs by about 50%. The analysis shows that the 150k grid size is sufficient to capture the flow separation on the cylinder. A large number of cells leads to more detailed velocity and vorticity contour plots in post processing. Thus for further simulations 250k cells were used that result in reasonable accuracy, quality of the contour plots and computational time.

3.3 Simulation results

The simulation results are analyzed in CFD-Post application provided by FLUENT.

3.3.1 Velocity field

The velocities in the fluid domain are plotted using the contour plot function. As the flow is unsteady, contour plots of instantaneous velocities are constructed. An

example of an instantaneous velocity field for u = 0.65 m/s is presented in Figure 3.13. From the figure, as the fluid flows past the cylinder, it accelerates due to the pressure gradient across the cylinder. In the wake of the cylinder, non-uniform velocity regions are observed which resemble the von Karman vortex street as a result of periodic vortex shedding by the cylinder. The cycle of vortex shedding is presented in Figure 3.14 that shows the instantaneous velocity field at different times. The period for one cycle of vortex shedding for u = 0.65 m/s is 0.04 s which agrees with the estimated period calculated in section 3.2.4.2. In Figure 3.14 the alternate shedding of vortices from the top and bottom of the cylinder can be seen. The vortices shed by the cylinder flow downstream resulting to the von Karman vortex street.

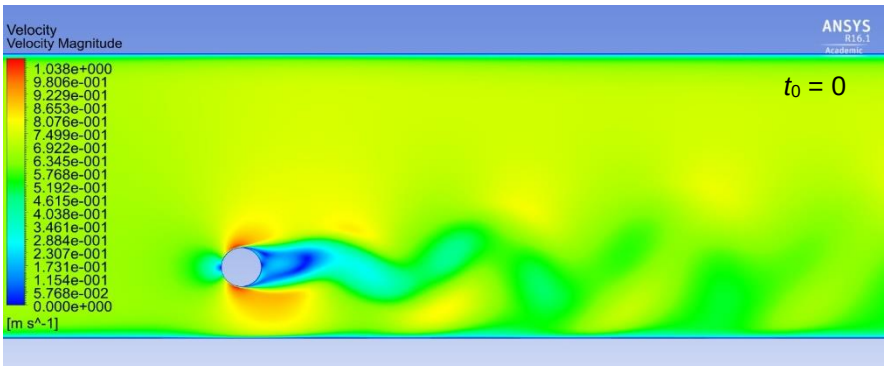

Figure 3.13: Instantaneous velocity field for u = 0.65 m/s.

3.3.2 Vorticity field

Vorticity is the measure of fluid rotation or circulation at any point in the fluid. The vortices shed by the cylinder lead to whirling motion of the fluid which can be represented by vorticity. The instantaneous vorticity field obtained from the simulation is displayed as a contour plot in Figure 3.15. The vorticity field resembles the von Karman vortex street and it corresponds to the location of vortices. It can also be observed that the magnitude of the vorticity decays downstream of the cylinder.

The visualization of velocity and vorticity contours showed that the simulations are able to capture the vortex shedding phenomena and the quality of the contours, which depends on the mesh size, is satisfactory. From both contour plots, no interaction between the vortices and the wall boundary layer at the bottom side of the cylinder is observed. This agrees with the PIV results of Chinaud et al. (2017) that the system resembles unbounded flow.

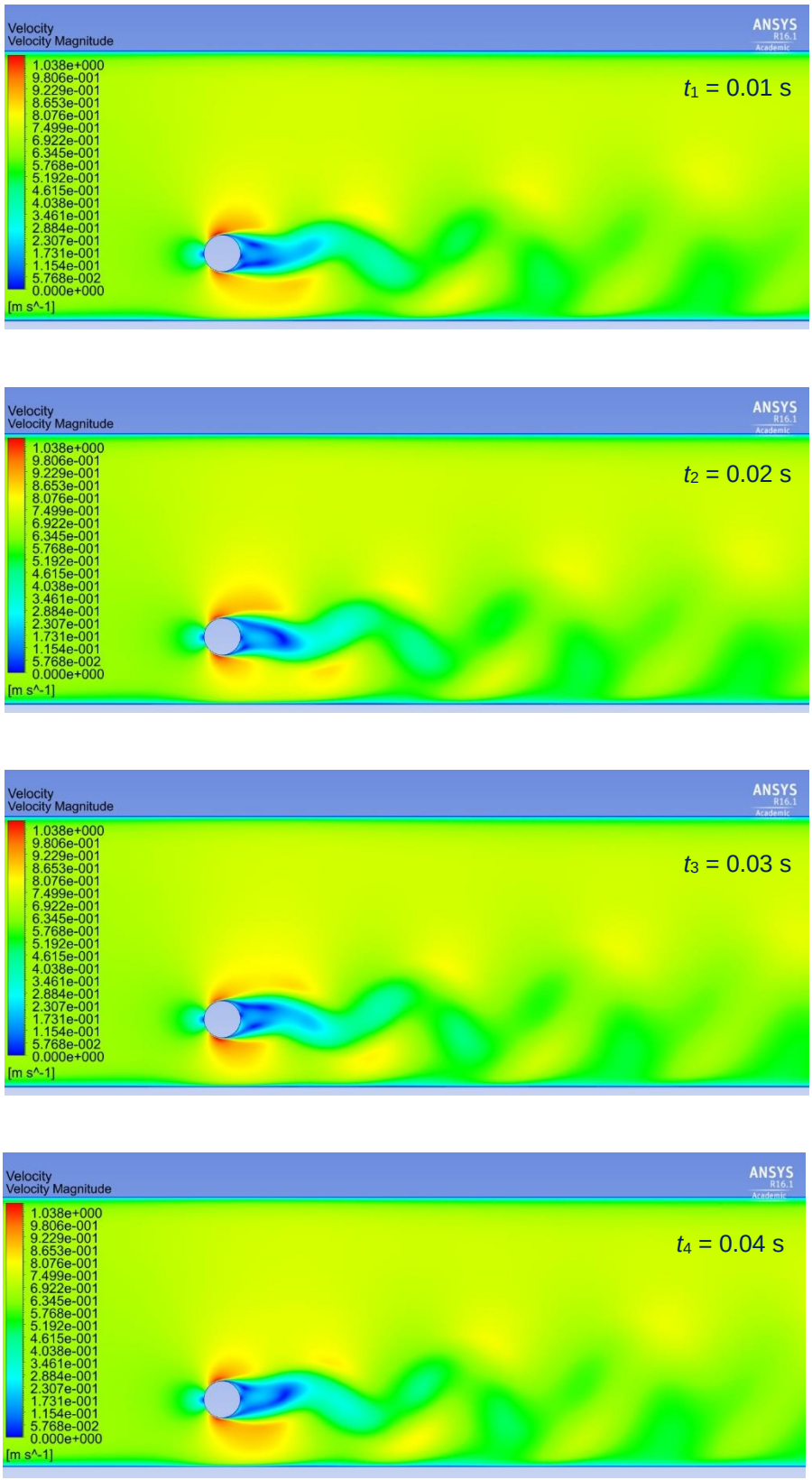

Figure 3.14: Instantaneous velocity field during one cycle of vortex shedding for u = 0.65 m/s.

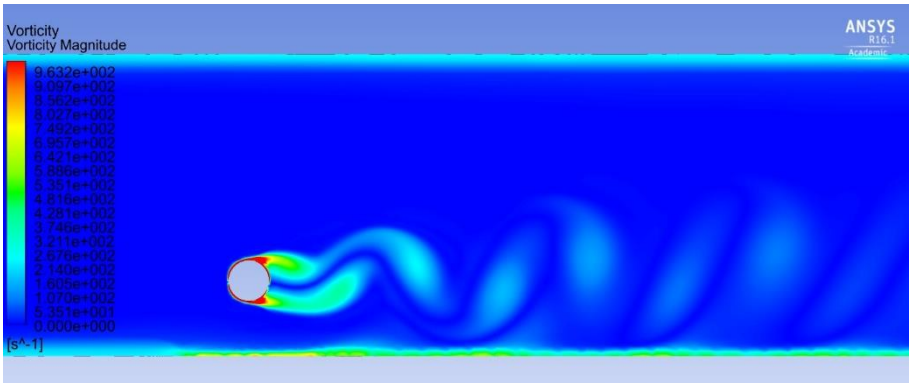

Figure 3.15: Instantaneous vorticity field for u = 0.65 m/s.

3.3.3 Lift coefficient

The action of alternate vortex shedding from the cylinder results to fluctuation of lift forces where the fluctuating lift is mainly caused by the fluctuating pressures acting on the surface of the cylinder (Norberg, 2001). The instantaneous lift coefficient, C_L acting on the surface of the cylinder is recorded in the simulation of the flow. The lift coefficients recorded over the flow time are presented in Figure 3.16 for two inlet velocities, u = 0.24 m/s and u = 0.65 m/s.

Fluctuations of the lift coefficients, C_L are observed due to variation of pressure acting on the cylinder during vortex shedding. It can also be seen that the C_L fluctuates at a constant frequency where this frequency corresponds to the frequency of the vortex shedding. Thus, the frequency of vortex shedding can be determined from the C_L fluctuations. Increasing the incoming velocity from 0.24 m/s to 0.65 m/s resulted to higher fluctuations of C_L as seen in Figure 3.16(b).

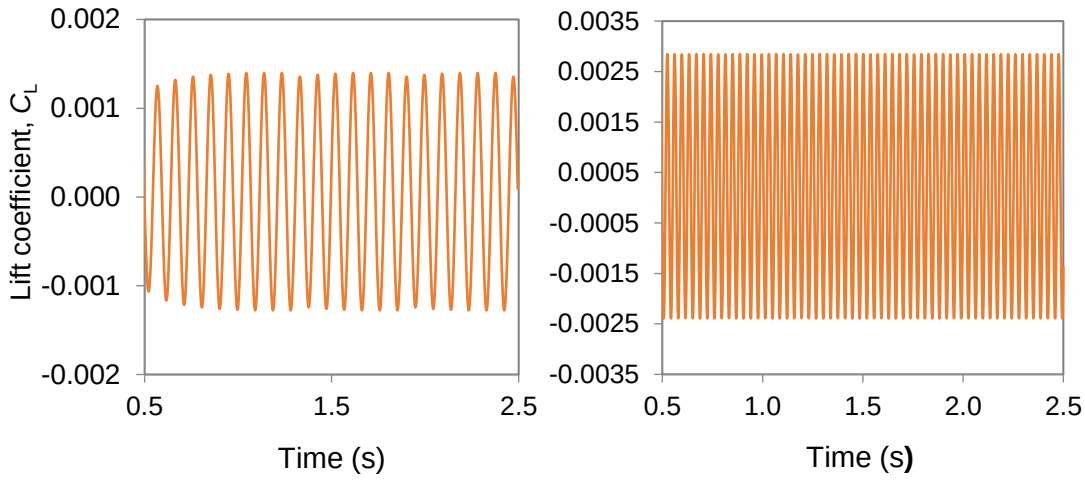

(a) u = 0.24 m/s

(b) u = 0.65 m/s

Figure 3.16: Lift coefficients, C_L. (a) u = 0.24 m/s and (b) u = 0.65 m/s

3.3.4 Comparisons with theoretical and experimental data

The simulation results are compared against experimental data by comparing the Strouhal number, *St* and the velocity profile in the wake of the cylinder. Similar procedures were taken by Kang (2006) and Patil and Tiwari (2008).

3.3.4.1 Strouhal number

The *St* is calculated from Eq. 3.9. In subcritical regime ($200 < Re_D > 3 \times 10^5$), the theoretical *St* for unbounded flow is 0.20. To determine the *St* for the simulated flow system, the frequency of vortex shedding has to be determined.

The alternate vortex shedding from the cylinder causes the fluctuations of lift forces on the cylinder wall and results to the formation of the von Karman vortex street. Therefore, the vortex shedding frequency can be estimated from the frequency of lift coefficient fluctuations on the cylinder and from the frequency of the velocity fluctuations in the wake of the cylinder. This can be achieved by performing Fast Fourier Transform (FFT) analysis on the recorded C_L velocity data to determine the dominant frequency in the signal. The results of FFT for C_L performed on the data in Figure 3.16 are presented in Figure 3.17. From the FFT, the dominant frequency of the lift coefficient for the cases of u = 0.24 m/s and u = 0.65 m/s are 10 Hz and 27.5 Hz respectively and these correspond to Strouhal number of 0.209 and 0.202 based on Eq. 3.9.

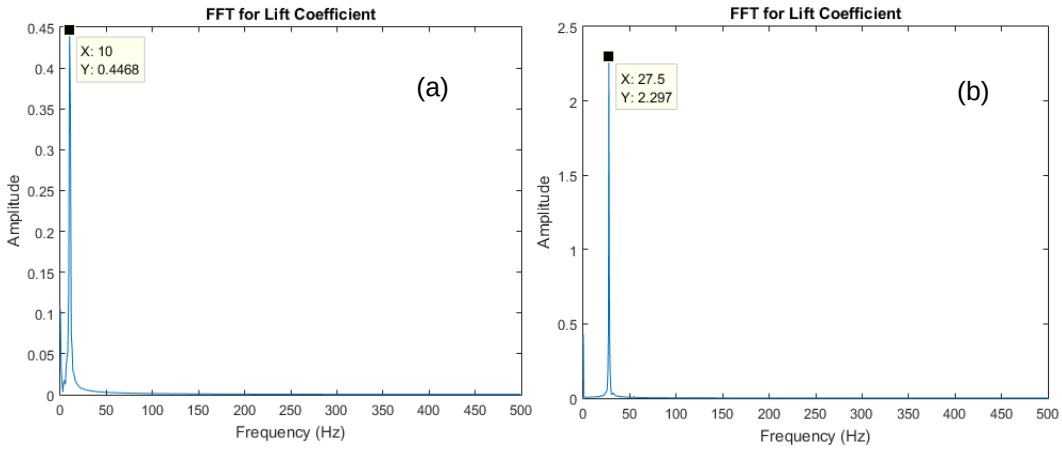

Figure 3.17: FFT of lift coefficients. (a) u = 0.24 m/s and (b) u = 0.65 m/s

To determine the vortex shedding frequency, f_v from the velocity, the y-direction velocity, v, at a point in the wake of the cylinder is tracked over time. The velocity fluctuation is then calculated by subtracting the time-averaged

velocity from the instantaneous velocity at this location. In Figure 3.18, the velocity fluctuations over time are presented for the case of u = 0.65 m/s. As can be seen, in the wake of the cylinder, the velocity fluctuates around the zero value. The fluctuations are caused by the vortices shed from the cylinder. The velocity fluctuates at a constant frequency that is similar to the frequency of vortices shed from the cylinder. FFT is performed on the velocity fluctuations and as shown in Figure 3.19, the dominant frequency is 26.32 Hz which corresponds to Strouhal number of 0.202. The result is in agreement with the *St* determined from the lift coefficient for the same incoming velocity.

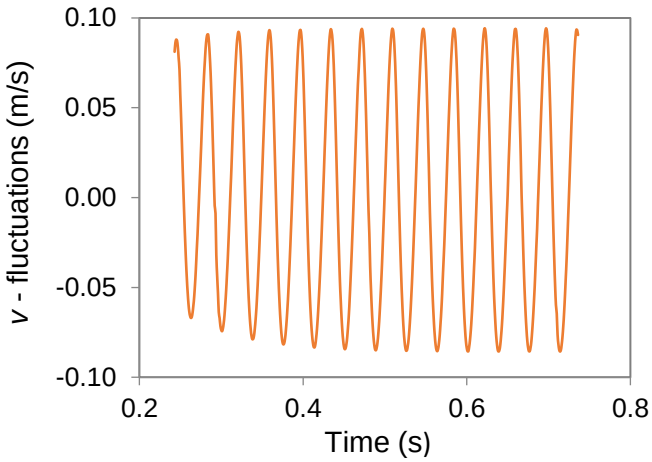

Figure 3.18: Velocity fluctuations at a point in the wake of cylinder for u = 0.65 m/s.

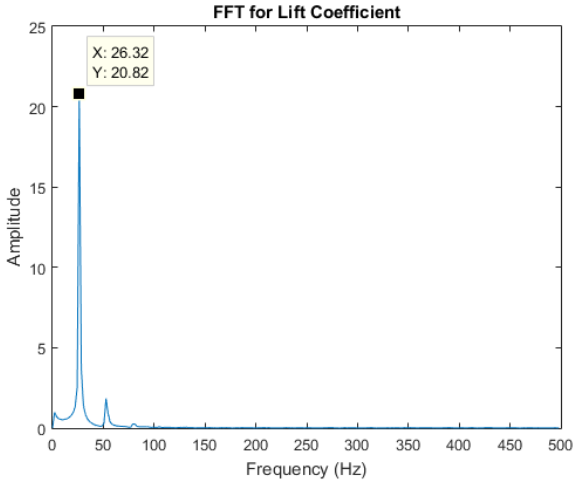

Figure 3.19: FFT of velocity fluctuations for u = 0.65 m/s.

The Strouhal numbers calculated from the lift coefficient, C_L and from the velocity in the wake of the cylinder are in agreement. They also agree with the

theoretical value of St = 0.20 for unbounded flows and with the experimental data by Chinaud et al. (2017). This also implies that that the two-dimensional simulations conducted in this work are able to capture the vortex shedding phenomenon in the wake of the cylinder with reasonable accuracy.

3.3.4.2 Velocity profile

To further validate the simulations, the simulated velocity profiles are compared against the experimental ones in a region where abrupt change in velocity occurs. The velocity profiles are time-averaged in the x-distance between the center of the cylinder (x = 0) to a distance equal to two cylinder diameters (x = 2D) and at the bottom half of the pipe as presented in Figure 3.20. In the figure, the center of the cylinder is located below the pipe center at y = -0.00925 m with the pipe center located at y = 0.

The time-averaged velocity profiles from the simulation of flow past the 5 mm cylinder for two Re_D are compared in Figure 3.21 against the experimental velocity profile obtained with PIV measurements by Chinaud et al. (2017). The velocity has been normalized with the maximum velocity, u/u_{max}. For both cases, the simulation results agree well with the experimental data, with average deviation of less than 6%. At the area just behind the cylinder (y = - 0.012 to - 0.009) the numerical simulation data shows a smoother profile compared to the experimental data. This may be caused by the fewer datas point considered in the experimental analysis.. This may be caused by the less data point considered in the experimental analysis. Therefore, it can be concluded that the numerical modelling is able to predict the velocity profile behind the cylinder with reasonable accuracy.

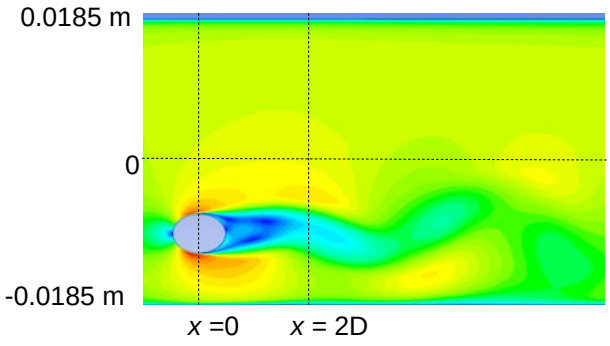

Figure 3.20: Locations for velocity profile comparison.

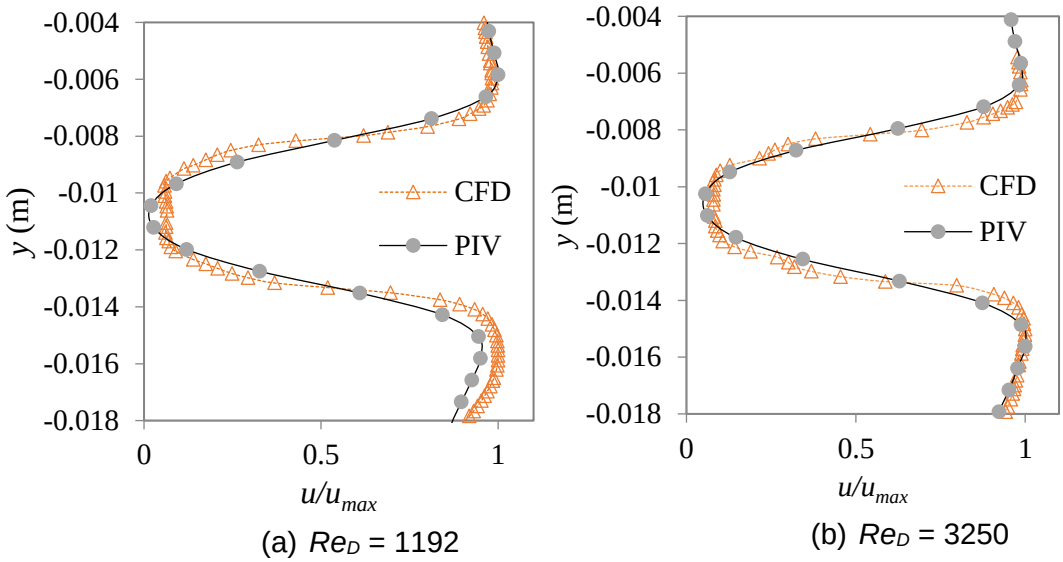

Figure 3.21: Velocity profile comparisons between CFD and PIV data.
(a) Re_D = 1192 and (b) Re_D = 3250 *Data taken from Chinaud et al. (2017)

3.4 Flow Past Cylinders of Various Sizes

In studies of Park et al., (2016), it was found that the bluff body actuates the transition from stratified to dispersed flows by generating interfacial waves in the wake of the cylinder. It was also found that the frequency of vortex shedding in the wake of the bluff body matched the frequency of interfacial waves. This allows the wave characteristics such as frequency and amplitude as well as the detachment of drops from them to be studied. In the work, a single size of the cylindrical bluff body was used and the range of frequencies generated was limited. Based on these findings, in this work the diameter of the cylinder will be varied experimentally, so that a wide range of vortex shedding frequencies is obtained. The effects of varying the vortex shedding behavior on the flow pattern transition and the resulting wave characteristics will then be studied. To this end, simulations of flow past cylinders of various sizes are conducted initially to select suitable cylinder sizes for the experimental analysis.

3.4.1 Design aspects

Several design aspects are considered when designing the bluff body diameter which are the vortex shedding frequency, position of the bluff body and possible wall effects.

The purpose of varying the cylinder diameter is to generate vortex shedding frequencies over at least 2 orders of magnitude, in the range of 1 to 100 Hz. Assuming unbounded flows where *St* = 0.20, this range of frequencies can be achieved by having cylinders with diameters in the range of 2 mm to 10 mm for velocities in the range of about 0.3 to about 1.1 m/s. These velocities correspond to volumetric flow rates 20, to 70 L/min which were also used in the previous works (Park et al., 2016; Chinaud et al., 2017) and result in stratified flows when there is no cylinder present. Suppression of vortex shedding is reported to occur when the gap ratio is below a critical value of approximately 0.30 as discussed in chapter 2 (Section 2.4.2). Therefore, in the simulations, cylinder sizes larger than 10 mm are not considered to avoid the suppression of vortex shedding while the 2 mm cylinder was chosen to increase the frequency of vortex shedding to 100Hz.

The cylindrical bluff body is located in the lower half of the pipe which is in the water phase in the two-phase flows. The center of the cylinder is positioned at 9.25 mm above the bottom of the pipe for all cylinder diameters investigated, the same as the one used for the 5 mm cylinder in the work of Park et al. (2016) and Chinaud et al. (2017) (Figure 3.22). The variation in the cylinder diameters leads to variations of the gap ratio. The resulting gap ratios for the cylinder diameters used in the simulations are presented in Table 3.6.

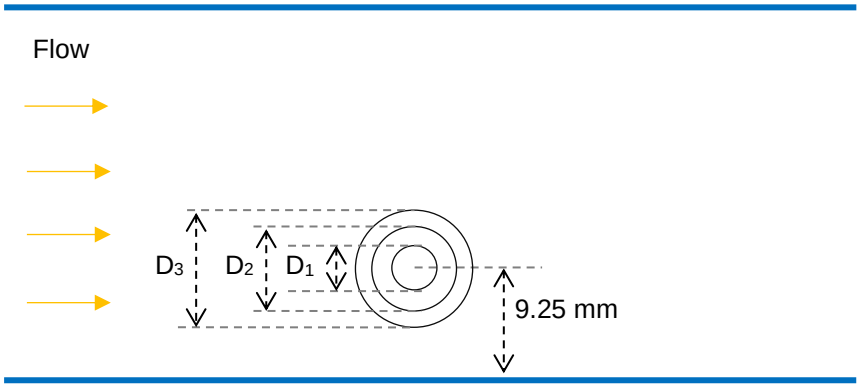

Figure 3.22: Position of the cylindrical bluff bodies.

3.4.2 Simulations of flow past cylinder with various sizes

With the validated two-dimensional single-phase simulation setup developed in Section 3.3, simulations of flow past cylindrical bluff bodies with various diameters are conducted. The cylinder diameters that are considered in the simulations are presented in Table 3.6 and they are 2, 5, 7, 8, 9 and 10 mm. For each case, simulations are performed for three velocities of 0.31, 0.62 and 1.09. From the simulation results the frequency of vortex shedding is determined from the lift coefficients and the Strouhal number, *St* is calculated. The results for all six cases are summarized in Table 3.6.

Table 3.6: Simulation results for Case 1 to Case 6.

Simulation Case	Cylinder Diameter (mm)	Gap Ratio, γ	Velocity (m/s)	Frequency (Hz)	Strouhal Number, *St*
1	2	4.125	0.31	29.85	0.214
			0.62	71.43	0.219
			1.09	117.20	0.23
2	5	1.35	0.31	10.00	0.209
			0.62	26.26	0.202
			1.09	46.29	0.230
3	7	0.821	0.31	8.87	0.206
			0.62	21.05	0.226
			1.09	34.00	0.237
4	8	0.656	0.31	8.00	0.213
			0.62	19.31	0.237
			1.09	34.00	0.280
5	9	0.528	0.31	8.00	0.230
			0.62	16.00	0.227
			1.09	32.00	0.288
6	10	0.425	0.31	8.00	0.260
			0.62	18.58	0.270
			1.09	40.00	0.280

According to the simulation results in Table 3.6, for Case 1 to 3 with cylinder diameters of 2, 5 and 7 mm, the Strouhal numbers at all velocities

investigated vary from 0.202 to 0.237 and are in agreement with the value in unbounded flows. Similar results are also obtained for Case 4 and 5 at velocity values of 0.31 and 0.62 m/s. The results imply that at these flow conditions and cylinder diameters, the vortex shedding is not affected by the presence of the wall. For Case 4 and 5, at the higher velocity of 1 m/s, however, higher values of *St* are obtained with *St* > 0.28 which signify the influence of the adjacent wall (at the bottom part of the cylinder) on the vortex shedding behavior. The wall causes the vortices to be shed at higher frequency compared to the case of unbounded flows, because the fluid accelerates in the smaller gap between the bottom part of the cylinder and the wall. As the gap is further reduced in Case 6, *St* values of 0.26 – 0.28 are obtained for all three velocities which indicate wall effects.

Based on the results of the numerical analysis, two cylinder diameters are considered for the experiments. In order to obtain vortex shedding frequency of around 100 Hz, the 2 mm cylinder diameter is selected. For the low limit of frequencies, both cylinders with diameters 8 mm and 9 mm show no wall effects at least at low velocities. Since both diameters give similar frequency of 8 Hz at 0.31 m/s, the 8 mm one is chosen to minimize the wall effects. Varying the size of the bluff body alters the vortex shedding frequency and results to change in the size of the circulation region in the wake of the cylinder.

At constant incoming velocity, reducing the size of the bluff body leads to increased vortex shedding frequency as visualized in Fig. 3.23 where the velocities in the wake of 2 mm and 5 mm cylinders are plotted for incoming velocity of u = 0.62 m/s. As can be seen the frequency is higher for the 2 mm cylinder compared to the 5 mm one. On the other hand, increasing the diameter of the cylinder leads to an increase in the recirculation regions in the wake of the cylinder. The contour plots of the instantaneous velocities in the wake of the 5 mm and the 8 mm cylinders are shown in Figure 3.24. As can be seen the size of recirculation regions generated behind the 8 mm cylinder is larger compared to the 5 mm one, while the recirculation regions are positioned closer to the pipe center.

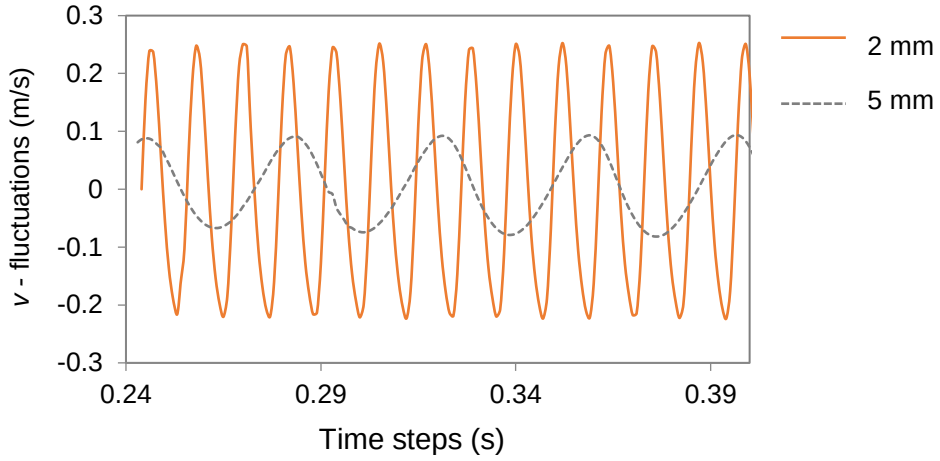

Figure 3.23: Velocity fluctuations in the wake for 2 mm and 5 mm cylinder.

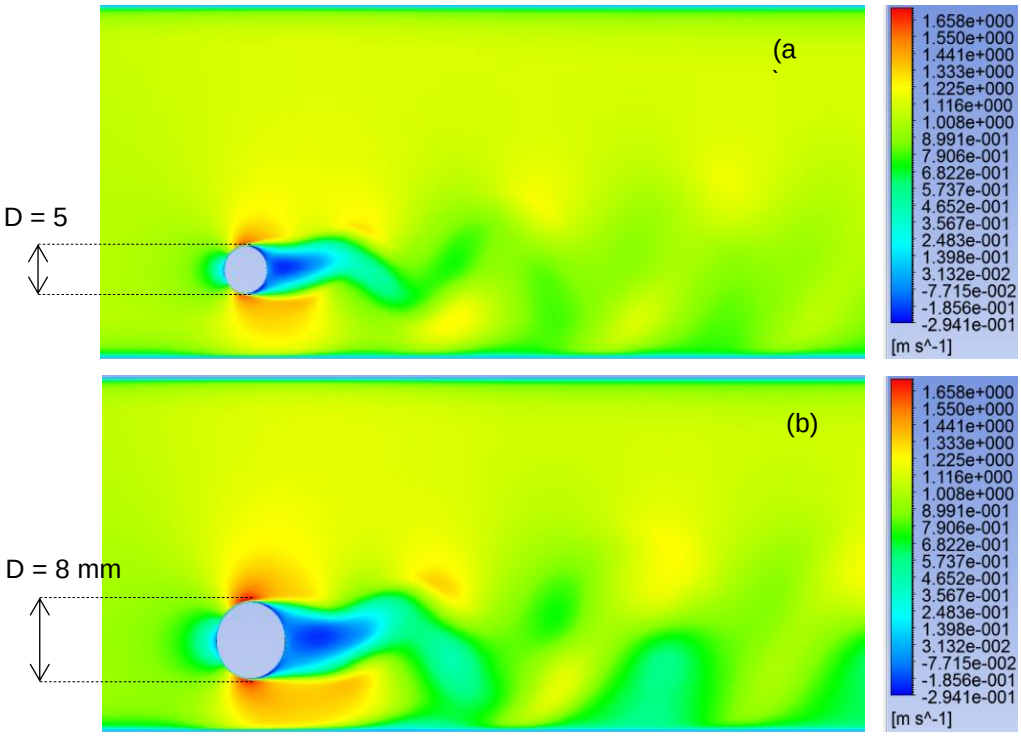

Figure 3.24: Instantaneous velocity in the wake of cylinder. (a) 5 mm cylinder and (b) 8 mm cylinder.

3.5 Summary

In this chapter, a numerical approach was employed to analyze the flow past cylindrical bluff body of various sizes. Based on the results of our previous work, two-dimensional single phase flows are used to guide the design of the bluff bodies. The commercial software FLUENT was used and the model was validated against experimental data from previous work on single phase flows past a 5 mm cylinder. The simulation results showed good agreements with experimental data, implying that experimentally, at the center of the pipe, the flow structure resembles two-dimensional flow.

The numerical model was then used to study vortex shedding from cylinders with diameters of 2, 5, 7, 8, 9 and 10 mm for flow velocities between 0.31 m/s and 1.09 m/s. These were considered because in unbounded flows they should produce vortices with frequencies in the range of 1 to 100 Hz and St = 0.20. For the cylinder diameters considered, the resulting gap ratio, γ is kept above the critical value of 0.30 where suppression of vortex shedding can occur.

From the results of the numerical analysis for various cylinder diameters, it was found that cylinders with diameters 2, 5 and 7 mm produce vortices similar to the case of unbounded flows with Strouhal numbers equal to about 0.2 for all velocities studied. As the gap from the low pipe wall is further reduced for the 8 and 9 mm cylinders, an increase in St is observed at high velocities which implies wall effects. For the 10 mm cylinder, $St > 0.26$ were obtained for all velocities investigated. Based on the simulation results, two cylinder diameters are chosen for the experimental investigations, 2 mm and 8 mm. The small cylinder with D = 2 mm is selected because it can generate vortices with frequency as high as 100 Hz. As an upper limit, a cylinder with D = 8 mm was chosen as above this size, significant wall effects were observed.

With the cylinder diameters chosen vortex shedding frequencies from 1 to 100 Hz should be obtained for velocities between 0.31 m/s and 1.09 m/s. Change on the cylinder diameter also modifies the size and the position of vortices/circulation regions in the wake of the cylinder. The influence of the cylinder size on the frequency of vortex shedding, the size and the position of the circulation regions is expected to have significant effects in two-phase flow where an interface is present.

Chapter 4

Experimental Methods

In this chapter, the experimental methods employed through the entire studies are presented and described. These include the details of the flow facilities and the test fluids, the design of inlet with the bluff body and the various optical techniques used. The chapter is separated into two main sections based on the two flow facilities used in this work: the first with a 37 mm internal diameter (I.D.) and the second with a 26 mm I.D. test section.

The studies of the characteristics of the vortex-induced interfacial waves and of the vortex-shedding properties in the wake of the bluff body were conducted in the 37 mm I.D. flow facility. High-speed visualization was employed to capture the interfacial waves while the velocity fields and the characteristics of the vortices were obtained with particle image velocimetry (PIV) for both single (water) and two-phase flows. For the studies of the drop entrainment mechanism, an advanced laser based technique (simultaneous PLIF and PIV) was employed in order to visualize and track the interface deformation and to obtain the instantaneous local velocities simultaneously during the drop entrainment process. For this purpose, a 26 mm I.D. flow facility was designed with test fluids of matching refractive index to facilitate the laser-based techniques.

Experimental analysis of the two-phase flows was conducted in the pilot scale flow facilities located in lab LB21a in the Department of Chemical Engineering, University College London (UCL). The facilities were designed for the studies of two-phase liquid-liquid flows in horizontal pipes. The main components of both facilities used in this work are similar. Both facilities consist of individual storage tanks for the test fluids, a Y-inlet used to bring the test fluids into contact, the test section made of acrylic and a gravity settler to separate the two fluids at the end of the test section.

4.1 Investigation of Flow Dynamics in the Wake of a Cylinder

4.1.1 Flow facility (37 mm I.D.)

Investigations of the dynamics of two-phase liquid-liquid flows in the wake of cylinder with varying diameters were conducted in a pilot scale two-phase flow loop with its schematic diagram presented in Figure 4.1 and detailed instrumentations shown in Figure 4.2. The horizontal test section is constructed with combinations of 37 mm I.D. transparent acrylic pipes of lengths ranging from 0.25 to 1 m which are connected by flanges. The test section is designed so that investigations can be conducted at any location along the pipe by simply rearranging the pipe sections and the transparent pipes allow the flow to be observed and recorded from the outside. The total length of the test section is approximately 16 m with two legs of 8 m long connected via two bends and a 0.25 m pipe section as illustrated in Figure 4.1. Experimental investigations in this work, however, are only conducted along the front leg to avoid any effects on the flow patterns due to the curvature.

Test fluids are stored in their individual storage tanks made of fiberglass. Each tank has a maximum capacity of 800 L with a water tap connected to the water tank to supply fresh water to the facility. The test fluids are introduced to the test section separately from their storage tanks via individual centrifugal pumps (Flowserve 2K40-25-250). The pumps have motors of variable speed that can reach up to 3000 rpm. The power of the pumps is 18.5 kW and is supplied by two three-phase Santerno Sinus Penta inverters. The total dynamic head for each pump is approximately 96 m with a capacity in the range of 0.35 to 20 m^3/h. The flow rates are digitally controlled by Coriolis mass flow meters (Proline Promass 80E by Endress & Hauser) with an accuracy of 0.2% as estimated by the supplier. The Coriolis flow meters can provide continuous measurements of the density of the liquids for monitoring of any significant change in the density during operations which may indicates possible temperature or separation issues. The flowrates are regulated through an automated flowrate controller (Allen Bradley-Panel View C400) that connects the flowmeters to the pump. After the test section, the two phases are separated in a gravity settler equipped with a KnitMesh^{TM} coalescer and they flow by gravity back to their respective storage tanks. The mesh is located at the center of the separator to inhibit development

of turbulence. The horizontal separator has a length of 2 m long and a diameter of 0.7 m with maximum capacity of 0.8 m^3.

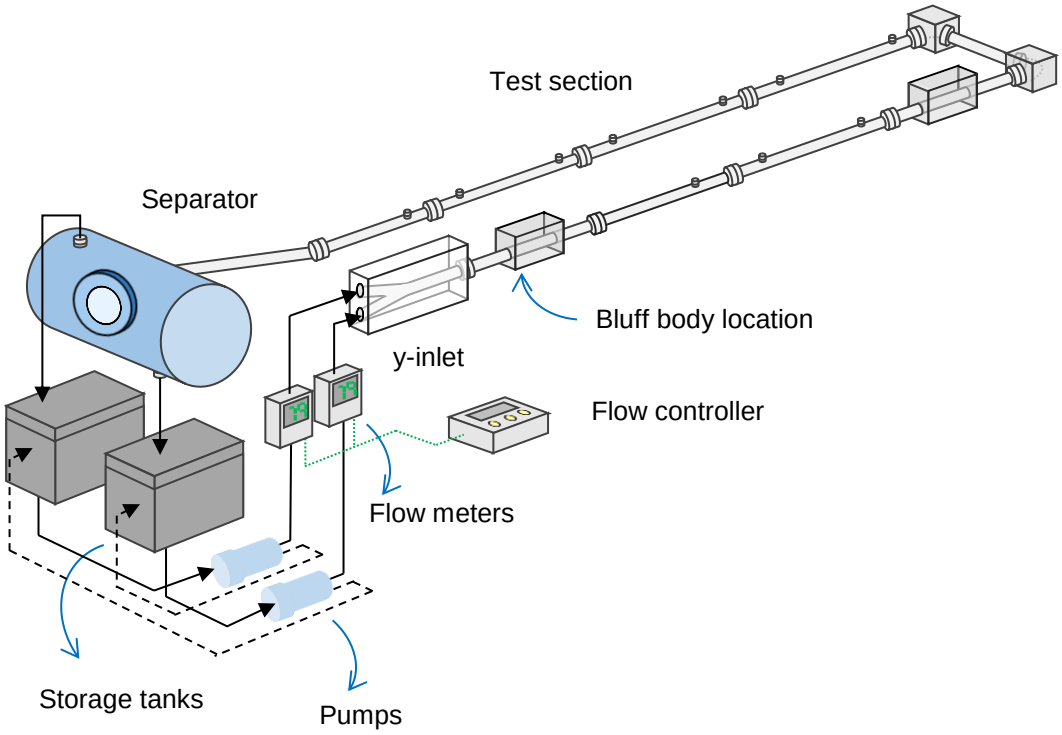

Figure 4.1: Schematic diagram of 37 I.D. oil-water flow facility.

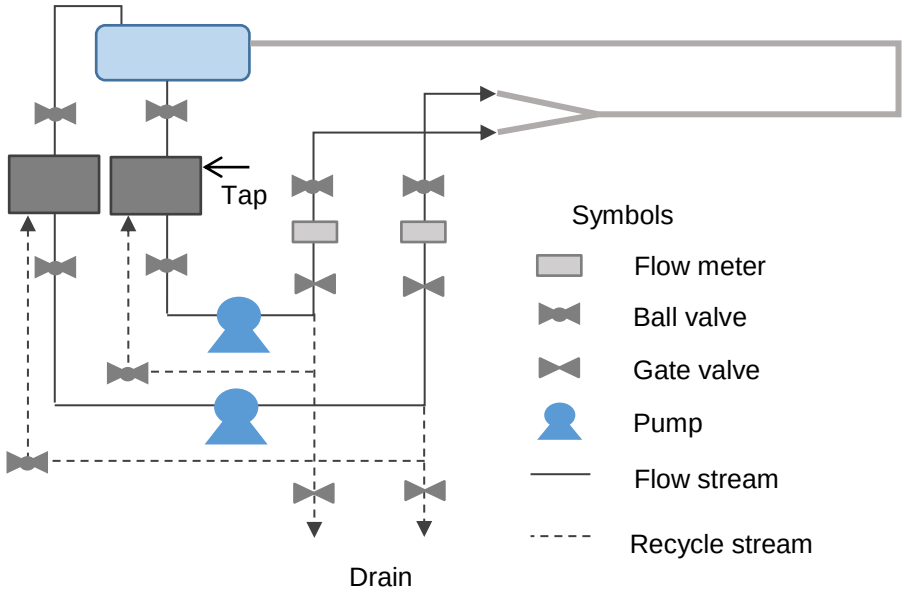

Figure 4.2: Process flow diagram for 37 I.D. oil water flow facility.

4.1.2 Liquid-liquid contactor: Y-Inlet

The two test fluids are introduced into the test section via a symmetrical Y-shaped inlet presented in Figure 4.3. The Y-inlet is designed to minimize the mixing of the two fluids. It is made of two inlet ducts of 37 mm I.D. at an inclination of ±10^{o} from the horizontal plane that eventually meet and form a single duct with I.D. of 37 mm. The low angle was chosen to minimize the effects of pipe bend when the respective fluids travels into the test section. The water phase with higher density is introduced in the bottom inlet while the oil with the lower density is introduced in the top inlet. The inlet is securely positioned along the test section on a heavy-duty support platform made of stainless steel where it is screwed for stability. The platform is fixed on the ground to minimize the impact of vibrations from the pump.

Studies of Barral et al. (2015), reported that although the impact of contact has been minimized, at high flow velocities, presence of interfacial waves is observed immediately after the two fluids are joined at the junction. However, the waves formed at the junction are damped and disappear at a short distance downstream the junction. In this work, investigations were conducted at low input velocities to form stratified flows approaching the cylinder. At these flow conditions, no interfacial waves were observed as the result of the contact of the two fluids.

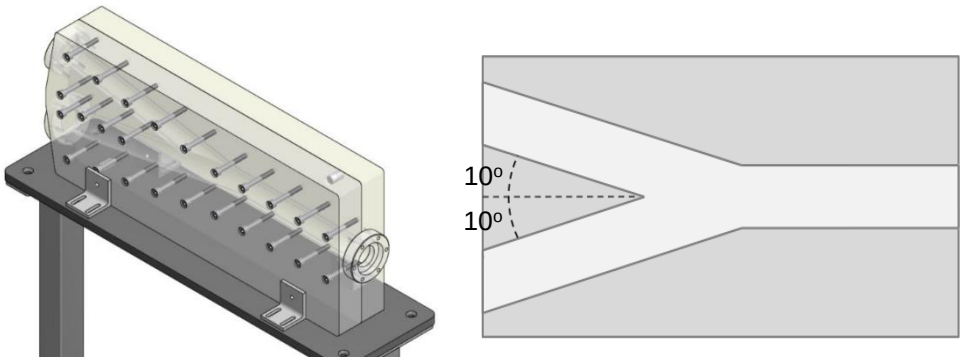

Figure 4.3: 3D design and schematic of Y-inlet.

4.1.3 Test fluids

The test fluids used in this flow facility are tap water and Exxsol D140 oil with the physical properties shown in Table 4.1. The water was replaced with fresh water

on daily basis during the experimental runs. The properties of the test fluids such as density and viscosity may vary depending on its temperature, which may rise if the rig is operated continuously for a long period (>2 hours). Therefore, for consistency, the temperature of the test fluids in the storage tanks is monitored during the experimental sessions to ensure that there is no significant change in the temperature ($\pm 2^{o}$C) that may affect their physical properties. The rig is operated for not more than 30 minutes before it is let to rest for 10 - 20 minutes.

Table 4.1: Properties of test fluids at room temperature.

Properties	Exxsol D140	Water
Density (kg/m^3)	830	997
Viscosity (kg/ms)	0.0055	0.001
Refractive Index	1.439	1.333
Interfacial tension (N/m)	0.0329	

4.1.4 Flow parameters

Experimental works on the two-phase oil and water flows in a pipe were conducted at various mixture velocities, u_{mix} and flowrate ratios, r which are defined as follows;

$$u_{mix} = u_{so} + u_{sw} \tag{4.1}$$

$$r = u_{so}/u_{sw} \tag{4.2}$$

In Eq. 4.1 and 4.2, u_{so} and u_{sw} represents the oil and water superficial velocities respectively. The superficial velocities depend on the input flowrates into the test section, and are calculated from the following equations:

$$u_{so} = Q_0/A \tag{4.3}$$

$$u_{sw} = Q_w/A \tag{4.4}$$

In Eq. 4.3 and 4.4, Q_o and Q_w are the water and oil flowrates and A represents the cross sectional area of the pipe, $A = \pi D^2/4$.

4.1.5 Inlet design

The pipe inlet section that contains the cylindrical bluff body was designed as 0.5 m pipe sections with flanges attached at their ends. As optical imaging is conducted from the side of the pipe, these inlet section is encapsulated in a visualization box filled with glycerol to minimize optical distortions due to the pipe curvature. The box was made of acrylic with almost matching refractive index to the refractive index of glycerol (refractive index of acrylic and glycerol is 1.49 and 1.47 respectively). The design of the pipe section containing the bluff body is presented in Figure 4.4.

As discussed in chapter 3, two cylinder diameters were chosen for further experimental studies, namely the 2 mm and 8 mm cylinders. The cylinder was located transverse to the flow direction with distance from the center of the cylinder to the bottom of the pipe equal to 9.25 mm. The cylinder location is selected to be similar to the previous work by Park et al. (2016) and Chinaud et al. (2017) to enable comparisons. Each cylinder is fixed permanently at its location with the distance from the Y-inlet where the two phases are contacted is approximately equal to 0.46 m. The short distance was designed to avoid the development of interfacial waves due to Kelvin-Helmholtz instability as the two fluids travels approaching the cylinder. The schematic of the inlet cross section is presented in Figure 4.5. Due to the pipe curvature, distance from the pipe bottom to the cylinder varies. Therefore, the gap ratio, γ is calculated at the middle plane of the pipe as illustrated in Figure 4.5. Details of the inlet designs and the corresponding gap ratio for the system with 2 mm and 8 mm are tabulated in Table 4.2.

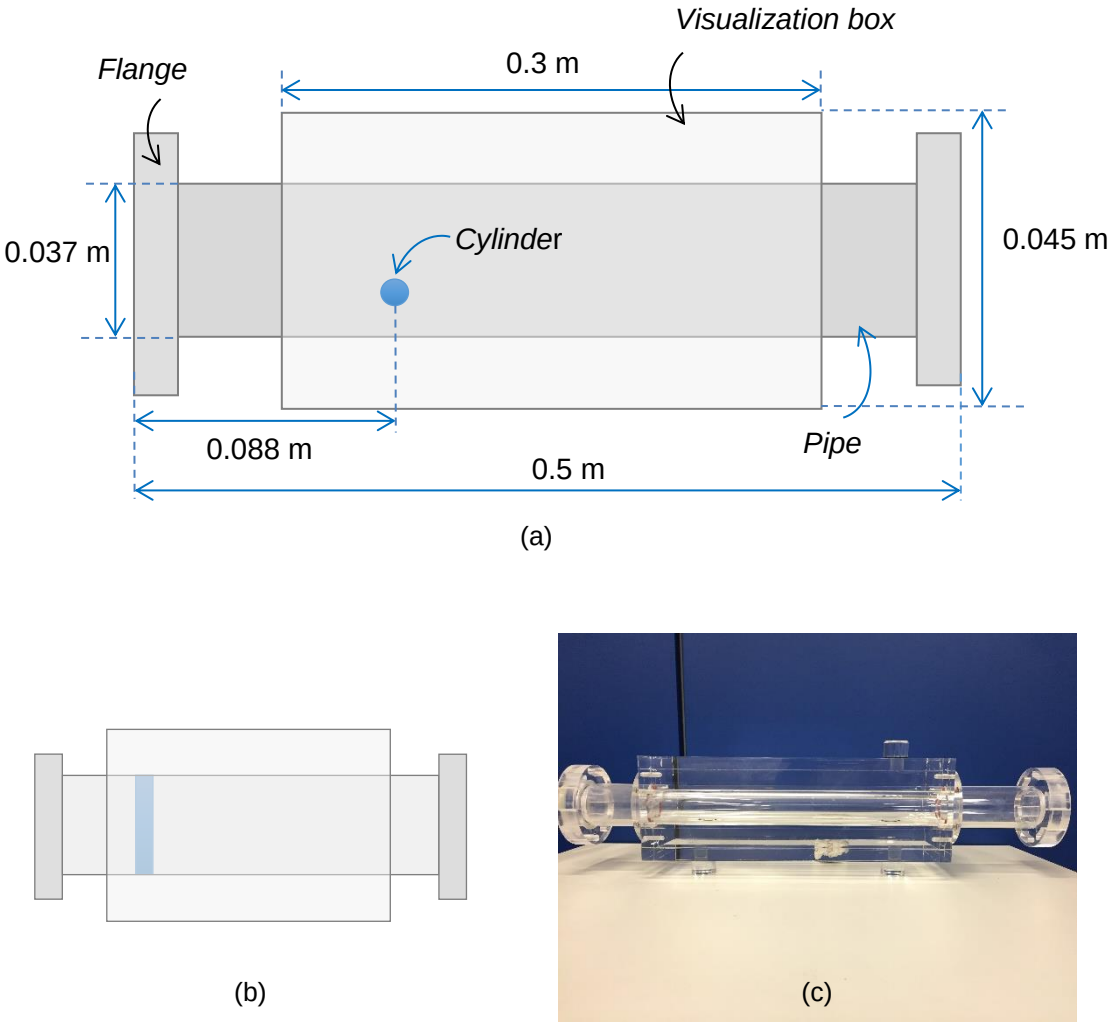

Figure 4.4: Pipe section with bluff body. (a) Side view (b) top View (c) Photograph

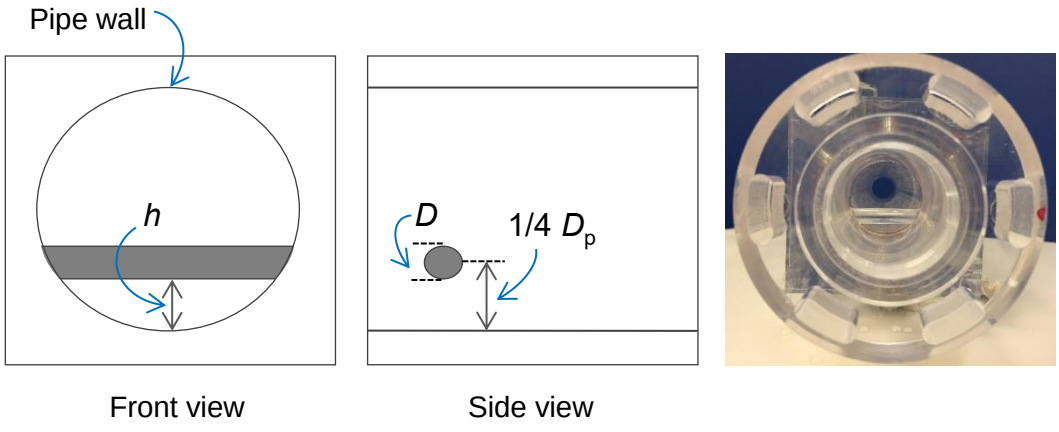

Figure 4.5: Schematic of inlet pipe section containing cylindrical bluff body.

Table 4.2: Inlets properties (37 mm I.D.)

Inlet Properties	Inlet 1	Inlet 2
Pipe diameter, D_p (mm)	37	37
Cylinder diameter, D (mm)	**2**	**8**
Distance from cylinder to wall, h (mm)	8.25	5.25
Gap ratio, γ (-)	4.13	0.66

4.1.6 Experimental techniques

4.1.6.1 High-speed visualization

High-speed visualization was employed in the investigations of vortex-induced interfacial waves in the wake of the cylinder and the identification of the flow patterns. Recordings were conducted from the side of the pipe with the camera located perpendicularly to the investigation section which is illuminated by the backlights. The height of the high-speed camera was adjusted with the use of a tripod which also ensures that the camera is stable and stationary throughout recordings. The visualization box was adjusted to be perpendicular to the camera by ensuring the top side of the box to be flat (0^o) and in line with the lens by using a mini spirit leveler placed on top of the box. The arrangements of the optical instruments with their details are presented in Figure 4.6. Photograph of the high-speed visualization setup is also shown in Figure 4.7.

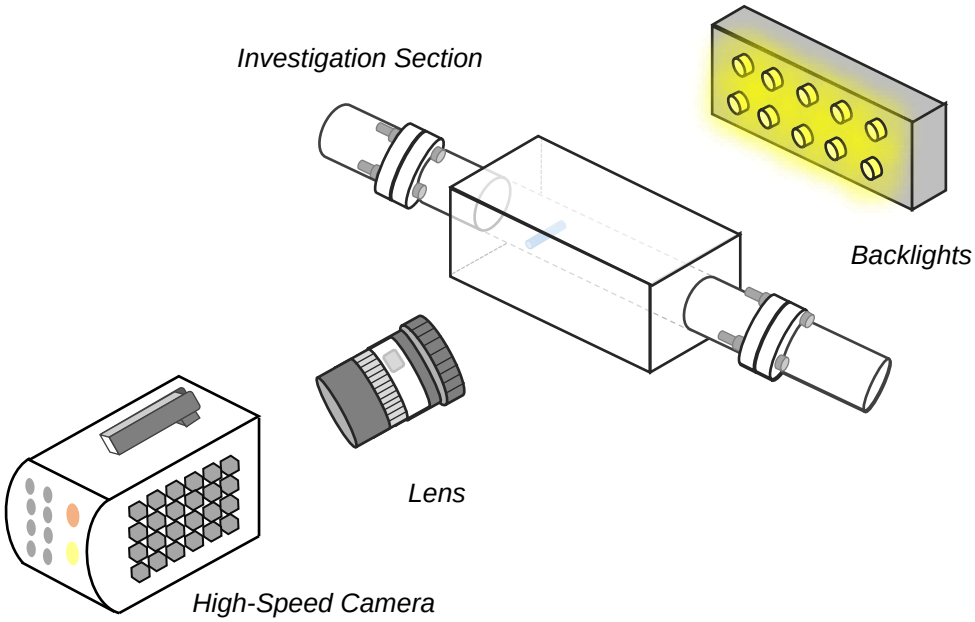

High-speed camera	• Photron SA-1 • Acquisition rate: 2000 to 5000 fps • Resolution: 1024 × 1024
Lens	• 105 mm f/2.8 macro

Figure 4.6: Arrangement of optical instruments for high-speed visualization.

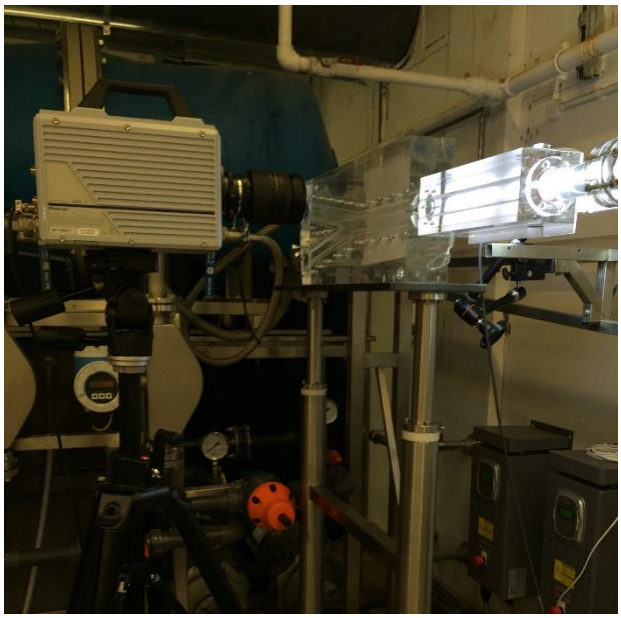

Figure 4.7: Photograph of high-speed visualization setup.

The investigation of vortex-induced wave properties is conducted in the wake of cylinder at a distance of 0.2 m from the Y-inlet while the flow pattern identification is conducted at 7 m downstream from the Y-inlet. The locations are shown in the schematic in Figure 4.8.

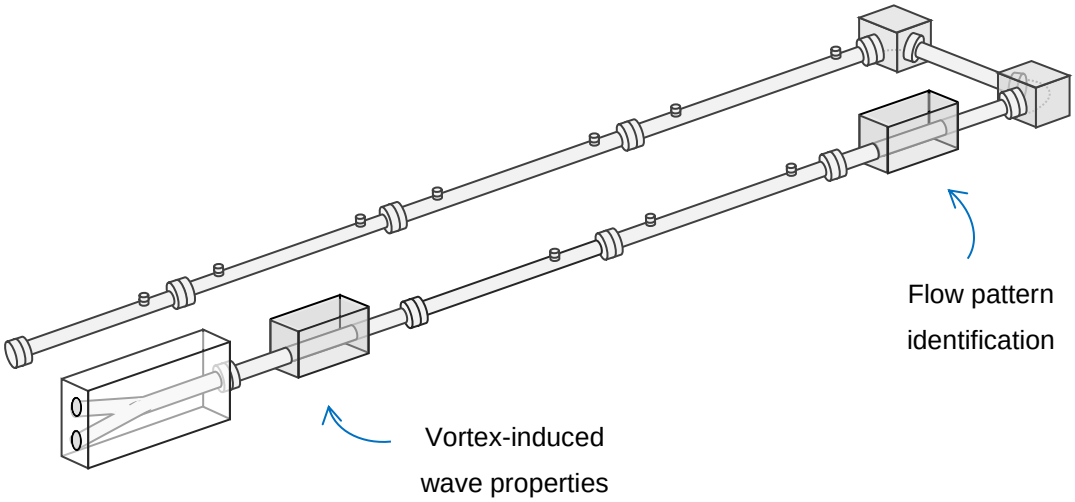

Figure 4.8: Locations of high-speed visualization investigations.

High-speed visualization was conducted at various mixture velocities and oil to water flowrate ratios. In the experiments, u_{so} and u_{sw} are varied from 0.16 m/s to 1.8 m/s respectively which correspond to u_{mix} ranging from 0.310 m/s to 2.169 m/s and r from 0.143 to 7.0.

The analysis of the captured high-speed images was conducted with the Photron FASTCAM Viewer software (PFV) which is integrated with the high-speed camera. The imaging software provides a user interface with image analysis functions including image enhancement, motion analysis and length measurements at accuracy of $\pm$ 2 pixel. An example of the image analysis using the software is presented in Figure 4.9. The software allows the high-speed images to be played as video thus further assisting the analysis at different flow times.

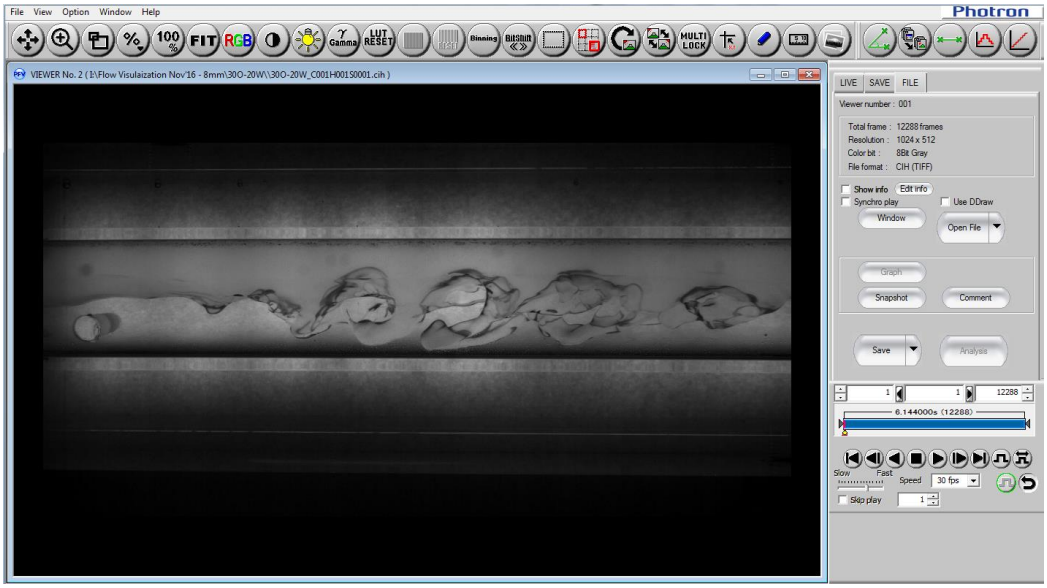

Figure 4.9: Photograph of PFV software used for image analysis.

4.1.6.2 Particle image velocimetry (PIV)

PIV technique was employed for the determination of velocity fields in the wake of the cylinder. For this technique, the water phase is seeded with silver coated hollow glass particles with diameter of 10 μm supplied by TSI instruments. The technique involves the use of a high-speed camera and a continuous laser with their arrangements presented in the schematic shown in Figure 4.10.

A continuous diode pumped solid state (DPSS) laser by Laserglow Technologies was used to illuminate the investigation section from underneath the pipe. The laser emits a beam of 4 mm thickness with a wavelength of 532 nm (green) at constant output of 3000 mW. A concave lens was used to transform the laser beam into a laser sheet of approximately 30 cm long while a collimator was used to reduce the sheet thickness to approximately 1 mm. The laser sheet was aligned to be at the center of the pipe in the axial direction of the flow with the help of an alignment paper printed with dots of known distance placed underneath the test section. This results to a two-dimensional plane of measurement in the center of the pipe.

Images were recorded with the high-speed camera located perpendicular to the laser sheet. Depending on the flow rate, the sampling frequencies of the images captured were varied between 3000 to 5000 fps. This corresponds to time differences δt from 0.20 to 0.33 ms between the image pairs that are used to calculate the velocity vectors. For each set of conditions, 6000 to 10000 images

were acquired corresponding to a flow time of 2 s for each condition. To obtain higher resolution of the vortices forming in the wake of the cylinder, the investigation region was focused at a distance of 0.1 m from the cylinder with full resolution of 1024 ×1024 pixels. The photograph of the setup is given in Figure 4.11.

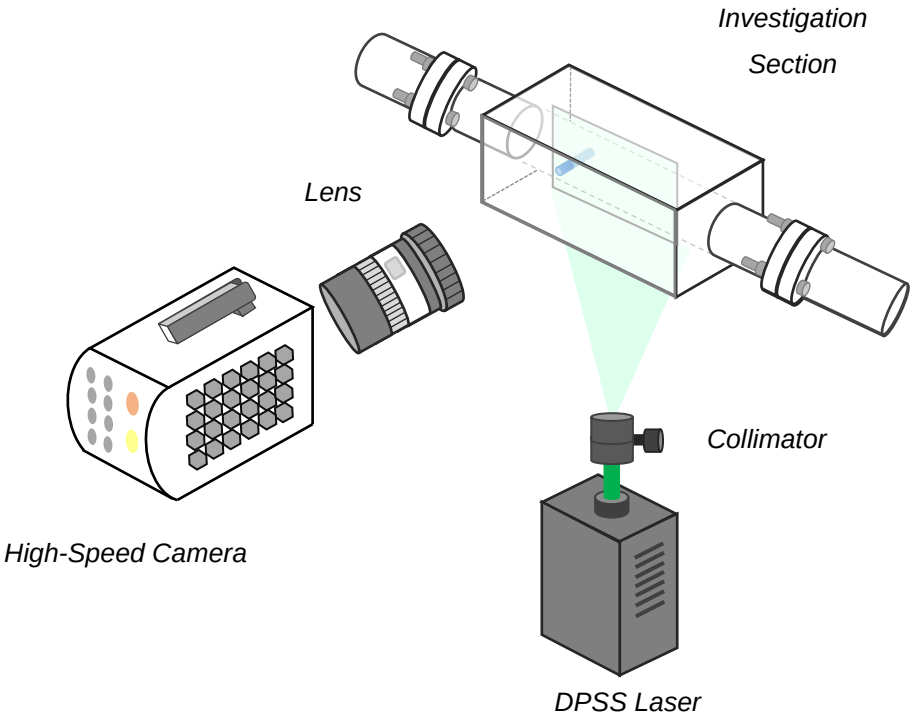

High-speed camera	• Photron SA-1 • Acquisition rate: 2000 to 5000 fps • Resolution: 1024 × 1024
Lens	• 105 mm f/2.8 macro
Laser	• DPSS • Wavelength : 532 nm (green) • Max output power: 3000 mW
PIV	• Silver coated hollow glass • Size: 10 μm

Figure 4.10: High-speed PIV technique setup and details.

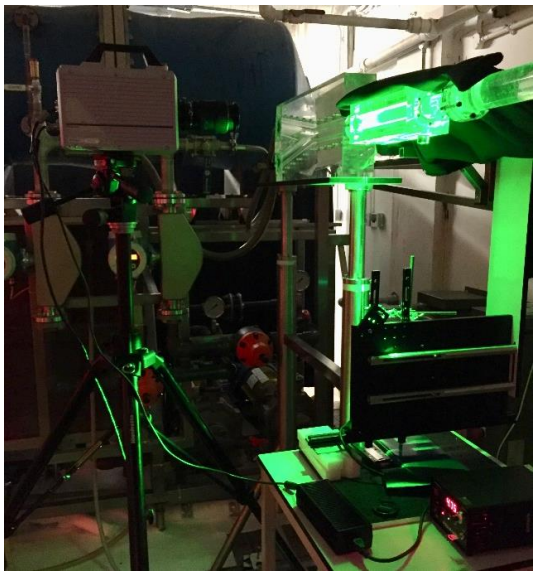

Figure 4.11: Photograph of high-speed PIV setup. * Setup is located in LB21a, UCL.

4.2 Investigations of Drop Entrainment Mechanism

4.2.1 Flow facility (26 mm I.D.)

Investigations of the drop entrainment mechanism in two-phase stratified liquid-liquid flows were conducted in a pilot scale two-phase flow facility that is shown schematically in Figure 4.12. The horizontal test section is constructed with combinations of 26 mm I.D. transparent acrylic pipes of lengths ranging from 0.5 m to 1 m which are connected by flanges. The total length of the test section is approximately 8 m with two legs of 4 m long connected via a pipe bend as illustrated in Figure 4.12. Experimental investigations in this work were only conducted along the front leg to avoid any effects of the pipe bend.

The facility consists of two storage tanks with maximum capacity of 170 L, one for each of the test fluids. The fluids from their respective storage tanks were fed separately to the test section via fixed flowrate centrifugal pumps (Procon, Sandtex; 12 l/min, 300kPa). Recycle loops were used to regulate the flowrates that are measured with variable area flowmeters (uncertainty of 0.013L/min), one for each fluid, located after the pumps. A Y-junction with a similar design to the one in Section 4.1.2 (with pipe diameter of 26 mm I.D. for this case), was used to bring the two fluids into contact at the beginning of the test sections. The junction was designed to create a smooth stratified flow with minimum mixing during the contact of the two phases. After the test section, the fluids were separated in a gravity settler from where they flow back to their respective storage tanks driven by gravity.

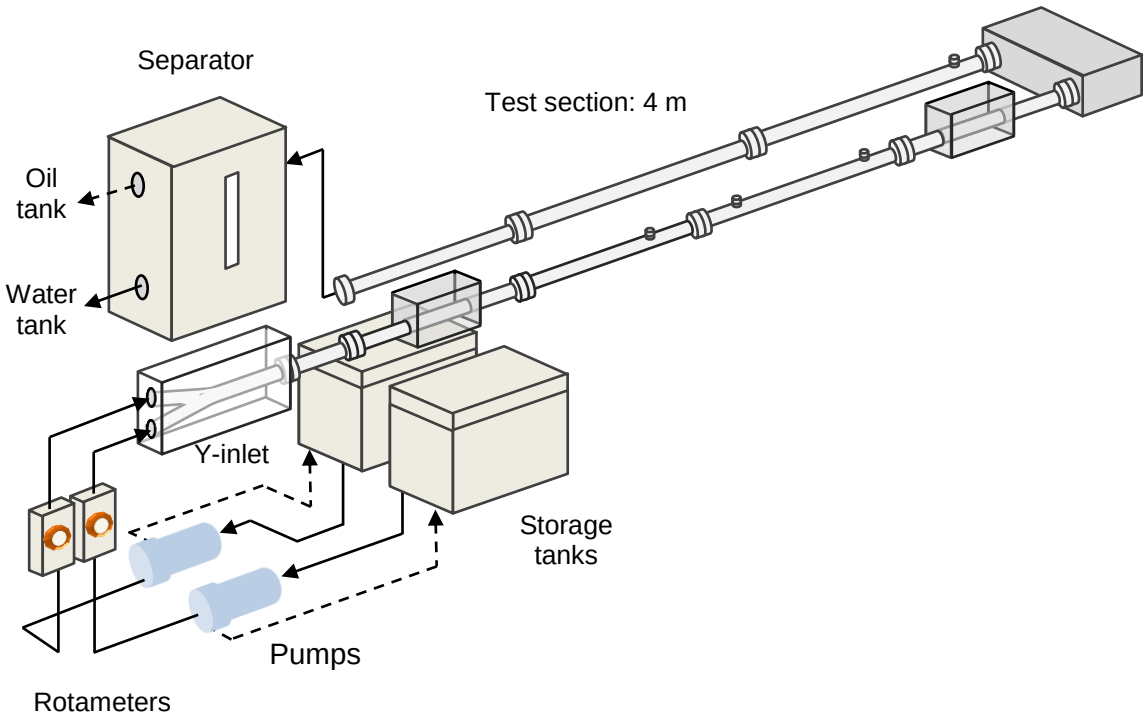

Figure 4.12: Schematic diagram of 26 mm I.D. flow facility.

4.2.2 Test fluids

The organic and aqueous test fluids used in this flow facility were chosen so that their refractive indices match to avoid laser light reflections at the interface. In the case where the indices was not matched, the light reflections at the wavy interfaces would be significant and interfere with the laser based measurements during visualization of drop entrainment. Silicone oil was used as the organic phase while the aqueous phase was a mixture of glycerol and water. To match the refractive index between the test fluids, glycerol is blended with water at approximately 1:1 volume ratio. The refractive index was measured with Abbe 5 refractometer on daily basis during the period of experiments. The properties of the test fluids are presented in Table 4.3.

Table 4.3: Properties of the test fluids at room temperature

Properties	Silicone Oil	Water/Glycerol
Density (kg/m^3)	913	1146
Viscosity (kg/ms)	0.0046	0.0083
Refractive Index (-)	1.396	1.396
Interfacial Tension (N/m)	0.0292	

4.2.3 Design of drop entrainment region

The investigation region in this work was created to observe the drop entrainment events. The region was established by the use of a cylindrical bluff body located transverse to the flow direction. The presence of the cylinder generates vortices in its wake that actuate the formation of unstable interfacial waves in two-phase flows and the drop entrainment. The design of the pipe section with a transverse cylinder is presented in a schematic in Figure 4.13. The test section was designed to be 0.5 m long with I.D. of 0.026 m with flanges at both ends for connection. A cylinder is located at 0.2 m from one end (front) and the section is enclosed in a visualization box filled with glycerol.

Figure 4.14 shows the schematic and a photograph of the pipe cross section with its dimensions tabulated in Table 4.4. The diameter of the cylinder is chosen based on our studies which demonstrate that the diameter alters the flow velocities for transition from stratified to dual continuous flow to occur. Increasing the cylinder diameter was seen to generate interfacial waves with higher amplitude and shifts the transition boundaries towards lower mixture velocities. From the studies, pipe configuration with gap ratio of 0.66 shows minimum wall effects while producing high interfacial instabilities which lead to higher possibility of drop entrainment events. Therefore, the gap ratio which corresponds to cylinder diameter of 5.5 mm in this pipe configuration (pipe I.D. = 26 mm) was used for investigation of drop entrainment mechanism.

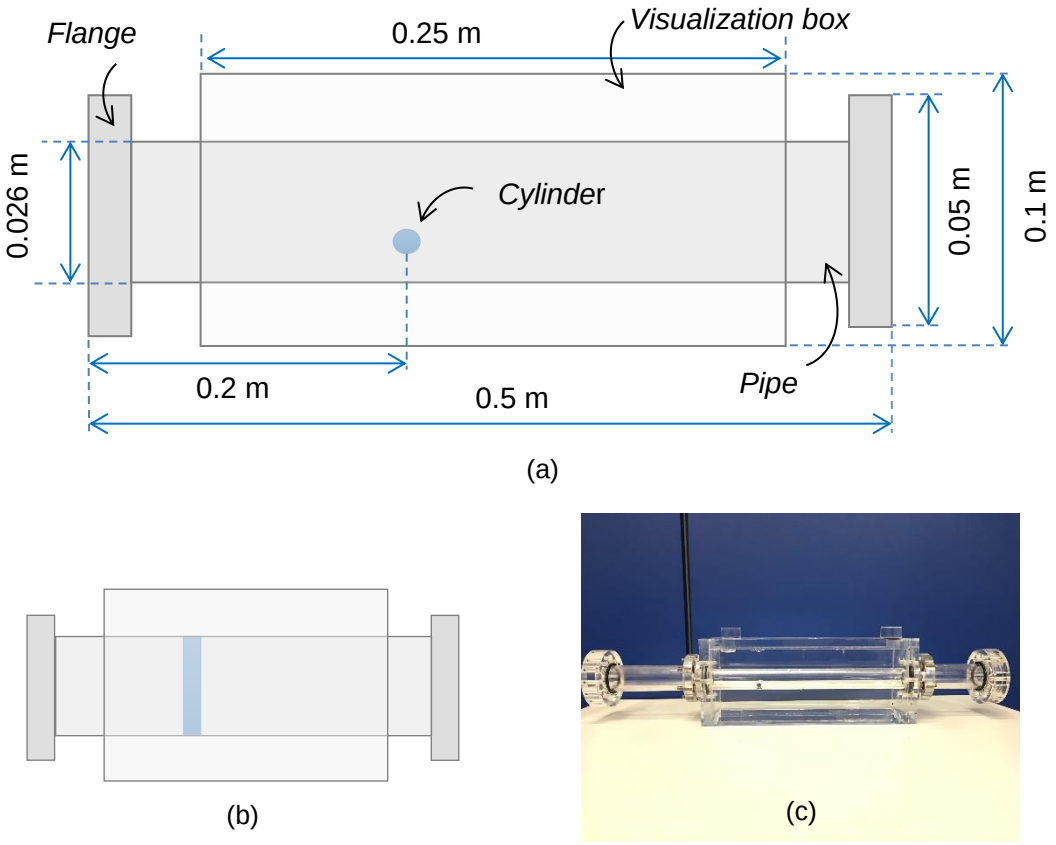

Figure 4.13: Pipe section with bluff body. (a) Side view (b) Top (c) Photograph

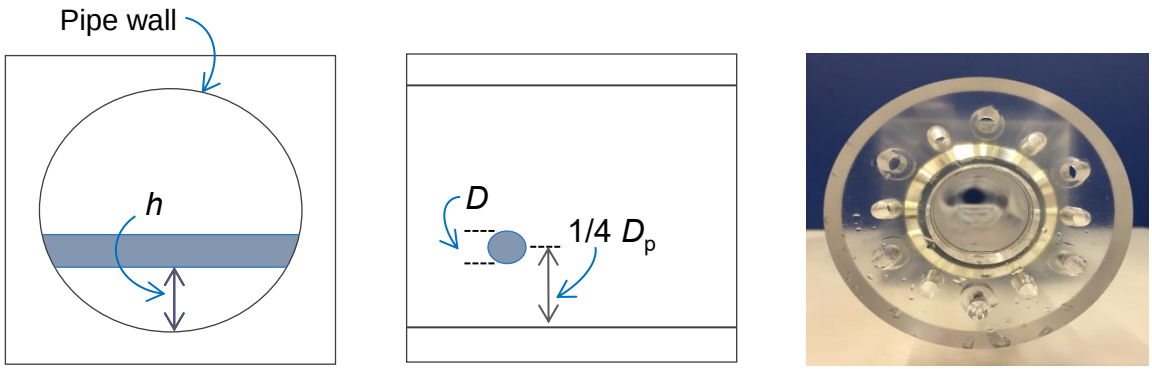

Figure 4.14: Schematic of inlet pipe section containing cylindrical bluff body.

Table 4.4: Inlet properties (26 mm I.D)

Inlet Properties	Value
Pipe Diameter, D_p (mm)	26
Cylinder Diameter, D_p (mm)	5.5
Distance from cylinder to wall, h (mm)	3.63
Gap ratio, γ (-)	0.66

4.2.4 Simultaneous PLIF and PIV techniques

The PIV technique employed for the determination of the instantaneous local velocity components requires the phase to be seeded with tracer particles. In this case, the mixture of water and glycerol was seeded with Rhodamine B particles with size ranging from 1 to 20 μm emitting at 590 nm. To observe the waves structure during the drop detachment process, the liquid-liquid interface should be identified. This is achieved by adding a fluorescent dye (Rhodamine 6G) in the continuous phase to obtain a clear distinction between the two phases. Both the tracer particles and the dye are supplied from Sigma Aldrich.

The set up consists of a DPSS green continuous laser system by Laserglow® and a Phantom v1212 high-speed camera by Vision Research. Figure 4.15 shows the arrangement of the equipment for the pipe experiments with the photograph given in Figure 4.16. The laser emits a beam of 4 mm thickness with a wavelength of 532 nm (green) and has an operating output set at 3000 mW. It was positioned below the pipe to illuminate the investigation section with a concave lens used to transform the laser beam into a sheet of approximately 30 cm long. A collimator was used to reduce the thickness of the laser sheet to approximately 1 mm. The laser sheet was aligned to be at the center of the pipe and in the axial direction of the flow with the help of an alignment paper designed with printed dots of known distance placed underneath the pipe.

The high-speed camera used to record the investigation region was located at the pipe side and is perpendicular to the flow. The camera has a maximum acquisition frequency of 12 kHz (12000fps) at a resolution of 1280×800 pixels. A high pass orange lens filter (> 580nm) is attached to the lens to eliminate any reflections of the laser light in the images from the pipe surface.

The PIV analysis was conducted with open source JPIV software, where cross correlation of successive images were conducted. Interrogation windows of 64×64, 32×32 and 16×16 pixels with 50% overlap were used for the first, second and final pass. The pixel size is 100 μm which gives a spatial resolution of 0.8 mm for the velocity vectors (half of the correlation box). The high-speed images were recorded at a frequency of 4000 fps (4 kHz) which corresponds to time difference Δ*t* of 0.25 ms; this difference was used for the calculation of the velocity vectors.

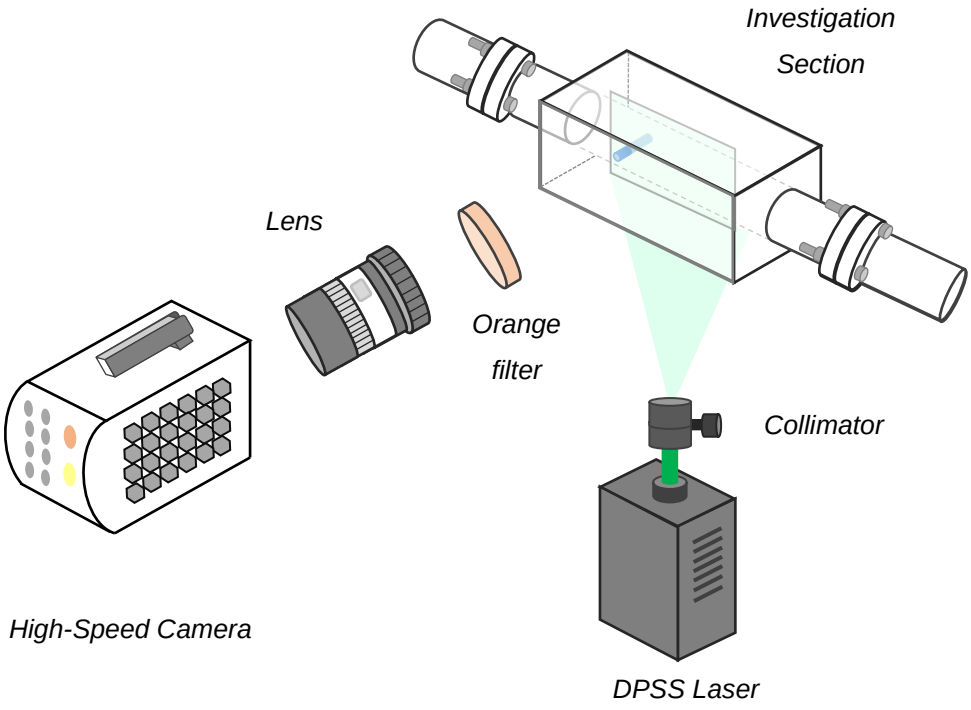

High-speed camera	• Phantom v1212 • Acquisition rate: 4000 fps • Resolution: 1280 × 720
Lens	• Leica
Laser	• DPSS • Wavelength : 532 nm (green) • Max output power: 3000 mW
PLIF	• Fluorescent die (Rhodamine 6G)
PIV	• Rhodamine B particles • 1 – 20 μm emitting at 590 nm

Figure 4.15: Simultaneous PLIF and PIV techniques setup and details.

The identification of the flow patterns was conducted downstream the test section at a distance of 3.5 m from the Y-inlet as shown in Figure 4.17. High-speed images of the flow regime were recorded at a resolution of 1280 × 720 pixels.

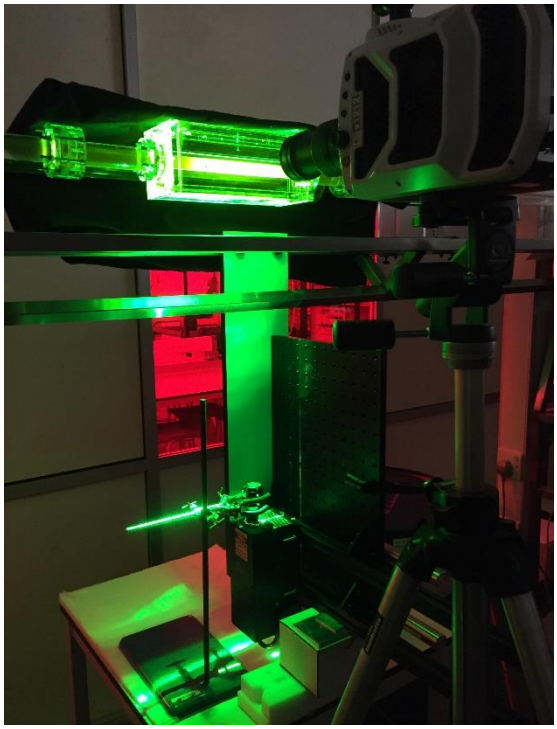

Figure 4.16: Photograph of PLIF-PIV setup. * Setup is located in LB21a, UCL.

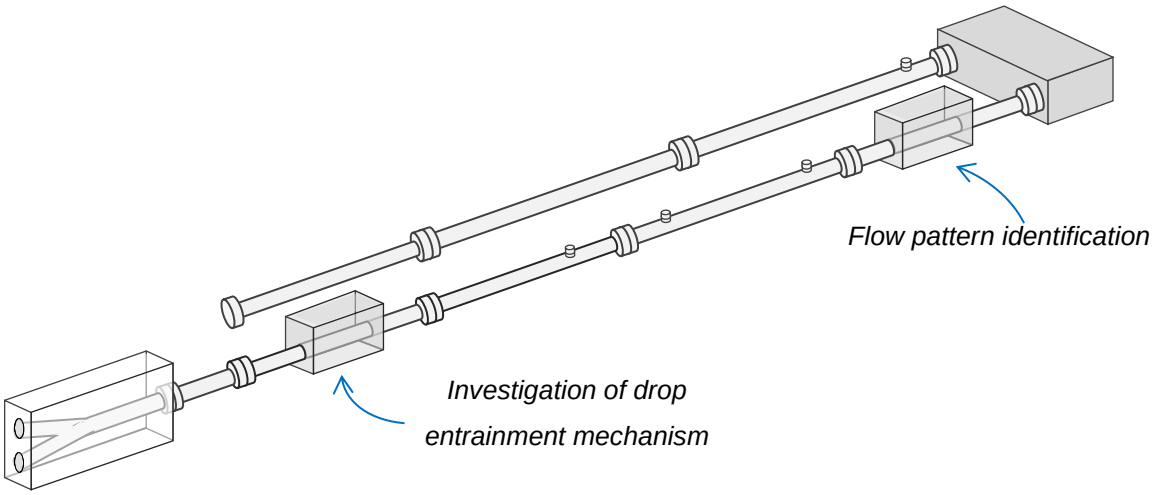

Figure 4.17: Locations of simultaneous PLIF and PIV techniques.

The drop entrainment events were recorded in the entrainment region behind the cylindrical bluff body. The test section which contains the bluff body was located at 0.5 m from the Y-inlet shown in Figure 4.17. Based on initial experiments, two regions were identified behind the bluff body, a wave formation region and a drop entrainment region as illustrated in Figure 4.18. In the wave formation region, interfacial waves are generated immediately behind the cylinder due to the interaction of the interface with the vortices shed by the cylinder (Chinaud et al., 2017). Unstable waves will grow in amplitude as they flow through this region and deformation of the wave crests can be observed. In the drop entrainment region, the developed wave crests/troughs will experience further deformation that may lead to drop entrainment. The two regions are recorded separately to increase the resolution as illustrated in Figure 4.18.

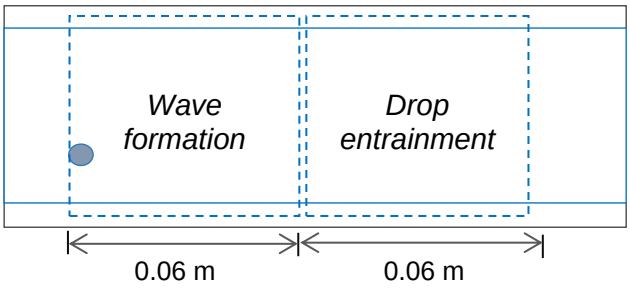

Figure 4.18: Wave formation and drop entrainment regions.

4.2.5 Flow parameters and flow conditions

The experimental investigations of the two-phase flows were conducted at various mixture velocities, u_{mix} and oil to water/glycerol flowrate ratios, r. The 26 mm I.D. flow facility uses centrifugal pumps with fixed flowrate. The flowrates of each phase are varied by the variable area meters. The experimental works are divided into two main parts. In the first part, flow pattern identification is conducted at a distance of 3.5 m from the Y-inlet. For this purpose, u_{mix} is varied from 0.225 to 1.174 m/s with r ranging from 0.46 to 4.65. From the flow patterns identification results, the flow conditions in which transition from stratified (ST) to dual continuous (DC) flow occurs are determined. These flow conditions are then used to investigate the drop entrainment events in the investigation region. The flow conditions for the studies of drop entrainment mechanism will be discussed in the results section based on the results of flow patterns identification.

4.3 Image Treatment

For investigations involving two-phase flows, the images captured from the PIV technique employed in this work were treated before cross-correlation are conducted. The purpose of this process is to remove any unwanted velocity vectors in the oil phase which was not seeded with particles. In the image treatment, a mask is created for each image by converting the PLIF image into binary image based on intensity threshold value as shown in an example in Figure 4.19. In the binary image, the phases are clearly distinguished with the two colors which are black and white, with the black region denotes oil phase and the white region denotes the water/glycerol phase. Creating the binary image allows measurements such as length to be conducted more conveniently compared to measurement on the raw image. Also, the binary image (mask) contains only two values for each pixel which is 0 (black) and 1 (white). The mask is then used to remove any vectors in the oil phase before PIV results analysis is performed. Due to the high amount of raw images obtained for each case, the image treatment is conducted through an algorithm developed in MATLAB.

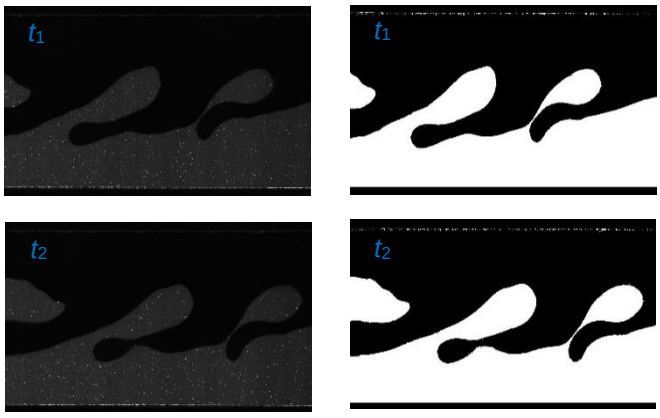

(a) Raw image (b) Mask

Figure 4.19: Example of mask creation in MATLAB. (a) Raw image (b) Mask created from the corresponding raw image.

4.4 Error Analysis

During the implementation of the techniques, possible errors may arise from the alignment of the camera and laser sheet to the visualization box in high-speed visualization and PIV techniques. In this section, the error analysis associated with the arrangements of the optical instruments will be discussed while statistical errors will be discussed separately for different properties in the results chapter.

4.4.1 High-speed camera alignment

The process of measuring various length properties from calibration based on the pipe diameter in the captured images which are presented in the results chapters (5, 6 and 7) may contribute to possible errors and uncertainty in the measurements. In ideal case where the camera is perfectly aligned, the line connecting two red dots in Figure 4.20(a) should be horizontal with 0° angle. However, in this works, the line connecting the dots was found to be at 0.3° (degree). This leads to variation of the length of pipe diameters, D_p at various axial locations shown in Figure 4.20a). To estimate the uncertainty in the calibration from pixel to m based on the pipe diameter, the D_p are measured at 4 locations along the axial locations with distance between each location is 0.05 m and average deviation was calculated. From the analysis, it was determined that the calibration uncertainty for the 37 mm I.D. system is 2.12% while for the 26 mm I.D. system is 1.97%.

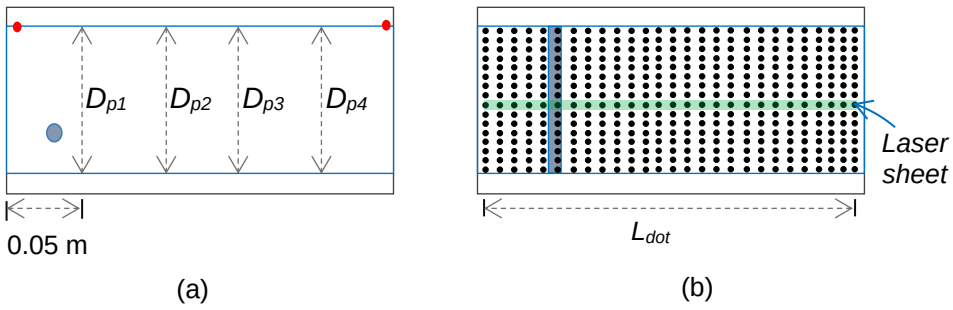

Figure 4.20: Estimation of measurement uncertainty. (a) Camera alignment (side view) and (b) Laser sheet alignment (bottom view)

4.4.2 Laser sheet alignment

To ensure that the laser sheet is straightly aligned on the visualization box, an alignment paper was used as a reference as shown in Figure 4.20(b). The

diameter of the dots are 0.02 m. Possible maximum alignment errors occurs when the laser sheet is located tangent to the opposite side of the dots (of same row) which can be estimated from;

$$\emptyset_{error} = \tan^{-1}(D_{dot}/L_{dot}) \quad (4.5)$$

In Eq. 4.5, D_{dot} and L_{dot} are the diameter of the reference dot and distance between the two references dots (0.2 m) used for the alignments respectively.

This lead to maximum possible misalignment at angle of 5.7° for both 37 mm I.D. and 26 mm I.D (the same reference paper was used). The alignment error can be calculated from the following;

$$allignment\ error = \emptyset_{error}/180° \quad (4.6)$$

For perfectly laser sheet alignment, the angle of alignment should be 0°. In this work, the possible maximum alignment error is determined to be 3.1%.

4.5 Summary

In this chapter, the flow facilities and the various techniques implemented in this works are described. Two flow facilities were designed with different test fluids to cater for the requirement of the different investigations and techniques. Summary of the experiment details for various investigation types are presented in Table 4.5.

Table 4.5: Summary of the details of experimental investigations conducted in this work.

Types	Vortex-induced waves characteristics	Vortex shedding characteristics	Drop entrainment mechanism
Flow Facility	37 mm I.D.	37 mm I.D.	26 mm I.D.
Test Fluids	Exxsol D140 and tap water	Exxsol D140 and tap water	Silicone oil and water/glycerol mixture (Matched refractive index)
Cylinder	2 and 8 mm (γ = 4.13 and 0.66)	2 and 8 mm (γ = 4.125 and 0.66)	5.5 mm (γ = 0.66)
Techniques	High-speed imaging	High-speed PIV	Simultaneous PLIF and PIV
Locations	• 7 m downstream cylinder (Flow pattern identification) • 0.2 m behind cylinder (wave characteristics)	0.2 m behind cylinder (Vortex shedding)	• 3.5 m downstream cylinder (Flow pattern identification) • 0.12 m behind cylinder (drop entrainment)

Chapter 5

Flow dynamics in the Wake of Cylinder of Various Diameters

This chapter presents the results and discussion for the first objective on the studies of transition from stratified to dispersed flows in two-phase oil-water flows with the use of cylindrical bluff body. For this purpose, investigations of the flow patterns, properties of vortex shedding and characteristics of vortex-induced interfacial waves in the wake of the cylinder were conducted in the 37 mm I.D. test section with high-speed visualization and PIV velocity measurements as described in chapter 4.

The flow patterns which were established at 7 m downstream from the cylinder are first discussed with relation to the cylinder size used at the inlet. Following this section, the findings in the vicinity of the cylinder (<0.5 m behind the cylinder) are discussed including single and two-phase flows. The investigations in single phase water flow are first shown followed by the findings in two-phase flows. For single phase flows, the vortex shedding characteristics in the wake of the cylinders are analysed and the experimental results are compared with the two-dimensional simulations shown in chapter 4. In two-phase flows, the vortex shedding characteristics and the resulting oil-water interfacial waves in the vicinity of the cylinder are analysed based on high-speed visualization and PIV measurements.

5.1 Flow Patterns (7 m downstream from the inlet)

Identification of the types of flow patterns established when cylinder of different sizes are placed at the inlet, were conducted at 7 m downstream of the cylinder via high-speed visualization. Approximately 1000 frames were recorded at a frame rate between 2000 to 4000 fps which corresponds to flow times of 0.25 to 0.5s. This allows detailed observations of the various flow configuration and phase distribution of the two phase flows established at various input conditions. With the PFV software described in chapter 4 (Section 4.1.1.1), the recorded high-speed images can be played as a video to monitor the flows for the purpose of flow pattern identification. The identified flow patterns are classified as suggested by Lovick and Angeli (2004) for consistency with the literature.

Figure 5.1 presents samples of high-speed images of the various flow patterns identified. The patterns formed with the 2 mm and the 8 mm cylinders present at the inlet are shown on the left and the right of the figure respectively, for various u_{mix} and at constant oil to water flowrate ratio, r = 1.0. At low mixture velocity u_{mix} = 0.31 m/s, the two phases form continuous layers separated by a clear smooth interface (stratified flow, ST). Increasing the mixture velocity results to interfacial wave formation. Oil drops started to form in the water continuous layer at u_{mix} = 0.62 m/s for the system with the 8 mm cylinder while for the 2 mm cylinder system, formation of oil drops occurs at a higher mixture velocity of 1.24 m/s (dual continuous with oil drops in water, DC (O/W)). Further increase in u_{mix} leads to formation of water drops in the oil continuous layer as well which presents simultaneously with the oil drops in water layer (dual continuous with drops of both phases present in the opposite phase, DC (O/W and W/O). For the flow conditions investigated, at high u_{mix}, both phases retain their continuity but the amount of drops dispersed in both phases is increased. Apart from the different u_{mix} where drops start to form, it can be seen that the density of drops present in the 8 mm systems is higher than in the 2 mm system. These flow patterns are commonly encountered in the flow of two immiscible liquids with small viscosity difference (i.e. in the work of Trallero et. al., 1997; Lovick and Angeli, 2004; Barral and Angeli, 2013).

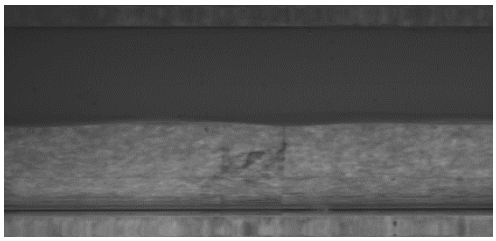

u_{mix} = 0.31 m/s (ST)

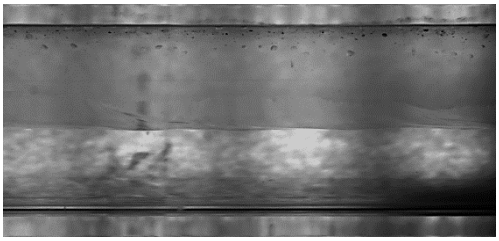

u_{mix} = 0.31 m/s (ST)

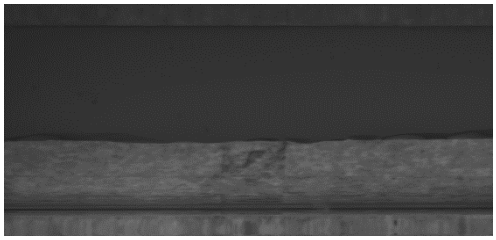

u_{mix} = 0.62 m/s (ST)

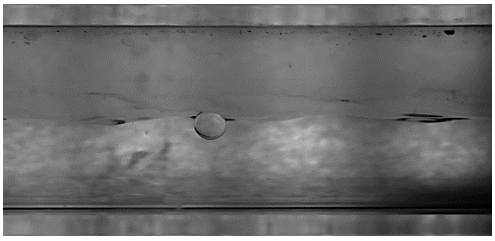

u_{mix} = 0.62 m/s (DC(O/W))

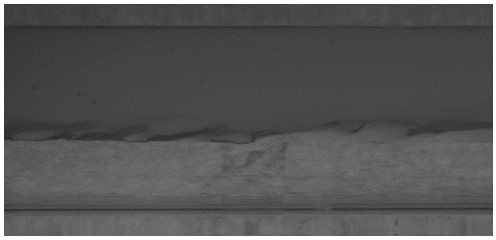

u_{mix} = 0.93 m/s (ST)

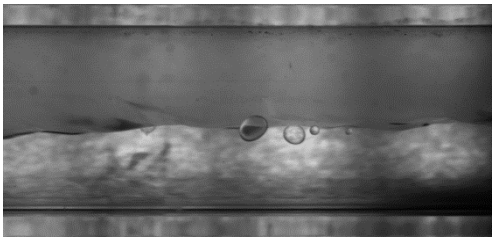

u_{mix} = 0.93 m/s (DC(O/W))

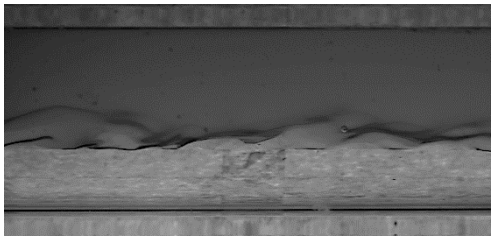

u_{mix} = 1.24 m/s (DC(O/W))

u_{mix} = 1.24 m/s (DC(O/W))

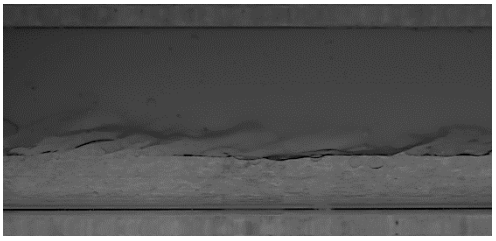

u_{mix} = 1.55 m/s (DC (O/W and W/O))

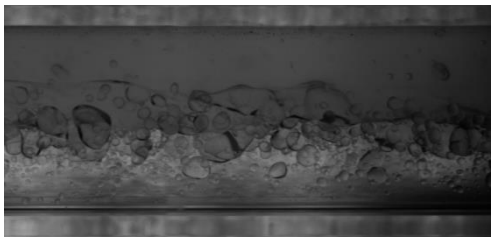

u_{mix} = 1.55 m/s (DC (O/W and W/O))

Figure 5.1: Oil-water flow image captured at various u_{mix} at r = 1 for system with D = 2 mm (left) and 8 mm (right).

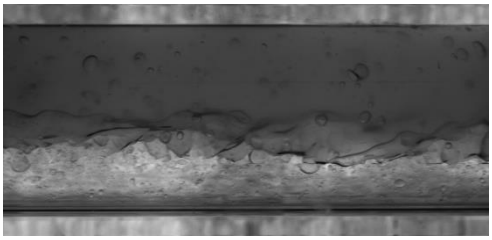

u_{mix} = 1.86 m/s (DC (O/W and W/O))

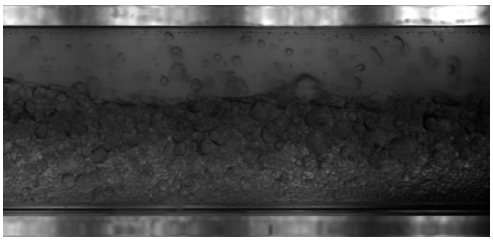

u_{mix} = 1.86 m/s (DC (O/W and W/O))

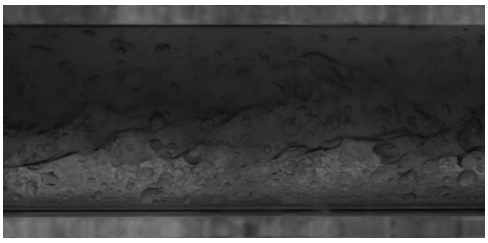

u_{mix} = 2.17 m/s (DC (O/W and W/O))

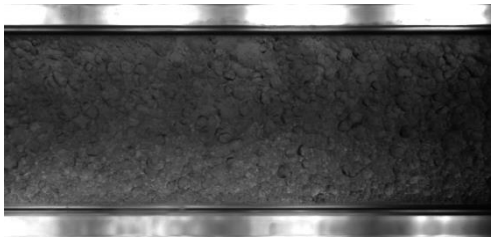

u_{mix} = 2.17 m/s (DC (O/W and W/O))

Figure 5.1 (**cont.**): Oil-water flow image captured at various u_{mix} at r = 1 for system with D = 2 mm (left) and 8 mm (right).

To analyse the flow pattern transition, flow pattern maps were constructed with the mixture velocity, u_{mix} and oil to water ratio, r as the coordinate systems. The corresponding flow pattern maps for the 2 mm and 8 mm cylinders are presented in Figure 5.2 in addition to the flow pattern map for the system without any cylinder. From the flow pattern maps in Figure 5.2, the region of stratified flow pattern, ST was observed to decrease while the dual continuous flow pattern, DC expands when a cylinder is placed at the inlet and with increase in cylinder size. This occurs as the presence of a transverse cylinder in this work actuates and facilitates the flow pattern transition by generating 'artificial' interfacial waves in the wake of the cylinder, shifting the boundaries towards lower mixture velocities. This is in agreement with the previous work of Park et al. (2016) and Chinaud et al. (2017) where a cylinder with D = 5 mm was used.

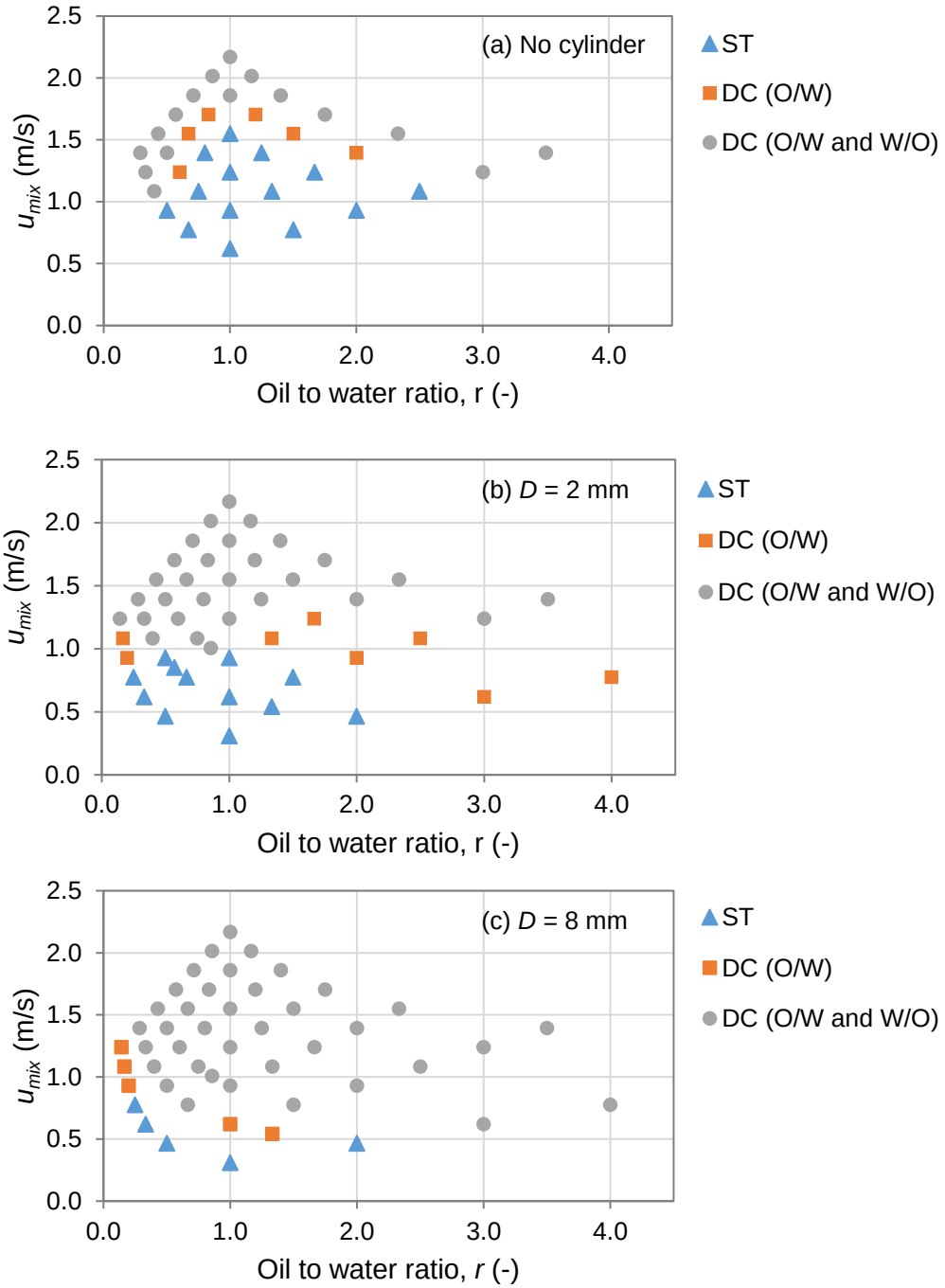

Figure 5.2: Flow pattern map for various system. (a) *D* = No cylinder; (b) *D* = 2 mm and (c) *D* = 8 mm. * Identified at 7 m downstream the cylinder

To further analyse the flow pattern transition of the various systems, the transition boundaries from stratified to dual continuous are plotted in the same graph in Figure 5.3 for all three cylinder sizes. The transition boundaries for the systems with cylinders are located at much lower mixture velocities, compared to the system without a cylinder. It can also be observed that for the system without cylinder, the transition occurs at the highest mixture velocity for oil to water flow

rate ratio r = 1. This is in agreement with the transition mechanism from separated to dispersed flows which is attributed to the development of interfacial waves and the detachment of drops from the waves when their amplitudes reach a critical value (Barral and Angeli, 2013). In the absence of a cylinder, interfacial waves are formed when velocity difference occurs between the two phases based on the Kelvin-Helmholtz instability. When a cylinder is present, the transition at r = 1.0, does not occur at the highest mixture velocity (absence of the peak). This shows that in this case, interfacial waves are generated by the cylinder and not by the difference in velocities between the two phases. Therefore, the introduction of the cylinder at the inlet actuates interfacial waves which are then responsible for the transition to dispersed flows.

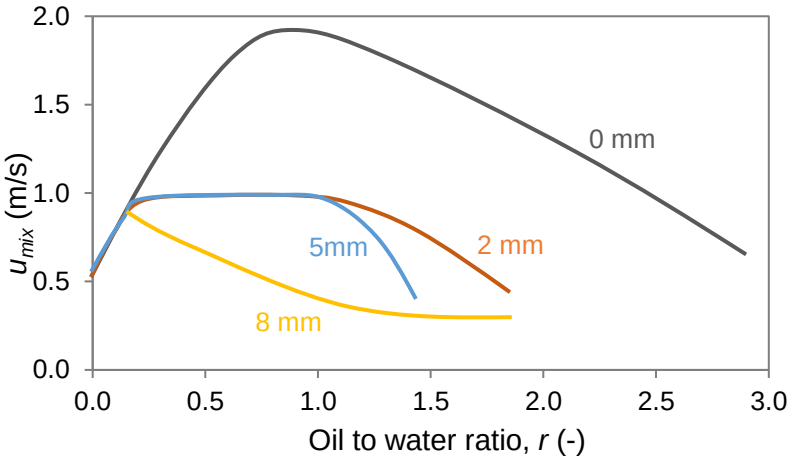

Figure 5.3: Transition boundaries for various system.

At low oil to water ratio, (r < 0.5), for the systems with the 2 mm and 5 mm diameter cylinder, the transition occurs at mixture velocities from 0.75 m/s to 1 m/s, similar to the system without a cylinder. At these conditions the average interface height approaching the cylinder is located in the upper half of the pipe, above 21.50 mm from the pipe bottom. This corresponds to submergence depths above 11.26 mm and 9.76 mm for cylinder diameters 2 mm and 5 mm respectively. The submergence depths in this cases are large and the interface is not influenced by the cylinder. The effects of the cylinders on the transition could be observed at oil-to-water flowrate ratios above 0.20, as the interface height and the cylinder submergence depth are reduced. At ratio equal to 0.20 both systems undergo transition at u_{mix} = 1 m/s. As the ratio is further increased to 1.5, the transition boundary for the 5 mm cylinder system lowers from 1 m/s to 0.5 m/s mixture velocity, while for the 2 mm cylinder system it remains at 1 m/s, and only

decreases at higher flowrate ratios. For the 8 mm cylinder system, transition occurred at very low mixture velocities, apart from the lowest oil-to-water flowrate ratio where the submergence depth is high (8.42 mm). For ratios up to 2.0, stratified flow was only seen at the lowest mixture velocities tested.

From the above analysis, it can be concluded that introducing a cylinder of any size at the inlet leads to actuation of flow pattern transition from stratified to dual continuous flow at lower mixture velocities. The actuation results from the generation of interfacial waves by the cylinder which occurred even without a velocity difference between the two phases (at r = 1.0). This suggests a modification of the mechanism of interfacial wave formation from the K-H instability. In addition, the cylinder submergence depth also influenced the interfacial waves. It was also found that the transition boundaries are affected by the cylinder size as presented in Figure 5.3. To further understand those phenomenon, detailed investigations in the vicinity of the cylinder (<0.5 m behind cylinder) are conducted where the velocity fields and the structure of the vortices shed by the cylinder are obtained from PIV while and the resulting interfacial wave properties are determined from high-speed visualization.

5.2 Investigations in The Vicinity of Cylinder (<0.5 m behind cylinder)

Investigations in the wake of cylinder were performed to determine the vortex shedding properties and interfacial wave characteristics in relation to the cylinder size. High-speed PIV (as described in chapter 4) was employed to track the velocity components in the wake of cylinder for both single and two-phase flows. From the data the vortex shedding frequency and the vorticity were calculated. The single phase results is first discussed followed by the findings in two-phase flows.

5.2.1 Single Phase Flows

The PIV measurements conducted for water flows in the test pipe across cylinders with diameter of 2 mm and 8 mm were analysed to obtain the vortex shedding frequency and the vorticity in wake of cylinder.

5.2.1.1 Frequency

The occurrence of alternate vortex shedding by the cylinder results to fluctuations of velocity in its wake. The vertical velocity, v, recorded at a location equal to 5 cylinder diameters (5D) downstream from the cylinder and at the vertical location

of the cylinder centre (see Figure 5.4) is presented in Figure 5.5. This location was chosen because it is at the area where vortices pass through as they travel downstream from the cylinder and therefore, shows high velocity fluctuations compared to other areas. The vertical velocity is recorded as it displays more significant fluctuations than the axial velocity.

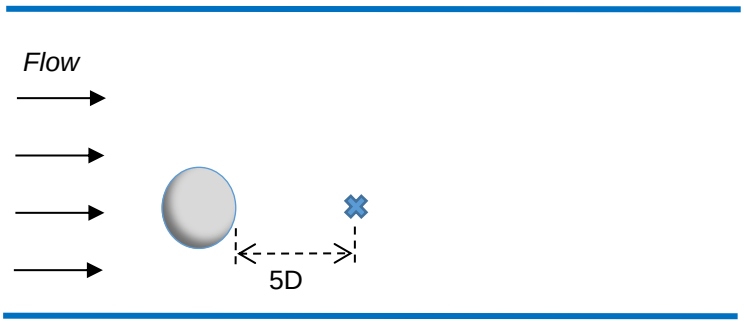

Figure 5.4: Locations where the vertical/radial velocity, *v* is recorded.

As can be seen in Figure 5.5, the fluctuations of *v* have higher frequency for the system with 2 mm cylinder compared to the 8 mm. The vortex shedding frequency, f_v is determined as the dominant frequency of the v fluctuations, which was obtained by performing Fast Fourier Transform (FFT) on the velocity data. The procedure is similar to the FFT performed on the lift data as discussed in Section 4.3.5. From the vortex shedding frequency, the Strouhal number, *St* is calculated based on Eq. 2.8. The calculated vortex shedding frequencies and Strouhal numbers at various flowrates are summarized in Table 5.1 for both cylinder diameters.

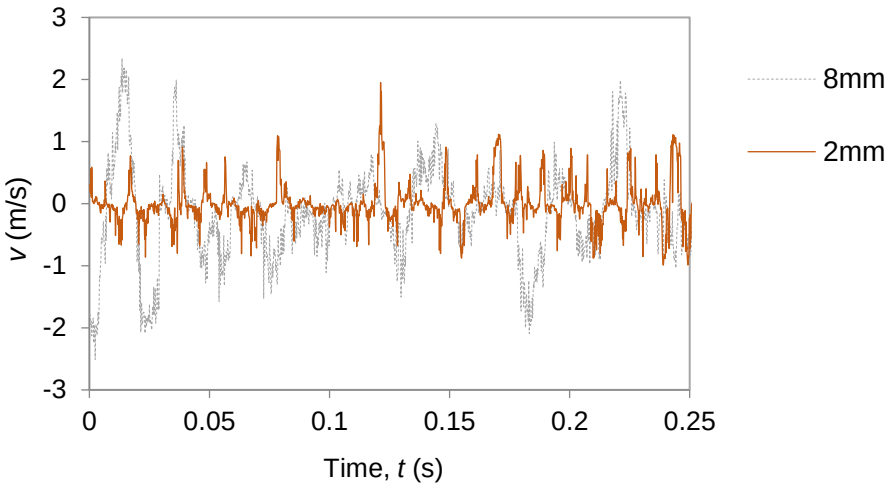

Figure 5.5: Vertical/radial velocity, *v* recorded at a location in the wake of cylinder (2 and 8 mm) over a period of time for water flow of u = 1.08 m/s

Table 5.1: Frequency and Strouhal number for vortex shedding in single phase flows at various cylinder sizes

Q (L/min)	**u (m/s)**	**Re_{pipe}**	**D = 2 mm**			**D = 8 mm**		
			Re_D	**f_v (Hz)**	**St**	**Re_D**	**f_v (Hz)**	**St**
10	0.16	5735	310	14.72	0.19	1240	5.43	0.28
20	0.31	11470	620	29.30	0.19	2480	10.94	0.28
30	0.47	17205	930	45.35	0.20	3720	16.42	0.28
40	0.62	22940	1240	60.49	0.20	4960	21.35	0.27
50	0.77	28638	1548	73.90	0.19	6192	26.22	0.27
60	0.93	34373	1858	88.67	0.19	7432	31.12	0.27
70	1.08	40108	2168	108.71	0.20	8672	37.86	0.28

From Table 5.1 it can be observed that with the chosen cylinder sizes the vortex shedding frequencies vary up to two orders magnitude between 1 to 100 Hz. For the range of flow velocities used, the 2 mm cylinder generates vortices with frequencies from 14.72 to 109.71 Hz while the 8 mm cylinder produces lower frequencies ranging from 5.43 to 37.86 Hz.

The average Strouhal number, St for the case of 2 mm cylinder diameter is St = 0.20 while higher value is obtained for the case of 8 mm with St = 0.28. The Strouhal numbers determined experimentally are consistent with the values from the numerical analysis of two-dimensional flows discussed in chapter 4, for all for both cylinder diameters. The Strouhal number for D = 2 mm also agrees well with the literature value for unbounded flows which implies that the system investigated resembles unbounded flow at least in the middle of the pipe. Park et al. (2016) reported similar observations for D = 5 mm in the same test pipe with a gap ratio of 1.35 in the middle of the pipe. The results indicate that for large gap ratio, γ where the distance between the cylinder and the wall is large, the middle plane of the pipe is not affected by the three dimensional pipe geometry.

The increase in Strouhal number for the 8 mm cylinder which is related to the reduced gap ratio (γ = 0.66) suggests the occurrence of interactions between the vortices shed by the cylinder and by the wall. The interactions result in increased vortex shedding frequency compared to the case of unbounded flows (Zovatto and Pedrizetti, 2001). The interaction was also observed in the work of Patil and Tiwari (2008) and Rehimi et al. (2008). Renfer et al. (2013)

reported that vortex shedding frequencies produced from micropin arrays increased with decreasing gap ratio. To further elucidate the wall effects on vortex shedding, the vorticity in the wake of cylinder was analysed from the PIV measurements.

5.2.1.2 Vorticity

The spanwise vorticity, ω_z, is computed from Eq. 5.1, where u and v are the horizontal and vertical velocity components respectively.

$$\omega_z = \frac{\partial v}{\partial x} - \frac{\partial u}{\partial y} \tag{5.1}$$

Examples of instantaneous vorticity fields in the wake of the cylinder are presented in Figure 5.6 for D = 2 mm and D = 8 mm at a flowrate of Q_w = 30 L/min, which corresponds to u = 0.47 m/s. The y-axis represents the pipe diameter with the bottom of the pipe positioned at y = 0. The scale has been increased in the y-direction to better show the vortices forming and for this reason the cylinder appears elliptical. In Figure 5.6, it can be seen that vortices are shed alternatingly behind the cylinder and are convected downstream, with the positive vorticity localized above the cylinder and the negative one below. The vortex shedding phenomenon is in agreement with literature for cylinder Reynolds numbers above the critical value (Re_D = 40) (Zovatto and Pedrizzetti, 2001; Chinaud et al., 2017).

For both cylinder sizes, the magnitude of vorticity fields decreases with increasing distance away from the cylinder. It can also be seen from Figure 5.6 that larger vortices are shed from the 8 mm cylinder compared to the 2 mm one. In addition, the vorticity field in the wake of 8 mm cylinder is sustained further downstream the flow.

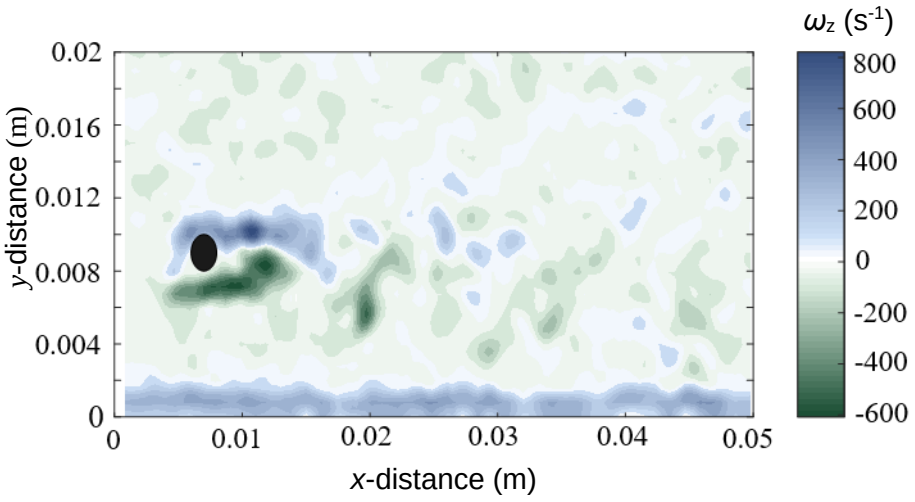

(a) D = 2 mm

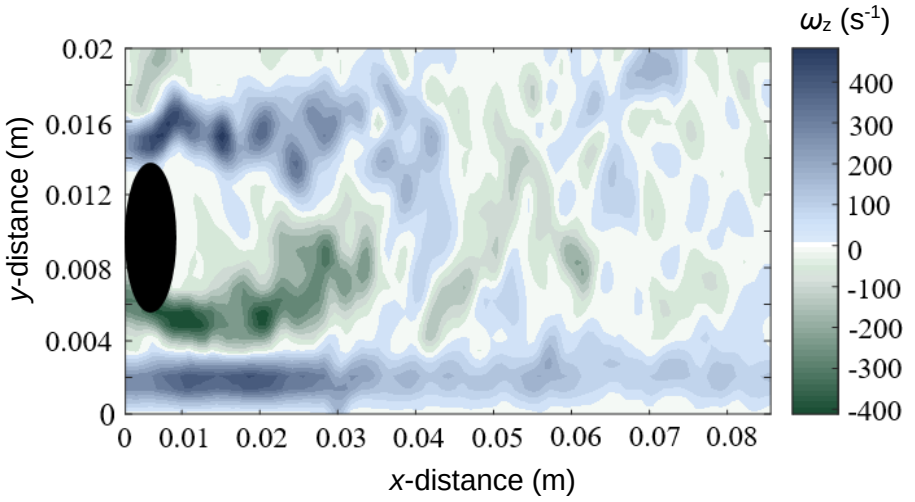

(b) D = 8 mm

Figure 5.6: Vorticity field in the wake of cylinders with different diameters for single phase water flow at Q_w = 30L/min, u = 0.47 m/s.

The time-averaged vorticity components for two velocity cases of u = 0.47 m/s and 0.93 m/s in the wake of the 2 mm and the 8 mm cylinders are presented in Figures 5.7 and Figure 5.8 respectively. As expected, for both cylinders, the main vorticity structures were formed on the top and at the bottom of the cylinder. For the case of the 2 mm cylinder in Figure 5.7 where the gap ratio is large (γ = 4.12), symmetrical vorticity structures are formed that resemble the case of unbounded flow. When the incoming velocity is increased from 0.47 m/s to 0.93 m/s, the magnitude of the vorticity increases (Figure 5.7(b)) but the structure of the vorticity fields remain identical.

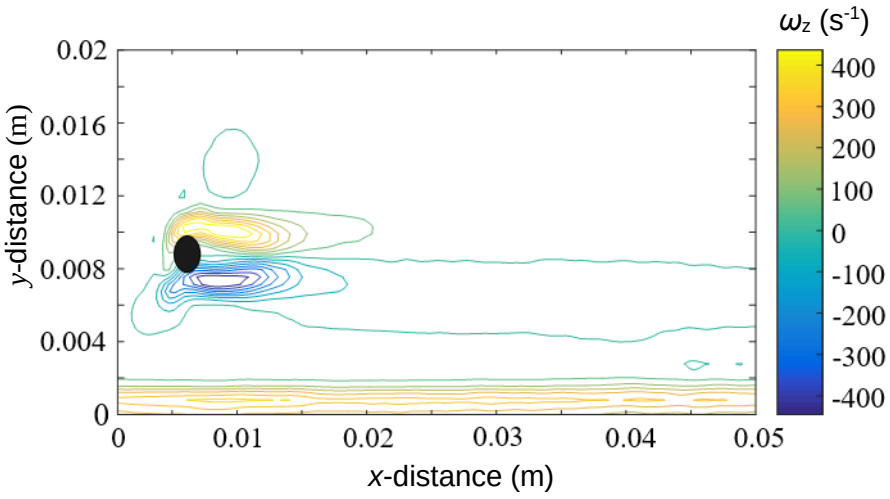

(a) u = 0.47 m/s

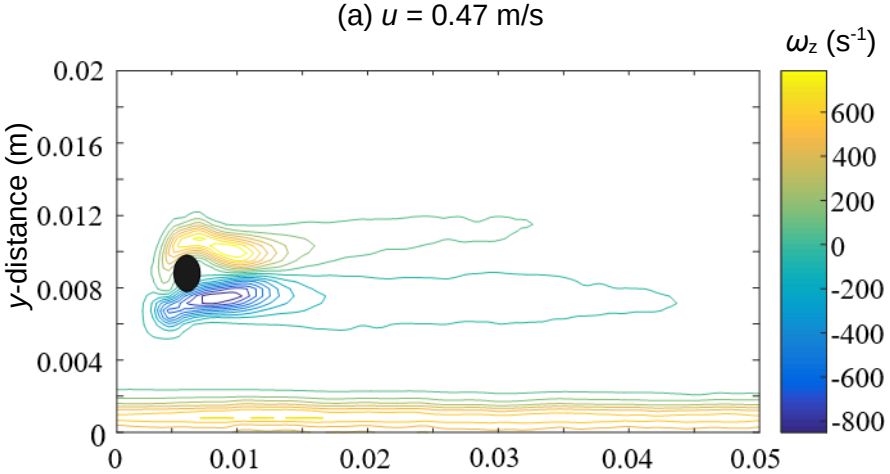

(b) u = 0.93 m/s

Figure 5.7: Time-averaged vorticity in the wake of the 2 mm cylinder for single phase water flow at different velocities.

For the case of the 8 mm cylinder in Figure 5.8, the vorticity structures are larger and spread further behind the cylinder compared to the 2 mm cylinder case. The wake structure is not symmetric and the vortices at the upper part of the cylinder are longer than those at the bottom part. The asymmetry is attributed to the presence of the wall; vorticity is generated at the wall boundary layer that interacts with the vorticity at the lower part of the cylinder. The effects of the wall on the wake structure are more pronounced at the higher velocity of 0.93 m/s and the asymmetry is increased as observed in Figure 5.8(b). The asymmetric wake structure which occurs at low gap ratios is in agreement with the numerical findings of Zovatto and Pedrizzetti (2001).

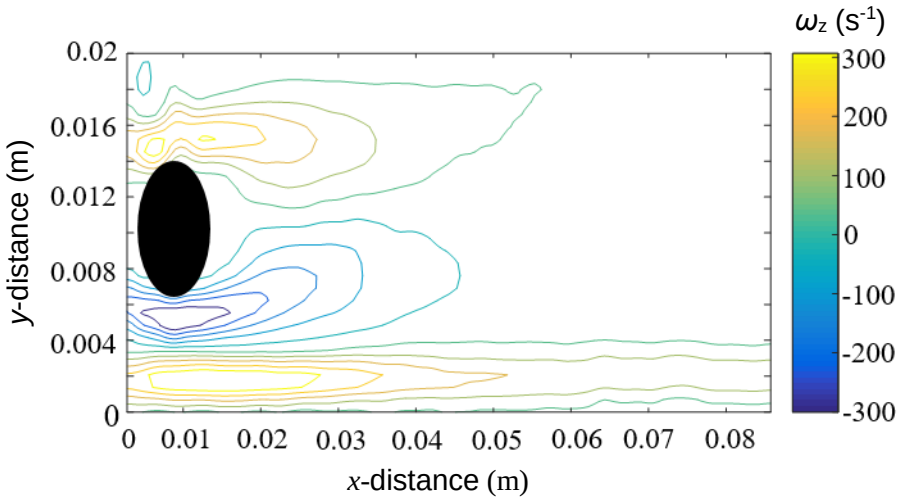

(a) u = 0.47 m/s

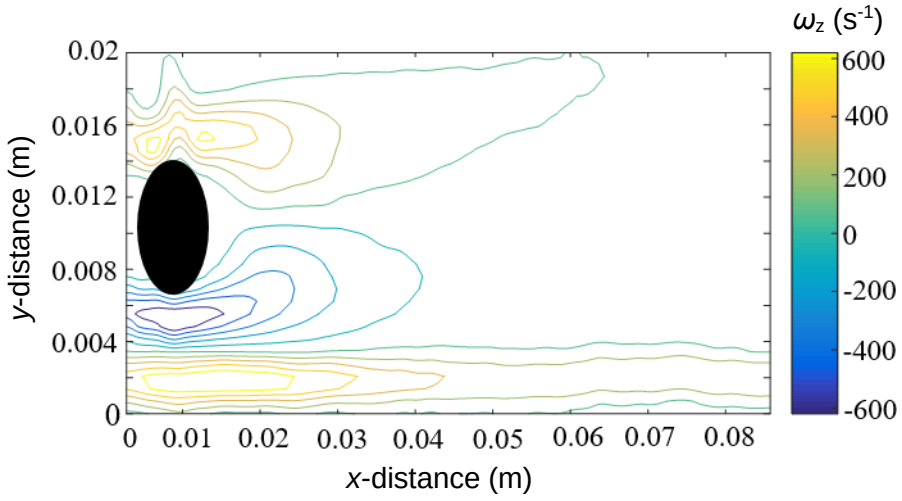

(b) u = 0.93 m/s

Figure 5.8: Time-averaged vorticity in the wake of the 8 mm cylinder for single phase water flow at different velocities.

To quantify the average vorticity region developed in the wake of the cylinder as observed in Figures 5.7 and 5.8, the vertical size of the vorticity region is measured for the cases shown in those figures. To ensure that the values are comparable for all cases, the vertical distance was measured for a similar value of vorticity which in this case is ωz = 60 s^{-1} and the results are presented in Figure 5.9. From the figure, it can be observed that increasing the cylinder diameter leads to the expansion of the vorticity region in its wake which was quantified by the increase in vertical distance from 0.003 m to 0.006 m. Also, the vertical distance remains almost constant with increasing incoming flow velocity. This suggests that the vorticity region is governed by the cylinder diameter and

increasing the velocity only leads to higher vorticity magnitude as discussed in Figures 5.7 and 5.8.

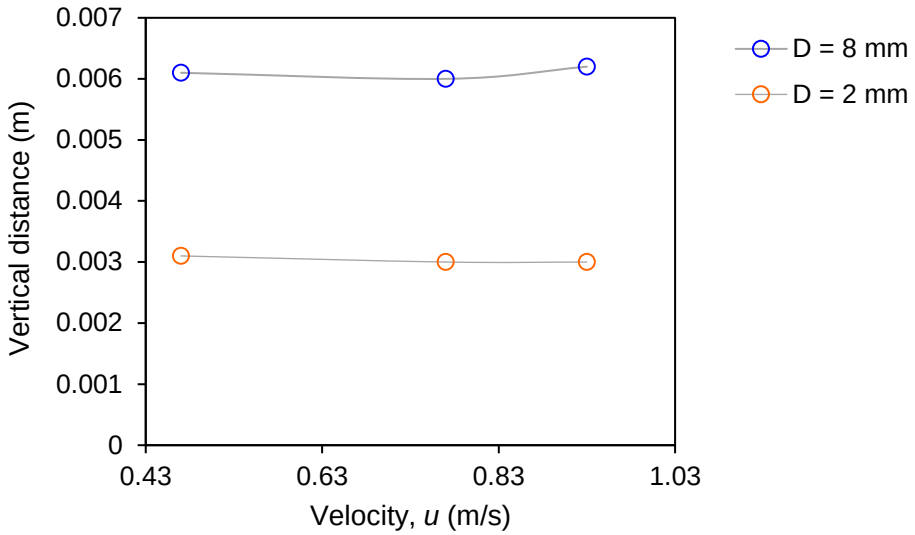

Figure 5.9: Vertical distance occupied by vortices of ω_z = 60 s^{-1} at different velocity and cylinder diameter

5.2.2 Two-phase flows

In this section, results obtained from the PIV in the water phase are first discussed followed by the analysis of the high-speed visualization data on the interfacial waves.

Several limitations were encountered during the analysis of two-phase flows with waves present. In the high-speed PIV technique, the presence of interfacial waves caused multiple reflections of the laser light on the interface especially for cases with very wavy interface at high mixture velocities. This phenomenon occurs due to the difference in refractive index between the two fluids used in this work (1.439 and 1.333 for Exxsol D140 and water respectively). As a result, the PIV tracer particles near the interface cannot be easily recorded. An example is presented in Figure 5.10(a). Thus, the analysis of the velocity and vorticity fields obtained with PIV is limited to low velocities (u_{mix} < 0.47 m/s) where the reflections at the interface are not significant.

From the two cylinders studied the small one produced very small and irregular interfacial waves as shown in Figure 5.10(b), which did not yield meaningful results. Therefore, the effect of cylinder diameter on the interfacial

wave characteristics will be discussed against the data by Park et al. (2016) who used a cylinder of with D = 5 mm at the same test system.

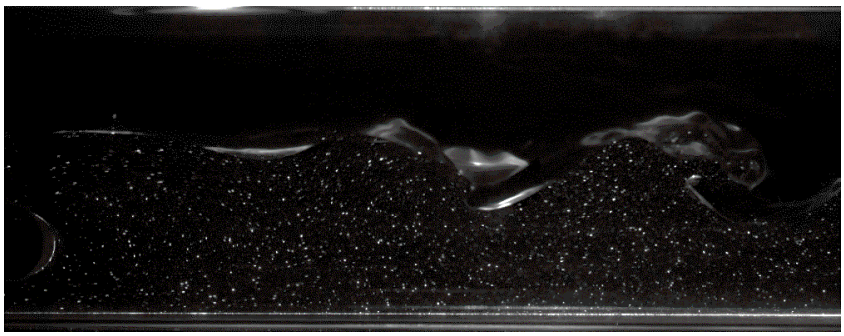

(a) Image obtained from PIV technique behind 8 mm cylinder

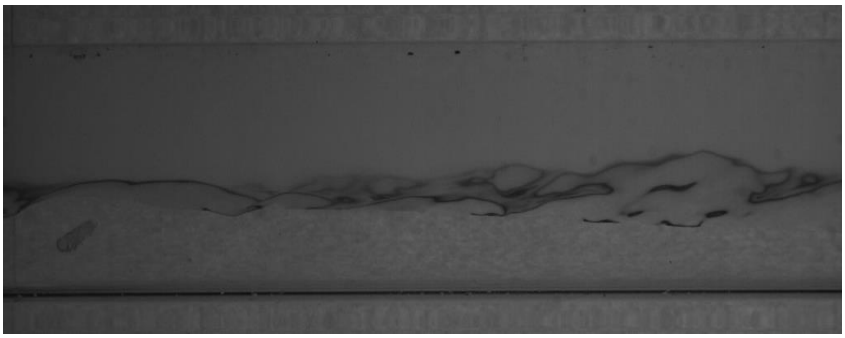

(b) Image obtained from high-speed visualization behind 2 mm cylinder

Figure 5.10: Limitations in the analysis of the flow dynamics in the wake of cylinder.

For the analysis of the characteristics of the waves, an appropriate number of waves to be studied needs to be selected to ensure that the results are statistically meaningful. The sample size is determined from the analysis of interface height and wave frequency. For each of these properties, 75 waves are analysed and the results are compared against those from samples with 25, and 50 waves (see Appendix A). It was found that for each of the properties, the average values agreed well for all sample sizes with an average deviation less than 2.2%. In what follows, sample sizes with 50 waves were analysed.

5.2.2.1 Frequency of interfacial waves and of vortex shedding

Figure 5.11 shows the locations of investigation in the wake of cylinder. For the interfacial wave measurements, 10 locations are chosen, 16 mm apart, while the distance from location 1 of the cylinder is 40 mm. This is because the vortices are formed between this region (location 0 to 1) and vortices are shed from location 1. The frequency of interfacial waves generated downstream of the cylinder is determined at location 2 in Figure 5.11, as the wave crests start to

form between locations 1 and 2. This is achieved by counting the number of wave crests passing through a fixed location (location 2 in this case) over a period of time;

$$wave\ frequency, f = \frac{number\ of\ crests\ passing\ through\ a\ fixed\ location}{time\ between\ the\ first\ and\ the\ last\ wave\ crest} \quad (5.2)$$

The Strouhal number, *St* is then calculated based on the wave frequency and the actual water velocity approaching the cylinder from Eq. 2.8. The actual water velocity is estimated from the area occupied by the water and the water flowrate. For the 2 mm cylinder system, the flow conditions to determine the frequency based on high-speed visualization are limited to high oil to water ratios (r > 2.0) as at lower ratios the cylinder generates very small waves which cannot be easily tracked and analysed. For the frequency of vortex shedding, f_v in the water phase results of the velocity fields acquired from the PIV measurements are used following similar procedures as for the single phase flows discussed previously.

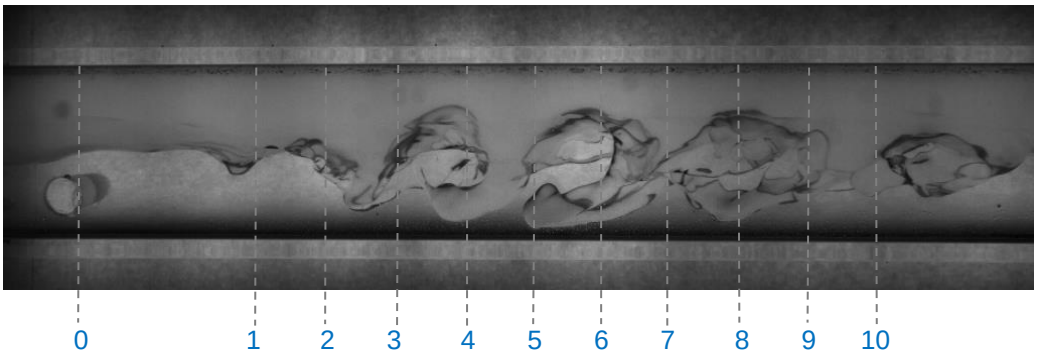

Figure 5.11: Locations for investigation of interfacial wave characteristics. *Picture shown for 8 mm cylinder. ** Distance between location 0 to 1 is 40 mm and each locations from 1 to 10 is 16 mm.

The frequencies of interfacial waves and vortices generated behind the 2 mm and 8 mm cylinders at various mixture velocities, u_{mix} and oil to water ratios, r are presented in Table 5.2 and Table 5.3 respectively and the comparisons between the frequencies are visualized in Figure 5.12. In the tables, the corresponding Strouhal numbers are also shown. With the 2 mm and the 8 mm cylinders used in the current work a large range of vortex shedding frequencies was generated between 1 to 100 Hz. The wave frequency was observed to increase significantly with u_{mix} for the case of 2 mm cylinder while for the 8 mm

cylinder the increase was not as pronounced. This suggest the potential of controlling the frequency of vortex shedding through a particular cylinder size.

In all cases, the vortex shedding frequency, f_v matches the interfacial wave frequency fairly well, as observed in Figure 5.12. The average *St* for the 2 mm cylinder system are in agreement with the literature values for unbounded flow (*St* = 0.20). However, for the 8 mm cylinder cases larger *St* are obtained. The smaller gap between the wall and the 8 mm cylinder, which alters the vortex shedding frequency (from the unbounded flow case), also modifies the frequency of the resulting interfacial waves. This dependence implies that the formation of waves at the interface of stratified oil-water flows was induced by the vortices generated behind the cylinders submerged in water. To analyse this phenomenon further, the vorticity field in two-phase flows is discussed in the following section.

Table 5.2: Frequency and Strouhal number of von Karman vortices.

D **(mm)**	u_{mix} **(m/s)**	***r*** **(-)**	u_w **(m/s)**	Re_D **(-)**	Re_{pipe} **(-)**	f_v **(Hz)**	***St*** **(-)**
2	0.31	1.00	0.34	684	26676	34.53	0.20
	0.47	2.00	0.41	828	35190	46.04	0.22
	0.62	1.00	0.65	1290	50310	62.06	0.20
	0.70	1.25	0.71	1410	55695	70.07	0.20
	0.77	1.50	0.76	1524	62484	75.08	0.20
	0.93	1.00	0.97	1932	75348	92.60	0.20
8	0.31	1.00	0.34	2736	26676	10.50	0.25
	0.47	0.50	0.52	4160	35360	16.03	0.25
	0.62	1.00	0.65	5160	50310	22.05	0.27
	0.70	1.25	0.71	5640	55695	24.02	0.27
	0.77	1.50	0.76	6096	62484	24.32	0.27

Table 5.3: Frequency and Strouhal number of interfacial waves.

D (mm)	u_{mix} (m/s)	r (-)	u_w (m/s)	Re_D (-)	Re_{pipe} (-)	f (Hz)	St (-)
2	0.47	2.00	0.42	830	35275	45.74	0.22
	0.62	3.00	0.54	1078	51205	60.30	0.22
	1.24	3.00	1.08	2156	102410	123.79	0.22
8	0.31	1.00	0.34	2736	26676	11.30	0.26
	0.47	0.50	0.52	4160	35360	17.25	0.27
	0.62	1.00	0.65	5160	50310	21.52	0.27
	0.77	1.50	0.76	6096	62484	25.85	0.27
	0.93	2.00	0.87	6976	74120	29.60	0.27

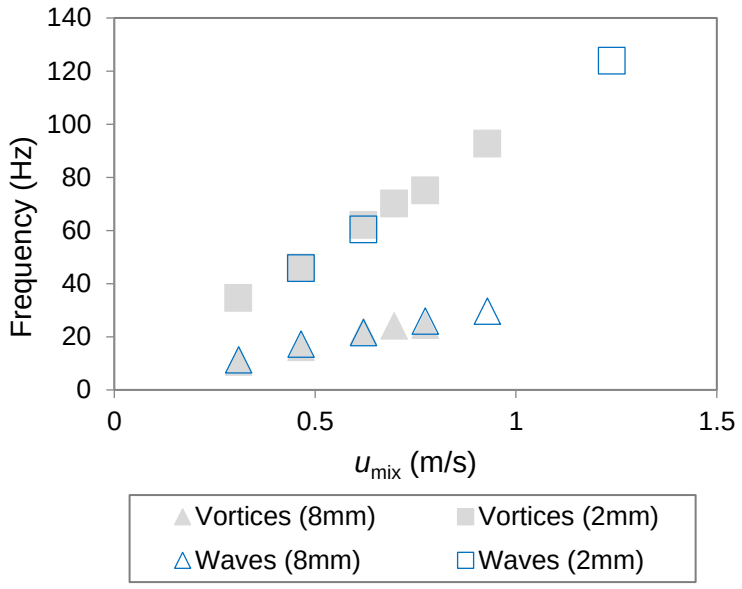

Figure 5.12: Comparisons of interfacial waves and of von Karman vortices frequencies.

5.2.2.2 Vorticity

The vorticity in the water phase is determined from following similar procedures to single phase flows in Section 5.2.1.2. The instantaneous vorticity fields for the systems with cylinder diameters of 2 mm and 8 mm are visualized in Figure 5.13 and Figure 5.14 respectively for Qo = 10 L/min and Qw = 10 L/min which corresponds to u_{mix} = 0.31 m/s. The oil-water interface in the figures is shown with a red line to better visualize the position and structure of the interface.

The size of the vorticity region in the wake of the 2 mm and 8 mm cylinders for the two-phase flows varies in a similar way to the single phase flow case where larger vorticity regions are produced in the wake of the 8 mm cylinder. The 8 mm case shown in Figure 5.14 demonstrates the mechanism of interfacial wave formation by the cylinder. The wave crests formed behind the cylinder coincide with the locations of the positive vorticity regions shed from the upper side of the cylinder. The positive sign represents the clockwise vorticity direction while the negative sign represents the anticlockwise vorticity direction). This occurs as the vortices on top of the cylinder attach to the interface as soon as they are generated, actuating the formation of vortex-induced waves which then travel downstream as the vortices are convected with the flow. A similar mechanism was observed in the work of Chinaud et al. (2017) which showed that vortices generated behind a cylinder in an oil-water flow are attached to the interface.

Focussing on the structure of the interface formed in both systems, at the same flow conditions, it can be seen that the waves have larger amplitude in the case of D = 8 mm compared to D = 2 mm. The interface in the case of the 2 mm cylinder is almost flat with small fluctuations. The variation of interface structures between the two systems is attributed to the combination of two factors, namely the cylinder submergence depth and the size of vortices generated by the cylinder. At constant oil to water ratio, the submergence depth is larger for the small cylinder. As a result, the interface is further away from the vortices generated behind the cylinder and is not significantly influenced by them; in addition to size of vortices generated in this case that are smaller than with the 8 mm cylinder.

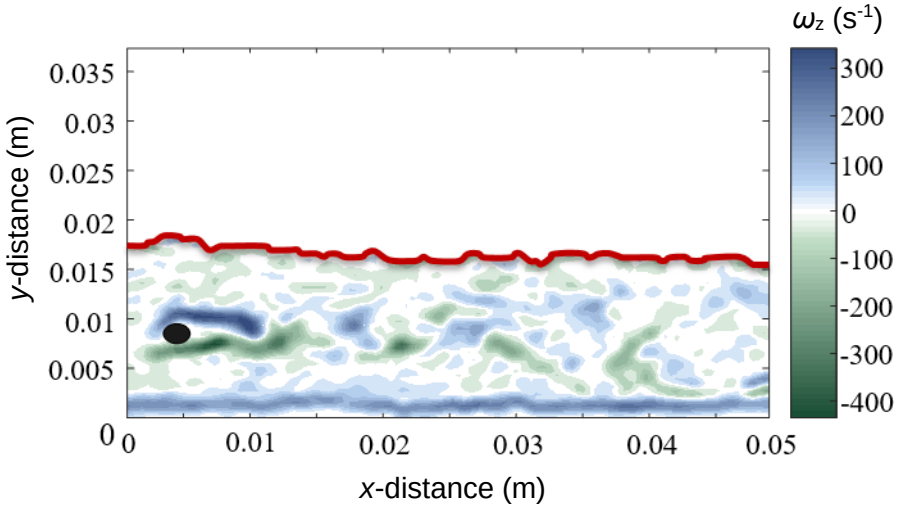

Figure 5.13: Vorticity field in the water phase of oil-water flows downstream of the 2 mm cylinder at Qo = 10 L/min and Qw = 10 L/min. *The interface is also shown as red line.

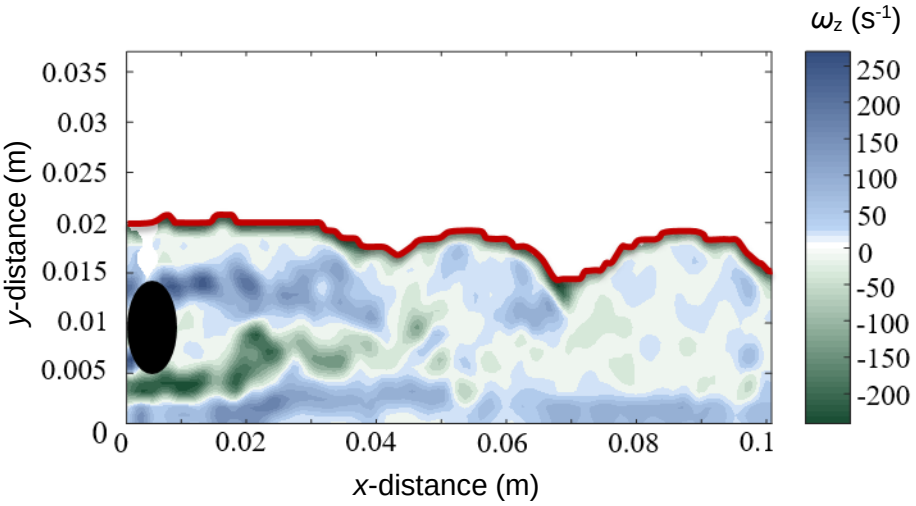

Figure 5.14: Vorticity field in the water phase of oil-water flows downstream of the 8 mm at Qo = 10 L/min and Qw = 10 L/min and *Fr* = 1.21 (*r* = 1.0). *The interface is shown as red line.

In stratified liquid-liquid flows in a pipe, the interface height depends in a non-linear way on the flow rates of the two phases. As a result, the interface height and the in-situ water velocity, or the depth of submergence and the Froude number, *Fr* based on water velocity, cannot be varied independently. Therefore, in this experiment, the effects of submergence depth and of Froude number on the shape of the interface could not be studied independently. To observe the influence of submergence depth the results for two Fr, *Fr* = 1.21 (*r* =1.0) and *Fr* = 1.86 (*r* = 0.5) which are very close, are compared from Figures 5.14 and 5.15 for two different submergence depths. As can be seen, when the submergence depth was increased from 4 mm to 8 mm, the amplitude of the interfacial waves decreases. Despite the increase in *Fr* (increase in water superficial velocity at constant oil superficial velocity), the vortices formed are further away from the interface and thus have less impact on the resulting interfacial waves. The increase in *Fr* with small increase in water velocity results in only a small increase of the vorticity magnitude while the size of vorticity regions remain almost the same; this is in agreement with the results in single phase flow in Figures 5.7 and 5.8. The influence of *Fr* and submergence depth on the amplitude of interfacial waves will be analysed further by measuring the amplitude of the interfacial waves.

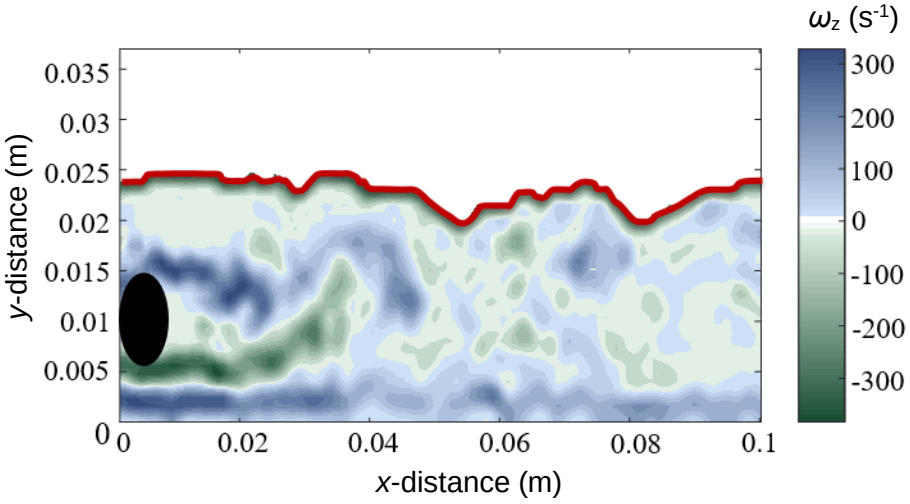

Figure 5.15: Vorticity field in the water phase of oil-water flows downstream of the 8 mm at Qo = 10 L/min and Qw = 20 L/min and *Fr* = 1.86 (*r* = 0.5).* The interface is shown as red line.

5.2.2.3 Amplitude

The amplitude of the interfacial waves is one of the important parameters related to the transition from separated to dispersed flows (Al-Wahaibi and Angeli, 2007; Al-Wahaibi and Angeli, 2011). Above a critical wave amplitude, the waves will grow and drops may detach from their crest leading to dispersed flows. Following the same procedures in the work of Castro et al. (2002) and Park et al. (2016), from the recorded high-speed images, the average wave amplitude is determined from the average wave crest and trough heights at each locations from 1 to 10 (refer to Figure 5.11). The average crest height is calculated by measuring the interface height of the wave passing through a measuring location for 0.5 s. Similarly, the average trough height is calculated by averaging the trough height at each measuring location over 0.5 s.

$$amplitude = \frac{avg\ wave\ crest\ height - avg.wave\ trough\ height}{2} \quad (5.3)$$

In this section, only results for the 8 mm cylinder system are included. This is because for the flow conditions investigated, the interfacial waves downstream of the 2 mm cylinder are very small and cannot be easily characterized.

The conditions investigated, the corresponding Froude numbers, *Fr* and the experimental incoming interface height are presented in Table 5.4 for reference. In this work, the experimental interface height is varied by the oil to water ratio, *r*; higher ratio leads to lower interface height and low submergence level of the cylinder (see Table 5.4).

Effects of Froude Number, *Fr*

The average wave amplitudes at constant flowrate ratio, r = 1 and different Froude number, *Fr* are shown in Figure 5.16 for the 8 mm cylinder. In the figure, the standard deviation of the samples used to calculate the average value is shown as error bars and the investigation locations are presented by the distance from cylinder in the y-coordinate. At the flow conditions shown, the incoming interface height and the submergence depth are constant. Thus, an increase in *Fr* in these cases is related to an increase in water velocity, u_w (as well as mixture velocity, u_{mix} at constant oil velocity, u_{oil}).

Table 5.4: Froude number and incoming interface height for all flow conditions studied.

Q (L/min)		u_{mix}	*r*	u_w	*Fr*		Interface
Oil	Water	(m/s)	(-)	(m/s)	*D* = 2 mm	*D* = 8 mm	(m)
10	10	0.31	1.00	0.34	2.43	1.21	0.017
10	20	0.47	0.50	0.52	3.71	1.86	0.021
20	20	0.63	1.00	0.65	4.64	2.32	0.017
20	30	0.78	0.67	0.83	5.94	2.97	0.020
30	20	0.78	1.50	0.76	5.43	2.71	0.016
30	30	0.93	1.00	0.97	6.93	3.46	0.017
30	40	1.09	0.75	1.16	8.28	4.14	0.019
40	30	1.09	1.33	1.09	7.78	3.89	0.013
40	40	1.24	1.00	1.29	9.21	4.60	0.017

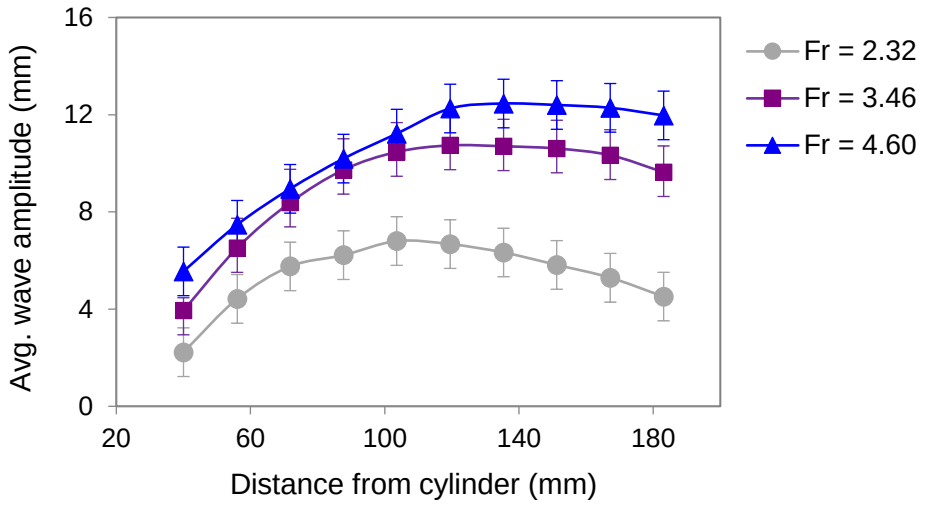

Figure 5.16: Effects of Froude number on interfacial wave amplitudes (*D* = 8 mm, *r* = 1.0).

For all flow conditions, a similar trend is observed where the wave amplitude increases downstream of the cylinder up to a maximum value before it declines. At the lowest *Fr* shows the decrease occurs at a distance closer to the cylinder compared to the other cases. This trend can be explained based on the vortices shed by the cylinder where at a certain distance from the cylinder, the vortices start to decay. This results to the reduction of amplitude of the vortex-induced waves. There is very limited work reported on the wake region behind a bluff body up to the distance investigated in this work. However, Williamson (1996) in a review reported that the von Karman street decays downstream of the bluff body. To support this further, an example of the CFD simulation of single-

phase flow from this work is shown in Figure 5.17 for u = 0.65 m/s which corresponds to Fr = 2.32 for the D = 8 mm. In the example, the vorticity region in the wake of the cylinder can be visualized. It can be seen that as the vortices are convected downstream the flow, the vorticity magnitude and the area covered by vorticity started to decrease at a certain distance behind the cylinder. The decrease happens further downstream of the cylinder as the Fr increases because as the water velocity increases, the vortices and the waves are convected faster over a longer distance downstream. It should be noted, however, that although the vortices and waves generated by the cylinder decay downstream, the drops which are formed in the wake of the cylinder can be sustained for a long distance and give rise to the dual continuous patterns.

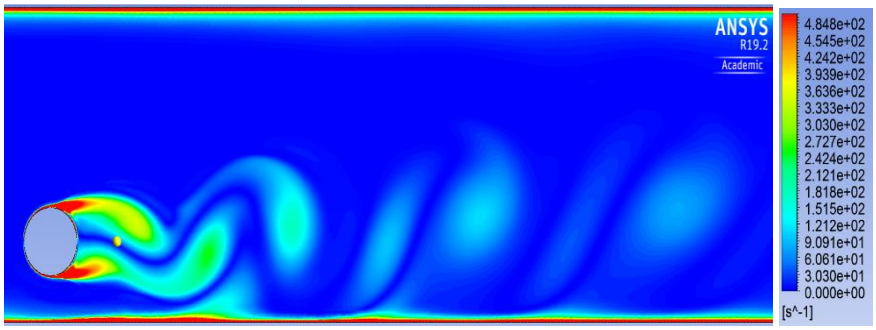

Figure 5.17: CFD simulation of instantaneous vorticity in the wake of 8 mm cylinder for single phase water flow at u = 0.65 m/s.

From Figure 5.16, it can also be observed that higher vortex-induced wave amplitudes are produced with increasing Fr for constant submergence depth. The trend is in agreement with the work of Park et al (2016) for a 5 mm cylinder. This is because as the water velocity increases, the magnitude of the von Karman vortices shed also increases which affects the amplitude of the interfacial waves.

Effects of incoming interface height/ submergence depth

The effects of incoming interface height (can also be represented by cylinder submergence depth as the cylinder position is constant) on the vortex-induced wave amplitude is presented in Figure 5.18 at constant u_{mix} = 0.78 m/s. When the interface height is low (low submergence depth) the von Karman vortices are closer to the interface (see Figure 5.14 and 5.15). As a result, vortex-induced waves with larger amplitudes are generated. The wave amplitudes generated with the 8 mm cylinder are also compared against those generated by a 5 mm cylinder measured by Park et al. (2016) in the same flow system in Figure 5.19.

For both cylinder sizes the wave amplitudes increase with distance from the cylinder. The large 8 mm cylinder produces waves with larger amplitude compared to the 5 mm cylinder at the same flow conditions. This is attributed to the size of the vorticity regions shed by the different cylinders. As was shown in Figure 5.9, the size of the vorticity region increases with the cylinder diameter.

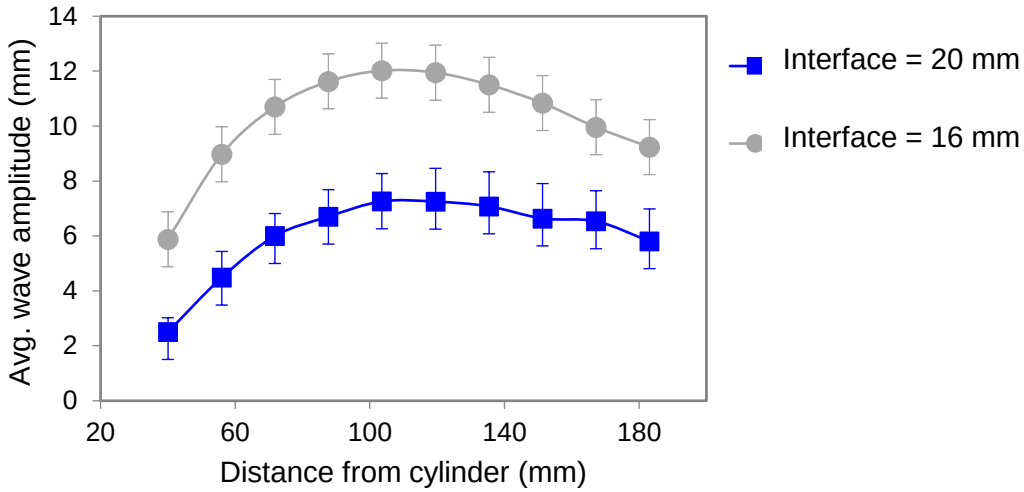

Figure 5.18: Effects of incoming interface height on interfacial wave amplitudes at u_{mix} = 0.78 m/s for system with cylinder D = 8 mm.
*Flowrates of Q_{oil} = 20L/min and Q_w = 30L/min (Interface height = 20mm)
*Flowrates of Q_{oil} = 30L/min and Q_w = 20L/min (Interface height = 16mm)

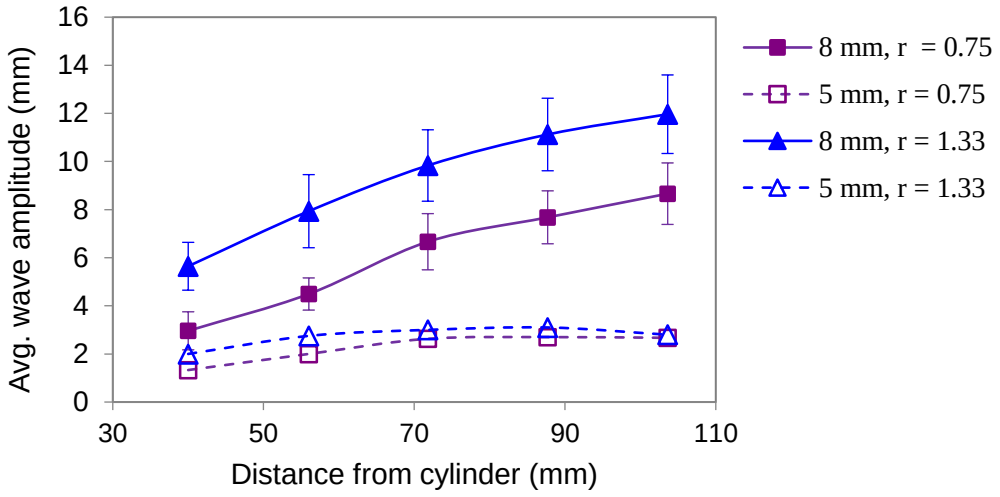

Figure 5.19: Effects of flowrate ratio, r on wave amplitude for D = 5 mm and 8 mm for u_{mix} = 1.09 m/s.
*Flowrates of Q_{oil} = 30L/min and Q_w = 40 L/min (r = 0.75)
*Flowrates of Q_{oil} = 40L/min and Q_w = 30 L/min (r = 1.33)
**Results for D = 5 mm is from the work of Park et al. (2016)

5.3 Summary

In this chapter, the experimental investigations of flow dynamics in the wake of cylinder of varying diameters are analysed and discussed. Cylindrical bluff bodies of various sizes were used to induce interfacial waves in two-phase, oil-water flows and to promote the transition from separated to dispersed patterns. The waves resulted from the interaction of the von Karman vortices shed by the cylinders with the oil-water interface in stratified flows. CFD simulations were used to select the bluff body diameters that would shed vortices with frequencies spanning two orders of magnitude. The simulations were 2D but agreed well with experimental velocity field data taken in the middle plane of the pipe, which demonstrates that fast 2D simulations can be used to estimate the flow properties behind a bluff body in pipes. The selected cylinder diameters, 2 mm and 8 mm, produced vortices with frequencies between 1 to 100 Hz in horizontal oil-water pipe flows. High speed visualization was used to acquire the flow patterns and the interfacial wave characteristics while PIV was used to obtain velocity fields and vortex properties behind the cylinders. The experimental data in single-phase water flow showed that the 2 mm cylinder produced vortices with Strouhal numbers that matched the literature values for unbounded flows, while the 8 mm cylinder resulted in vortices with higher Strouhal numbers. This increase was attributed to the short distance between the cylinder and the bottom pipe wall.

For all two-phase flow cases studied, the frequencies of the vortices and the corresponding Strouhal numbers match the frequencies of the vortex induced interfacial waves. This suggests that changes in the vortex shedding behaviour with flowrates or with bluff body size are reflected on the interfacial wave characteristics. It is possible, therefore, to control the properties of the interfacial waves in oil-water flows through the bluff body design. The transition boundary from stratified to dispersed flows shifted towards lower mixture velocities when cylinders were present in the water phase and was affected by the cylinder size. It was found that the large, 8 mm, cylinder generated interfacial waves with larger amplitude compared to the 2 mm cylinder, and caused an earlier transition to dispersed patterns.

By using fluids with matching refractive index, it is possible to obtain measurements close to the interface for very wavy interfaces and when drops detach. This will extend the range of flowrates than can be investigated with PIV and reveal the mechanisms of drop detachment from the interfacial waves.

Chapter 6

Drop Entrainment from Interfacial Waves in Stratified Flows

This chapter presents the results and discussion of the second main objective of this work, which is to investigate the mechanism of drop entrainment from interfacial waves in stratified liquid-liquid flows. Following a novel approach, vortex-induced waves in the two-phase flows are generated with the use of a cylindrical bluff body. In chapter 5, the limitations of particle image velocimetry (PIV) were discussed when test fluids of different refractive indices are used. The flows in the pipes are three dimensional and, at conditions where drops form, the interfaces are very disturbed which cause multiple reflections. This limits the applicability of the technique to low velocities where the interfaces are smooth; drops however detach at high velocities from highly fluctuating interfaces. To overcome this limitation matching refractive index liquids need to be used which led to the design of a 26 mm I.D. test section two-phase flow facility with test fluids of matching refractive index (see chapter 4).

To better understand and model the drop formation process from waves, it is important to know the velocity fields in the continuous phase around the forming drop which cannot be obtained from visual observations alone. The transient local velocity profiles around the waves and drops can be measured with PIV. A similar approach has been used for velocity measurements around a drop forming in a microchannel (Timgren et al., 2008; Chinaud et al., 2015; Roumpea et al., 2018). Since the two liquids have matching refractive indices the interface cannot be visualized with simple video imaging. For the visualization, planar laser-induced fluorescence (PLIF) is used therefore, where a fluorescent dye is added to one of the phases. The implementation of simultaneous PLIF and PIV techniques provides information on the wave breaking events and the velocity fields around the waves at the same time. This combination of techniques has recently been employed in the studies of oil-water flow dynamics

in a pipe for stratified (Ibarra et al., 2018) and for dispersed patterns (Voulgaropoulos and Angeli, 2017). The work presented here is the first attempt to experimentally study the detailed mechanism of drop entrainment from stratified liquid-liquid flows by the simultaneous application of the PLIF and PIV techniques.

The flow patterns identified for a wide range of flowrates at 3.5 downstream of the inlet are first discussed. The studies of flow pattern types serve two purposes which is to identify the flow conditions where transition from stratified to dual continuous flow occurs and to demonstrate the shift of the boundary to lower mixture velocities when a cylinder is located at the inlet. The flow conditions at the transition boundary signify the lowest velocity at which drop entrainment starts to occur. This is preferred for the investigations of drop entrainment from interfacial waves as at low velocity, the waves are less deformed and the detachment can more easily be observed.

Following the flow pattern identification, drop entrainment events are presented and discussed. In this section, the deformations of the interfacial waves that lead to drop entrainment are identified and analyzed. From the findings, a mechanism of drop entrainment is proposed based on the physical observations. In the last section of this chapter, a drop entrainment model is developed based on force balance7m] on the deformed waves. The experimental data on wave deformation and velocity fields around the deformed waves are implemented in the proposed model to predict drop detachment.

6.1 Flow Pattern Transitions

Examples of gray scale images of the flow acquired by the PLIF, taken at a frame rate of 4000 fps, are presented in Figure 6.1. In the images, the gray region represents the water/glycerol phase while the black region is the oil phase. The images presented in Figure 6.1 show the flow configuration on a thin plane at the center of the pipe. Approximately 20,000 frames were recorded at each flow condition corresponding to 5 s of flow.

The flow patterns are characterized based on the classification by Lovick and Angeli (2004). In general, four types were identified namely, stratified with smooth or wavy interface, ST, dual continuous flow with oil drops in water/glycerol, DC (O/W), dual continuous flow with both oil and water/glycerol drops, DC (O/W and W/O), and dispersion of oil in water/glycerol, Disp (O/W). To analyze the flow pattern transitions, flow pattern maps were constructed with the oil superficial velocity, u_{so} and water superficial velocity, u_{sw} as the coordinate systems. The corresponding flow pattern maps for a system with the cylinder located at the inlet and for a system without the cylinder are presented in Figures 6.2(a) and (b) respectively. In the maps, the transition boundary between stratified to dual continuous flow is shown as a dashed line. As can be seen, the region of stratified flow is significantly reduced and the boundary between stratified and dual continuous flow is shifted towards lower mixture velocities when the bluff body is present. This indicates that the bluff body actuates the drop entrainment to occur at lower mixture velocities. Details on how the bluff body actuates the flow pattern transition from stratified to dual continuous flows have been discussed in chapter 5.

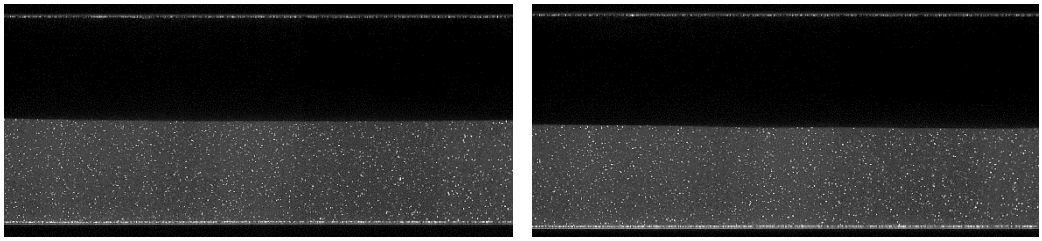

u_{sw} = 0.153 m/s – u_{so} = 0.123 m/s

u_{sw} = 0.153 m/s – u_{so} = 0.175 m/s

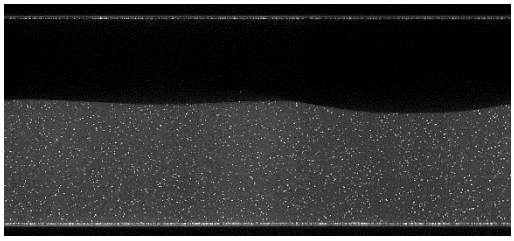

u_{sw} = 0.246 m/s – u_{so} = 0.123 m/s

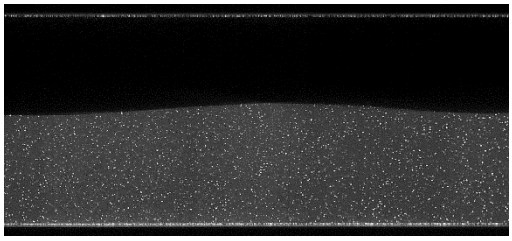

u_{sw} = 0.246 m/s – u_{so} = 0.175 m/s

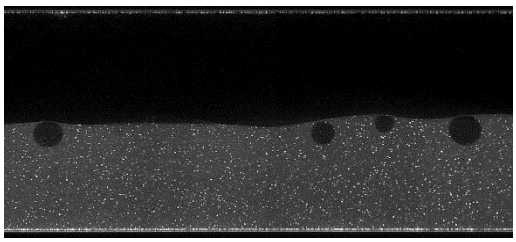

u_{sw} = 0.246 m/s – u_{so} = 0.280 m/s

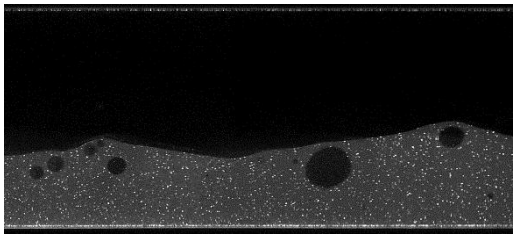

u_{sw} = 0.246 m/s – u_{so} = 0.605 m/s

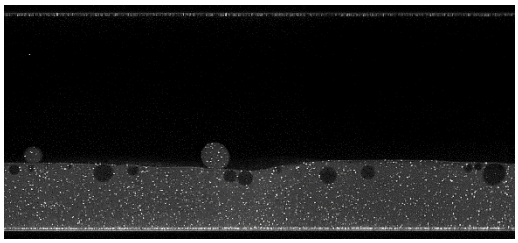

u_{sw} = 0.153 m/s – u_{so} = 0.605 m/s

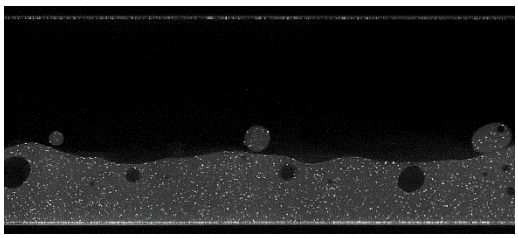

u_{sw} = 0.246 m/s – u_{so} = 0.716 m/s

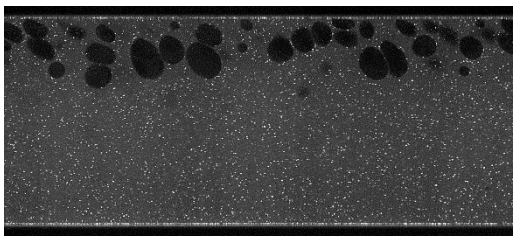

u_{sw} = 0.679 m/s – u_{so} = 0.071 m/s

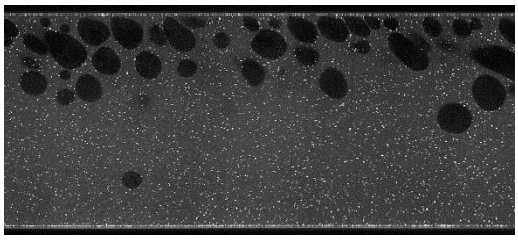

u_{sw} = 0.679 m/s – u_{so} = 0.071 m/s

Figure 6.1: Sample of images of the flow acquired at 3.5 m from the test section inlet.

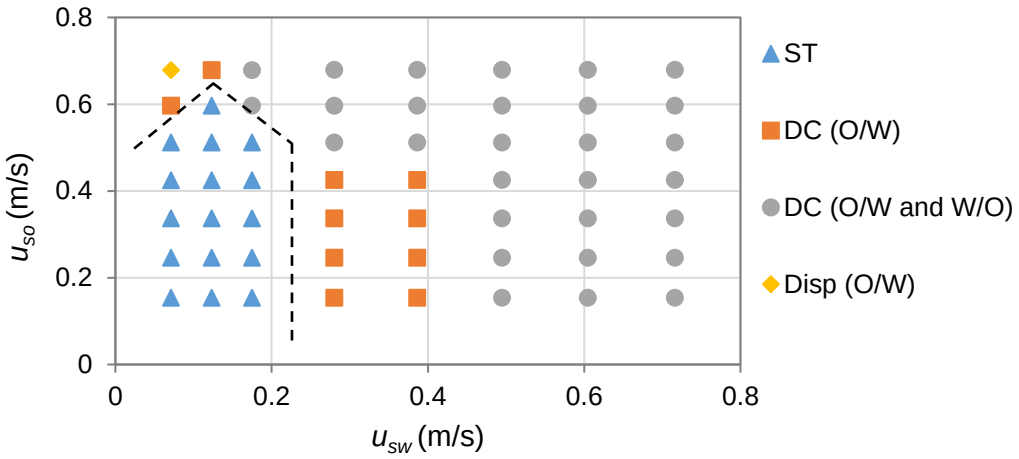

(a) System with cylinder at inlet

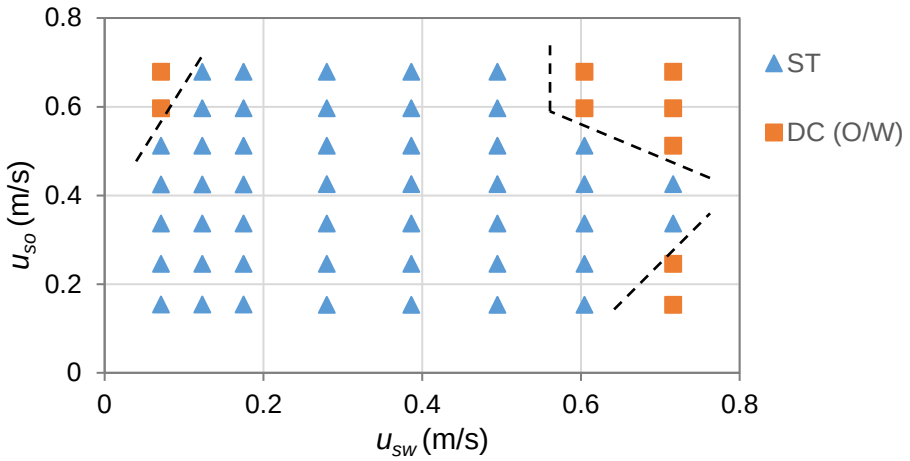

(b) System without cylinder at inlet

Figure 6.2: Flow pattern maps for various systems (26 mm I.D.). (a) bluff body present at inlet (b) without bluff body at inlet

6.2 Investigation of Drop Entrainment in Stratified Flows

6.2.1 Investigation region

A schematic of the side view of the pipe test section with the cylinder is presented in Figure 6.3. An investigation region is established just behind the cylinder, where the unstable interfacial waves started to form and undergo deformation. This leads to an increase in the possibility of drop entrainment from the breakage of interfacial waves as has been previously reported (Trallero et. al., 1997; Al-Wahaibi and Angeli, 2007; Al-Wahaibi and Angeli, 2011; Barral et. al., 2015).

Based on preliminary observations, the region behind the cylinder can be segmented into two separate regions based on the state of interface, namely the *wave formation region* and the *drop entrainment region* (refer Figure 6.3). In the wave formation region, interfacial waves are generated immediately behind the cylinder from the interaction between the von Karman vortices shed by the cylinder with the oil-water interface as discussed in chapter 5. The unstable waves grow in amplitude as they travel through this region and start to deform. In the drop entrainment region, the waves experience further deformation that can lead to drop detachment. Due to the large size of both regions, measurements in the regions are conducted separately to increase the image resolution.

In this work, the cylinder is located in the water/glycerol phase (lower half of the pipe as shown in Figure 6.3), which leads to the promotion of oil drop entrainment due to the interactions of the interface with the vortices generated in the water/glycerol phase. The wave formation which leads to drop entrainment follows the similar mechanism discussed in Chapter 5. In this chapter, the focus is on the entrainment of oil drops.

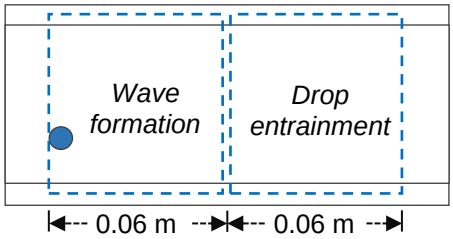

Figure 6.3: The use of cylindrical bluff body to establish investigation region for the investigation of drop entrainment.

6.2.2 Experimental observation of drop entrainment events

The experimental flow conditions for the visualization of the drop entrainment events are selected to ensure that the interfaces are not very disturbed while only a few drops are present so that the entrainment events can be observed clearly. For this reason, flow velocities close to the transition boundaries shown in Figure 6.2(a) were chosen. For each of the flow conditions investigated, images were captured at frame rate of 4000 fps with approximately 20,000 frames recorded, which correspond to a flow time of 5 s. From the recorded high-speed images, the interface is monitored to track the evolution of the interfacial waves that lead

to drop entrainment events. This is performed with the image processing software (Photron Fastcam Viewer, PFV).

6.2.3 Drop entrainment events and mechanism

Generally, the drop entrainment in stratified flows (which in this case is the entrainment of oil drops) was observed to occur through separation or detachment of a part of the wave (wave trough for the case of oil phase entrainment) into the opposite phase. After the separation, the wave retracts towards its continuous layer, leaving behind the detached drop. The drop entrainment events are divided into three stages prior to breakup; *wave formation*, *ligament formation* and *necking and ligament thinning*. The first two stages occur in the wave formation region while the necking and ligament thinning stage are observed in the drop entrainment region (see Figure 6.3). The drop entrainment process was also found to be consistent at the various flow conditions investigated in this work. A detailed description of the stages is given below.

6.2.3.1 Wave formation stage

In stratified flows, formation of interfacial waves can lead to the onset of entrainment (Al-Wahaibi and Angeli, 2007). In non-obstructed flow, according to the Kelvin-Helmholtz instability, interfacial waves are generated when there is average velocity difference between the two phases. However, in this work, the use of cylindrical bluff body acts as passive actuator to generate interfacial waves even when there is no velocity difference between the two phases (r = 1). The process of wave formation is presented in Figure 6.4. An interfacial wave (oil trough in the water phase) is observed to be generated immediately after the cylinder at t_1 due to the action of vortices as discussed in Chapter 5. The wave grows in size from t_2 to t_4 as it propagates along the pipe with increasing volume of fluid submerged in the opposite phase.

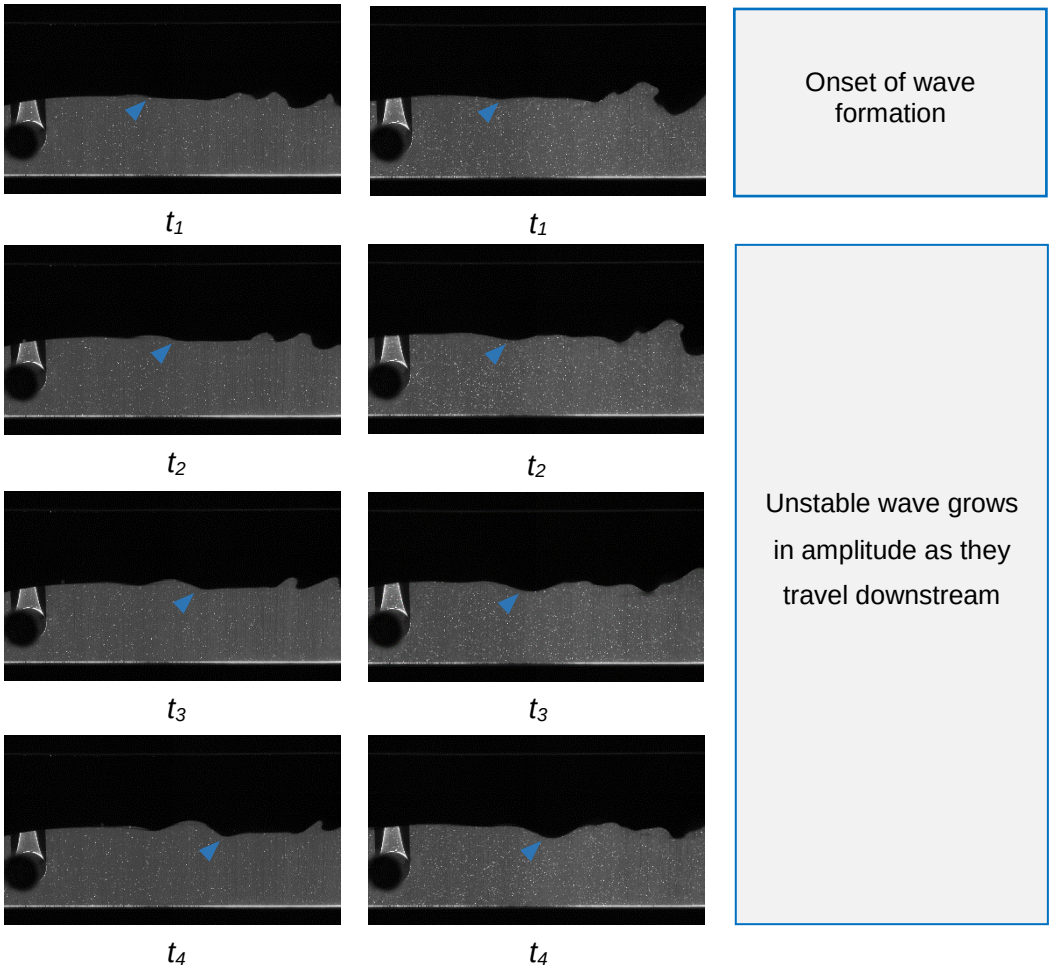

Figure 6.4: Wave formation events in the wake of cylinder.
Left (u_{so} = 0.386 m/s, $u_{sw/g}$ = 0.154 m/s) and right (u_{so} = 0.386 m/s, $u_{sw/g}$ = 0.246 m/s)

6.2.3.2 Ligament formation stage

The ligament formation stage which follows the wave formation stage can be seen in Figure 6.5. The images are continuation of the sequence of images shown in Figure 6.4.

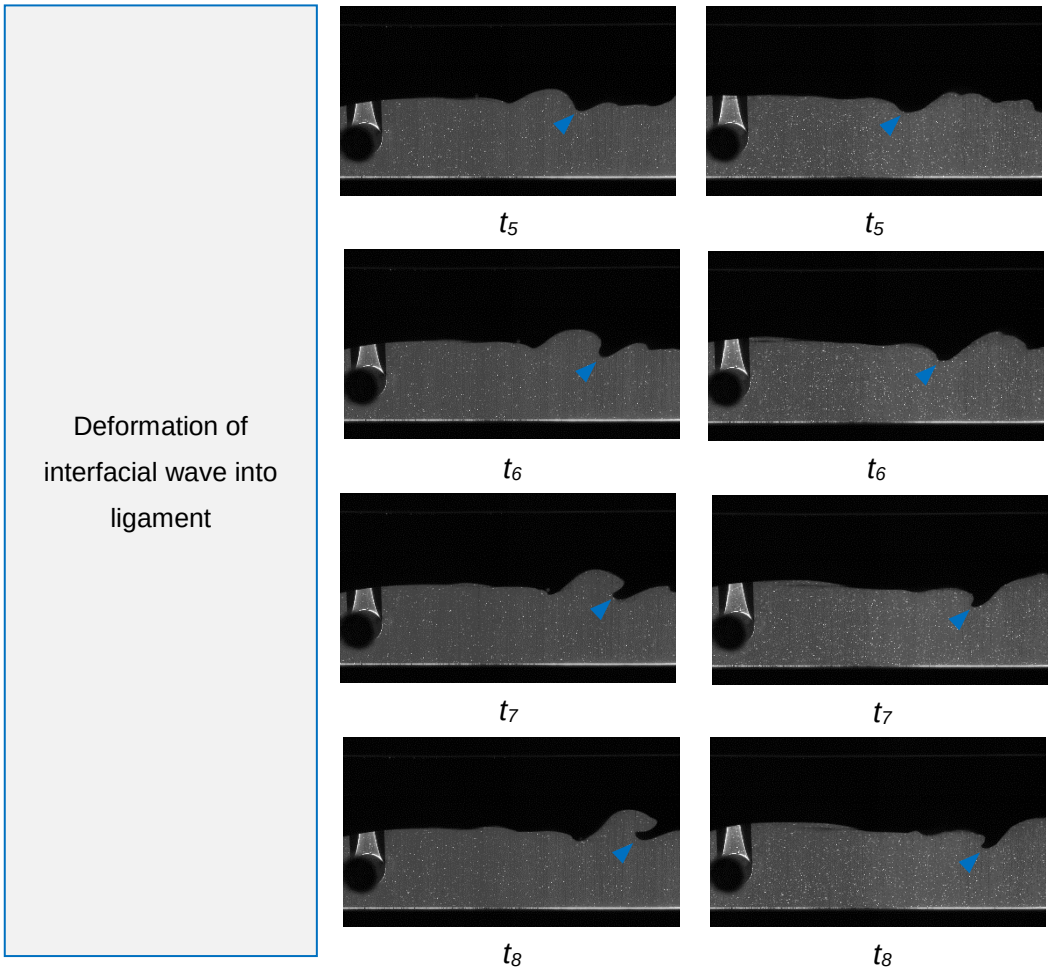

Figure 6.5: Deformation of developed wave into ligament.
Left (u_{so} = 0.386 m/s, $u_{sw/g}$ = 0.154 m/s) and right (u_{so} = 0.386 m/s, $u_{sw/g}$ = 0.246 m/s)

In this stage, the oil wave trough undergoes deformation into a ligament shape. This phenomenon is attributed to the drag force experienced by the wave trough, as it is submerged in the opposite phase, because of the velocity difference between the wave trough and the surrounding fluid. For the cases shown in Figure 6.5, the drag force acts to the opposite direction of the main flow, thus resisting the flow of the wave trough. As a result, the wave trough moves at a lower velocity compared to its continuous layer and forms a long ligament pointing to the opposite direction of the flow. The forces acting on the wave trough will be analyzed in Section 6.3.

6.2.3.3 Necking and ligament thinning

The ligament undergoes further deformation forming a neck with a swell at its front, as can be seen in Figure 6.6 for the same conditions as those presented in Figures 6.4 and 6.5 (it has to be noted that the images for this stage are obtained in the drop entrainment region; see Figure 6.3).

From Figure 6.6, initially at t_1, a swelling is formed at the end of the ligament which was formed from the previous stage. From t_1 to t_2, the wave troughs travel downstream the flow without deformation (displacement). At t_3, the neck thickness begins to decrease until it collapses at t_4 and the swell is separated from the wave trough, forming a drop. Immediately after the breakup, at t_5 to t_6, the wave trough retracts towards its continuous layer while the drop becomes spherical. In particular

- Displacement, t_1 to t_2: The deforming force acting on the wave trough is not sufficient to overcome the resisting interfacial force that keeps the wave to its current shape. Therefore, the wave trough travels without any deformation.

- Neck thinning, t_3: The deforming force overcomes the resisting force which results to reduction of the neck thickness.

- Drop detachment, t_4: The neck collapse and drop is detached.

- Wave trough retracts and formation of drop, t_5 to t_6: The interfacial tension force pulls the wave towards its continuous layer and the surface tension of the detached drop cause it to form spherical shape.

The resisting and deforming forces acting on the wave trough will be identified and analyzed in details during the modeling of drop entrainment.

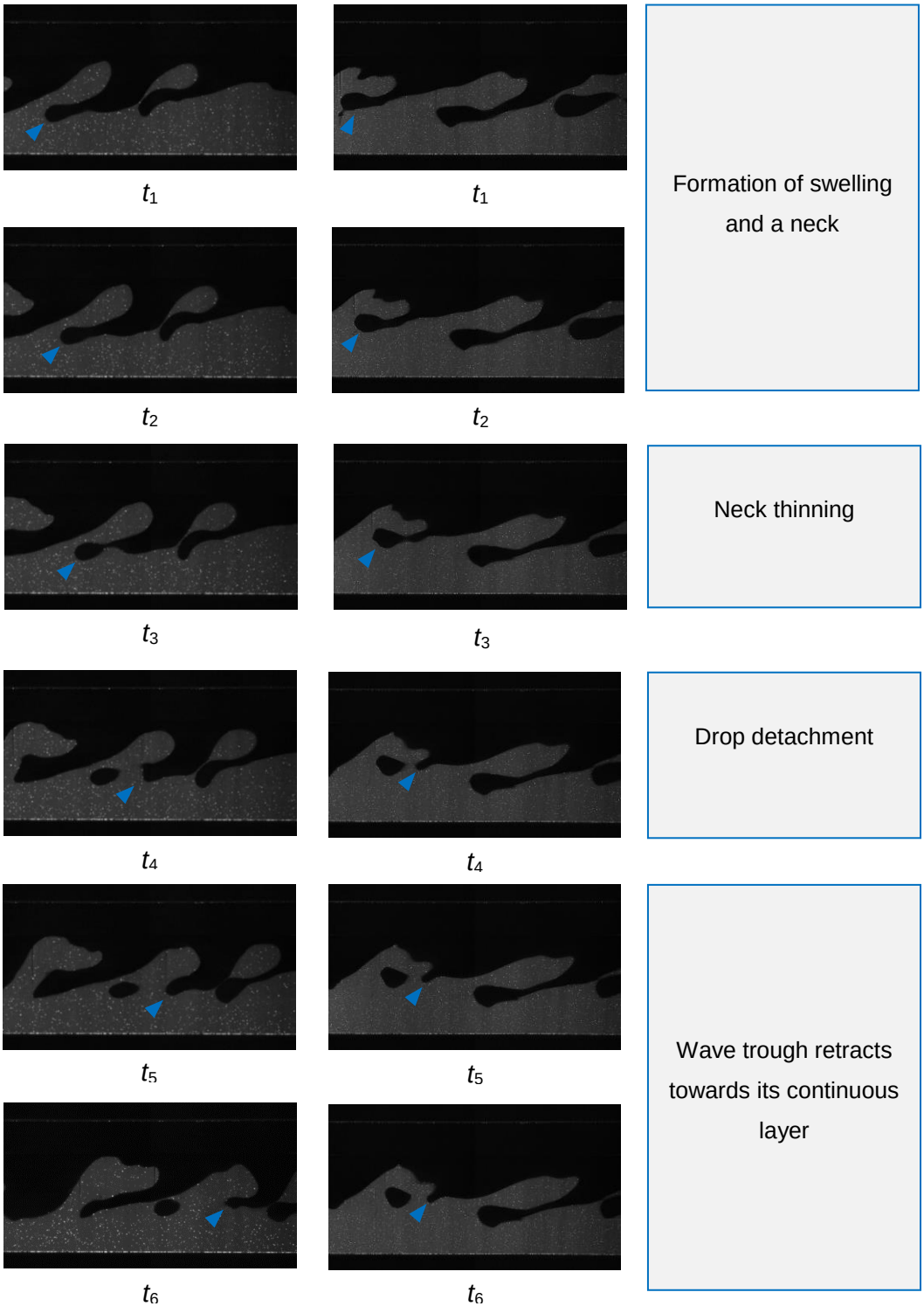

Figure 6.6: Necking, ligament thinning and drop detachment events.
Left (u_{so} = 0.386 m/s, $u_{sw/g}$ = 0.154 m/s) and right (u_{so} = 0.386 m/s, $u_{sw/g}$ = 0.246 m/s)

More examples of necking and ligament thinning events captured at the entrainment region for various flow conditions are presented in Figure 6.7. The images show sequence from swelling formation to detachment. From the figure, although the drops are observed to detach following a similar process, variations of the deformed wave trough properties in terms of the size of swells and resulting drop size, the amplitude of the waves, the length of the ligaments and the detachment location (height from pipe bottom) can be seen. This implies the possible influence of the flow conditions on the properties of the wave trough. A map which shows the process of ligament formation from wave troughs prior to drop detachment at various flow conditions is presented in Figure 6.8 with the superficial oil and water/glycerol velocities at the as the x and y coordinates.

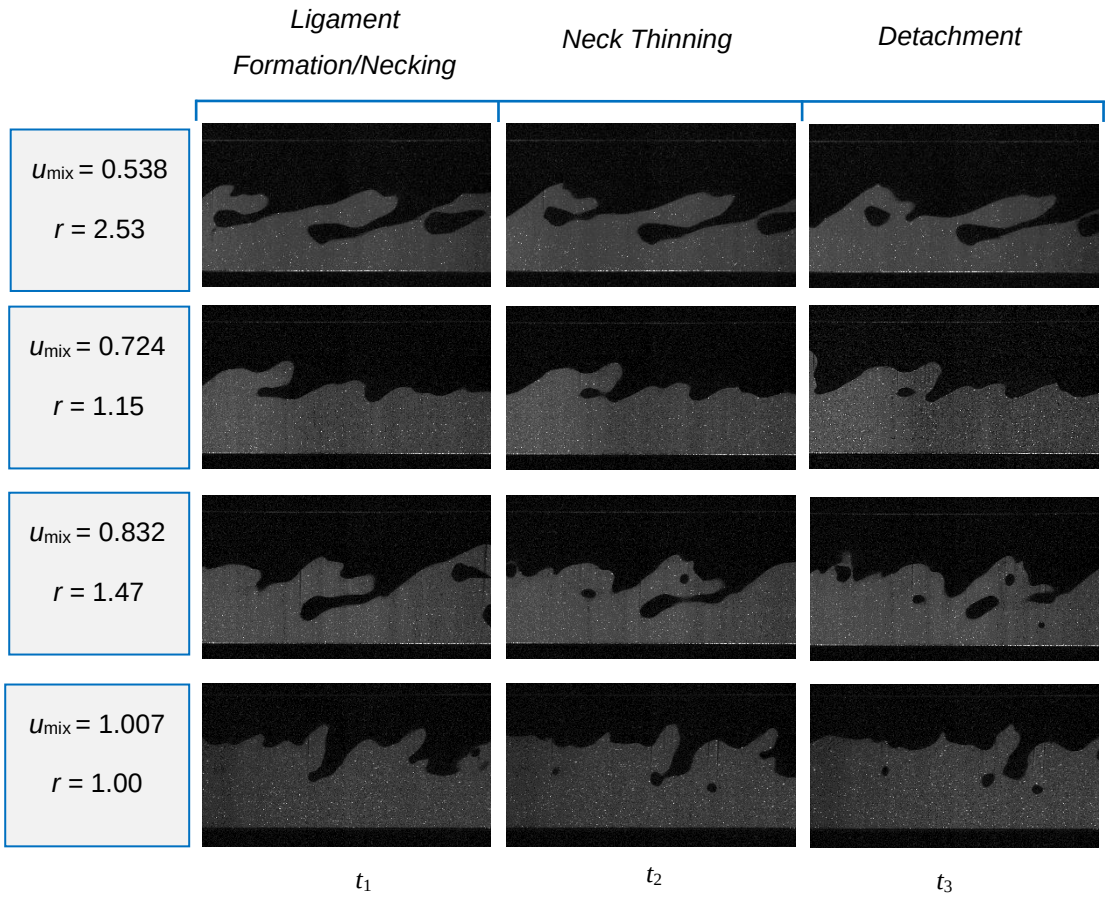

Figure 6.7: Sequence of drop detachment events at various flow conditions.

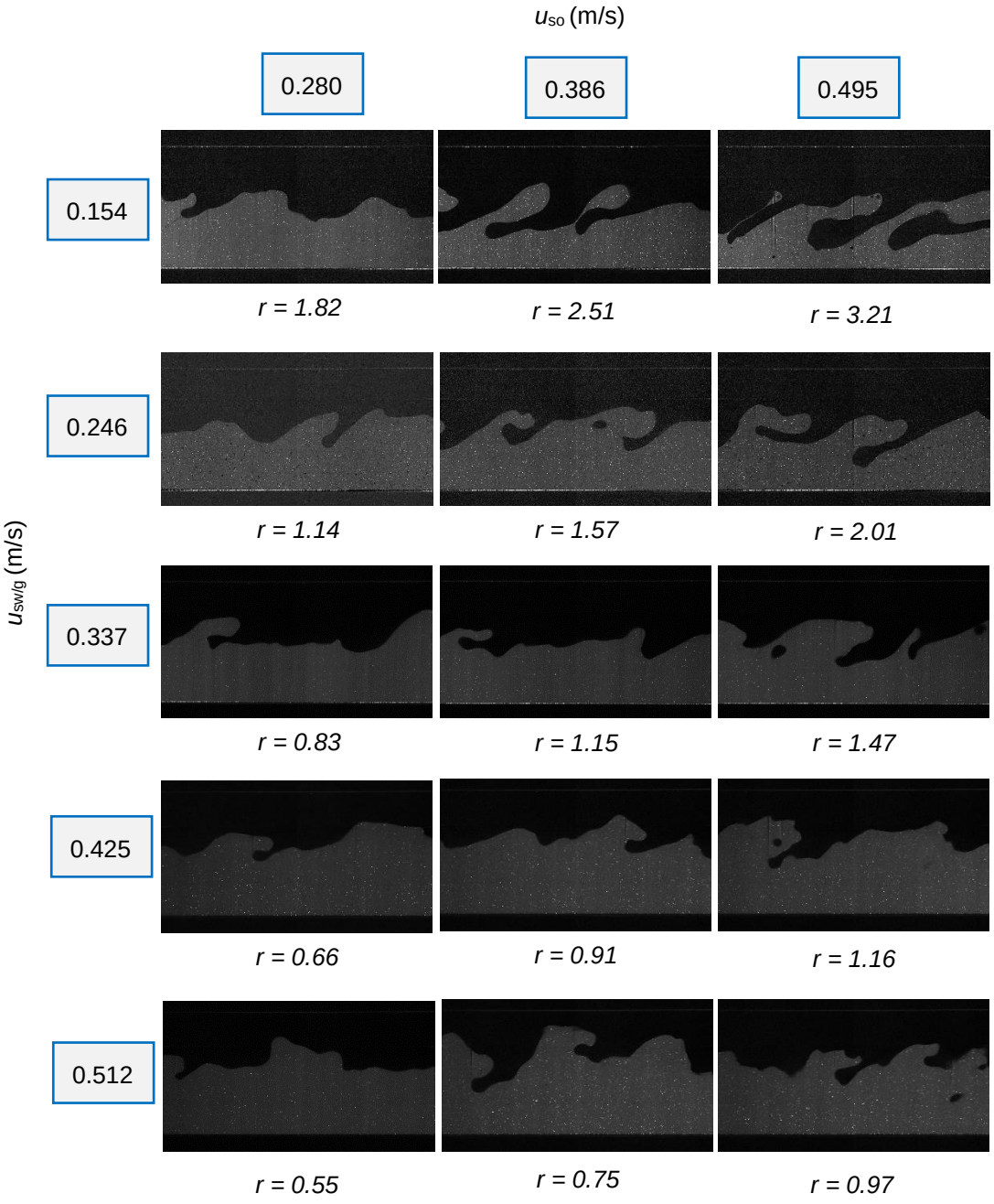

Figure 6.8: Images of ligament formation prior to drop detachment at various flow conditions.

The flow conditions shown in Figure 6.8 are the conditions near the transition zones in the flow pattern map in Figure 6.2(a). As can be seen the size and length of the ligaments increases with increasing oil to aqueous phase flowrate ratios, *r*. The variation of the ligament size and length is attributed to the amplitude of interfacial waves and the drag force experienced by the wave

troughs. In Figure 6.9, the average wave amplitudes at various *r* are presented for the cases shown in Figure 6.8. The wave amplitudes are measured in the wave formation region just before the waves deform into ligaments. As can be seen, the average amplitudes increase with *r*. Increase in the wave amplitude leads to larger size of the oil wave trough submerged in the water/glycerol phase. Therefore, with the assumption of constant wave volume between the wave formation and the ligament formation stages, the initial ligament length corresponds to the amplitude of the wave trough. The mixture velocity, u_{mix}, also influences the interfacial waves. At high u_{mix}, ripples or capillary waves can be observed at the interface especially for r = 1.16 and r = 0.97 as observed in Figure 6.8. The formation of capillary waves, however, does not affect the mechanism of drop entrainment.

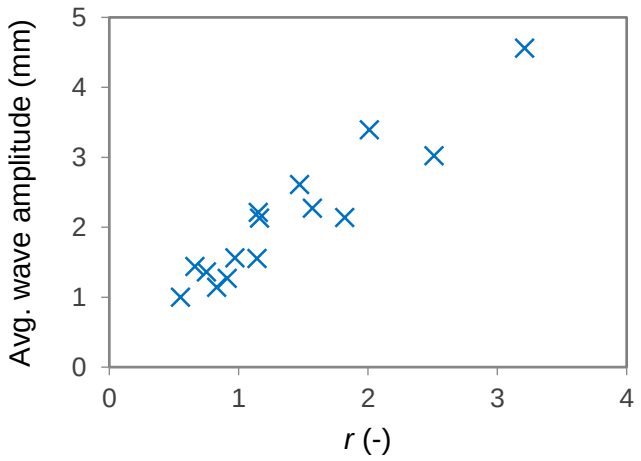

Figure 6.9: Average wave amplitude at various flow rate ratio. *Measurements were taken at 0.043 m behind the cylinder

6.3 Modeling of Drop Detachment

In many attempts of modeling the drop entrainment process, force balance had been employed. Pioneering works of Scheele and Meister (1968), Ishii and Grolmes (1975) and Kataoka et al. (1983) are several examples as discussed in Section 2.3.2 in chapter 2.

The aim here is to develop a model that describes the final stages of drop entrainment where a neck forms. The modeling process is divided into several stages. First, the criterion for drop detachment is discussed based on force balance. Then, the types of forces involved during the detachment process

are identified and a mathematical model based on the detachment criterion is proposed. Finally, experimental data obtained from this work will be compared with the model predictions.

6.3.1 Development of entrainment criterion

Based on the experimental observations, waves first deform to ligaments with a swell at the end. The swelling is connected to the remaining wave through a neck. Drop entrainment then occurs when the neck thins and breaks. To determine the criterion of drop detachment, a force balance is applied on the swelling and the neck as illustrated in Figure 6.10 which shows a deformed oil wave crest in the water phase.

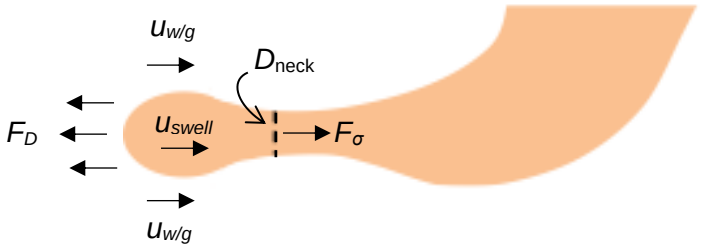

Figure 6.10: Model for drop detachment from a deformed wave.

The interfacial wave experienced various deforming forces. For co-current flows, the dominant deforming force is the drag force, F_D, arising from the relative velocity between the wave and the surrounding fluid (Holowach et al., 2002; Al-Wahaibi et al., 2007). The force resisting the deformation, on the other hand, is the interfacial tension force, F_σ while the gravitational force, F_G can be neglected due to the small buoyancy effects.

The deforming force tends to separate the swell from the remaining body of the wave that is connected by a neck. The deforming force is acting on the opposite direction of the wave flow and is resisted by an interfacial; tension force. When the deforming force overcomes the resisting force, the neck will thin and eventually it will break, leading to drop entrainment;

$$Deforming\ force > Resisting\ force \tag{6.1}$$

6.3.2 Modeling of forces

6.3.2.1 Interfacial tension force

The deformation of the interfacial wave as illustrated in Figure 6.10 resembles the process of drop formation from a nozzle (Scheele and Meister, 1968) and from a T-shaped junction in a microchannel (Glawdel et al. 2012). In those cases, the following equation has been used to model the interfacial tension force (Husny and Cooper-White, 2006);

$$F_\sigma = \pi \sigma D_{neck} \tag{6.2}$$

In Eq. 6.2, where σ is the interfacial tension and D_{neck} is the diameter of the neck. In the case of drop formation in microchannel and nozzles, the width of the channel or opening of the orifice/nozzle is used as the neck is bounded in this dimension. In this case, D_{neck} varies and is measured directly from the captured images.

6.3.2.2 Deforming force

The deforming force is the drag force originating from the velocity difference between the two phases. The drag force can be estimated from:

$$F_D = C_D A_{eff} \rho_{w/g} \frac{(u_{w/g} - u_{swell})^2}{2} \tag{6.3}$$

In Eq. 6.3, where C_D is the drag coefficient, A_{eff} is effective area of the swell, $\rho_{w/g}$ is the density of the surrounding water/glycerol phase, $u_{w/g}$ is the water/glycerol velocity around the swell and u_{swell} is the velocity of the swell. From equation 6.1 the criterion for drop detachment can be written as;

$$C_D A_{eff} \rho_{CP} \frac{(u_{surr} - u_{swell})^2}{2} > \pi \sigma D_{neck} \tag{6.4}$$

The deforming and resisting forces are tracked at time steps of 0.75 ms during the necking and ligament thinning stages. The drag force, F_D and the interfacial tension force, F_σ are determined from Eq. 6.2 and 6.3 where experimental data

acquired with the PIV and the PLIF techniques were implemented in the forces calculation..

The deforming and resisting forces are tracked at time steps of 0.75 ms during the necking and ligament thinning stages. The drag force, F_D and the interfacial tension force, F_σ are determined from Eq. 6.2 and 6.3 where experimental data acquired with the PIV and the PLIF techniques were implemented in the forces calculation. A sample calculation of the forces is shown below for a low mixture velocity case with u_{so} = 0.386 m/s and $u_{sw/g}$ = 0.154 m/s which corresponds to r = 2.51. This was chosen because at high u_{mix}, the interface is disturbed with formation of capillary waves. In addition, the presence of already detached drops (see Figure 6.7) could interfere with the calculation of the velocity field from PIV. In addition, the flowrate ratio chosen is high so that the waves have large amplitudes and the process of drop detachment is clear.

6.3.3 Calculations of drag force and interfacial tension force

Drag coefficient, C_D

To calculate the drag force, F_D from Eq. 6.3, the drag coefficient, C_{D}, effective swell area, A_{eff}, swell velocity, u_{swell} and the local velocity around the swell, $u_{w/g}$ are determined from the experimental data. In drops, unlike solid particles, the drag coefficient depends on the internal circulation. Buzzard and Nedderman (1967) found significant dependence of C_D from the drop viscosity. The effect of internal circulation can be characterized by the viscosity ratio between the drop and the surrounding fluid which has to be considered in the estimation of C_{D} (Kelbaliyev, 2011). Kataoka et al. (1983) proposed the following correlation for C_{D}, and used it to determine the drag force acting on a liquid wave crest in gas-liquid annular flow:

$$C_D = 286 Re_{Lf}^{1/6} Re_g^{-2/3} \left(\frac{\rho_g}{\rho_{Lf}}\right)^{1/3} \left(\frac{\mu_g}{\mu_{Lf}}\right)^{-2/3} \tag{6.5}$$

In Eq. 6.5, Re is the phase Reynolds number, ρ is the phase density and μ is the phase viscosity, and the subscripts L_{f} and g stand for the annular liquid film and the gas phase respectively. Al-Wahaibi et al. (2007) modified the correlation for liquid-liquid systems as follows:

$$C_D = 286 Re_{slower\ phase}^{1/6} Re_{faster\ phase}^{-2/3} \left(\frac{\rho_{oil}}{\rho_{w/g}}\right)^{1/3} \left(\frac{\mu_{oil}}{\mu_{w/g}}\right)^{-2/3} \quad (6.6)$$

In Eq. 6.6, the phase Reynolds number is defined as $Re_i = u_i D_{hi} \rho_i / \mu_i$ where u_i is the in situ phase velocity and D_{hi} is the hydraulic diameter. Eq. 6.6 is used to estimate the drag coefficient in this work. The velocities of the phases and the hydraulic diameters are calculated using the interface height of the incoming stratified flow to estimate the occupied area by each phase with details of the calculation are presented in Appendix B (see also Edomwonyi-Otu and Angeli, 2015). For the flow conditions considered, the incoming interface height was 0.107 m and the in situ Reynolds numbers for oil and water/glycerol phases were 5846 and 3215 respectively. From the data, the C_D was found to be equal to 4.65 from Eq. 6.6 and is of the same order of magnitude as the C_D estimated by Bozzano and Dente (2001) for bubbles in a liquid (C_D = 2.61) at Re > 1530.

Swell effective area, A_{eff}

The effective area of the swelling, A_{eff} is determined as the area of the swell projection area on the flow direction. This is estimated by measuring the effective diameter, D_{eff} of the swell (vertical) from the instantaneous images during the necking and ligament thinning stages. The cross section area of the swell is calculated as;

$$A_{eff} = \pi \left(\frac{D_{eff}}{2}\right)^2 \quad (6.7)$$

The effective diameter, D_{eff} of the swell measured during the necking and ligament thinning stages at time intervals equal to 0.75 ms is presented in Figure 6.11. The error bars represent the maximum possible error of the measurement and are ± 0.1 mm. As can be seen, D_{eff} remains almost constant and the corresponding average cross-sectional area is equal to 10.2 mm^2. This implies that during the necking and thinning stages, there is no new fluid added into the swell. To confirm this, the horizontal diameter of the swell (which had an ellipsoidal shape) was also measured and shown in Figure 6.11. This also does not vary significantly, further suggesting that the volume between the developed wave trough and the resulting ligament remains the same.

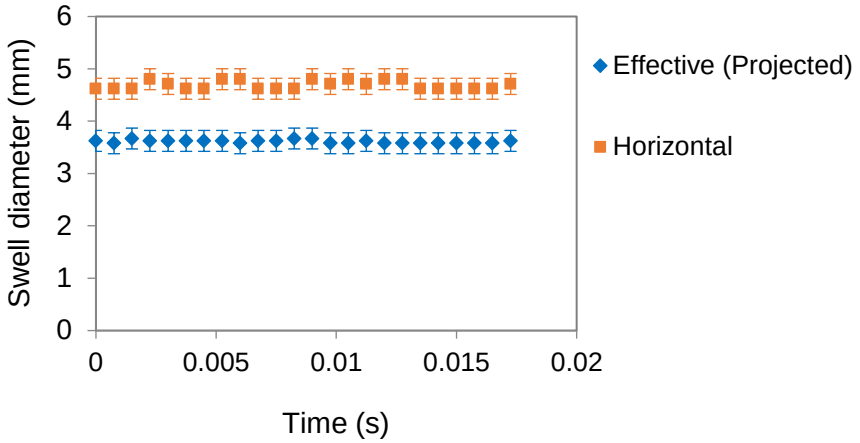

Figure 6.11: Swell diameters during the drop detachment process

Swell velocity, u_{swell}

The swell velocity, u_{swell} is estimated by measuring the displacement of the swell between frames at every 0.75 ms. The velocity was found to be constant and equal to u_{swell} = 0.544 m/s ± 0.06.

Surrounding phase velocity, u_{surr}

To calculate the drag force, F_D, the velocity difference between the swell and the continuous phase is required. From the PIV measurements the actual local velocity surrounding the drops can be calculated. To determine the local phase velocity, the masked images are further processed to acquire the velocity vectors using the JPIV software where an adaptive correlation tracking was used to obtain the two-dimensional velocity fields.

The velocity field in the aqueous phase surrounding the deformed oil ligament is shown in Figure 6.12 for the case considered. A magnified image of the velocity vectors around the swell is shown in Figure 6.12(b). In this figure, the velocity components are shown as vectors while the magnitude is shown in color. To determine the velocity difference for the drag force calculation, the velocity around the swell is taken as the local continuous phase velocity, $u_{sw/g}$. This is estimated from the velocity above, in front and below the swell. From Figure 6.12, it can be seen that the velocity varies significantly at the region above the swell, towards the middle of the pipe, while at the front and bottom it remains almost constant with a deviation of less than 2%. The average velocity calculated above the swell was also found to be almost constant (deviation less than 1.5%) when the velocity components are averaged from the swell perimeter (0 mm) to a

distance of 4.8 mm and above. Therefore, the local velocity around the swell, $u_{sw/g}$, is determined by averaging the velocity over a distance of 4.8 mm from the top, front and bottom of the swell. This distance may vary with the time step and the flowrates; it may also be limited by the presence of the interface.

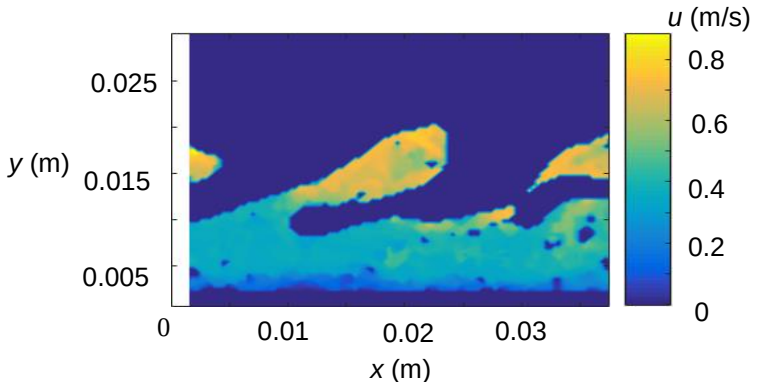

(a)

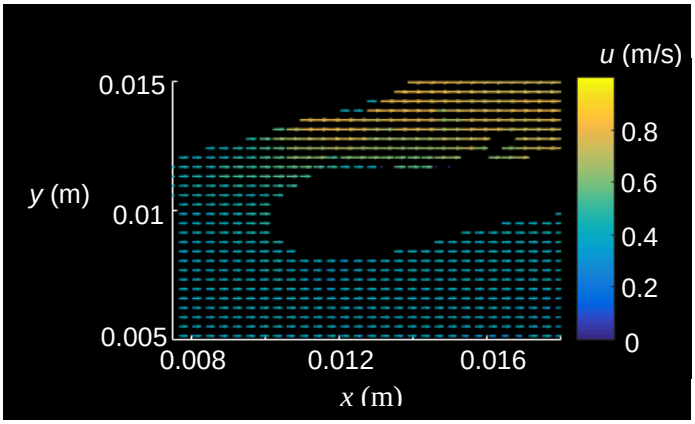

(b)

Figure 6.12 Example of the instantaneous water/glycerol phase velocity for u_{so} = 0.386 m/s and $u_{sw/g}$ = 0.154 m/s and r = 2.51. (a) Velocity contours (b) Velocity vector field in the vicinity of a swell.

6.3.4 Tracking the forces during drop detachment process

The drag, F_D and interfacial tension, F_σ, forces are determined as discussed above every Δt = 0.0025s and are shown in Figure 6.13 for the necking and ligament thinning stages. The evolution of the forces is compared with the corresponding images at which the calculations are made.

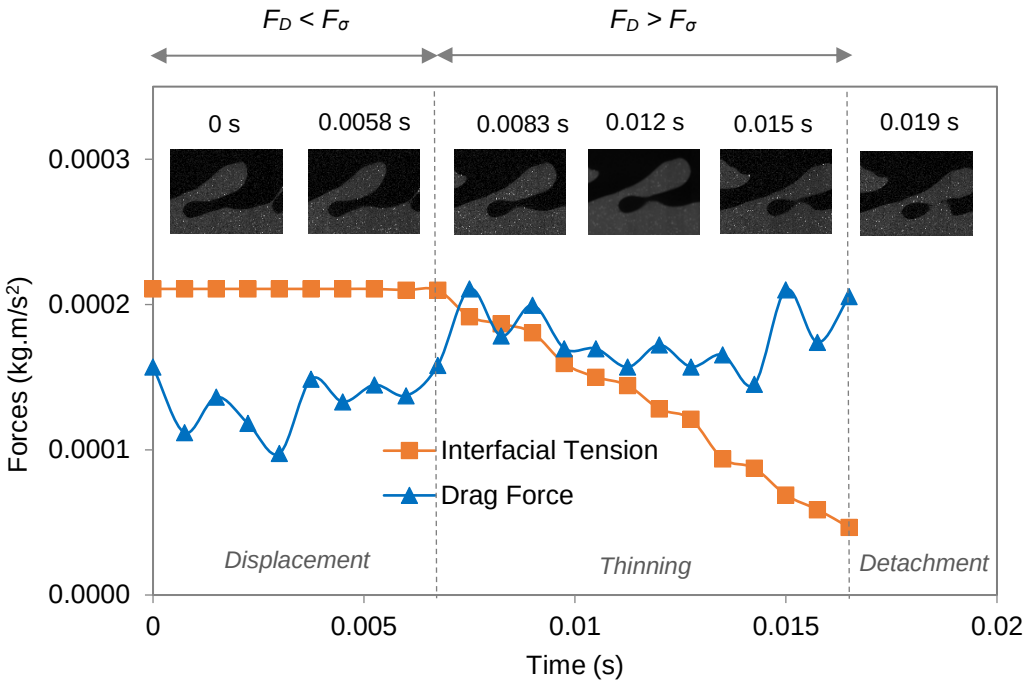

Figure 6.13: Drag and interfacial tension forces calculated during a drop detachment event in the case of u_{so} = 0.386 m/s, $u_{sw/g}$ = 0.154 m/s, r = 2.51.

As can be seen, from t = 0 to t = 0.0058s, there is no significant change in the ligament thickness as the wave trough travels with the flow. During this period, the interfacial tension, F_σ which is proportional to the ligament thickness (Eq. 6.2), remains constant. The drag force, F_D acting on the swell is seen to fluctuate but its value does not exceed that of F_σ. In this period, the drag force is not sufficient to overcome the interfacial tension force on the neck and, therefore, only displacement of the ligament takes place without any deformation.

When the F_D starts to overcome the F_σ at t = 0.0068 s, beginning of the neck thinning is observed on the high-speed images. As the neck thickness decreases, the corresponding interfacial tension force starts to decrease as well. The ligament continues to thin until it collapses at t = 0.01725 s resulting to detachment of the swell as a drop into the aqueous phase. Similar trends were found for the other cases studied, where the drag force is observed to overcome the interfacial tension at the onset of neck thinning. Additional examples are presented in Figure 6.14 (a) and (b) for different detachment events. This implies the agreement between the actual drop detachment phenomenon and the drop detachment model proposed in Eq. 6.4.

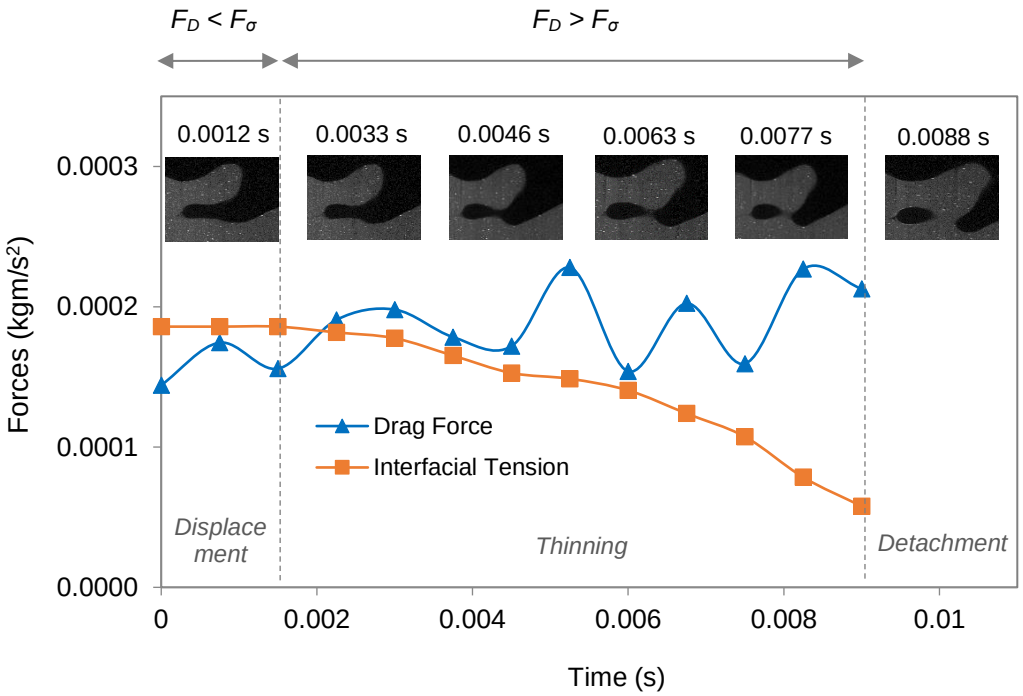

(a) u_{so} = 0.386 m/s, $u_{sw/g}$ = 0.337 m/s, r = 1.15

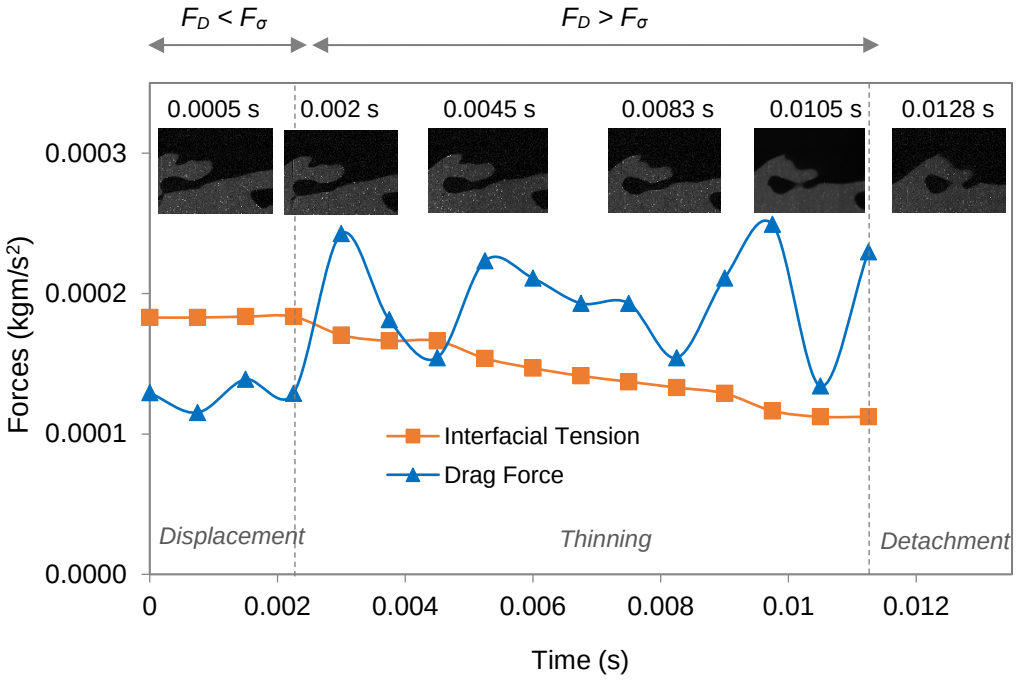

(b) u_{so} = 0.386 m/s, $u_{sw/g}$ = 0.154 m/s, r = 2.51

Figure 6.14: Drag and interfacial tension forces during a drop detachment events for different flow conditions.

6.3.5 Factors influencing the drop detachment

The proposed analytical model of Eq. 6.4 which uses the simplified force balance, describes the force required for the onset of ligament thinning during the necking stage based on the fluid properties and flow conditions. The drag force, F_D, is influenced by the relative velocity between the aqueous phase and the swell (Eq. 6.3). As the swell velocity, u_{swell} was found to be almost constant during the detachment process, the drag force is mainly dependent on the surrounding instantaneous velocity of the continuous phase, $u_{w/g}$. In the case of two-phase stratified flow, velocity fields in the water/glycerol layer can be complex especially if the interface is wavy. This is exemplified in Figure 6.15 by the instantaneous axial velocity profiles at two different stream wise locations obtained with PIV. The locations shown are in the drop entrainment region, at 0.08 and 0.09 m away from the cylinder (see Figure 6.3).

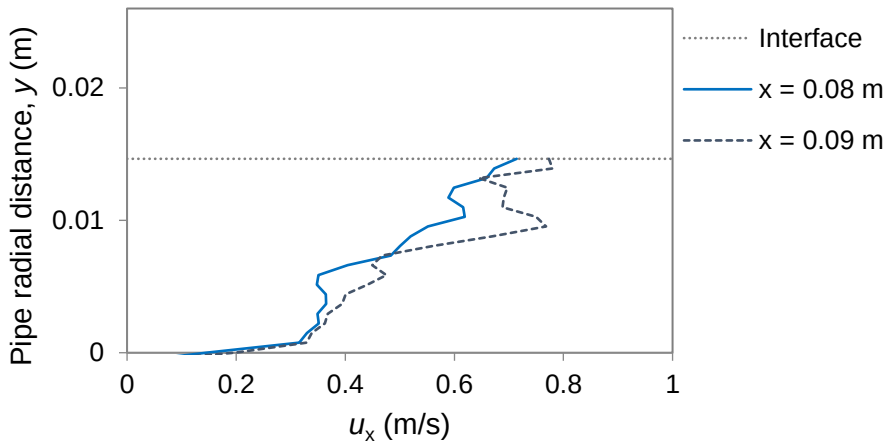

Figure 6.15: Instantaneous axial velocity profile in the water/glycerol phase at two axial locations behind the cylinder.

As can be seen the velocity profile appears to fluctuate at the two axial locations. This explains the fluctuations of F_D during the drop detachment events calculated at various stream wise directions as the wave travels downstream (see Figures 6.13 and 6.14). The axial velocity profiles also appear to be rough which implies unsteadiness as the result of velocity fluctuations. The velocity profile structure shown in Figure 6.15 is in agreement with the work of Ibarra et al. (2018), who recently applied simultaneous PLIF and PIV to investigate the

dynamics of stratified oil-water flows. The authors suggested that the fluctuations of the velocity profiles at various axial locations are linked to the shape of the interface; the profile is not smooth when the interface is wavy, while no significant fluctuations are observed in the case of flat interface. Eq. 6.2 also suggests that the fluid properties can have a significant effect on the drop detachment.

6.4 Conclusion

In this chapter, the results from the experimental studies of drop entrainment in stratified liquid-liquid flows in the presence of the bluff body are presented and discussed. The use of the bluff body localizes the formation of the waves and the detachment of drops in a well-defined area behind the bluff body and makes possible their formation at low velocities. Measurements were carried out with a combination of PIV and PLIF techniques and detailed data on wave characteristics and drop detachment events were obtained. This allows the deformation of interfacial waves to be tracked and the entrainment mechanism to be identified and separated into different stages. The velocity fields in the water/glycerol phase were also acquired during the entrainment events. The information was used in the model development of drop entrainment.

The drop entrainment process was divided into three stages. In the first stage, waves form, while in the second stage, the waves deform within the opposite phase into the shape of a ligament that begins to thin with a swell at its end. In the last stage, the ligament breaks and the swell detaches to form a drop. The ratio of the flowrates of the two phases was found to affect significantly the degree of deformation of the waves. It was proposed that the drop will detach from the deformed wave when the drag force that tends to thin the ligament exceeds the interfacial tension force that resists the deformation. This mechanism was supported by the experimental findings where it was demonstrated that the onset of ligament thinning occurs when the drag force, overcomes the interfacial tension force acting on the ligament that connects the swelling to the wave.

Chapter 7

Dynamics of wave deformation during drop entrainment

In chapter 6, successful visualizations of interfacial wave deformations and entrainment events in stratified flows in a pipe were demonstrated when a bluff body was used close to the inlet. From the findings, a physical mechanism for drop detachment was proposed based on the balance between deforming and resisting forces acting on the interfacial waves. To further analyze the drop entrainment phenomenon, it is important to distinguish the relation between the dynamics of wave deformation during entrainment to the characteristics of the waves from which it deforms from, which are governed by the input flowrates. In this case, the waves are generated immediately after the cylinder, in the wave formation region in Figure 7.1. In this chapter, investigations of the dynamics of wave deformation during entrainment are conducted and its relation with the characteristics of wave generated by the cylinder is identified.

To analyze the dynamics of wave deformation during the drop entrainment process, the properties of the deformed waves were obtained in this chapter. These include the position, size and velocity of the swell at the end of the deformed wave ligament and the length of the deformed waves (ligament length). Measurements were conducted on the deformed waves using the PLIF technique in the drop entrainment region as illustrated in Figure 7.1 (see also Section 6.2.1).

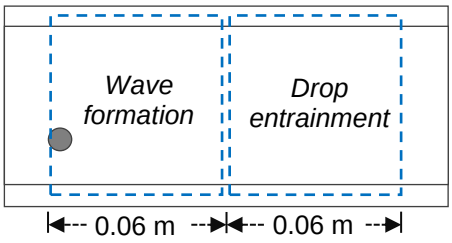

Figure 7.1: Investigation regions for the properties of deformed waves.

In chapter 6, it was observed that waves undergo deformation as it travel through the investigation region. However, there is significant irregularity of the shape of the waves and the location where detachment occurs. Therefore, in order to ensure that the measured properties at various flow conditions are comparable, a criterion for measurement is specified based on the stage of wave deformation. Measurements of the wave properties are conducted at the final stage of the entrainment process where the swell has formed and before drop is detached. In the following sections, it will be demonstrated that the properties remain constant during this period.

The raw gray scale PLIF images are treated prior to measurements. For this purpose, an algorithm is developed in MATLAB to detect the interface and reveal the structure of the deformed wave. The algorithm is also capable of removing any unwanted drops around the waves that could interfere with the measurements. The image treatment process is presented in Figure 7.2. Examples of the raw image and the corresponding extracted interface structure from the PLIF images at various flow conditions are presented in Figure 7.3. In the plots, the y-axis represents the vertical axis (pipe diameter of 26 mm). From the figure, variations of the deformed wave structures at different flow conditions can be observed.

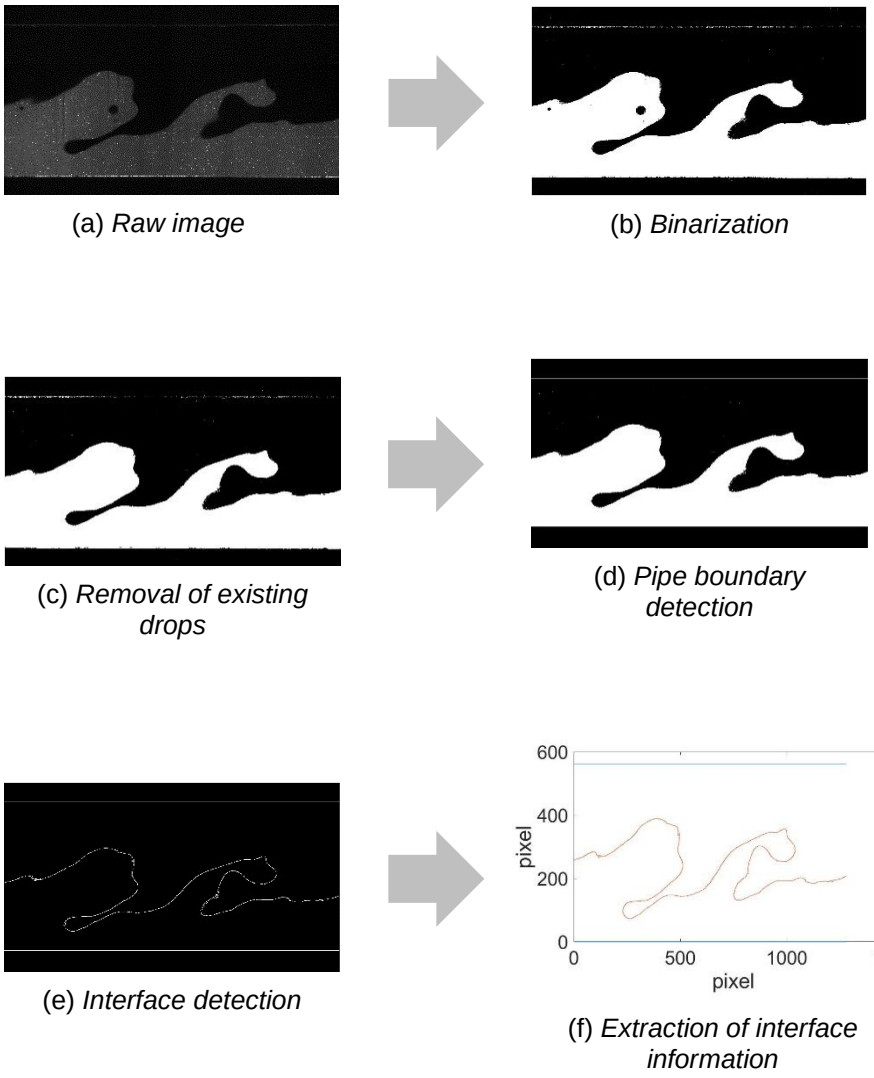

(a) *Raw image*

(b) *Binarization*

(c) *Removal of existing drops*

(d) *Pipe boundary detection*

(e) *Interface detection*

(f) *Extraction of interface information*

(g) *Conversion to pipe*

Figure 7.2: The image processing followed from a raw PLIF image to detect and extract the information of the interface structure.

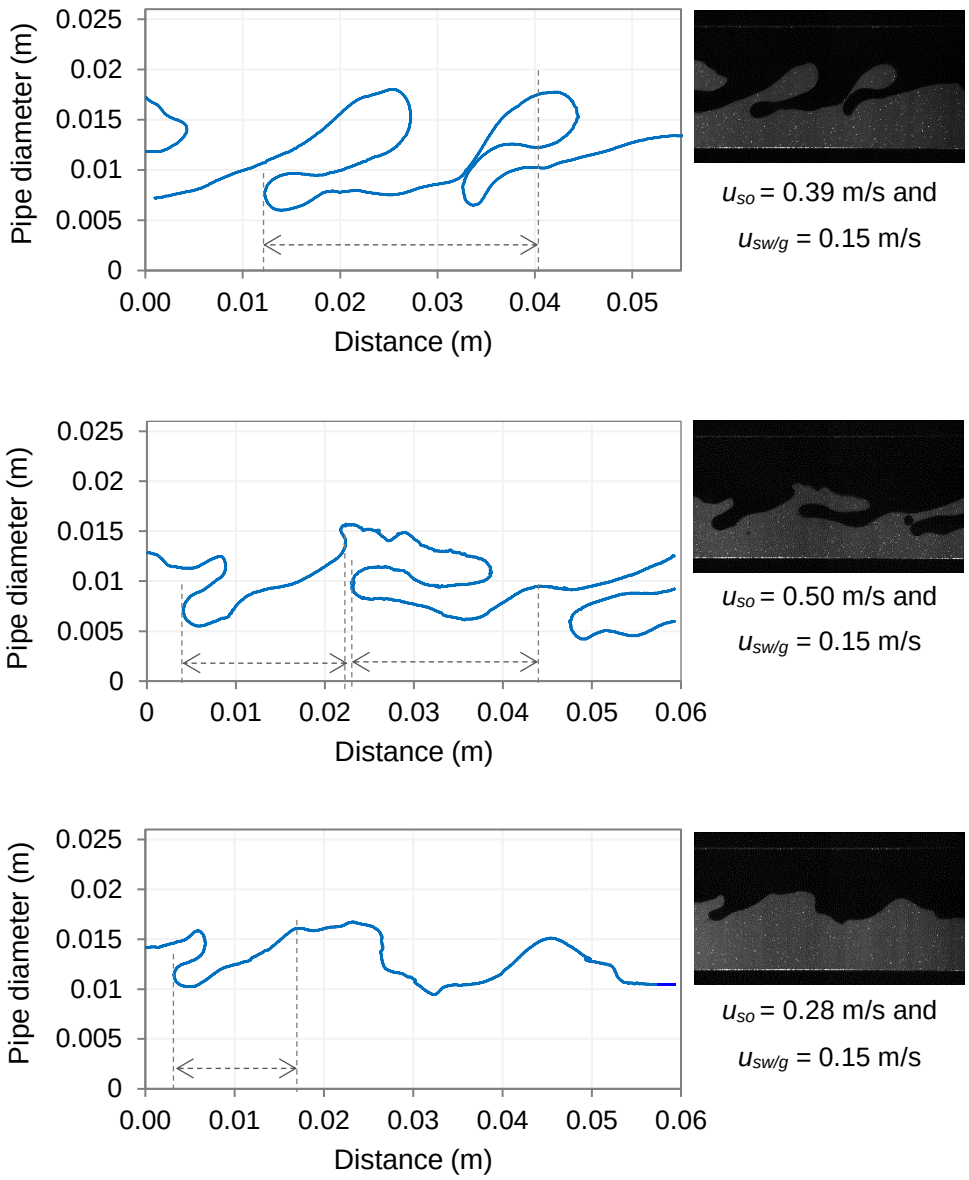

Figure 7.3: Interface structures extracted from their corresponding raw PLIF image.

7.1 Ligament Length

In chapter 6 (Section 6.2.3.2: *Ligament formation stage*), it was found that the length of deformed waves which form ligament, vary depending on the flow conditions. To analyze the phenomenon further, a parameter is introduced to characterize the degree of wave deformation, namely the length of the ligament (deformed wave). For this purpose, measurements of the ligament length were performed from the treated images. The length is taken as the axial distance of the ligament that is submerged into the opposite phase as illustrated in Figure 7.3. The average ligament length, measured at various flow conditions investigated are plotted in Figure 7.4 as function of the input flowrate ratio, *r*.

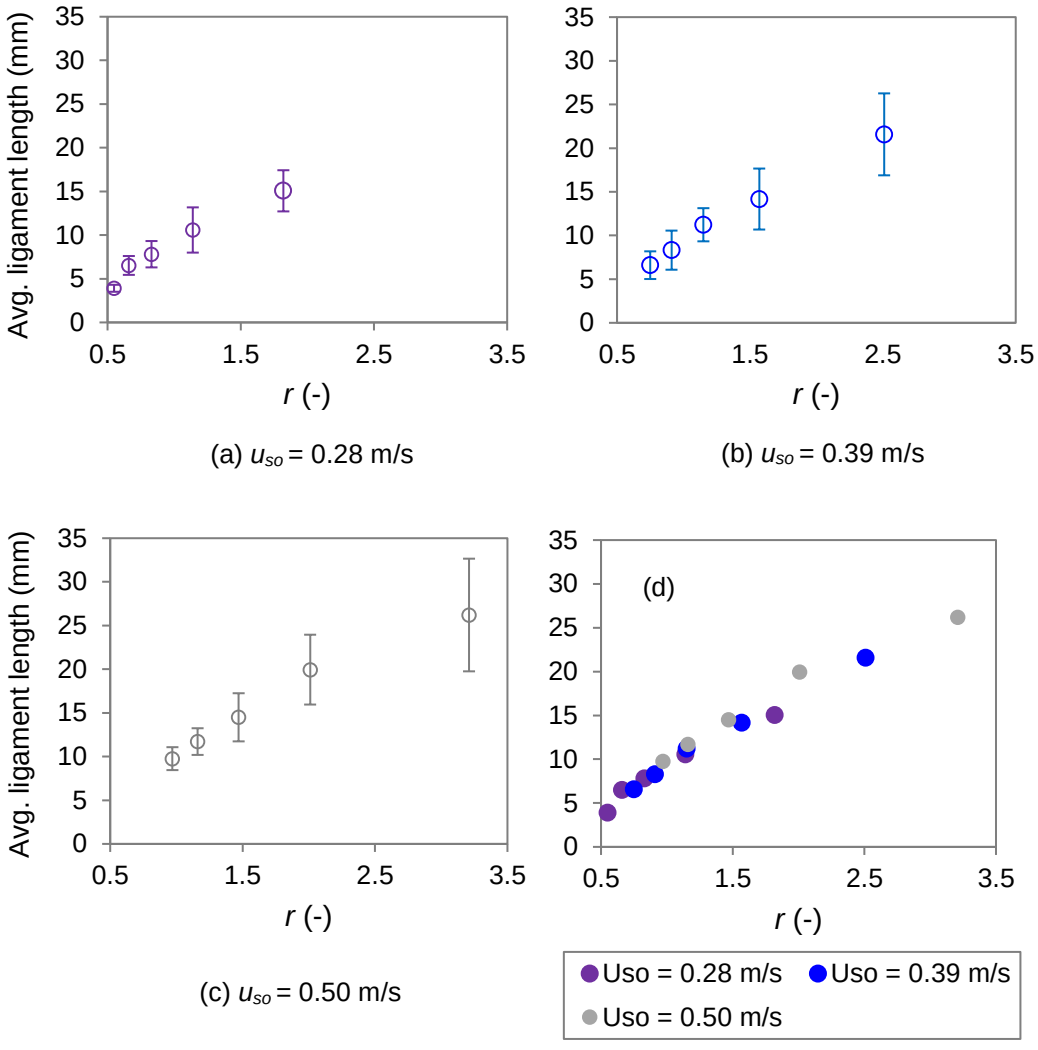

Figure 7.4: Effects of flowrate ratio on ligament length at various flow conditions.

As can be seen in Figure 7.4, average ligament length increases with increasing *r* which implies that higher degree of wave deformation occurs at large oil to water flowrate ratios. The error bars show that higher variations of the length are recorded with increasing *r.* The ligament length indicates how much the wave deforms during detachment. As was discussed in chapter 6 (Figure 6.11) the volume of the wave submerged in the opposite phase is constant, which implies that the degree of deformation is equal to the volume of the submerged wave; this can be presented by the wave amplitude. In Figure 7.5, the average ligament length is plotted as a function of the average wave amplitude, measured in the wave formation region (refer to Figure 7.1). The average ligament length increases with increasing wave amplitude where the increase in amplitude is a result of the increase in the flowrate ratio, *r* as demonstrated in Figure 6.9. This explains the influence of the input flowrate ratio on the degree of wave deformation.

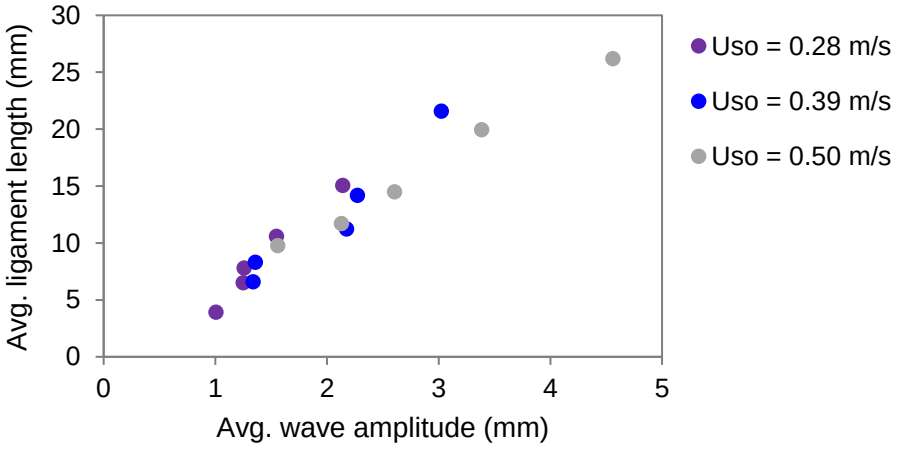

Figure 7.5: Effects of the wave amplitude on the ligament length.

The ligament length is expected to influence the dynamics of deformed wave during drop detachment process. In the following section, the dynamics of the swell forming at the end of the ligament are analyzed, such as the swell height, $h_{swell,}$ swell diameter, D_{swell} and swell velocity, u_{swell}.

7.2 Swell Height

The instantaneous velocity profiles in the water/glycerol phase were shown in Figure 6.15. The profile shows increasing fluid velocity towards the centre of the pipe. According to Eq. 6.3, the velocity of the phase surrounding the swell, $u_{w/g}$, is needed to calculate the drag force on the swell. Therefore, the swell height and its position in the pipe govern the $u_{w/g}$ which then influences the drag force, F_D. In this section, the swell heights are measured at various flow conditions. The swell height, h_{swell}, is determined by measuring the height of the swell top, h_{top} and of the bottom, $h_{bottom,}$ from the pipe bottom. The h_{swell} is then calculated as the height from the pipe bottom to the center of the swell from Eq. 7.1 as illustrated in Figure 7.6.

$$h_{swell} = 0.5 \times \left(h_{top} + h_{bottom}\right) \tag{7.1}$$

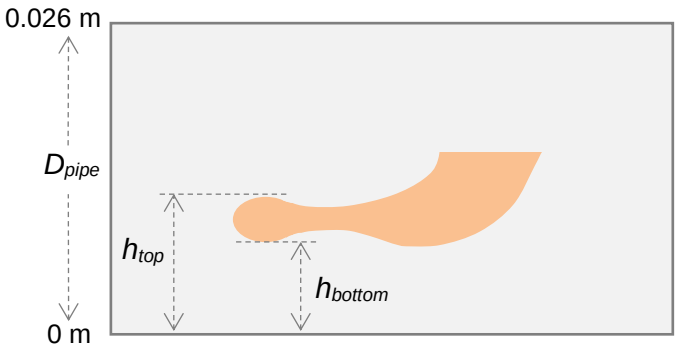

Figure 7.6: Determination of swell height.

During necking and the ligament thinning stage, the position of the swell is observed to be almost constant as it travels along the pipe. An example is presented in Figure 7.7, which shows the measured h_{swell} at various time steps before drop detachment. The average swell heights at various flowrate ratio, r at constant oil superficial velocity, u_{so} are presented in Figure 7.8 with the y-axis represents the pipe diameter and the error bars in the figure serve as the indicator of the variation from mean value.

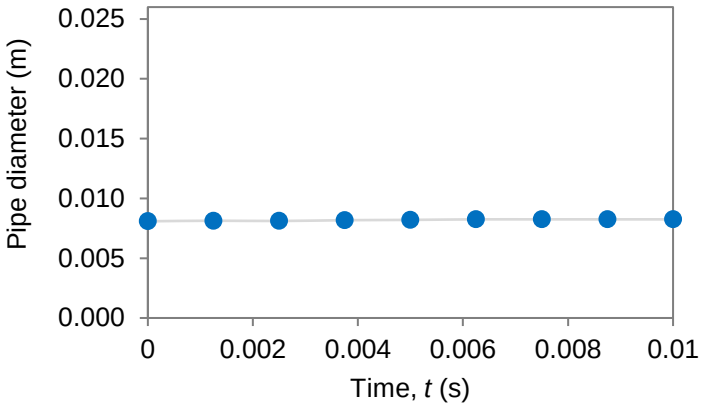

Figure 7.7: Swell position during drop detachment process.

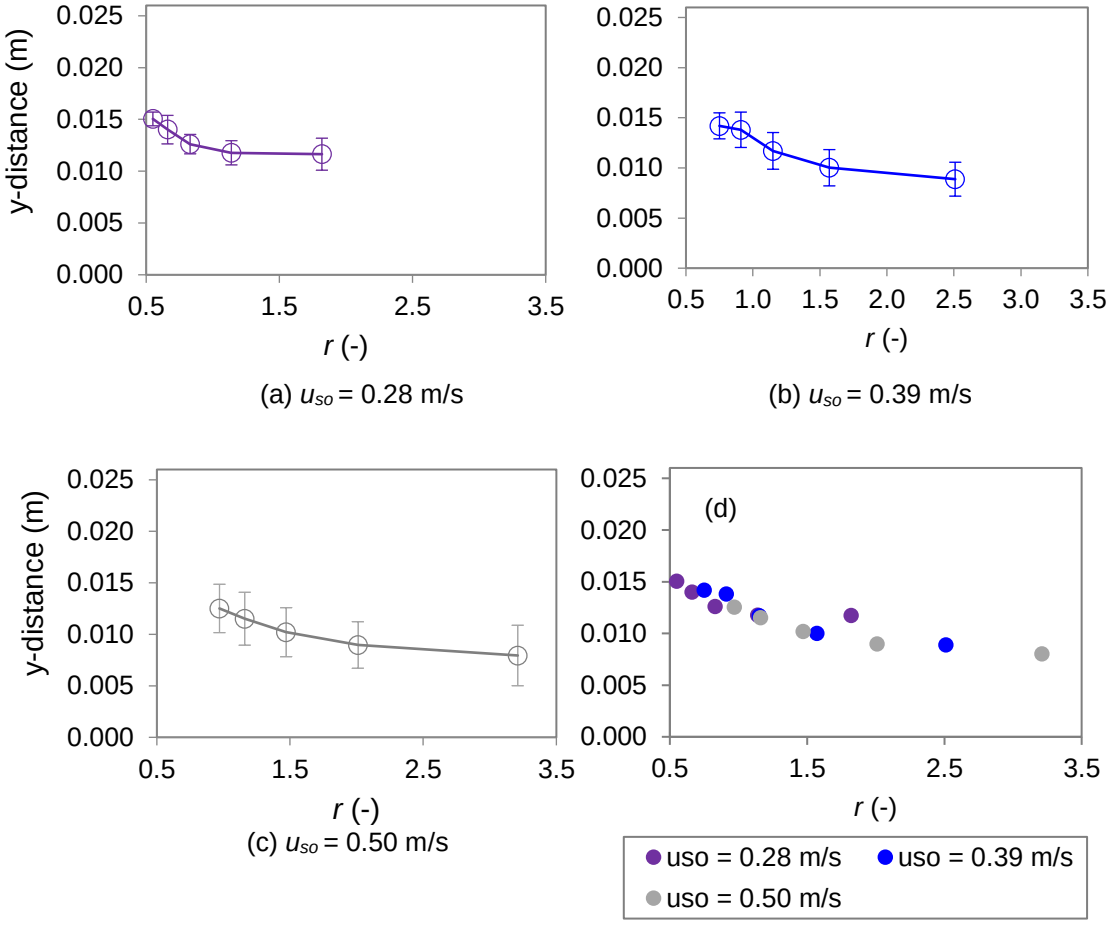

Figure 7.8: Effects of flowrate ratio, r on the swell height at various flow conditions.

For all u_{so} cases, the swell height decreases with increasing r, and drop detachment occurs at the lower part of the pipe. Also, increase in the u_{so} results in larger variations of the swell height as indicated by the error bars, which

suggest possible variation of the detachment location along the y-axis. The behavior can be explained to be attributed to the combination of two factors which are the interface height of the two phases and the amplitude of the generated waves (in the wave formation region in Figure 7.1). Increase in *r* in these cases results to lower average interface height as the pipe is occupied by more oil phase than water/glycerol phase. Consequently, the deformed waves are located at the lower part of the pipe. The influence of the interface height on the detachment position is demonstrated in Figure 7.9(a). From the figure, it can be seen that the position of the swelling height increases with increase in interface height.

The swell height is also influenced by the amplitude of the waves before it deforms into the ligament shape. In chapter 6, (Section 6.2.3 : *Drop entrainment mechanism*), it has been demonstrated in Figure 6.9 that the flow rate ratio, *r* affects the resulting wave amplitude, where increase in *r* leads to generation of waves with larger amplitude. Figure 7.9(b) shows the effects of generated wave amplitude on the swell height. Declines of the swell height can be seen with increase in wave amplitude. The influence of the wave amplitude on the swell height can be further explained from the relation between the wave amplitude and the ligament length as discussed in the previous section. With the increase in ligament length, the deformed waves reach towards the lower part of the pipe.

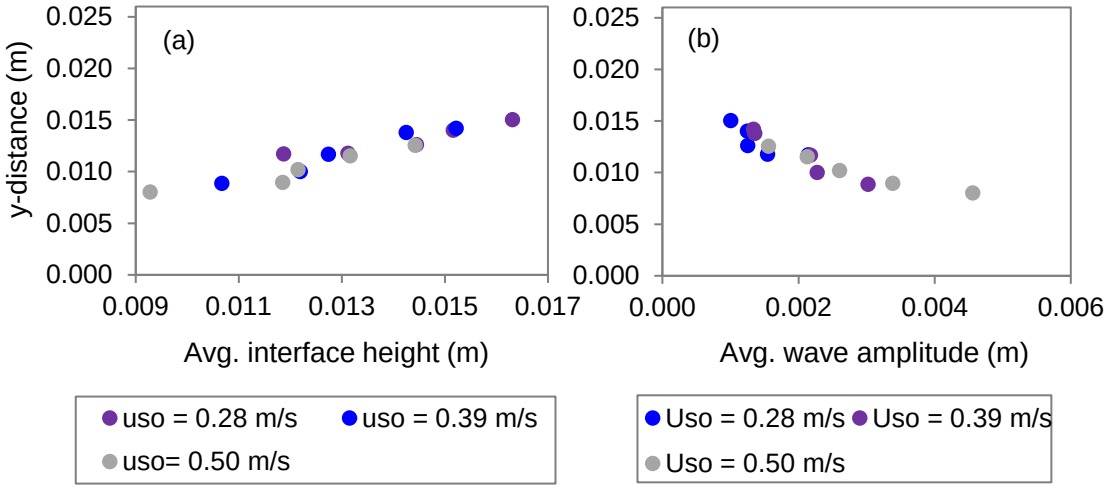

Figure 7.9: Swell heights during detachment. (a) Effects of the interface height (b) Relation with the normalized wave amplitude

7.3 Swell Diameter

The drag force, F_D is calculated from the reference area, A_{eff} of the swell, which is taken as the projected area to the flow direction. To determine the reference area, the swell diameter, D_{swell} is measured as the projected diameter as discussed in chapter 6 (Section 6.3.3: *Calculation of drag force and interfacial tension force*). It was shown that the D_{swell} remains constant during the ligament thinning stage (see Figure 6.11).

The average swell diameters at various flowrate ratios, r at constant oil superficial velocity, u_{so} are presented in Figure 7.10. For all u_{so} cases investigated, the average D_{swell} is observed to increase with increasing r. The influence of r on D_{swell} is attributed to the generation of larger amplitude waves with increasing r. The relation between the swell diameter and the wave amplitude can be seen in Figure 7.11. For all cases investigated, an increase in the wave amplitude results to an increase of the average D_{swell}. Waves with higher amplitude indicate that more volume of one phase is submerged into the opposite phase. This results to higher degree of wave deformation that leads to formation of the swell.

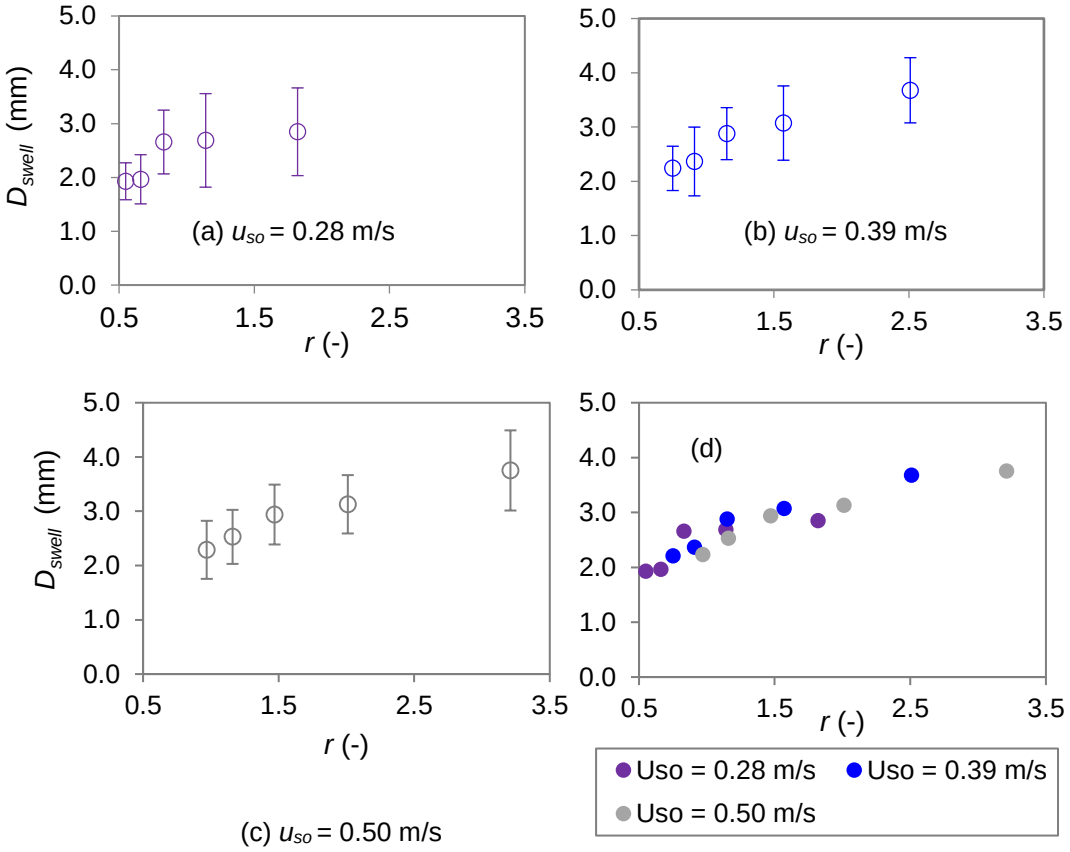

Figure 7.10: Effects of flowrate ratio on swell diameter at various flow conditions.

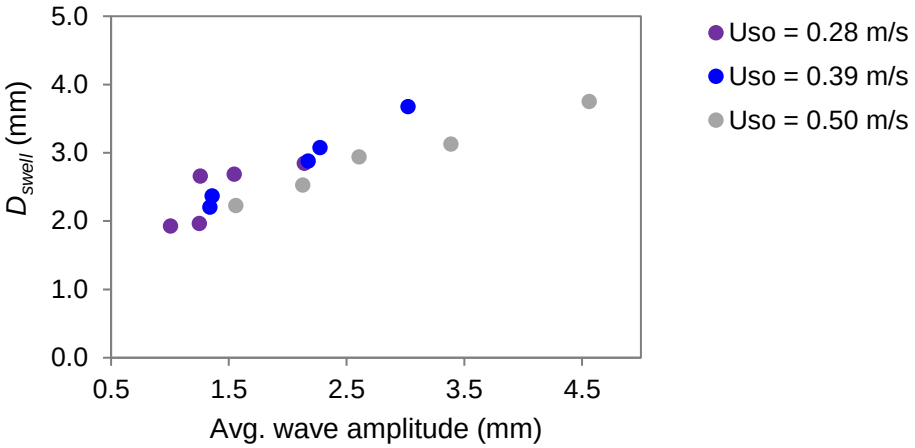

Figure 7.11: Average swell diameter at various average wave amplitude.

7.4 Swell velocity

The swell velocity, u_{swell} during drop detachment is calculated following the procedure described in chapter 6 (Section 6.3.3.3: Swell velocity), at various flow conditions. The swell velocity was found to be almost constant during the detachment process. The average swell velocities at various flowrate ratios, r at constant oil superficial velocity, u_{so} are presented in Figure 7.12.

From Figure 7.12, the average u_{swell} are observed to decrease with increasing r. Increase in r at constant u_{so} as shown in Figure 7.12 results from a decrease in the water/glycerol superficial velocity, $u_{sw/g}$. In Figure 7.12(d), the direct influence of u_{so} on the average u_{swell} can be observed where drop travels at higher velocities at high u_{so}, which is the phase layer where the drops are attached to. To visualize the influence of $u_{sw/g}$, the average u_{swell} are plotted againts $u_{sw/g}$ in Figure 7.13. From the figure, the average u_{swell} are observed to increase with increasing $u_{sw/g}$. It can also be seen that the influence of u_{so} is more significant on the u_{swell} at high $u_{sw/g}$.

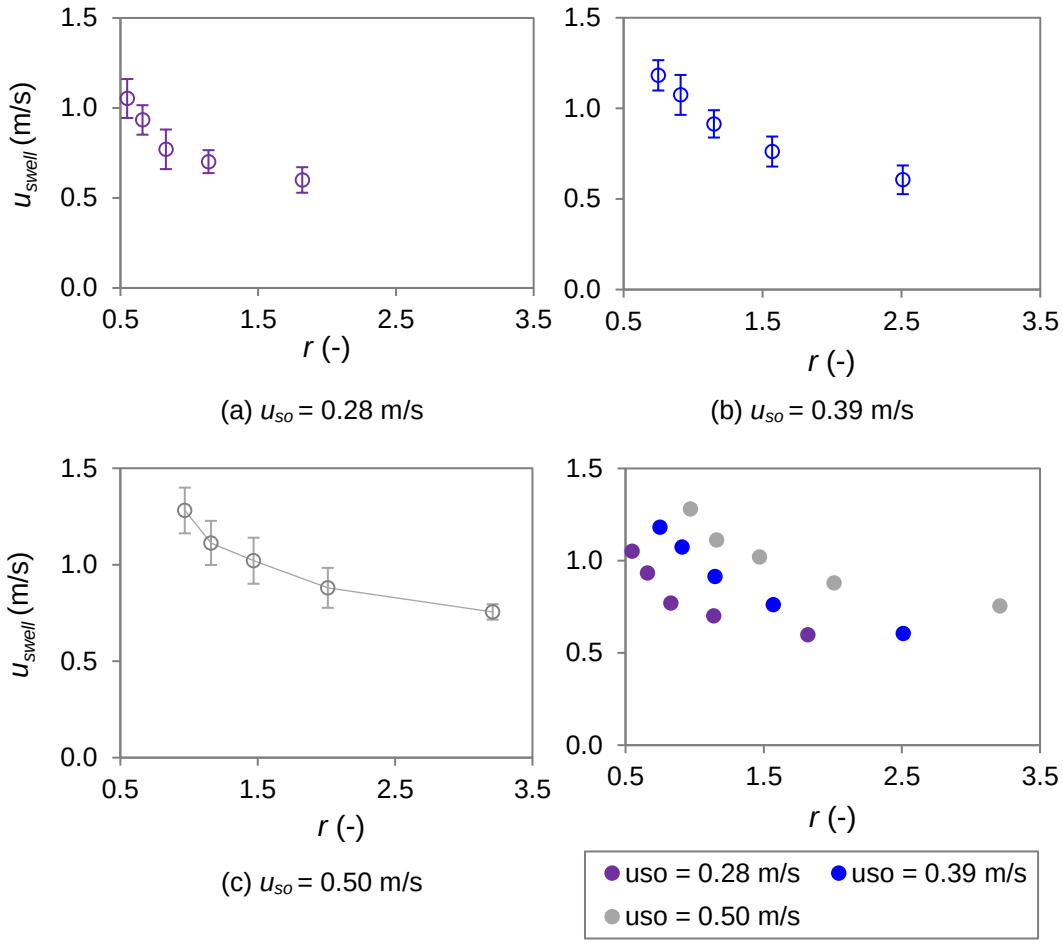

Figure 7.12: Effects of flowrate ratio on swell velocity at various flow conditions.

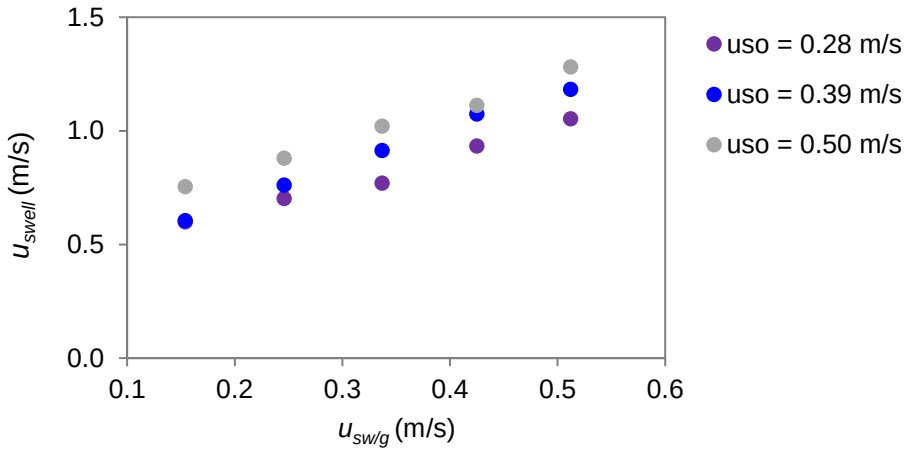

Figure 7.13: Effects of superficial water/glycerol phase velocity on the swell velocity.

7.5 Summary

In this chapter, the dynamics of the wave deformation have been further investigated and parameters such as ligament length, swell height, h_{swell}, swell diameter, D_{swell} and swell velocity, u_{swell} were measured. These parameters are used in the calculation of the drag and interfacial tension forces, in the model developed in chapter 6. In addition, the relation between the dynamics of wave deformation and the input flowrate ratio of the two phases, r, was also discussed.

As discussed in chapter 6, the degree of the deformation and ligament length were to vary with r. Long ligaments were observed for the flow conditions that correspond to high value of r while shorter ligaments were seen at low r. From the analysis, the ligament length was found to be related to the amplitude of the wave from which it deforms; waves with large amplitude deform into long ligaments. Large wave amplitudes have been associated to increased instability in stratified flows that leads to drop detachment and transition to dispersed flows (Al-Wahaibi and Angeli, 2007; Al-Wahaibi and Angeli, 2011; Castro et al., 2012). From the findings of this investigation, the wave deformation that leads to drop detachment has been linked to wave amplitude.

Analysis of the $h_{swell,}$ D_{swell} and u_{swell} at which the properties were obtained just before drop is detached shows their link to the ligament length. Increase in ligament length were found to leads to higher variation of deformed wave dynamics, where higher range of h_{swell}, D_{swell} and u_{swell} were observed. As the ligament length is governed by the amplitude of the waves (from which it deforms), this signifies the relationship between the investigated deformed wave dynamics to the input flowrate ratio, r.

Chapter 8

Conclusion

In this chapter, the main findings of this works are summarized and the conclusion from each chapters are drawn. Recommendations for future works are proposed.

8.1 Conclusions

This thesis investigates the flow patterns transition process from stratified to dispersed patterns for immiscible liquid-liquid flows in horizontal pipes. The formation of interfacial waves in stratified flows was identified to be the key factor for transition to non-stratified flows and to drop detachment. Therefore, to facilitate the study of this particular flow pattern transition, a novel approach was introduced in which a cylindrical bluff body, located at a transverse position to the flow direction, was used to induce formation of unstable interfacial waves immediately behind the cylinder that lead to generation of drops. The cylinder diameters used in this work were designed numerically. A commercial CFD code, FLUENT was used to simulate two-dimensional single-phase flows across cylinders of various diameters. The numerical setup used in this work was able to reproduce the flow in the wake of the cylinder, which supports the validity of the Standard k-ε (SKE) turbulence model for the simulations. The findings also supported that at the middle of the pipe, the flows are two-dimensional. This was demonstrated from the consistency between the velocity profiles in the region behind the cylinder between the simulation and experimental data of Chinaud et al. (2017) in a pipe and also the agreement between the Strouhal number obtained from simulations and experimental data of this work.

The flow across bluff body has a great potential to be implemented in numerous industrial applications to control various flow properties such as flow patterns in petroleum industry for flow assurance and in chemical industry to enhance mixing between two liquids for improvement of mass or heat transfer rates. The interface dynamics of immiscible liquid-liquid flows in the wake of a

bluff body are influenced by the vortex shedding and therefore can be controlled by the modification of vortex shedding properties through different bluff body designs. The increase in vortex shedding frequencies achieved with the use of cylinders of different diameters (2 and 8 mm) in this work matched the frequency of the resulting interfacial waves generated behind the cylinder.

The instability of stratified two-phase flows that is associated with high amplitude interfacial waves can be amplified through the increase of interface distortion and was achieved in this work through the increase in cylinder diameter. Increase in cylinder diameter results to formation of larger vorticity region in its wake and interactions between the vortices and the interface leads to generation of interfacial waves with larger amplitude. The greater instability with increasing cylinder diameters shifts the transition boundaries towards lower mixture velocities.

From the successful visualization of drop entrainment events, it can be concluded that drop entrainment in stratified flows specifically near the transition boundary occurs through detachment of drops from interfacial waves. From the experimental images obtained with advanced laser based techniques, a mechanism of drop entrainment in stratified flows was proposed. Waves deform to a ligament shape with a swell on its end and the neck connecting the swell to the wave decreases in thickness until a drop is detached.

Based on the findings of the force balance analysis, drop detachment occurs when the deforming force acting on the swell overcomes the resisting force on the neck. Drag force, F_D and interfacial tension force, F_σ were identified as the dominant deforming and resisting forces respectively and were formulated based on the experimental observations of this work. Tracking both forces during the drop detachment events from local instantaneous data showed that ligament thinning occurs when F_σ exceeds F_D, which supports the proposed model.

Further understanding of the transition from stratified to dispersed flows which is commonly reported to be linked with increase in wave amplitude was also obtained in this work. Analysis of the dynamics of deformed waves that lead to drop detachment events revealed that the deformed waves are related to the input oil to water flowrate ratio, *r*, through the wave amplitude. Increase in the flowrate ratio leads to an increase in the wave amplitude (which in this work was due to the reduction of submergence depth of the cylinder as *r* increased) and this results to formation of longer ligaments (deformed waves). Consequently,

this lead to larger variation of the swell position and larger swell diameter, which then influence the criterion (forces) for drop detachment.

8.2 Recommendations

From this studies, several recommendations for improvements and future work are proposed;

- Designing a bluff body with adjustable height

  The cylinder in this study was designed at a fixed position in the pipe (cylinder center located at $1/4D_p$ from pipe bottom). As a result, the cylinder submergence depth, h_s and the flowrate ratio, r of the two phases could not be varied independently. Therefore, for studies in which the effects of these two parameters have to be studied independently, bluff bodies with adjustable height can be designed.

- Variation of the bluff body shape and number

  In these studies, the shape of the bluff body was limited to a circular cylinder for simplification as an initial approach. From the findings, it was observed that the variations of the wake characteristics of the cylinder wake (which in this case was achieved by changing the cylinder diameter) were reflected on the liquid-liquid interfacial wave structure. This suggests that control of the interface dynamics can be achieved through change of the bluff body design. Therefore, to further vary the vortex shedding in the wake of the bluff body, depending on the application, various shapes of the bluff body can be designed.

- Extending the applications of bluff body approach in liquid-liquid flows

  In this work, from flow assurance point of view, the bluff body approach was applied for the investigation of the flow pattern transitions. Increase in the cylinder diameter was observed to produce wakes with larger vorticity region while smaller cylinders generated higher vortex shedding frequency at lower inlet velocity. Thus, the bluff body approach can be extended for various applications in liquid-liquid flows such as to enhance mixing or mass transfer between two fluids.

- Simulation of two-phase flows

  Simulations of two-phase flows can be conducted in future works to elucidate in detail the relation between the vortices shed by the cylinder and the evolution of the interface in its wake. For this purpose, three-dimensional simulations are required. It is also suggested to use that large eddy simulation (LES) instead of URANS (which were demonstrated to be sufficient for two-dimensional case in this work) as it were reported in the literature that LES is more accurate for 3D simulations. To reduce the computational cost, adaptive meshing can also be implemented.

Bibliography

Al-Wahaibi, T., and P. Angeli. 2007. Transition between stratified and non-stratified horizontal oil-water flows. Part I: Stability analysis. *Chemical Engineering Science* 62 (11): 2915–2928.

Al-Wahaibi, T., and P. Angeli. 2011. Experimental study on interfacial waves in stratified horizontal oil-water flow. *International Journal of Multiphase Flow* 37 (8): 930–940.

Al-Wahaibi, T., Smith, M., and P. Angeli. 2007. Transition between stratified and non-stratified horizontal oil – water flows. Part II : Mechanism of drop formation. *Chemical Engineering Science* 62 (11): 2929–2940.

Alekseenko, S. V., Cherdantsev, A. V., and D. M. Markovich. 2014. Investigation of droplets entrainment and deposition in annular flow using LIF technique. *Atomization and Sprays* 24 (3): 193–222.

Angeli, P., and G. F. Hewitt. 2000. Flow structure in horizontal oil-water flow. *International Journal of Multiphase Flow* 26 (7): 1117–1140.

Angrili, F. F., Bergamaschi, S. S., and V. V. Cossalter. 1982. Investigation of wall induced modifications to vortex shedding from a circular cylinder. *Journal of Fluids Engineering* 104 (4): 518–522.

Anna, S. L., Bontoux, N., and H. A. Stone. 2003. Formation of dispersions using “flow focusing” in microchannels. *Applied Physics Letters* 82: 364 – 366.

Bai, H., and J. Li. 2011. Numerical simulation of flow over a circular cylinder at low Reynolds number. *Advanced Materials Research* 225–260: 942–946.

Barral, A. H., and P. Angeli. 2013. Interfacial characteristics of stratified liquid–liquid flows using a conductance probe. *Experiments in Fluids* 54 (10): 1604.

Barral, A. H., Ebenezer, A., and P. Angeli. 2015. Investigations of interfacial waves at the inlet section in stratified oil–water flows. *Experimental Thermal and Fluid Science* (60): 115–122.

Bearman, P. W., and M. M. Zdravkovich. 1978. Flow around a circular cylinder near a plane boundary. *Journal of Fluid Mechanics* 89: 33–47.

Bentley, J. P., and J. W. Mudd. 2003. Vortex shedding mechanisms in single and dual bluff bodies. *Flow Measurement and Instrumentation* 14: 23–31.

Beretta, A., Ferrari, P., Galbiati, L., and P. A. Andreni. 1997. Horizontal oil-water flow in small diameter tubes. Flow patterns. *International Communications in Heat and Mass Transfer* 24 (2): 223–229.

Berna, C., Escrivá, A., Muñoz-cobo, J. L., and L. E. Herranz. 2014. Progress in nuclear energy review of droplet entrainment in annular flow: Interfacial waves and onset of entrainment. *Progress in Nuclear Energy* 74: 14–43.

Blackburn, H. M. 1994. Effect of blockage on spanwise correlation in a circular cylinder wake. *Experiments in Fluids* 18: 134–136.

Bozkaya, C., and S. Kocabiyik. 2014. Free surface wave interaction with an oscillating cylinder. *Applied Mathematics Letters* 27: 79–84.

Bozzano, G., and M. Dente. 2001. Shape and terminal velocity of single bubble motion: A novel approach. *Computer and Chemical Engineering* 25 (4-6): 571–576.

Brauner, N. 2002. Modelling and control of two-phase phenomena: liquid–liquid two-phase flow systems. School of Engineering Tel Aviv University, Tel Aviv.

Breuer, M. 1998. Large eddy simulation of the sub-critical flow past a circular cylinder : Numerical and modeling aspects. *International Journal for Numerical Methods in Fluids* 28, 1281–1302.

Bruno, L., Fransos, D., Coste, N., and A. Bosco. 2010. 3D flow around a rectangular cylinder : A computational study. *Journal of Wind Engineering & Industrial Aerodynamics* 98(6–7), 263–276.

Buresti, G., & Lanciotti, A. 1979. Vortex shedding from smooth and roughened cylinders in cross-flow near a plane surface. Aeronautical Quarterly, 30(1), 305-321.

Buzzard, J. L., and R. M. Nedderman. 1967. The drag coefficients of liquid droplets accelerating through air. *Chemical Engineering Science* 22(12), 1577–1586.

Carmo, B. S. 2009. On wake interference in the flow around two circular cylinders : Direct stability analysis and flow-induced vibrations. (Ph.D. thesis), Imperial College London.

Catalano, P., Wang, M., Iaccarino, G., and P. Moin. 2003. Numerical simulation of the flow around a circular cylinder at high Reynolds numbers. *International Journal of Heat and Fluid Flow* 24(4), 463–469.

Chakraborty, J., Verma, N., and R. P. Chhabra. 2004. Wall effects in flow past a circular cylinder in a plane channel : A numerical study. *Chemical Engineering and Processing: Process Intensification* 43(12), 1529–1537.

Chen, B., Lu, L., Greated, C. A., and H. Kang. 2015. Investigation of wave forces on partially submerged horizontal cylinders by numerical simulation. *Ocean Engineering* 107, 23–31.

Chinaud, M., Roumpea, E., and P. Angeli. 2015. Studies of plug formation in microchannel liquid – liquid flows using advanced particle image velocimetry techniques. *Experimental Thermal and Fluid Science* 69, 99–110.

De Castro, M. S., Pereira, C. C., Dos Santos, J. N., and O. M. H. Rodriguez. 2012. Geometrical and kinematic properties of interfacial waves in stratified oil-water flow in inclined pipe. *Experimental Thermal and Fluid Science* 37, 171–178.

Dipankar, A., and T. K. Sengupta. 2005. Flow past a circular cylinder in the vicinity of a plane wall. *Journal of Fluids and Structures* 20, 403–423.

Drumm, C., and M. W. Hlawitschka. 2011. CFD Simulations and particle image velocimetry measurements in an industrial scale rotating disc contactor. Fluid Mechanics and Transport Phenomena 57(1), 10 - 26.

Edomwonyi-Otu, L. C., and P. Angeli. 2015. Pressure drop and holdup predictions in horizontal oil-water flows for curved and wavy interfaces. *Chemical Engineering Research and Design*, 93, 55 - 65.

Garstecki, P., Fuerstman, M. J., Stone, A., and G. M. Whitesides. 2006. Formation of droplets and bubbles in a microfluidic T-junction - scaling and mechanism of break-up. Lab Chip 6, 437 – 446.

Glawdel, T., Elbuken, C., and C. L. Ren. 2012. Droplet formation in microfluidic T-junction generators operating in the transitional regime. I. Experimental observations. *Physical Review E* 85, 016322, 1–9.

Graftieaux, L., Michard, M., and N. Grosjean. 2001. Combining PIV, POD and vortex identification algorithms for the study of unsteady turbulent swirling flows. *Measurements Science and Technology* 12, 1422–1429.

Guzhov, A. I., Grishan, A. L., Medredev, V. F., and O. P. Medredeva. 1973. Emulsion formation during the flow of two immiscible liquids in a pipe. *Neftianoe Khoziastvo Oil Industry*, 8, 58–61.

Hanafizadeh, P., Hojati, A., and A. Karimi. 2015. Experimental investigation of oil-water two phase flow regime in an inclined pipe. *Journal of Petroleum Science and Engineering* 136, 12–22.

Hewitt, G. F., and N. S. Hall-Taylor. 1970. Annular Two-Phase Flow. Pergamon Press.

Holowach, M. J., Hochreiter, L. E., and F. B. Cheung. 2002. A model for droplet entrainment in heated annular flow. *International Journal of Heat and Fluid Flow* 23(6), 807–822.

Huang, Z., Olson, J. A., Kerekes, R. J., and S. I. Green. 2006. Numerical simulation of the flow around rows of cylinders. *Computers and Fluids* 35, 485–491.

Husny, J., and J. J. Cooper-White. 2006. The effect of elasticity on drop creation in T-shaped microchannels. *Journal of Non-Newtonian Fluid Mechanics* 137(1–3), 121–136.

Iaccarino, G. 2001. Predictions of a Turbulent separated flow using commercial CFD codes. *Journal of Fluids Engineering* 123, 819–828.

Ibarra, R., Zadrazil, I., Matar, O. K., and C. N. Markides. 2018. Dynamics of liquid-liquid flows in horizontal pipes using simultaneous two-line planar laser-induced fluorescence and particle velocimetry. *International Journal of Multiphase Flow* 101, 47–63.

Ishii, M., and M. A. Grolmes. 1975. Inception criteria for droplet entrainment in two-phase concurrent film flow. AIChE Journal 21(2), 308 – 318.

Kalro, V., and T. Tezduyar. 1997. Parallel 3d computation of unsteady flows around circular cylinders. *Parallel Computing* 23, 1235–1248.

Kang, S. Ã. 2006. Uniform-shear flow over a circular cylinder at low Reynolds numbers. *Journal of Fluids and Structures* 22, 541–555.

Kataoka, I., Ishii, M., and K. Mishima. 1983. Generation and size distribution of droplet in annular two-phase flow. *Journal of Fluids Engineering* 105(2), 230–238.

Kelbaliyev, G. I. 2011. Drag Coefficients of variously shaped solid particles, drops, and bubbles. *Theoretical Foundations of Chemical Engineering* 45(3), 248–266.

Kumagai, I., Murai, Y., and Y. Tasaka. 2011. Science and bubble generation by a cylinder moving beneath a free surface. *Journal of Fluid Science and Technology* 6(6), 851–859.

Launder, B. E., and D. B. Spalding. 1972. Mathematical Models of Turbulence. Academic Press, New York.

Lecoeur, N., Hale, C. P., Spelt, P. D. M., and G. F. Hewitt. 2010. Visualization of droplet entrainment in turbulent stratified pipe flow. In: Proc. of 7th International Conference of Multiphase Flow, paper ICMF7th 2010 1-6.

Lei, C., Cheng, L., and K. Kavanagh. 1999. Re-examination of the effect of a plane boundary on force and vortex shedding of a circular cylinder. *Journal of Wind Engineering and Industrial Aerodynamics* 80(3), 263–286.

Lei, C., Cheng, L., and K. Kavanagh. 2000. A finite difference solution of the shear flow over a circular cylinder. *Ocean Engineering* 27(3), 271–290.

Liang, H., Zong, Z., Zou, L., Zhou, L., and L. Sun. 2014. Vortex shedding from a two-dimensional cylinder beneath a rigid wall and a free surface according to the discrete vortex method. *European Journal of Mechanics B/Fluids* 43, 110–119.

Lin, M. Y., and L. H. Huang. 2010. Free-surface flow past a submerged cylinder. *Journal of Hydrodynamics* 22(5), 209–214.

Loizou, K., Wong, V.-L., and B. Hewakandamby. 2018. Examining the effect of flow rate ratio on droplet generation and regime transition in a microfluidic T-junction at constant capillary numbers. *Inventions* 3(54),

Lovick, J., and P. Angeli, P. 2004. Droplet size and velocity profiles in liquid-liquid horizontal flows. *Chemical Engineering Science* 59(15), 3105–3115.

Mazumder, Q. H. 2012. CFD Analysis of single and multiphase flow characteristics in elbow. *Engineering* 4, 210–214.

Miyata, H. 1990. Forces on a circular cylinder advancing steadily beneath the free-surface. *Ocean Engineering* 17(1), 81–104.

Murakami, S., and A. Mochida. 1995. On turbulent vortex shedding flow past 2D square cylinder predicted by CFD. *Journal of Wind Engineering and Industrial Aerodynamics* 55, 191–211.

Nadler, M., and D. Mewes. 1997. Flow induced emulsification in the flow of two immiscible liquids in horizontal pipes. *International Journal of Multiphase Flow* 23(1), 55–68.

Ong, M. C., Kamath, A., Bihs, H., and M. S. Afzal. 2017. Numerical simulation of free-surface waves past two semi- submerged horizontal circular cylinders in tandem. *Marine Structures* 52, 1–14.

Park, K. H., Chinaud, M., and P. Angeli. 2016. Transition from stratified to non-stratified oil – water flows using a bluff body. *Experimental Thermal and Fluid Science* 76, 175–184.

Patil, P. P., and S. Tiwari. 2008. Effect of blockage ratio on wake transition for flow past square cylinder. *Fluid Dynamics Research* 40, 753–778.

Price, S. J., Sumner, D., Smith, J. G., Leong, K., and M. P. Païdoussis. 2002. Flow visualization around a circular cylinder near to a plane wall. *Journal of Fluids and Structures* 16(2), 175–191.

Rahman, M., Karim, M., A. Alim. 2007. Numerical investigation of unsteady flow past a circular cylinder using 2-D finite volume method. *Journal of Naval Architecture and Marine Engineering* 4(1), 27 – 42.

Rehimi, F., Aloui, F., Nasrallah, S. Ben, Doubliez, L., and J. Legrand. 2008. Experimental investigation of a confined flow downstream of a circular cylinder centered between two parallel walls. *Journal of Fluids and Structures* 24(6), 855–882.

Reichl, P., Hourigan, K., and M. C. Thompson. 2005. Flow past a cylinder close to a free surface. *Journal of Fluid Mechanics* 533, 269–296.

Renfer, A., Tiwari, M. K., Meyer, F., Brunschwiler, T., Michel, B., and D. Poulikakos. 2013. Vortex shedding from confined micropin arrays. Microfluidics and Nanofluidics 15(2), 231–242.

Rocchi, D., and A. Zasso. 2002. Vortex shedding from a circular cylinder in a smooth and wired configuration : Comparison between 3D LES simulation and experimental analysis. Journal of Wind Engineering and Industrial Aerodynamics 90(4-5), 475–489.

Rodriguez, O. M. H., and L. S. Baldani. 2012. Prediction of pressure gradient and holdup in wavy stratified liquid-liquid inclined pipe flow. *Journal of Petroleum Science and Engineering* 96–97, 140–151.

Roshko, A. 1961. Experiments on the flow past a circular cylinder at very high Reynolds number. *Journal of Fluid Mechanics* 10 (3), 345–356.

Rouhani, S. Z., and M. S. Sohal. 1983. Two-phase flow patterns: A review of research results. *Progress in Nuclear Energy*, 11(3), 219–259.

Roumpea, E., Kovalchuk, N. M., Chinaud, M., Nowak, E., Simmons, M. J. H., and P. Angeli. 2019. Experimental studies on droplet formation in a flow-focusing microchannel in the presence of surfactants. *Chemical Engineering Science* 195, 507–518.

Salim, S. M., Ong, K. C., and S. C. Cheah. 2011. Comparison of RANS, URANS and LES in the prediction of airflow and pollutant dispersion. In: Proc. of The World Congress on Engineering and Computer Science, WCECS 2011, 673 – 678.

Scheele, G. F., and B. J. Meister. 1968. Drop formation at low velocities in liquid-liquid systems: Part I. Prediction of drop volume. *AIChE Journal* 14(1), 9–15.

Schewe, G. 1983. On the force fluctuations acting on a circular cylinder in crossflow from subcritical up to transcritical Reynolds numbers. *Journal of Fluid Mechanics* 133, 265–285.

Shao, J., and C. Zhang. 2006. Numerical analysis of the flow around a circular cylinder using RANS and LES RANS and LES. *International Journal of Computational Fluid Dynamics* 20(5), 301–307.

Sheridan, J., Lin, J.C., and D. Rockwell. 1997. Flow past a cylinder close to a free surface. *Journal of Fluid Mechanics* 330, 1–30.

Shi, H., Cai, J., and W. P. Jepson. 2001. Oil-water two-phase flows in large-diameter pipelines. *Journal of Energy Resources Technology* 123, 270–276.

Shi, J., and H. Yeung. 2017. Characterization of liquid-liquid flows in horizontal pipes. *AIChE Journal* 63(3), 1132–1143.

Singha, S., and K. P. Sinhamahapatra. 2010. Flow past a circular cylinder between parallel walls at low Reynolds numbers. *Ocean Engineering* 37(8–9), 757–769.

Taniguchi, S., and K. Miyakoshi. 1990. Fluctuating fluid forces acting on a circular cylinder and interference with a plane wall. *Experiments in Fluids* 204, 197–204.

Timgren, A., Trägårdh, G., and C. Trägårdh. 2008. Application of the PIV technique to measurements around and inside a forming drop in a liquid-liquid system. *Experiments in Fluids* 44(4), 565–575.

Torres, C. F., Mohan, R. S., and L. E. Gomez. 2016. Oil – water flow pattern transition prediction in horizontal pipes. Oil – water flow pattern transition prediction in horizontal pipes, Journal of Energy Resources Technology 138(2), 022904-022904-11.

Trallero, J. L., Sarica, C., and J. P. Brill. 1997. A study of oil-water flow patterns in horizontal pipes. *Society of Petroleum Engineers*, 165–172.

Voulgaropoulos, V., and P. Angeli. 2017. Optical measurements in evolving dispersed pipe flows. *Experiments in Fluids* 58(12), 1–15.

Wang, X. K., and S. K. Tan. 2008. Comparison of flow patterns in the near wake of a circular cylinder and a square cylinder placed near a plane wall. *Ocean Engineering* 35(5–6), 458–472.

Williamson, C. H. K. 1996. Vortex dynamics in the cylinder wake. *Annual Review in Fluid Mechanics* 28, 477–539.

Zdravkovich, M. M. 1985. Flow induced oscillations of two interfering circular cylinders. *Journal of Sound and Vibration* 101(4), 511–521.

Zhai, L., Jin, N., Zong, Y., Hao, Q., and Z. Gao. 2015. Experimental flow pattern map, slippage and time – frequency representation of oil – water two-phase flow in horizontal small diameter pipes. *International Journal of Multiphase Flows* 76, 168–186.

Zovatto, L., and G. Pedrizzetti. 2001. Flow about a circular cylinder between parallel walls. *Journal of Fluid Mechanics* 440, 1–25.

Appendix A

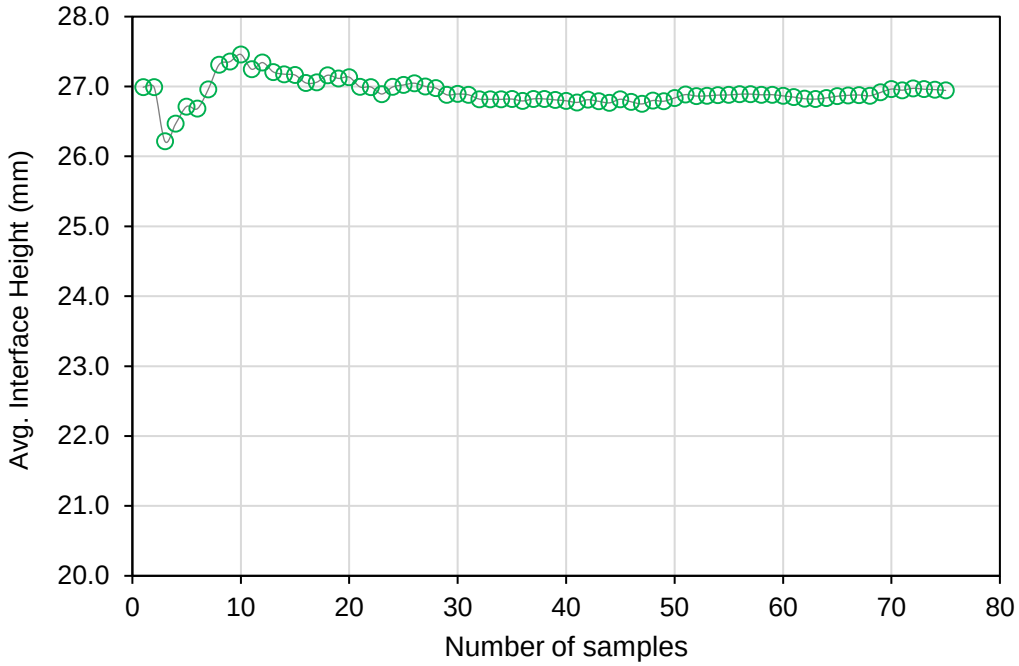

Figure A.1: Sample size selection for interface height

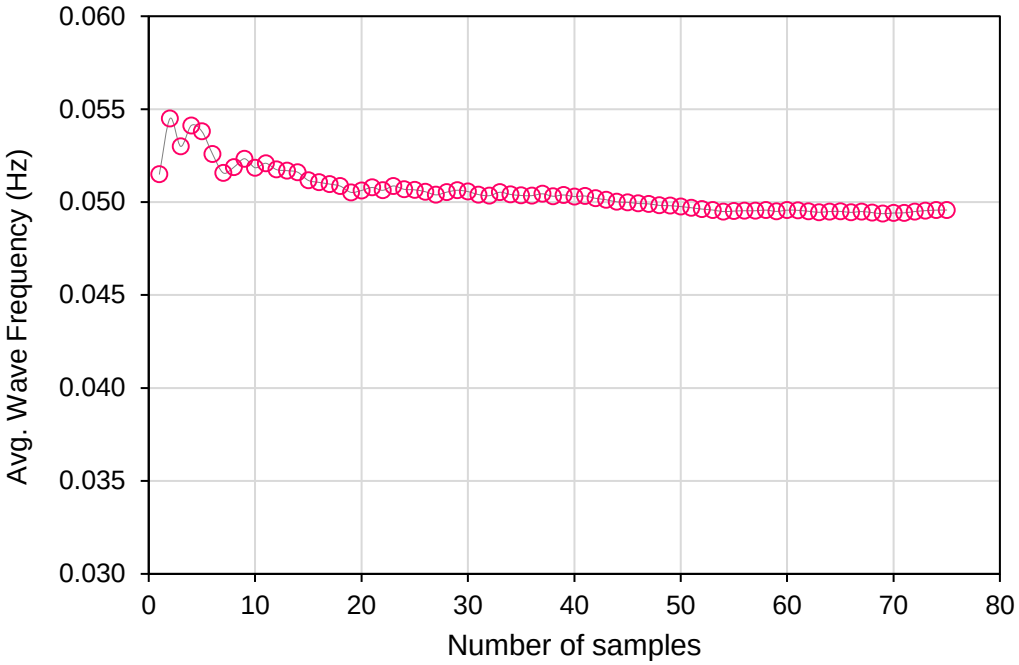

Figure A.2: Sample size selection for wave frequency

Appendix B

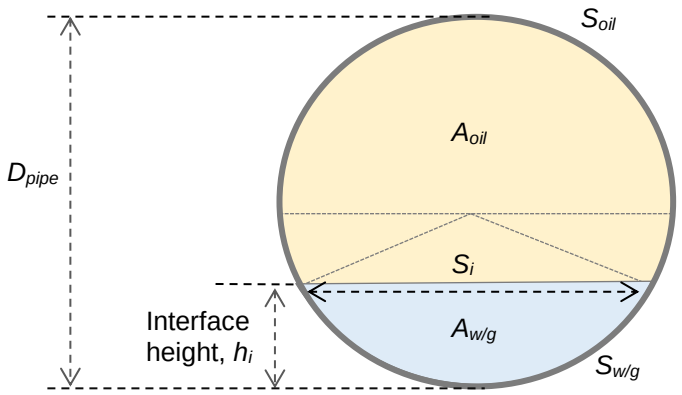

Figure B1: Calculation of area occupied by each phase

Table B1: Formulas for the determination of occupied area

Parameter	Formula
Interfacial length, S_i	$D_{pipe} \times \left(1 - \left(2\frac{h_i}{D_{pipe}} - 1\right)^2\right)^{1/2}$
Wall perimeter of oil phase, S_{oil}	$D_{pipe} \times \cos^{-1}\left(2\frac{h_i}{D_{pipe}} - 1\right)$
Wall perimeter of water/glycerol phase, $S_{W/g}$	$\pi D_{pipe} - S_{oil}$
Cross sectional area of pipe, A	$\frac{\pi}{4}D^2$
Are oil phase, A_{oil}	$\frac{D_{pipe}}{4} \times \left(S_{oil} - S_i \times \left(2\frac{h_i}{D_{pipe}} - 1\right)\right)$
Area of water/glycerol phase, $A_{w/g}$	$A_{w/g} = A - A_{oil}$